Increasing Access and Capabilities of CubeSats for Investigation of Earth Trojan Asteroids

Paul J Sturmer

A dissertation

submitted in partial fulfillment of the

requirements for the degree of

Doctor of Philosophy

University of Washington

2020

Reading Committee:

Robert Winglee, Chair

Marcel den Nijs

Paul Wiggins

Program Authorized to Offer Degree:

Physics

University of Washington

Abstract

Increasing Access and Capabilities of CubeSats for Investigation of Earth Trojan Asteroids

Paul J Sturmer

Chair of the Supervisory Committee:
Robert Winglee
Earth and Space Sciences

This thesis develops the requirements of a low-cost spacecraft mission to the Sun-Earth Lagrange point L4 and L5 to search for Earth Trojan asteroids, and develops and demonstrates a specialized communication system needed to facilitate such a mission. Asteroids serve as time capsules into the historical past of our solar system, and have been critical components to our understanding of the formation and evolution of our solar system. A subset of Earth co-orbital asteroids, Earth Trojans, being close to our home can help us understand things like the conditions present during Earth's initial formation or the Moon-Earth formation impact theory. Considering there is only one identified Earth Trojan asteroid, 2010 TK7, and the fact that numerical analysis and additional searches support a population of at least one hundred Trojans, a dedicated mission is well warranted. With the Earth Trojan asteroid regions particularly difficult to view when using Earth-based telescopes, an alternative approach is described herein: send a small low-cost spacecraft, called a CubeSat, directly to these regions for in-situ imaging.

CubeSats present a paradigm shift in spacecraft development and are beginning to offer a new low-cost and highly accessible regime to Earth and space science. CubeSats are small, typically 1-10L and 1-10kg, and leverage the recent miniaturization of smartphones and their

related technologies. The result is that in the past 10 years CubeSats have proven themselves to be invaluable for carrying out Earth-based science missions at a fraction of the cost using traditional methods. And more recently CubeSats have begun to leave Earth orbit, such as providing an auxiliary communication relay role on the latest NASA Mars mission.

With ever increasing fiscal pressures limiting the development of planetary probes, developments herein lay the groundwork for an Earth Trojan prospecting mission costing less than $500,000. This mission is facilitated by the developments of a compact communication system described in this thesis that includes: (1) low-cost application of high-gain reflectarray antenna technology to the CubeSat form factor, and (2) low-cost and low-risk design technique development of radio frequency circuitry needed to interface with the antenna. Furthermore, development of a CubeSat demonstrator mission was undertaken, called the HuskySat-1, providing proof of concept implementations of these technologies as well as additional technological innovations required to support a deep space mission to the Earth Trojans. The HuskySat-1 successfully deployed into a low-Earth orbit on January 31, 2020 with operational success.

TABLE OF CONTENTS

Acknowledgements

I would like to thank a number of key individuals at the University of Washington who made this work possible. A special thanks goes to my committee members, especially Professor Robert Winglee, who continually pushed me to think outside of the box, who provided room to grow and explore new ideas, and by example taught me the importance of student education. I am also grateful to Research Associate Professor Michael McCarthy, whose open-door policy and methodical technical approach was invaluable when working through problems and in supporting the development of HuskySat-1.

The HuskySat-1 project also involved significant contributions outside of the university. The team from the Radio Amateur Satellite Corporation (AMSAT) was invaluable for providing a radio, primary contributors were Gerald W. Buxton, Burns W. Fisher, Chris E. Thompson, Eric N. Skoog, and Carl E. Wick. The Amateur Radio community provided vital ground support, special thanks to Kenneth Swaggart as well as Don Sandstrom and the Boeing Employees Amateur Radio Society at the Museum of Flight. Hunter Mellema was invaluable for kick-starting the project and giving it its initial momentum. Paige Northway led the final push to launch the satellite into space. Jeff Chrisope developed and implemented the software framework for the satellite and operations, as well as mentored students in these areas. Nathan Wacker led various efforts within the project associated with software and operations.

For the development of COM2, Nicolas Gutierrez, provided assistance in electromagnetic simulation and design efforts. For evaluating the launch window sensitivity in the Earth Trojan mission, Robin Pflager helped with developing a 2D orbit propagator. I would like to thank my parents. I would also like to thank my employer, Blue Origin, for allowing me to work part-time while I finish my graduate work. Lastly, I would like to thank Jasper Yao for editing this work.

Chapter 1. Sun-Earth Trojans

1.1 Solar System Formation

This section provides an overview of the formation of our solar system with emphasis on general material transport, compositional stages, and formation of the inner planets. Today's understanding of the solar system relies on ideas developed from the 15th to 20th century by Copernicus, Kepler, Galileo, Newton, Descartes, Maxwell, Buffon, and Kuiper [6]. The overall theme of their inquiries were trying to answer: were the planets and the sun formed together? Do the planets consist of material that originated in the sun or are they interstellar material? Through the use of ground based telescopes, we continued to discover new objects as well gather more information of known objects. These observations demonstrated that all planets rotate in the same direction around the sun and all planets have nearly circular orbits.

Our solar system began formation 10^9 years ago starting as a large gas cloud, called a nebula. In 1796 Pierre-Simon Laplace showed that a large and dense enough spherical nebula contracts under its own gravity, and as it does its rotational velocity increases [53]. As the spinning increases the shape flattens out into a disk. This process resulted in an accretion disk [6]. Today we can observe this by the overall regulatory of the planets and their moons which are all nearly coplanar [6].

Temperature distribution began to play an important early role, with temperatures closer to the sun prohibitive for ice particle formation. Compositionally, water, methane, troilite, pyroxene, and corundum were present and whose concentrations varied with the distance from the Sun's location. The effect of temperature distribution can be observed today by the fact that the inner planets are primarily composed of rocky and metallic material whereas the outer planets are

primarily gaseous with their moons primarily ice [1]. Overall temperatures began to increase due to inhibition of radiative cooling by the increasing protoplanetary disk density. Temperatures peaked at ~2000K at a distance of 1 AU from the Sun as indicated by meteor evidence [1]. The result of this heating was the breaking up of existing dust resulting in enhanced transparency therefore allowing radiative cooling to begin lowering temperatures. As the temperature dropped, new compounds and dust were formed [1].

Accretion began through the process of coagulation with dust condensing into larger pieces. With mutual gravitational attraction too small to bring these small particles together, this process is primarily driven by collisions and is therefore highly dependent on initial dust densities [1]. However, much of this initial dust was blown away when the Sun went through a violent change transitioning from a protostar to a T Tauri star. This transition is demarcated by the switch over point from being fueled from thermal energy generated from gravitational contraction to being fueled by nuclear energy. Violent stellar winds blew out all bodies smaller than ~10m from the solar system. It is therefore understood that any resulting material within our solar system today, must have previously formed into bodies greater than ~10m before the T Tauri phase began [1]. This also suggests that any pieces today less than ~10m were created after the T Tauri phase through collisional processes.

The leftover accreted material continued to increase in size to become planetesimals as their size became ~10km and gravitational attraction became influential [1]. Continued collisions and aggregation started to form planetary embryos [1]. Until now, the shape of objects was believed to be lumped due to minimal self-gravitational attraction. As planetary growth continued the gravity became strong enough to shape the object to a sphere which occurs at approximately

~100km or larger [6]. For example, see Fig. 1.1 of 243 Ida which has an overall elongated shape with a mean size of ~32km [55].

Figure 1.1: Asteroid 243 Ida Close up Taken by Galileo Spacecraft [54]

The formation of the inner planets formed from the solar nebula through the process of accretion. The growth rate at this stage was centimeters per year [56]. Evidence from isotopes also suggests later bombardments occurred from planetesimals originating from the outer solar system. The leading theory of the moon's formation was that it was caused by a mars-sized collision with the Earth. The ejected material, some of which originating from Earth's mantle, reformed into the Moon [6]. Asteroids, as discussed in the next section, have a played a key role in helping build this story.

1.2 Asteroids

In 1801 Giuseppe Piazzi discovered a new object in the sky which at the time was thought to be the "missing planet" lying between the orbits of Mars and Jupiter [6][46]. As discoveries of additional objects continued, and by the mid-19th century the idea of the "missing planet" and Titius-Bode law gave way to the modern idea of the asteroid belt. Giuseppe is credited for discovering the first asteroid, called Ceres, which is just one of out of the main belts 10^5 asteroids [6]. In 2006, Ceres was reclassified as a dwarf planet, and is the largest object in the asteroid belt

[59]. The main asteroid belt lies in a region 2 to 3.5 AU from the Sun between Mars and Jupiter, see Fig. 1.2-1.3. It is a highly populated region with asteroids understood to contain leftover remnants of planet formation. Asteroids representing leftover remnants, or planetesimals, are an important part of current scientific understanding of the solar system's formation since they provide snapshots of the past solar system conditions during various formation stages. The main belt is unique in that the region is so highly populated even today, whereas in other regions most planetesimals went on to form planets. However, at this location they were never able to accrete into a planet due to the continued gravitational perturbations caused by Jupiter. While there are 10^5 main belt asteroids today, it is believed that the population was once much greater, and that perturbations by Jupiter ejected a high percentage of the initial population, which we can see the result of today by the vast number of large craters on every solid surface we've inspected. Planetesimals containing water were perturbed by Jupiter for a crash course towards Earth and are thought to be our sole source of water [6].

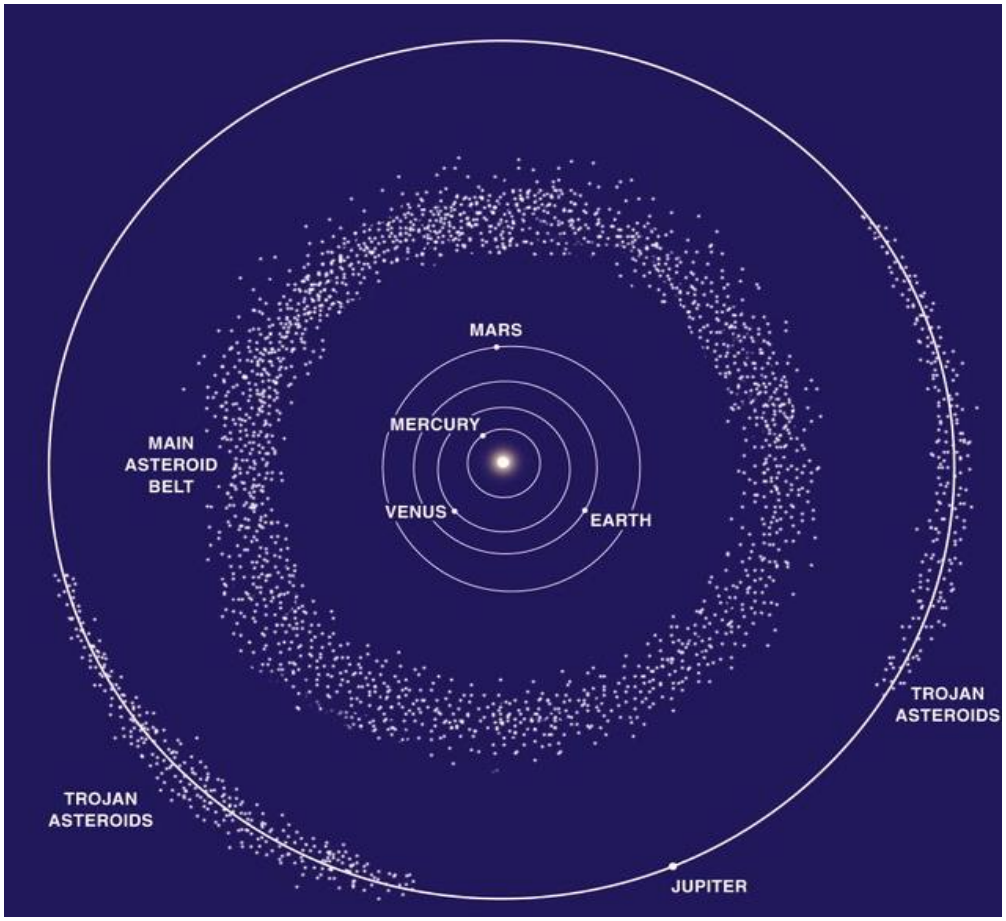

Figure 1.2: Asteroid Belt [47]

Today there are an estimated 10^6 asteroids within our solar system with varying orbital parameters. Generally orbital eccentricities are less than 0.3, and orbital distance and inclinations are shown in Fig. 1.3-1.4 [9]. Data from Jet Propulsion Laboratory (JPL) Small Body Database was used to create Fig. 1.3-1.5. The database contained 957481 asteroids, for which 136210 were used in this analysis for having defined diameter, inclination, and semi-major axis information [41].

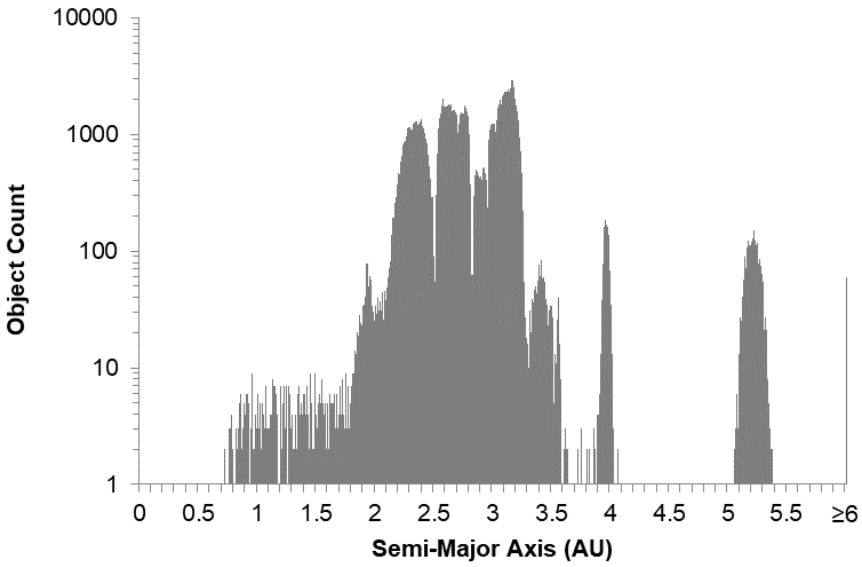

Figure 1.3: Solar System Distribution of Asteroid Semi-Major Axis

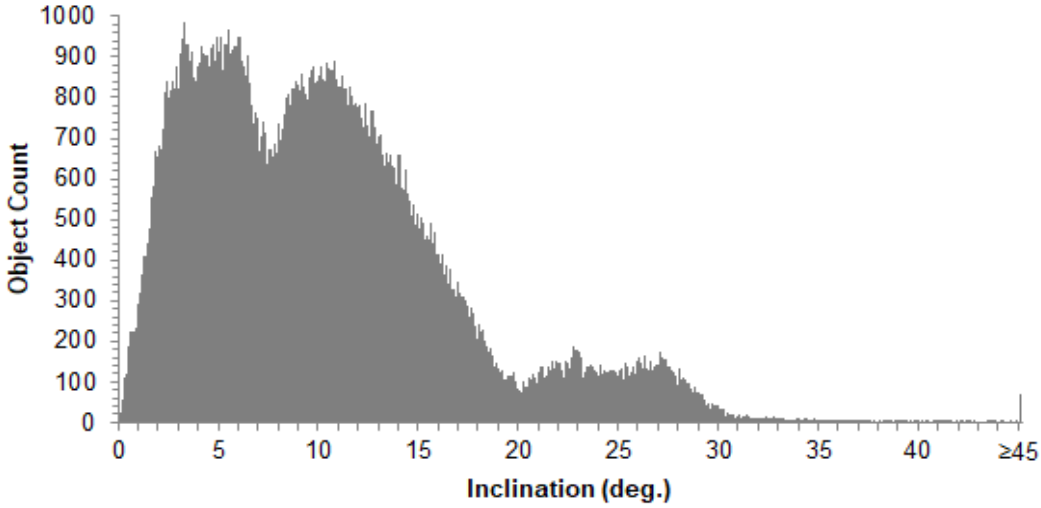

Figure 1.4: Solar System Distribution of Asteroid Inclinations

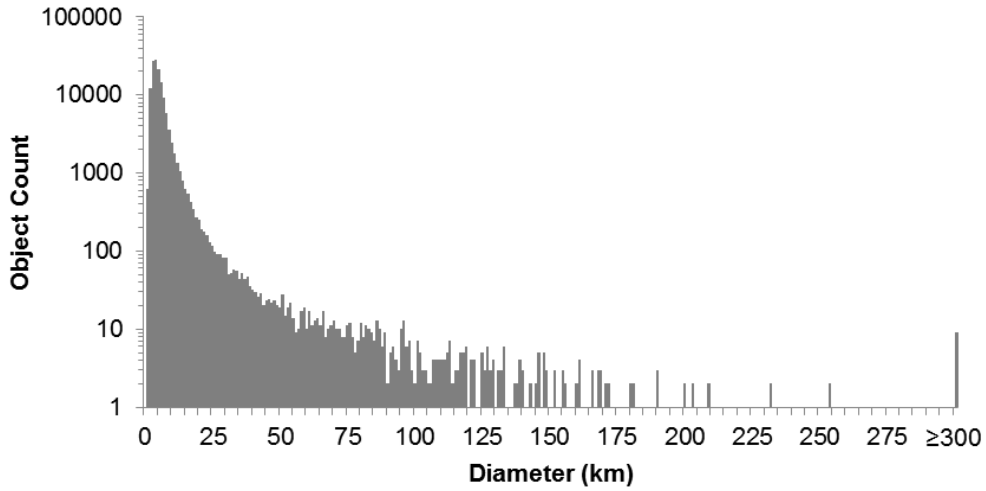

Figure 1.5: Solar System Distribution of Asteroid Sizes

While the precise initial conditions, sequence of events, and phenomenon of the formation and evolution of the solar system, laid out in Section 1.1, continues to develop, asteroids serve as a valuable resource in helping our understanding because they serve as time capsules into earlier formation stages and subsequent dynamical evolution. Knowledge of their sizes, distributions, morphologies, and cratering or fragmentation can help provide constraints for our computation models. The Planetary Science decadal survey recognizes the following objectives for the continued studies of asteroids [57]:

- Understand pre-solar processes recorded in the materials of primitive bodies
- Study condensation, accretion, and other formative processes in the solar nebula
- Determine the effects and timing of secondary processes on the evolution of primitive bodies
- Assess the nature and chronology of planetesimal differentiation. Additionally, Earth specific questions asteroids can help answer [30]:

- What accounts for the discrepancy between the ratio of crater density on the leading versus trailing sides of the moon?
- What role does the Yarkovsky-O'Keefe-Radzievskii-Paddack (YORP) effect have on dynamical evolution models?

The scientific importance of asteroids are due to their prominent role in helping develop our theories of solar system formation and dynamical evolution. Some of most early analysis of the chemical composition and structure of asteroids came from those reaching Earth in the form of meteorites and have been foundational to our understanding of the solar system. Another method of obtaining samples are previously fallen meteorites [9]. For example, as of June 2020, 268 meteorites have been found on Earth and have been identified as having Martian origin [147]. Successful sample return missions include asteroid 25143 Itokawa from the Hayabusa mission [148], comet 91P/Wild from the Stardust Mission [149], and lunar rocks and regolith [152]. Additionally, there are two asteroid sample return missions underway: JAXA's Hayabusa2 has already collected samples from asteroid 162173 Ryugu and is expected to return to Earth in late 2020 [150], and NASA's OSIRIS-Rex is planning to return samples of asteroid 101955 Bennu in 2023 [151].

Asteroid compositions are classified into three groups: (1) C-type, also called chondrite, which are made up of silicate rocks and clay, (2) M-type which are made of nickel-iron alloy, and (3) S-type, all called stony, which are a combination of silicates and nickel-iron [9]. The composition and structure of these samples provides insight into the type of conditions present during their initial formation. Asteroid composition is important because after they initially formed their internal structure has been wholly unchanged, and their battered surfaces over time created a layer of regolith debris offering a time capsule to their collisional behavior. Mapping out the mass,

composition, rotational characteristics about their axes, and size distribution of asteroids helps us understand the collisional frequency, initial populations, and dynamics of the solar system. It also helps augment our computational tools being limited due to the vast number of species to track and timescales involved [6].

1.3 Trojans

Trojans are a unique subset of asteroids because they populate stable equilibrium regions about the orbit of two larger masses.

1.3.1 Lagrange Points L4 and L5

While there are no general solutions for the 3-body orbital mechanics problem, in 1765 Leonhard Euler discovered for circular orbits there exist three equilibrium points now called L1, L2 and L3. This assumes the body placed at one of these points to be of negligible mass [48]. Shortly after, in 1772, Joseph-Louis Lagrange discovered two additional points, L4 and L5, which assume the two larger masses to have a mass ratio of at least ~25:1 [49]. Shown in Fig 1.6, points L1, L2, and L3 are unstable equilibrium, while points L4 and L5 are stable [11][12]. Another interpretation is that L4 and L5 are the locations which form circular orbits about the barycenter formed by the two main masses. His theory predicted that an accumulation of matter, such as asteroids, should exist in points L4 and L5.

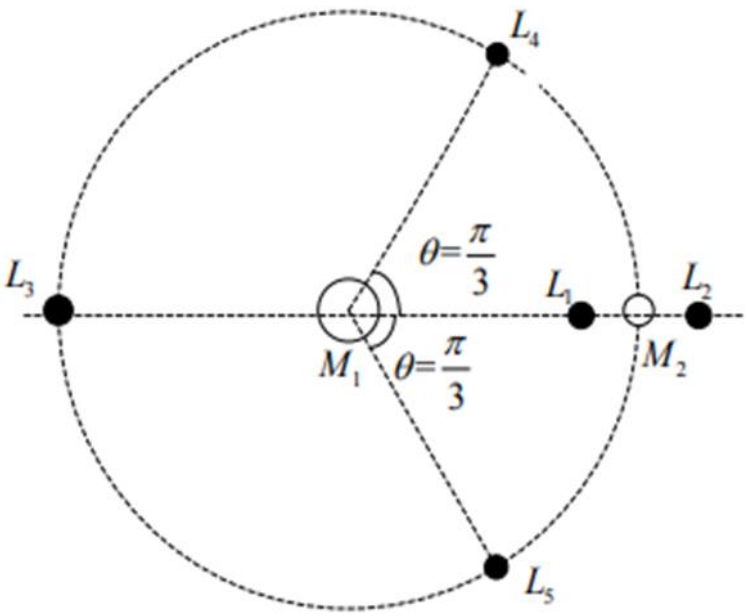

Figure 1.6: Lagrange Points [10]

Lagrange laid the groundwork for explaining the clustering of asteroids shown in Fig. 1.2. Starting in 1906, astronomical observations began to confirm this theory with the discovery of the first Sun-Jupiter Trojan asteroid coined as 588 Achilles in 1906 [24]. With today's population of over 7000 asteroids, the Sun-Jupiter Trojan population is the largest Trojan population in our solar system, see Fig. 1.2 [16].

Beyond the highly populated Sun-Jupiter Trojan regions, Trojans of other planets have also been discovered, see Table. 1.1. Numerical analysis for Saturn suggest the gravitational perturbations caused by Jupiter are too large for a stable Trojan population, and numerical analysis involving Mercury suggests Trojans can indeed exist, though detection would be difficult due to their proximity to the Sun [50][51][52].

Table 1.1: Trojans throughout Solar System

Planet	Number of known L4 or L5 asteroids
Jupiter	7079 [16]
Venus	1 [13]
Mars	9 [14]
Earth	1 [15]
Neptune	23 [17]
Uranus	2 [18][19]

1.3.2 Earth Trojans

Unlike the abundant Jupiter Trojan population, Earth Trojans asteroids (ETA) are especially difficult to detect due to the apparent location near the sun [24]. From Earth's vantage point, ETAs are never observed at opposition, which makes them even fainter due to their angle to the Sun [58]. Furthermore, since ground based searches must be completed at dawn and dusk due to ETA's normally being in the daytime sky, a higher air mass further hinders observations [58]. In 2010 the first Sun-Earth Trojan was discovered called 2010 TK7 [25]. It has a 380m diameter and orbits about L4 and 21 degree inclination [21]. Within the class of Near-Earth Asteroids (NEA), 2010 TK7 is a relatively standard size. A NEA is defined as an object with a closest approach to the Sun is less than 1.3 AU [45]. The sizes for all known NEA's of size 3km across or less are shown in Fig. 1.8 [41]. The orbit of 2010 TK7 propagated into the future, Fig. 1.7, shows it's tadpole orbit and demonstrating the spatial extent of the region encompassed by L4 or L5 [22][24].

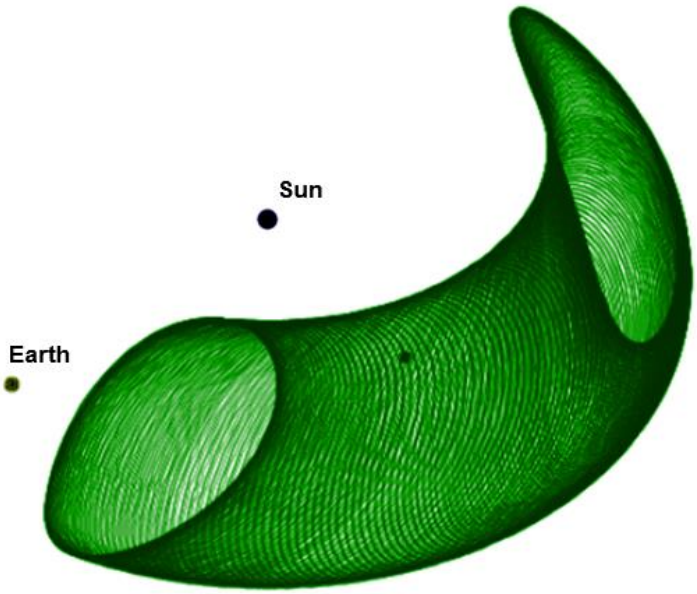

Figure 1.7: 2010 TK7 Orbit in co-Rotating Frame

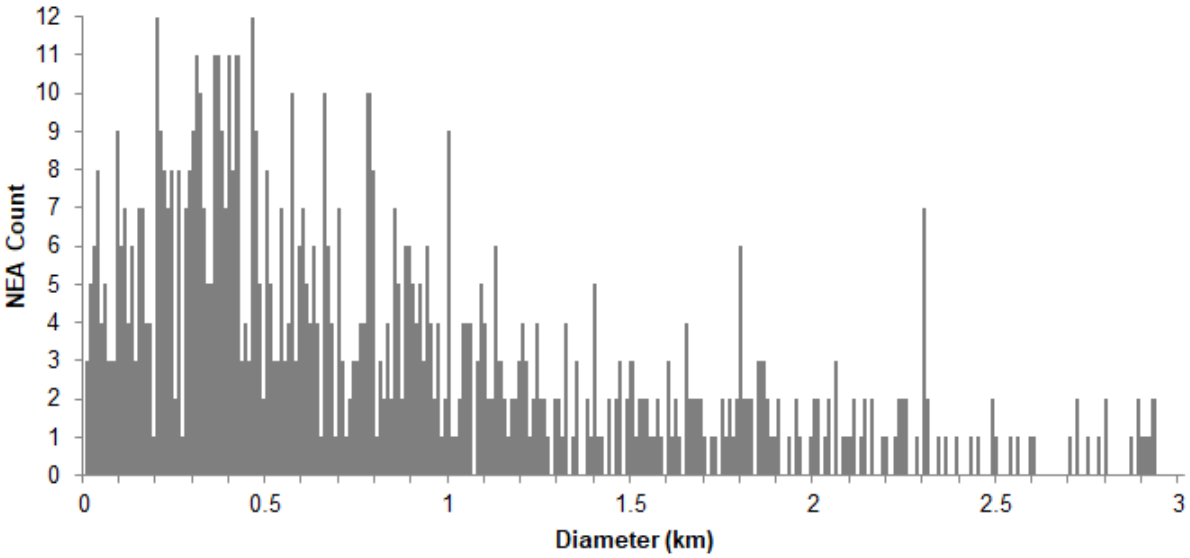

Figure 1.8: Near-Earth Asteroid Diameters Distribution for Diameters Less Than 3km

Previous work using Monte Carlo simulations have shown ETA regions to be stable suggesting that a large population could exist [23]. It is difficult to assess long term stability on

the timescales of solar system evolution. Numerical studies of this type are able to extend up to time scales of the Earth's age of 10^7 years due to limited computational resources [26]. Studies have furthermore shown that, for all planets except for mercury, L4 and L5 are stable for at least 1 million years [29]. Through simulation, it has also been found that moderate inclinations, of about 10-40 degrees, yields the most stable of orbits. These types of analyses can be used to develop optimal search strategies for maximizing the probability of finding additional ETAs.

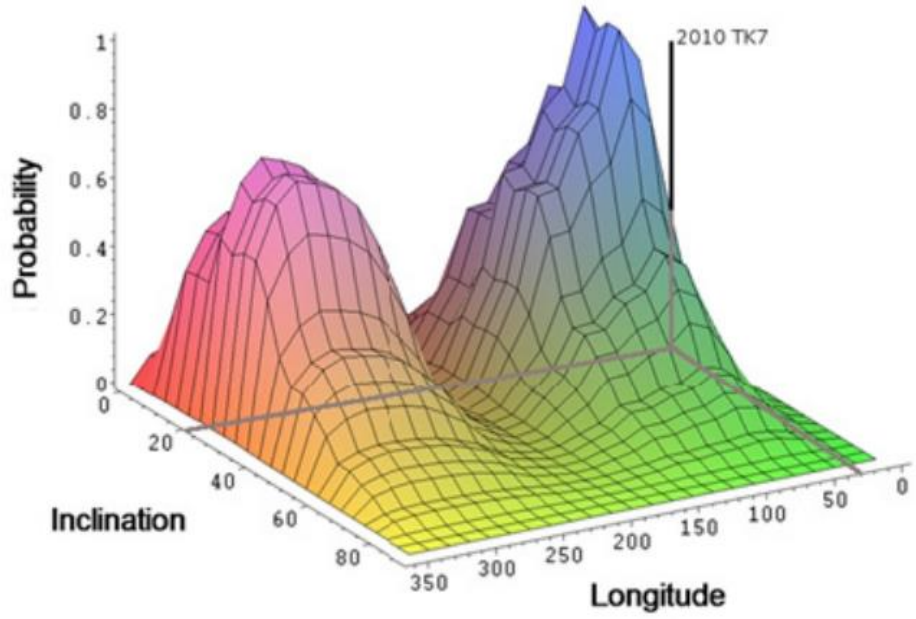

Figure 1.9: Earth Trojan Asteroid (ETA) Orbital Probability [32]

1.3.3 Previous Searches

Ground based observations are particularly restricted due to time-limited observational windows. The L4 and L5 regions are typically in the daytime sky limiting any observations to dawn (L4 region) or dusk (L5 region). Dawn and dusk measurements, which much be short by necessity, are hampered by the additional air mass through which the observations must be made through [27][29]. In addition to ground based searches, previous attempts for discovering additional ETAs have utilized pictures taken during flybys of the L4 or L5 regions. However, all

flyby missions, discussed further below, have had ETA searches as their secondary mission goal making them arguably not ideally suited for ETA discovery.

Ground based attempts at discovering ETAs were made by various groups in 1983, 1998, 2000 [27]. The most significant was using the University of Hawaii 2.24-m telescope in 1998 [29]. Their work focused on a $0.35\ \mathrm{deg}^2$ area focused at L4 and L5 [29]. While this null result was used to set a rough upper bound to the number of ETAs, results from Fig. 1.9 calls to question the significance of this null result since regions of higher inclinations than those imaged are predicted to have a higher probability of ETAs. From Fig. 1.9, the region of the sky where ETAs are most likely to be found is $\sim 3500\ \mathrm{deg}^2$ [32]. In 2020 another search was carried out using the Dark Energy Camera (DECam) instrument on the 4m Blanco Telescope at the Cerro Tololo Inter-American Observatory (CTIO). DECam is a CCD imager with a 2.2 degree field-of-view. The study did was unable to detect any new ETAs, but it did set the upper bound at L5 to be <1 ETAs for H<15.5, 60−85 ETAs with H<19.7, and 97 ETAs with H<20.4 [58].

There are a number of prominent space missions relevant to the search for ETAs; these are WISE, Gaia, OSIRIS-REx, Stereo A and B, and Hayabusa:

- Wide-field Infrared Survey Explorer (WISE) was a NASA mission launched in 2009 with the purpose to perform a full sky astronomical survey in the 3.4, 4.6, 12 and 22 μm bands (38). While previous ground based searches were unable to discover any ETAs, this discovered the first and only known ETA: 2010 TK7 [25]. Even though the intent of this mission was to discover new asteroids, the mission design hindered its ability to discover ETAs. The limitation of WISE to search for ETAs was from the look angle which was 90 degrees from the sun at all times [38]. In addition to a single ETA discovery, this mission successfully discovered hundreds of new asteroids [25]. . As shown in Fig. 1.7 the WISE

viewing angle intersects with the orbit of 2010 TK7 but was unable to view directly at the center of L4 or L5.

- Gaia, coined the "Billion Star Surveyor", was developed by ESA and launched in 2013 with the purpose of precisely cataloging the motions of ~1 billion astronomical objects using an optical telescope [28][39]. With expected operation to continue through 2022, no ETAs have yet been detected. Previous work did consider this feasibility, and concluded that while Gaia spatial coverage does include regions where ETAs are likely to exist, it's optical telescope is limited to detecting ETAs down to ~600m diameter assuming an albedo of 0.2 [23][24][28]. Only ~300m across, 2010 TK7 is predicted to not be detectable by Gaia [28].
- Origins, Spectral Interpretation, Resource Identification, Security, Regolith Explorer (OSIRIS-REx) is a NASA asteroid sample return mission launching in 2016 with a planned return in 2023 [4]. While flying past L4 in early 2017, this mission used an optical camera searching for ETAs. During this 10 day survey it detected 16 previously identified main belt asteroids, but no new ETAs [33]. From this null result, an upper limit of L4 ETAs was determined to be 73 +/- 22, and L5 of 194 +/- 116, consistent to the earlier results of a few hundred [33]
- Stereo A and Stereo B, launched in 2006, was a solar observation mission. Two identical satellites leaving Earth on orbits putting one of the satellites towards L4 and the other toward L5. While not their primary mission, NASA had planned to repurpose this mission to search for asteroids using an onboard wide-field-of-view telescope when passing through these regions. No follow-up reports were found regarding the conclusion of these searches or even if they were attempted. The only known information available from the

literature is just before reaching L4 in August 2009, STEREO experienced onboard anomalies, [34][35][36].

- Hayabusa2, a mission developed by the Japanese Space Agency (JAXA), is a follow-up mission from the initial Hayabusa asteroid sample return mission. Like its precursor mission, Hayabusa2 rendezvoused with an asteroid, collected samples, and is returning to Earth in 2020 [42]. During Hayabusa2's departure from Earth it passed through L5 on April 18, 2017 during with 3 sets of optical band pictures, but was unsuccessful in detecting any new ETA's [37][43].

1.4 Conclusion

Serving as time capsules into the past, asteroids help us understand the formation and evolution of our solar system. Moreover, ETAs can help us answer: While the inner rocky planets and outer gaseous planets show a systematic chemical gradient in our solar system, is the same true for asteroids within the inner solar system? What role do primitive bodies have in the creation of planets and life? What is the original source of ETAs? Are they primordial leftovers from the initial protoplanet formation, debris from the crater impact resulting in the moon's formation, or are they captured objects from the main belt?

Not finding ETAs in a follow-on mission, such as that described in chapter 4, is still valuable because it would provide more robust upper limits on a possible ETA population. Characterizing these limits is important to use to help refine initial conditions in computation models of the evolutionary history. For instance, during the formation of the inner planets, there was thought to be residual planetesimal populations responsible for helping dampen orbital inclinations and eccentricities to today's values. Such a residual population should then of lead to a small fraction of these materials being trapped at L4 or L5. With only one identified ETA, 2010

TK7, there is much to be gained by the discovery of additional ETAs. Discovery of at ETA population can provide constraints on the boundary conditions on the solar system's dynamical and evolutionary history [58]. While numerical simulations predict the existence of a population of ETAs, no ground based efforts or flyby missions have yet to discover said population. Current upper limit for ETA's is at least one hundred asteroids of ~300m or greater in size [30]. And considering the size distribution of the NEAs, see Fig. 1.8, it is therefore likely many additional smaller ETAs exist. It is noteworthy that given the area where ETAs are likely to be found, $\sim 3500\ \mathrm{deg}^2$ from Fig. 1.9, surveying this large area with any currently ground based telescopes is not practical [32]. Therefore, a new approach to discovering an ETA population would be highly valued.

An additional benefit of discovering an ETA population are the opportunities provided for follow-on in situ characterization, sample return missions, in-situ resource utilization, and testing of space other space systems hardware. The energy requirements for visiting an asteroid, measured in ΔV, are best understood by considering the population of Near-Earth Asteroids (NEA). A NEA is defined as an object with a closest approach to the Sun is less than 1.3 AU [45]. Data from rendezvous calculations performed for all known NEAs in January 2018, totaling 4972 objects, was used to create Fig. 1.10 [44]. The lowest ΔV energy requirement for rendezvous for these NEAs is ~3.8 km/s, while the mode is ~7 km/s. In contrast, as will be detailed in Chapter 4, Lagrange point L4/L5 can be accessed with ~10x lower energy.

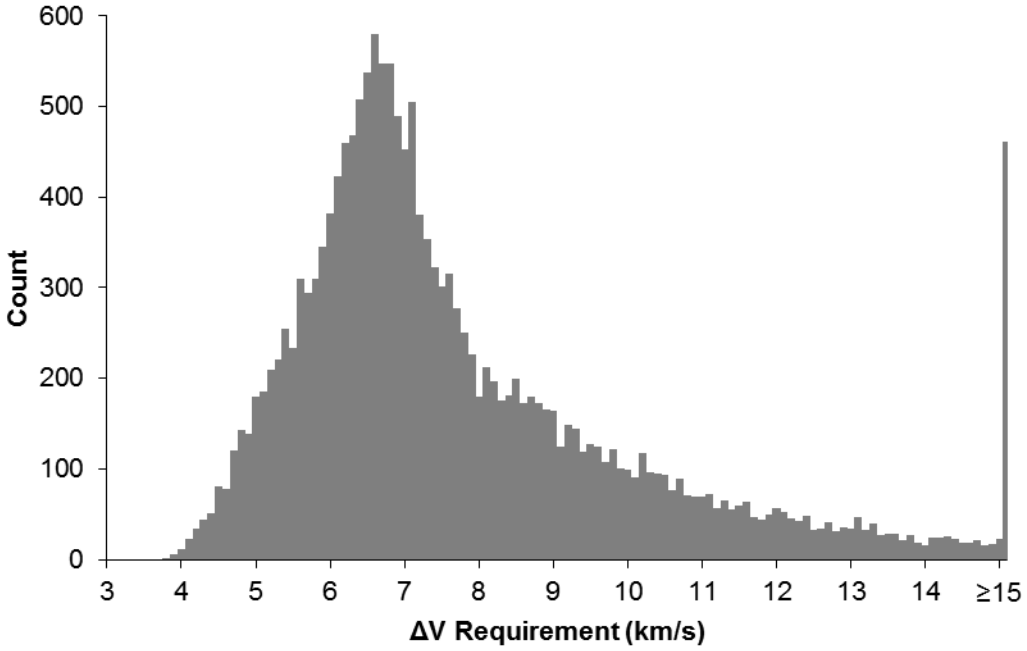

Figure 1.10: Energy Requirement for Rendezvous with Known Near-Earth Asteroids

The proceeding chapters of this dissertation describes the novel approach for discovering an ETA population. This approach relies on performing in-situ observations leveraging a low energy transportation method and an extremely low cost and short development time spacecraft. This type of spacecraft is called a CubeSat, and is the topic of Chapter 2.

Chapter 2. CubeSats: An Upcoming Low-Cost Deep Space Probe

In Chapter 1, the scientific motivation was provided for sending a spacecraft directly to the Earth Trojan Asteroid regions for investigation of detecting new asteroids. The proposed solution is to utilize a new type of standardized low-cost spacecraft called a Cube Satellite, or CubeSat. While previous space system development was primarily military, civil, and commercially motivated, CubeSats present a paradigm shift in spacecraft development enabling education institutions direct access to spacecraft development for Earth and space science. CubeSats are small, typically 1-12L and 1-16kg, and leverage the recent miniaturization of smartphones and their related technologies. The result is that in the past 10 years CubeSats have proven themselves to be invaluable for carrying out Earth-based science missions at a fraction of the cost using traditional methods. Beyond the lowered cost of spacecraft development, the other significant cost driver for space missions, access to space on a launch vehicle, is beginning to significantly decrease. While these circumstances provide the education sector a new low-cost opportunity to lead the development and execution of the Earth Trojan Asteroid mission, discussed in Chapter 4, CubeSat limitations still need to be overcome. The improve CubeSats performance addressed within this dissertation is the development of a low-cost high-performance communication systems required for downlinking science data and spacecraft position determination.

2.1 History

The Hubble Space Telescope and the Voyager space missions demonstrate the significant impact artificially built satellites have had on increasing our understanding of the solar system and universe. To understand the history of the CubeSat, it is important to consider the traditional

paradigm of space system development. Initial technology development was primarily military motivated and funded, followed by later use in the civil, such as NASA, and commercial industries. One notable example of this is the Hubble Space Telescope which utilized a 2.4m main mirror leveraging fabrication techniques developed for military spy satellites [60]. Another example is with the development of ground based navigation using radio frequency (RF) signals from satellites, which was first demonstrated by the military in 1960, and in 1983 was made available for civilian use [61][62]. In the traditional paradigm of space mission development the overall cost is high: launch costs are high, risk posture pushes for high reliability, long developmental times, and fulfilling the mission objectives often requires development of entirely new spacecraft instrumentation.

In parallel with the shrinking of consumer electronics, such as with the smart phones, and ever smaller die sizes in Complementary Metal Oxide Semiconductor (CMOS) and gallium nitride (GaN) substrates, a new type of satellite design paradigm emerged shifting from a low risk and high reliability to the idea of leveraging commercial developments and minimizing cost. This was codified in 1999 with a partnership between California Polytechnic State University and Stanford creating the standardized and modularized CubeSat specification [63]. Rather than being a useful scientific instrument, the initial purpose of the CubeSat was to provide undergraduate and graduate students with direct access to space systems engineering and science mission development.

CubeSats are a type of small satellite which have the form factor of multiple 10x10x10cm units (1U) each with a mass of 1.3kg or less. The most common size is 10x10x30cm (3U) and is shown in Fig. 2.1. Typically as secondary launch payloads, CubeSats receive low launch priority and have design/operational restrictions to further reduce their risk to the primary launch payload. Some of these restrictions include needing to keep the spacecraft unpowered before deployment,

3 inhibits for inadvertent operation of communication and propulsion systems, and total chemical stored energy under 360kJ [64]. Pressurized vessels used in the propulsion system pose an increased risk to the primary launch vehicle, and therefore are not preferred, and at times prohibited, on CubeSats. Furthermore, since CubeSats 'piggyback' on larger missions their choice of orbit is limited. These rigid requirements for CubeSats have, on the one hand, quickly created a market of suppliers and consumers of CubeSat standardized hardware, but have also changed what types of missions can be completed. The standardization of CubeSats also contributed to their low launch costs compared to their full-size satellite counterparts because fewer resources are necessary for their integration into launch vehicles.

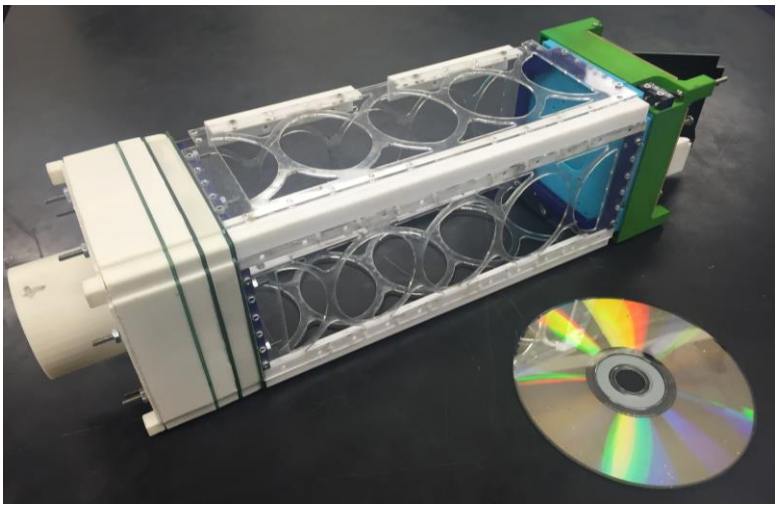

Figure 2.1: UW HuskySat-1 CubeSat Concept Design (3U)

While initially conceived as a higher education learning tool, the CubeSat community continued to reach into increasingly complex missions, and slowly CubeSats began successfully carrying out publishable science missions. One notable mission was GeneSat [66]. Launched in 2006, it was significant because it demonstrated that CubeSats could be quickly developed and yield significant scientific results. From initial concept to orbital data was only 3 years, something

highly unusual for any satellite mission development. The mission carried suspended E. coli bacteria in a miniature laboratory that was monitored and stabilized for temperature, humidity, and pressure. A ground command then released an E. coli nutrient starting its growth. The growth was monitored using a fluorescent protein. The purpose of this experiment was to investigate how lack of gravity affects mass transport and nutrient delivery. Additionally, it studied how E. coli's growth is affected due to increased space radiation from being outside of Earth's ionosphere. Beyond the GeneSat, past NASA and NSF CubeSat funding has spanned across a wide variety of sciences, as is shown in Table 2.1.

Table 2.1: CubeSat Science Mission Distribution Funded by NASA and NSF 2006-2016 [66]

Astronomy and Astrophysics	Biological and Physical Sciences	Earth Sciences	Solar and Space Physics	Planetary Sciences
1	8	8	24	3

One of the large appeals to CubeSats is their low cost relative to their full-size satellite counterparts. Consider NASA's Cassini, New Horizons, and Europa missions, each having a price tag of $3.3 billion, $700 million, and $2.5 billion, respectively [68]. Part of this high cost is due to the launch cost itself, since most satellites launched are flown as primary cargo. For example, SpaceX Falcon 9 launch to LEO is $62 million [69]. There is no standardized satellite shape, so each launch requires mission-specific integration. The CubeSat's low mass and conformity to a standardized geometry lessens the launch requirements and reduces the cost ranging from being free-of-charge up to ~$300,000 [70]. My efforts aligned with the principle of reducing CubeSat costs by: (1) developing low cost methods of printed circuit board fabrication and assembly; (2) building a CubeSat program with supported the recruitment and training of undergraduate talent to develop CubeSat hardware and software; (3) adopting the "design and build it" mentality in

place of the “buy it” mentality for all HuskySat-1 components; and (4) fostering a relationship with the volunteer AMSAT organization to enable integration a AMSAT radio. See chapter 5 for more detail.

Beyond the launch itself, CubeSat development costs range from being crowd sourced using simple commercially available components and volunteer labor, or at times into the multi-million dollars endeavors, such as with NASA’s upcoming CAPSTONE CubeSat costing $13.7 million [125]. The allure of CubeSats has definitely caught on as is evident in their recent proliferation in Fig. 2.2.

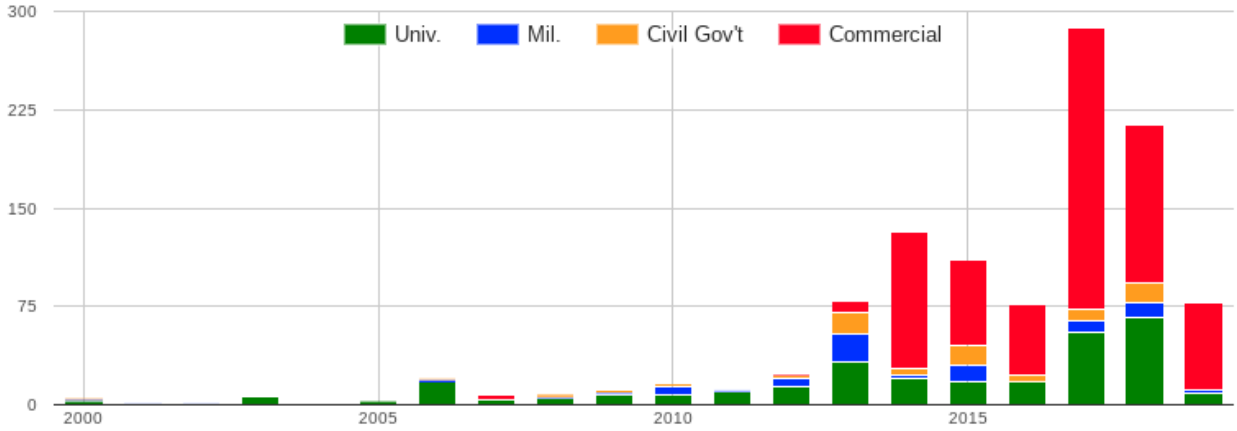

Figure 2.2: Yearly CubeSat Launches [67]

From their inception, CubeSats heavily rely on commercial-off-the-shelf (COTS) components. While these components provided student accessibility and increased accessibility to space, this design methodology is at contrast with the robustly-engineered and radiation-hardened components regularly used in the space industry. Although the use of COTS necessarily decreases spacecraft reliability, this weakness has created a paradigm shift in the space industry towards trial-and-error improvement. The academic environment of publishing and sharing ideas has allowed for quick progression to determine which types of COTS components work best, and what

design principles to follow. For instance, what is the best balance point between simplicity and redundancy? Redundancy entails complexity, and complexity entails increased development and testing time. Working on an academic time schedule, in which student presence is limited due to other academic commitments, means that a more redundant system may not receive as much testing time as a simple architecture. Another advantage of CubeSats being low-cost and more tolerant to risk making them suitable for testing and quickly adopting new technologies before they are adopted by the larger satellites. HuskySat-1 project contributions relate to these themes by leveraging state-of-the-art COTS solutions for critical subsystems. In particular, the microprocessor architecture was extremely unique being: (1) highly distributed, (2) interconnected nodes utilizing the CAN bus, (3) master-less, (4) in-house developed board support package, SPI/I2C libraries, and an abstracted CAN layer, and (5) utilizing the MSP430FR59xx processor which was released only in 2016. Additionally, the HuskySat-1 final design utilized 3 separate software stacks made to all be interoperable on the CAN bus to support cross-family microprocessor communication support. My contributions in the microprocessor implementation was the down selection to the MSP430FRxx and CAN bus, as well as architecting the distributed architecture. The HuskySat-1 also had two advanced technology demonstrations, the pulsed plasma thruster and the 24 GHz transmitter. The pulsed plasma thruster used a high voltage charging topology and printed circuit board design developed by myself, while the 24 GHz transmitter was developed entirely by myself and is described in chapter 3. And lastly, the satellite structure design, also developed by me, was unique in allowing each of these two aforementioned advanced technologies to be single point grounded to the bus.

While most functionalities of CubeSats, at their best, are less capable than a full size satellite, they do have the potential of increasing scientific return through constellations. Examples

of when constellations are useful are situations requiring higher temporal resolution, Doppler ranging and object tracking, and higher spatial resolution by phase cohering multiple CubeSat receivers. An example of a future constellation is with Jet Propulsion Laboratory (JPL) CubeSat Constellation at Mars. With a 60 satellite constellation at Mars, geography and atmospheric electrical properties will be studied [72].

CubeSats also have applications in supplementing primary satellite missions. This is feasible because a typical satellite has a mass that is much larger than the CubeSat. Some examples of this utility: (1) the CubeSat could be ejected from the primary satellite and used to collect additional scientific measurement data, (2) it could be deployed and used as an interferometer mirror to measure small gravitational perturbations, (3) or it could be used in a bistatic radar setup to map out a planetary surface. While these examples do not require active spatial control of the ejected CubeSat relative to a mothership satellite, gaining this degree of freedom opens up a variety of additional data gathering options. Professor Robert Winglee, graduate student Paige Northway, and I made contributions to this type of application by supporting a Europa CubeSat concept study in response to a JPL solicitation to carry CubeSats as secondary payloads onboard the upcoming Europa Clipper mission. The MAgnetics CUbe SATellite (MACUSAT) was a 3U CubeSat focused on providing supplemental magnetic field measurement data beyond that gathered by the Clipper. Two orbital scenarios were evaluated, as well as evaluation of the communication link being optimized for total science data transfer back to the Clipper. For background, the Europa clipper will orbit Jupiter 44 times, where its orbit has been optimized to map out Europa's magnetic field. I evaluated the two orbit scenarios using the System Tool Kit (STK) and Astrogator software package. In the first scenario, MACUSA could be dropped off before a fly by, providing additional spatially magnetic field data, see Fig. 2.3. In the second scenario, direct orbit insertion via a polar

orbit was considered which would have tremendous value over the Clipper measurement data since the Clipper is performing flybys only, see Fig. 2.4. This scenario required a 3.26 km/s ΔV.

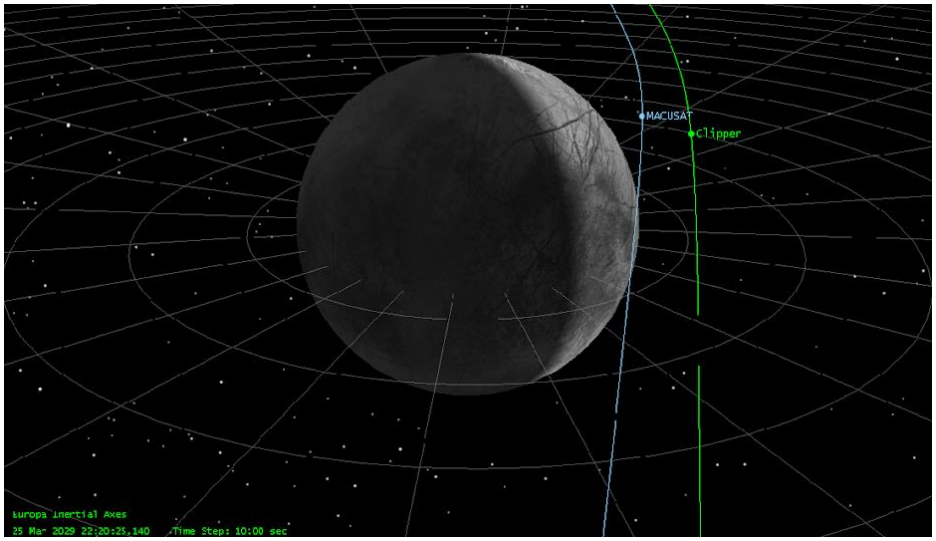

Figure 2.3: MACUSAT Trailing Orbit to Europa Clipper

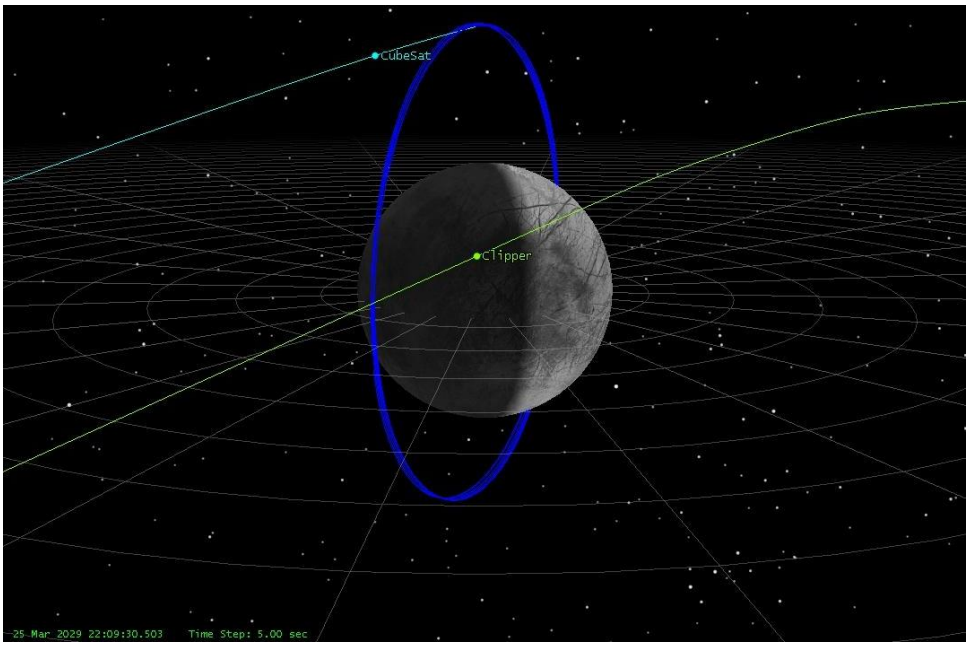

Figure 2.4: MACUSAT Europa Direct Orbit Insertion

The second contribution I made to the MACUSAT concept study was evaluating the

communication link necessary in the previously described direct insertion orbit scenario. This evaluation consisted of providing zeroth order estimate on the MACUSAT's ability to transmit science payload data back to the Europa Clipper. The assumptions were: UHF band, 6 dB gain Clipper antenna, 0 dB gain MACUSAT antenna, 20 dB analysis margin, receive system noise temperature 150 K, required Eb/N0 11.3 dB for BPSK uncoded, a 0.5 kg battery at $200\ \mathrm{W \cdot hr/kg}$, and a 10% DC to RF efficiency. These assumptions are very conservative and represent an upper bound, see Fig. 2.5 for results.

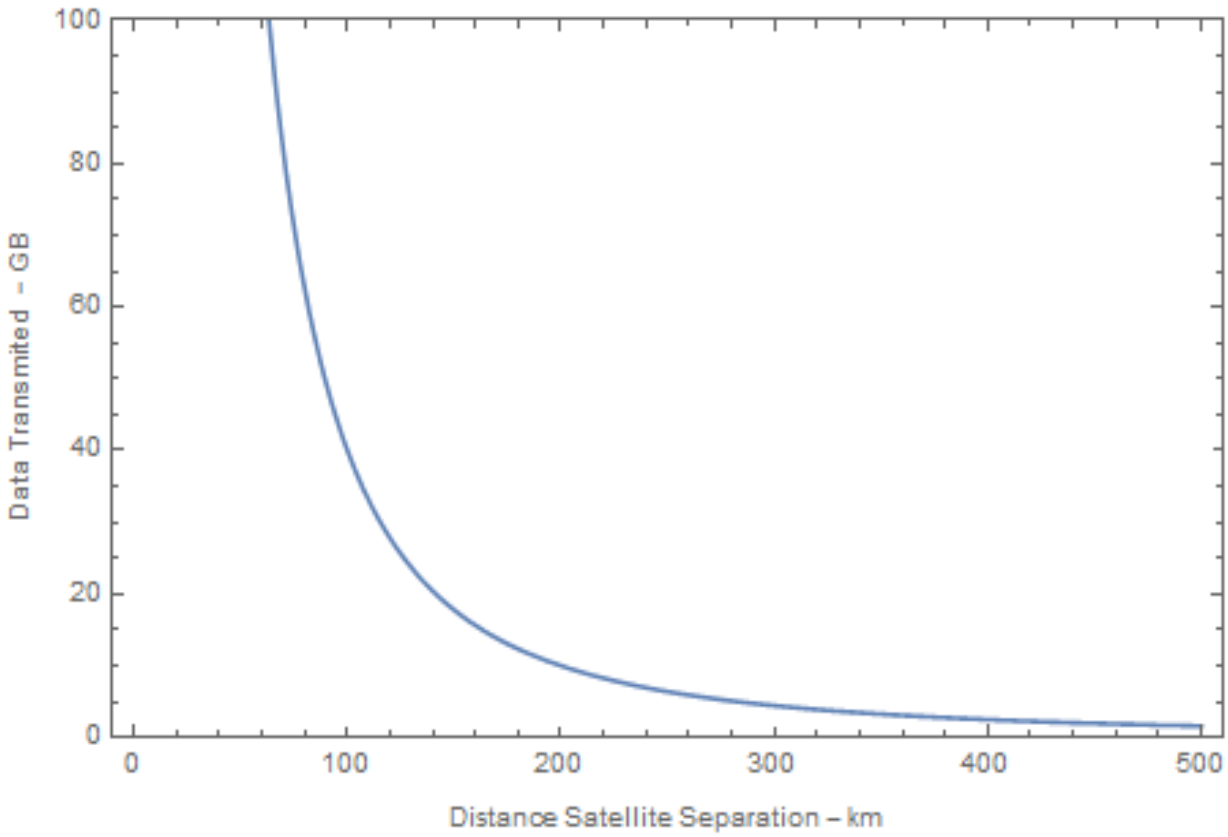

Figure 2.5: MACUSAT to Europa Clipper Data Transfer

2.2 Beyond Low-Earth Orbit Launches

Following the same course full-size satellites have taken from starting in LEO orbits followed by venturing to the Moon, Mars, Jupiter, and beyond, CubeSats have only recently begun

leaving Earth's haven. With CubeSat's success owed to utilizing the increasingly lowering cost and increasing capabilities of COTS, and with beyond Earth orbit launch costs substantially reduced, their full potential has yet to be seen. The key enabler for successful deep space CubeSat missions led by universities hinges on affordable launch costs, efficient propulsion, and long-range compact communications. Efforts to address these issues are currently underway due to renewed interest in lunar and Martian explorations.

Understanding of beyond Low-Earth Orbit launches is an important consideration for the Earth Trojan Asteroid mission, the topic of Chapter 4, because to keep costs to a minimum the novel approach proposed is to piggyback as secondary cargo on a lunar bound mission, except be ejected in route on the trans-lunar injection orbit which can substantially reduce ΔV requirements for accessing the Trojan regions thereby substantially reducing mission cost and complexity.

With renewed interest in lunar missions, the past 2 years have seen three lunar landing attempts including (a) Chandrayaan-2 led by the Indian Space Research Industry [75], (b) Beresheet led by the Israel Aerospace Industries [74], and (c) Chang'e-4 led by the China National Space Administration [73]. NASA has also been focused on returning human presence on the moon in 2024 through its Artemis program and development of its new Super heavy-lift launch vehicle, the Space Launch System [76]. NASA has also leveraged the commercial industry by providing funding to three different companies to develop a lander [77]. Beyond national competition and science motivations, there is a new push by the private sector such as by Jeff Bezos to colonize the moon [78]. Jeff Bezos' company, Blue Origin, is currently developing the New Glenn reusable heavy lift vehicle intended to build a road to space by decreasing launch costs [81]. Additional commercial lunar endeavors also exist, such as a tourist venture which will leverage SpaceX's under development StarShip launch vehicle [80]. In addition to revitalized lunar

ambitions, sights have also been set for the red planet. By 2024 there are 8 missions planned for visiting Mars [85][86][87][88][89][90][91][92].

As the demand for launch access beyond LEO continues to grow, including the proliferation of commercial launch, it is reasonable to expect launch costs will continue to decrease and CubeSat launch availability increasing. While it is too early to know exact CubeSat launch costs for deep-space applications, LEO cost trends are a useful indication. Take for instance SpaceX who now regularly flies their first stage reusable Falcon 9 launch vehicle to LEO costing $62 million with a payload capacity to LEO of 22,800 kg. Contrast this with their upcoming fully reusable Starship vehicle estimated to cost $2 million per launch with a payload of 100,000 kg, or a cost savings per kg of two orders of magnitude [93][94]. Considering that India's latest launch cost to the moon was $3.75 billion, or two orders higher than a Falcon 9 LEO cost, it is not unreasonable to assume future deep-space launch costs for CubeSat could be similar to today's launch into LEO [95]. Another bounding datapoint is the upcoming launch of NASA's CAPSTONE 12U CubeSat which has a launch cost to the moon of $9.95 million using a dedicated Rocket Lab launch vehicle [122]. Note that this launch cost does not utilize any ride sharing, therefore it should be considered an upper bound only.

2.3 Previous Deep Space Applications

As of May 2020, there has been only one deep space CubeSat mission, with deep space defined as more than 2,000,000 km away from Earth [96]. Launched in May 2018, the Mars Cube One (MarCO) were a pair of 6U CubeSats used to provide relay communications for the last Mars rover, InSight lander [97]. For background, there are additional CubeSat deep missions in the development phase, such as: Lunar Flashlight, Cupid's Arrow, and CAPSTONE, which are all being developed by JPL [121][122]. However, these missions, as well as other planned missions

are lunar bound. This is significant because the regions of the Earth Trojan Asteroids are ~1 AU away, and with the moon being 2 orders of magnitude closer, is not a representative comparison when considering closing communication links and transfer science data. This section therefore focuses on MarCO only, since it is the only CubeSat mission to have demonstrated successful Earth communication at distances significantly beyond the moon.

The MarCO mission was initially conceived as a means to provide improved communication relay during the Mars InSight entry, descent, and landing, as shown in the Fig. 2.6 conceptual operations. The primary elements of MarCO were a deployable solar array, X-band reflectarray antenna, UHF antenna, as well radios, electrical power, attitude control, structural/thermal, cameras, and command and data handling systems [123]. Fig. 2.7 shows the MarCO spacecraft bus overview. MarCO was designed to achieve a data rate of 8 kbps at 1.05 AU [123]. As discussed in Section 2.4.1, 8 kbps is sufficient for spacecraft telemetry and very low bandwidth science applications, but is insufficient for heavy image and video based science missions.

While the MarCO mission was developed by JPL, it did leverage developments from the previous Earth orbiting mission, the Interplanetary Nano-Spacecraft Pathfinder in Relevant Environment [123]. This leveraging of previous developments is a quintessential example of how CubeSats can manage the risk of using lower cost components and simpler design when operated for operation in new deep space regimes. In this vein, the HuskySat-1 mission and its various subsystems described in the following chapters is detailed with the intent of enabling this work to contribute directly to the Earth Trojan Asteroid mission.

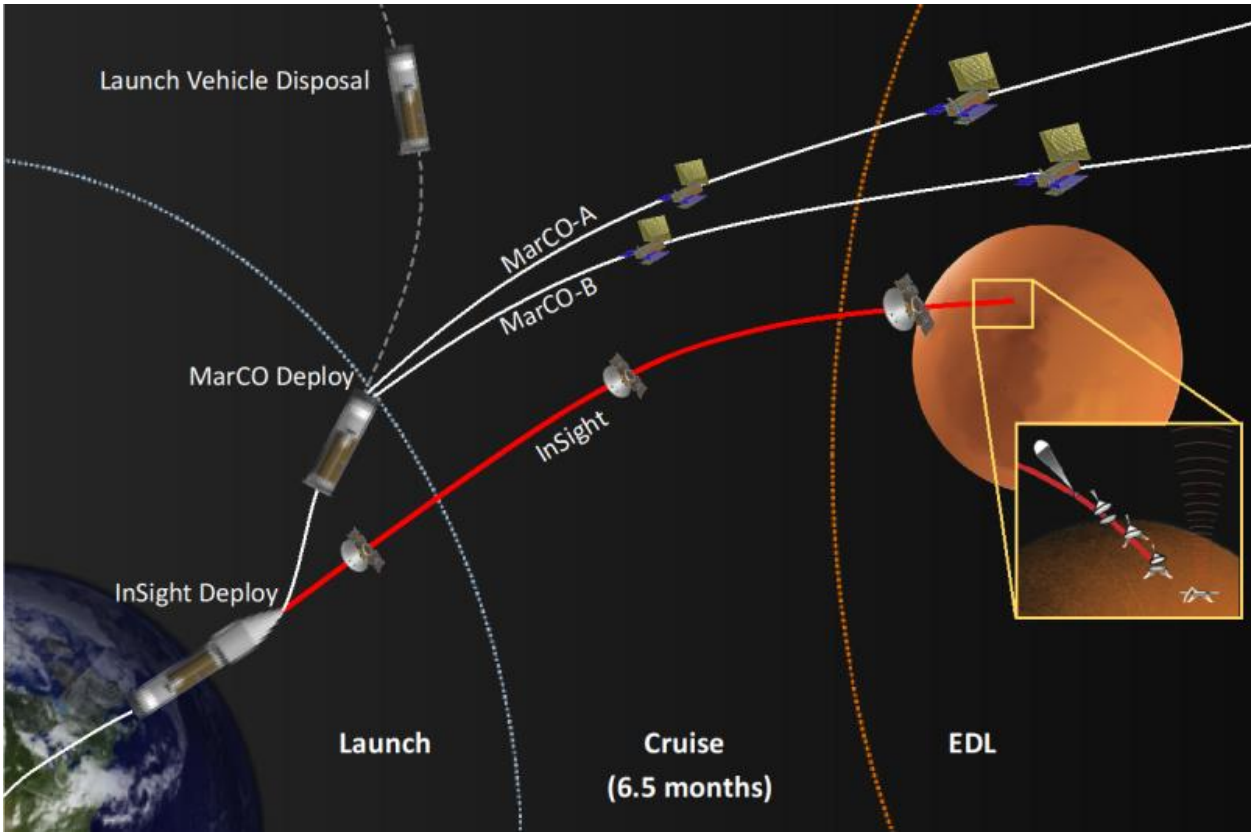

Figure 2.6: Mars Cube One Conceptual Operations [123]

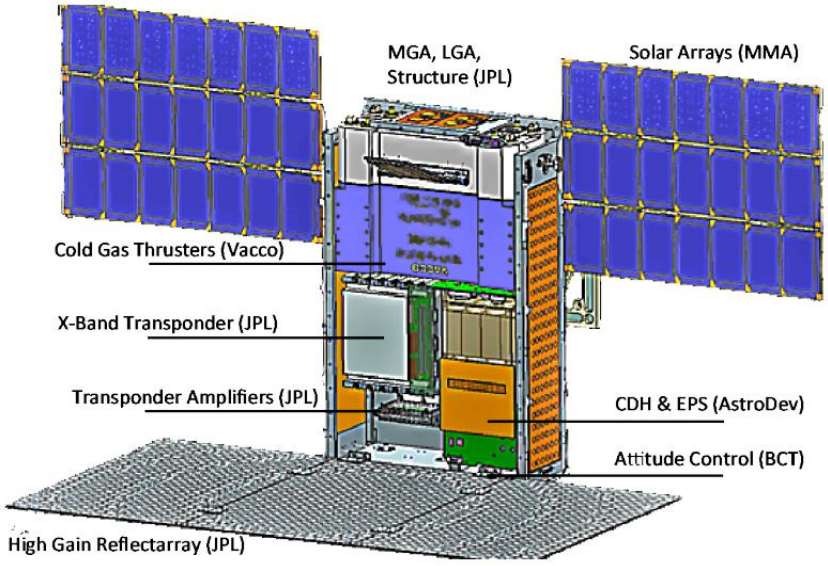

Figure 2.7: Mars Cube One Spacecraft Overview [123]

2.4 Limitations for Investigation of Earth Trojan Asteroids

Increasing access and capabilities of CubeSats for Investigation of Earth Trojan Asteroids requires addressing three primary limitations: lowering overall mission cost, increasing CubeSat technical capabilities, and improvement on the procedural, developmental, and operational framework applicable to the University setting. This lattermost limitation is addressed further in Chapter 5.

Mission cost for deep space CubeSat missions is prohibitively expensive, significantly limiting access to cost-constrained universities. For reference, the HuskySat-1 cost ~$300,000, which was ~$40,000 for flight hardware and the rest for student stipends. In general, the two largest costs are the development of the CubeSat itself and then the launch and deployment. In Section 2.2 the launch cost market was evaluated, and it is expected that significant cost reductions are being driven primarily by the commercialization of lunar endeavors, along with a continued interest for science-based missions. However, the development cost of deep space CubeSats remains high. The MarCO mission, consisting of a pair of CubeSats cost $18.5 million, and NASA's upcoming CAPSTONE lunar CubeSat mission is $13.7 million [124][125]. While NASA's funding of flagship deep space CubeSat missions will continue, along with the continued commercialization of CubeSat components for LEO applications, another significant driving force is technology development directly within academia. The academic environment, being financial and resource constrained, promotes students to think outside of the box when developing scientific questions and technological solutions for CubeSat applications. The reflectarray antenna developments, detailed in Chapter 3, are aligned directly to decreasing the cost of high-performance CubeSat communication technology.

The second limiting factor for carrying out the Earth Trojan Asteroid mission are limited technical capabilities such as large ΔV propulsion systems, deep space communications, and

radiation tolerant electronics. For specific performance metrics of what is available for a CubeSat, readers are referred to NASA State of the Art Small Spacecraft Technology [127]. Over their 20+ years of evolution, CubeSats have become highly capable, but their success is not without shortcomings. Miniaturization of various components is inherently difficult due to scaling. For example, aperture size sets the angular resolution in sensing applications, and in communication systems aperture size directly limits data transfer rates. Solar panel collection area limits the communication system transmit power, computational performance, and attitude control and propulsion systems. This has evolved to CubeSats increasingly using deployables. Additionally, NASA has been tackling these issues head on by providing various funding avenues to increase student participation in aerospace engineering. For instance, in 2015 NASA hosted the CubeQuest Lunar Derby Centennial Challenge that focused on pushing the state of the art in CubeSat communication and propulsion technologies [128]. Paige Northway and I supported a CubeQuest mission design response where initial concepts to overcome the above limitations were outlined.

2.4.1 Communication System Limitations

CubeSats communication systems still require many of the same functions from their larger satellite counterparts. Traditionally, satellites typically have multiple communication systems providing both increased reliability as well as for serving separate functions. Communication systems always have a tradeoff between available power, gain, beam width, weather dependency, data rate, etc. Low gain communication systems typically use monopole, dipole, quadrupole, or patch antennas which relax pointing requirements of the spacecraft but also limit the data rate. Low gain systems are useful for spacecraft commands and telemetry. Data rates needed to accomplish this can function on the order of 0.01 - 1.0 kbps. For example, spacecraft telemetry may be 20x 5bit numbers, and a spacecraft command can be as little as an 8bit address with a 1bit

Boolean on/off value. On CubeSats, low gain communication systems have ported over nicely using the matured amateur radio technology. For reference, the HuskySat-1 utilized a low gain communication radio developed by Amateur Radio in Space (AMSAT) operating at 1.2 kbps. The majority of CubeSats historically have used the amateur UHF-band with typical data rates of 1.2 kbps to 9.6 kbps [129]. Low gain antennas are easily implemented in the form of deployable metal conductors, as shown in Fig. 2.8. The HuskySat-1 CubeSat utilized this same antenna and had a 1.2 kbps downlink.

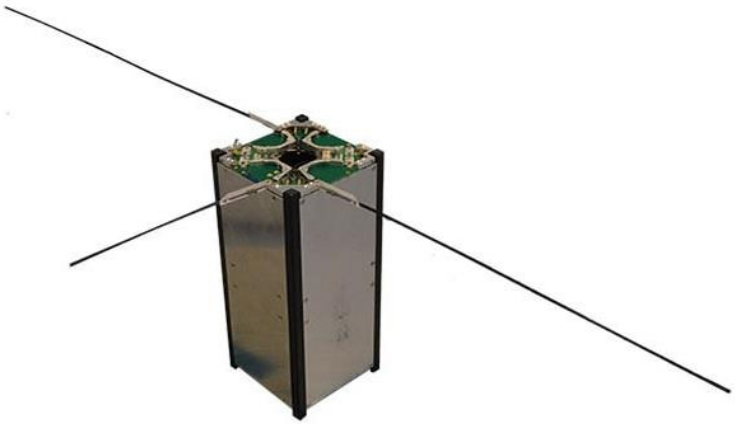

Figure 2.8: Typical Low-gain Antenna for CubeSats [130]

Nominal bitrates of 9.6kbps from low Earth orbit is acceptable for many low data overhead science experiments/studies, such as those that use spectrometers, magnetometers, and other single value measurements. However, once leaving low Earth orbit this bitrate will drop due to the squared inverse proportional dependence. This reduced communication limits their usage for science data downlinking for deep space missions. Traditionally, satellites have overcome this issue by using fixed large parabolic dishes or large phased arrays, as well as using higher frequencies. Going to a larger antenna and high frequencies decreases the beam width of the antenna and increases the gain which is highly advantageous for minimizing wasted radiated RF

energy. However, a physically large antenna for a CubeSat is not possible. On the ground side, NASA has supported these high gain systems with the Deep Space Network (DSN) 34m and 70m dishes, see Fig. 2.9 [131]. With antennas distributed through the globe, thereby providing constant coverage to anywhere in the ecliptic plane, the DSN has proven to be an invaluable asset for NASA missions, for it has provided extremely high-gain ground antennas as well as Doppler ranging and tracking services used for spacecraft location determination. The Earth Trojan Asteroid mission requires spacecraft position knowledge, and to date deep spacecraft all have relied on ground-based Doppler ranging. Therefore, DSN interoperability was a significant driver when developing the reflectarray antenna and radio electronics in Chapter 3.

Figure 2.9: Deep Space Network 34m dish antenna (left), Voyager spacecraft with a 4m dish antenna (right)

University sponsored CubeSats cannot compete with the performance of large satellite communication systems because the hardware is simply not available or it is cost prohibitive. Unlike the low gain systems which have been ported over from Amateur radio technology, there is simply no analog for high gain communication systems. The primary difficulty is the CubeSat's small rectangular shape, which limits the size of any fixed aperture antenna, like that of the

Voyager spacecraft in Fig. 2.9. Increasing the center frequency of operation does help in boosting the antenna gain, and this is a technique NASA has used, but this is not without limit. Due to atmospheric attenuation at higher frequencies, RF spectrum allocations, and pointing requirements, NASA has increasingly converged to using k-band frequencies (~30GHz) for their high gain communication systems. The primary technological difficulties of implementing high gain k-band systems on CubeSats are the antenna, transmitter, and receiver. Contributions have been made through the development of a low-cost, CubeSat form factor, deployable high-gain k-band reflectarray antenna, and associated RF driving electronics. In comparison to other similar technologies, my contributions demonstrate how a high gain reflectarray antenna system can be implemented using low cost materials, as well as using an improved method of differential phase control. These contributions are the topic of Chapter 3.

Chapter 3. Deep Space CubeSat Communication Systems

CubeSats in deep space applications require high performance communications systems to offload science data as well as Doppler ranging with Earth stations for navigation purposes. There currently exists an outstanding gap in available low-cost and high-performance COTS components fulfilling these needs. This chapter describes achievements towards satisfying these needs through the development of a high-gain high-frequency antenna system and transmitter suitable for deep space CubeSat applications. Work of this type is normally completed out with significantly larger teams and budgets, so these contributions are particularly impactful because they are the first of the kind to be carried by a single graduate student and a very limited budget. My contributions include the development of a high gain antenna system which is adaptable to a variety of CubeSat applications as well as the development of a high frequency transmitter. This chapter is broken into three parts, reflectarray, RF Front End, and the overall completed system.

3.1 Reflectarray

3.1.1 Competing Technologies

High-gain communication systems require electrically large antennas. Electrical size here is with respect to the operating wavelength of the communication system. While the CubeSat is of fixed size (~10cm), higher frequencies can be used to increase electrical size. Electrical size is the size of the overall antenna aperture with respect to the wavelength. Increasing frequency has the practical limitation of compatibility with atmospheric attenuation, see Fig. 3.1. For this reason, NASA's DSN highest supported band is Ka with allocations for uplink of 34.2GHz to 34.7GHz and a downlink of 31.8GHz to 32.3GHz [96]. Ka-band corresponds to a ~1cm wavelength.

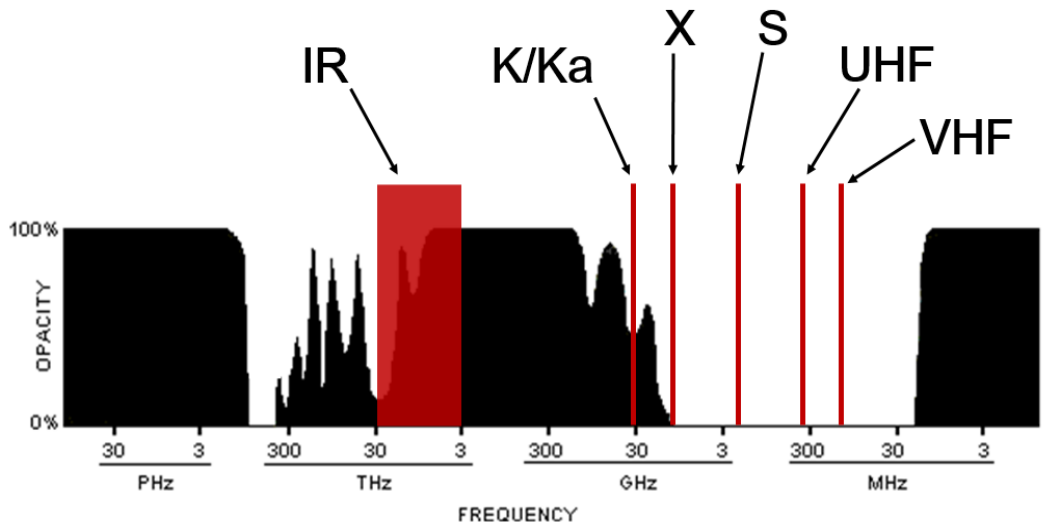

Figure 3.1: Atmospheric Opacity and Common RF Bands

Going to higher frequencies within THz atmospheric window and using laser communications is in the very early feasibility testing stages for CubeSats [146]. Additionally, Doppler ranging for navigation using lasers has yet to be demonstrated. Therefore, the efforts within this dissertation focus on using the well-established navigation and communication methods and existing ground infrastructure of the DSN. Therefore, for full interoperability with the DSN and achieving highest performance is pursued through use of the Ka-band. Without utilizing any deployable structures, the largest antenna operating in Ka-band compatible with a CubeSat is about 10 wavelengths.

The traditional approach of achieving high gain antennas is with parabolic antennas. With the fixed size of the CubeSat deployable parabolic reflectors have been attempted [135][136]. The two flavors, shown in Fig. 3.2 are deployable mesh utilizing unfolding truss and supporting structures or inflatable-type antenna. Both of these methods produce surfaces which will unavoidably exhibit imperfect curvatures impacting their overall antenna efficiency in addition to

high mechanical complexity. Deployable reflector surfaces utilizing any supporting structures also have the downside of consuming a considerable amount of volume within the CubeSat in their pre-deployed state. For instance, the mesh deployable in Fig. 3.2 consumes about 3U of volume, or 25% of the overall spacecraft volume when stowed.

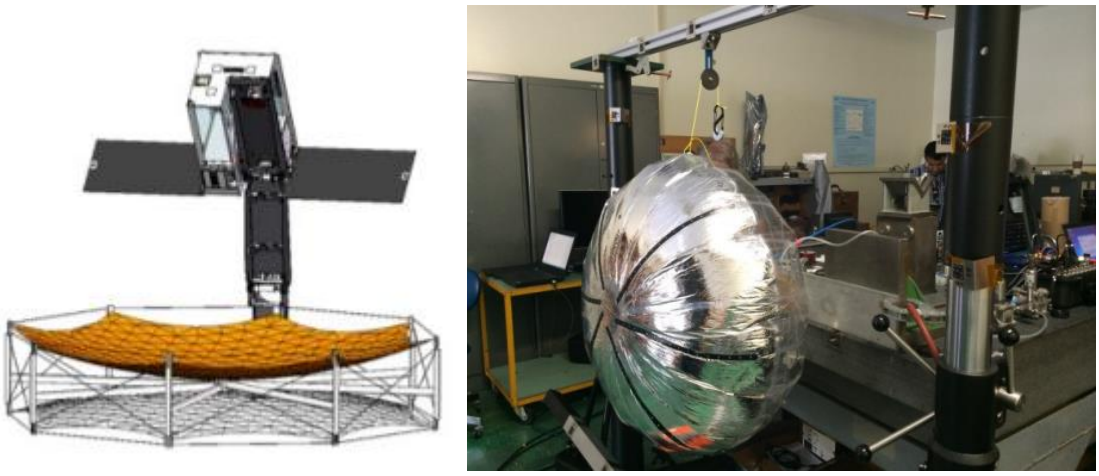

Figure 3.2: Deployable Mesh (left), Inflatable Reflector (right) [135][137]

The second approach of achieving high gain antennas is with phased arrays. Phased arrays combine multiple low-gain radiating elements to achieve an overall higher gain. Each of the elements within a phased array is fed the appropriate phase by the feed network, see Fig. 3.3. A common feeding approach is to feed all elements in phase to provide a nadir pointing beam. The inherent limitation of phased arrays is when scaling to larger sizes their feed networks become more complicated and incur significantly higher losses. One traditional approach to overcome this loss is to use the lower loss waveguides instead of microstrip or patch technology; however CubeSat form factors are not conducive to the use of waveguides. While phased array efficiency decreases at large sizes, they are still very useful for the feed antenna in reflectarray applications, see Section 3.1.5.

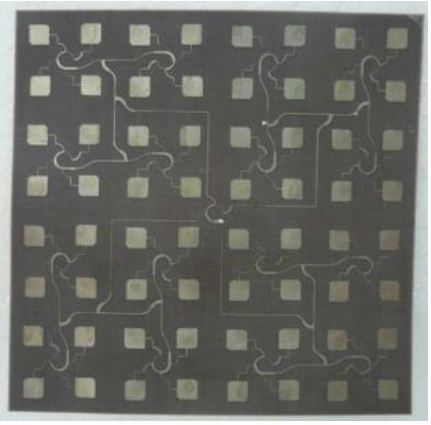

Figure 3.3: 64-element Phased Array Antenna [134]

3.1.2 Reflectarray Fundamentals

The reflectarray antenna was conceived in 1963 as a hybrid between traditional reflector antennas, such as the parabolic dish, and more traditional array antennas [132]. While they have only recently begun to see practical use outside of academia, they were initially recognized as a means to overcome the geometry limitations of reflector antennas and the feed complexity and losses associated with large array antennas. Reflectarrays are similar to parabolic antennas in that the feed antenna illuminates a surface which reflects the incident waves. However, whereas traditional reflector-type antennas use the geometrical length between the feed antenna and points on the reflecting surface to create the necessary phase delays for building a coherent outgoing wave front, the reflectarray surface has an added degree of freedom being able to adjust the phase delay specific to different locations on its surface. This type of antenna is suitable for the CubeSat form factor since flat panels can more easily be deployed compared to curved geometries. Reflectarrays also overcome the inherent scaling limitation of traditional phased array antennas, since the main antenna does not have any feed structures.

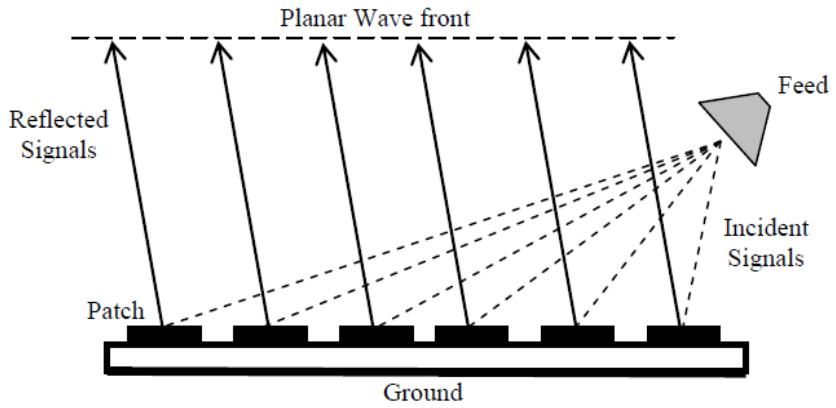

Figure 3.4: Reflectarray Overview [139]

The planar wave front in Fig. 3.4 is formed when all incident signals from the feed are redirected in phase in a particular direction. From ray tracing, the phase at the i^{th} element is:

$$\varphi_i = k\left(\left|\vec{R}_i\right| - \vec{r}_i \cdot \hat{r}_0\right)$$

From Fig. 3.5, $\vec{r}_i$ is the position vector to the i^{th} element, $\hat{r}_0$ is the main beam direction and k is the wavenumber in free space, or $2\pi/\lambda$, and $\vec{R}_i$ is from the feed phase center the distance from the phase center of the feed to the i^{th} element location. In practice, the reflectarray patch elements can provide up to 2π of phase delay. Additionally, all phases are relative, so the above equation becomes:

$$\varphi_i = k\left(\left|\vec{R}_i\right| - \vec{r}_i \cdot \hat{r}_0\right) + 2\pi n + \varphi_0$$

where n is an integer to wrap the calculated element phase around a 2π range, and φ_0 is an arbitrarily set constant.

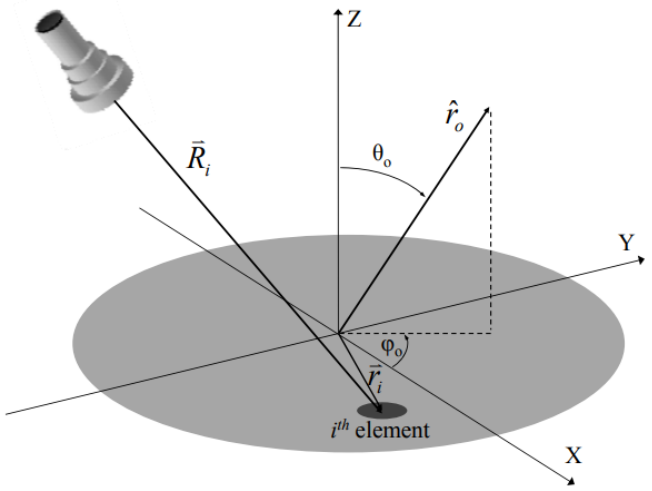

Figure 3.5: Reflectarray Geometry [145]

Since their inception, new methods have been introduced to achieve phase control on the reflectarray surface. The most notable advancement here was the implementation of patch antenna design and fabrication techniques; this allowed for the reflectarray to be lightweight, low volume, and allowed leverage of common low-cost Printed Circuit Board (PCB) fabrication techniques. For any method of phase control, practical characteristics sought after are: beam width, efficiency, bandwidth, multi-band support, off-frequency transparency, phase delay range, size, polarization (linear, dual, or circular), and sensitivity to manufacturing tolerances. The general construction is in Fig. 3.6. Note that for the application of deep space CubeSat applications, the single frequency downlink band is targeted as well as being circular polarized to minimize the impact of Faraday rotation and be interoperable with the DSN.

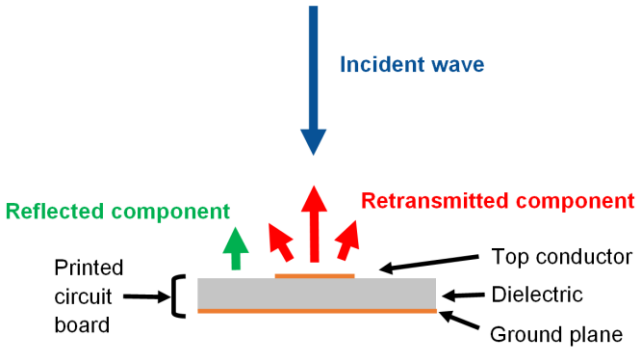

Figure 3.6: Element Overview

Maximizing efficiency, which directly impacts gain, is an important consideration at the element level. From Fig. 3.6 one can observe the reflected component is unwanted since it does not undergo the designed phase delay and therefore degrades overall array efficiency. Common element types, shown in Fig. 3.7, are (a) linear patch with variable length transmission line, (b) and (c) variable resonant frequency to provide phase delay, and (d) phase change via variable rotation for circular polarized incident waves.

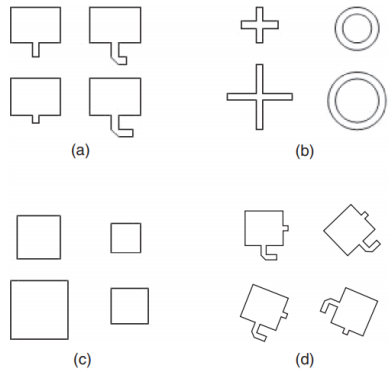

Figure 3.7: Common Element Types [134]

To understand how the variable rotation method works, consider a left handed circular polarized (LHCP) plane wave traveling in the $-\hat{z}$ direction incident upon a reflectarray element lying in the XY plane:

$$\vec{E}_{\text{incident}} = \left(x + iy\right) E_0 e^{i(-kz-\omega t)}$$

With the reflectarray element design to retransmit LHCP, the retransmitted component is:

$$\vec{E}_{\text{retransmitted}} = \left(x - iy\right) E_0 e^{i(kz-\omega t+a_0)}$$

Here a_0 is a constant phase shift and is dependent on the element geometry. Now let the coordinate system $(x, y, \hat{z})$ be rotated in the XY plane by angle ϕ resulting in the new coordinate system $(x', y', \hat{z})$. In this new coordinate the incident wave becomes:

$$\vec{E}_{\text{incident}} = \left[\left(x'\cos(\phi) - y'\sin(\phi)\right) + i\left(x'\sin(\phi) + y'\cos(\phi)\right)\right] E_0 e^{i(-kz-\omega t)}$$

Which can be rearranged to:

$$\vec{E}_{\text{incident}} = \left(x' + iy'\right) e^{i\phi} E_0 e^{i(-kz-\omega t)}$$

Expressed in the $(x', y', \hat{z})$ coordinates the retransmitted component becomes:

$$\vec{E}_{\text{retransmitted}} = \left(x' - iy'\right) e^{i\phi} E_0 e^{i(kz-\omega t+a_0)}$$

Projecting back to the $(x, y, \hat{z})$ coordinate system this becomes:

$$\vec{E}_{\text{retransmitted}} = \left[\left(x\cos(\phi) + y\sin(\phi)\right) - i\left(-x\sin(\phi) + y\cos(\phi)\right)\right] e^{i\phi} E_0 e^{i(kz-\omega t+a_0)}$$

Which can be rearranged to:

$$\vec{E}_{\text{retransmitted}} = \left(x - iy\right) e^{i2\phi} E_0 e^{i(kz-\omega t+a_0)}$$

The result is that by rotating the reflectarray patch element by angle ϕ results in a retransmitted phase shift of 2ϕ.

3.1.3 Space Applications

There have been two previous CubeSats which have flown with a reflectarray. Both developed by JPL, they are the Integrated Solar Array and Reflectarray (ISARA) and Mars Cube One (MarCO) [140][141]. Operating in K-band, the ISARA was an important mission since it provided on-orbit performance measurements of the first reflectarray deployed from a CubeSat. MarCO, while operating at a lower frequency of 8.4GHz, was still important as it was the first fully operational reflectarray on a CubeSat to support a flagship mission. See Fig. 3.8 and Fig. 3.9.

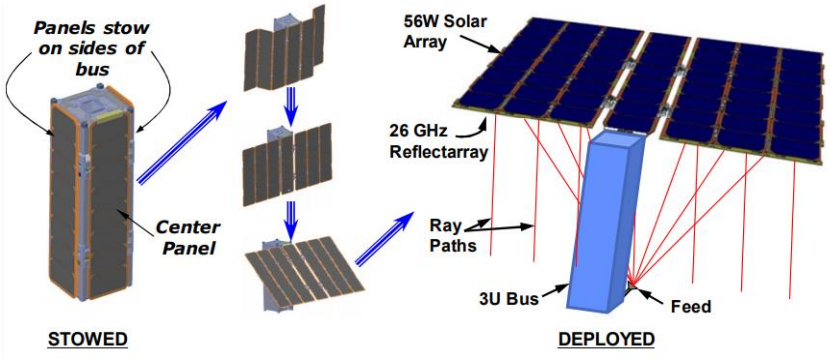

Figure 3.8: Integrated Solar Array and Reflectarray [141]

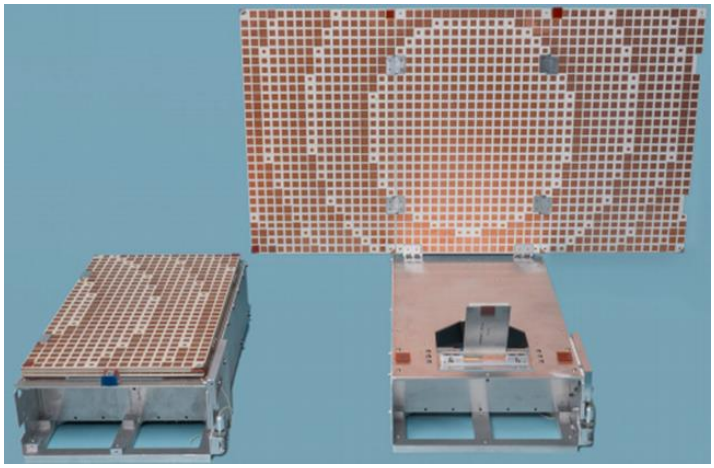

Figure 3.9: Mars One Cube Reflectarray [140]

The limitations of these two designs are cost, complexity, and inherent phase error. The cost of MarCO was $18.5 million for two identical CubeSats, and ISARA was $5.5 million [124][132]. Complexity was also high, such as using exotic reflectarray substrates and deployable feed antennas. Lastly, the choice of using variable patch size to obtain phase shift cannot provide the full 360 degree of phase control which leads to unavoidable inefficiencies [133]. My contributions overcome these limitations by using a reflectarray element type which can provide full 360 degree of phase control, has low design complexity for easy adaption to different applications, and has very low cost.

3.1.4 Element Characterization

The element phase control was chosen to be the variable rotation method in order to provide the full 360 degrees of phase control to minimize phase error enabling higher array efficiencies. Unlike the Fig. 3.7 (c) which uses a dual linearly polarized patch with the co- and cross-polarizations offset by 90 degrees using two different transmission line lengths, a less complex element was sought after. To minimize crosstalk between neighboring elements, only elements

with a circular footprint were considered. Ansys High Frequency Structure Simulator (HFSS) full 3D wave solver was utilized to analyze the performance of 3 different element types: circle with a slit, single split ring, and double split ring [134]. Analysis of each element type consisted of full geometrical parametrization to enable sweeping. The goal at this stage was to find geometries where the retransmitted wave is significantly greater than the reflected wave. For this to occur the element must inherently have good cross-polarization rejection during resonance, and the element itself must resonate. The HFSS simulation was set up with an incident right-handed circular polarized (RHCP) wave, while the reflected wave off-resonance effectively is transparent to the element and flips polarization from the ground plane generating LHCP, and the retransmitted wave was RHCP. The optimization goal was to maximize the cross-polarization suppression, or maximizing the strength of the outgoing RHCP wave compared to the LHCP wave. Results from initial optimization of the geometrical parameters are in Fig. 3.10 showing a strong suppression of cross-polarization at 39.2GHz indicating strong resonance.

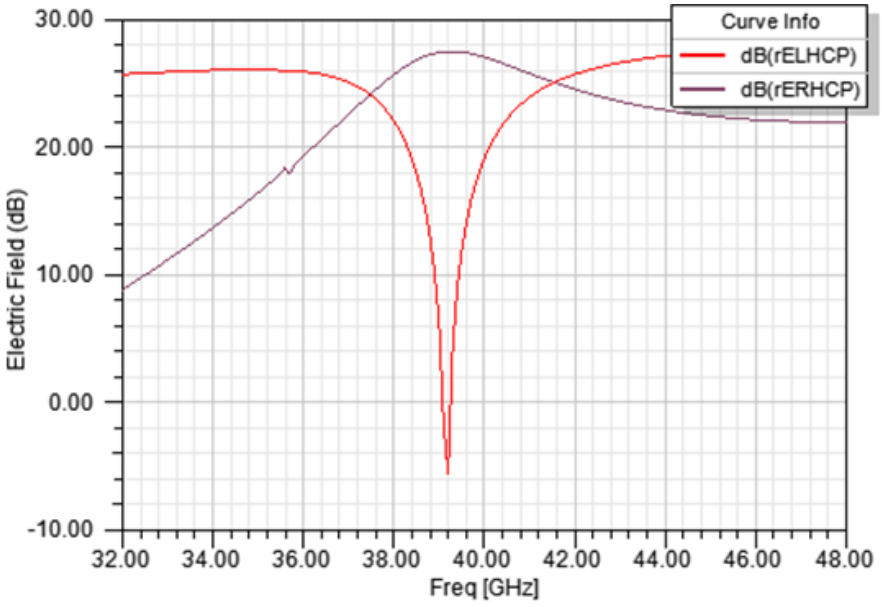

Figure 3.10: Double Split Ring Cross-Polarization Suppression

The double split ring geometry, shown in Fig. 3.11, does not have an analytic solution and therefore all optimizations were completed using HFSS in addition to physical measurements. The final dimensions for operation at 24GHz were: outer diameter 3.7mm, outer width 0.4mm, gap width 0.7mm. Note however, that these dimensions are application dependent due to varying array size (mutual coupling changes overall resonant frequency), substrate type and thickness, element spacing, and frequency.

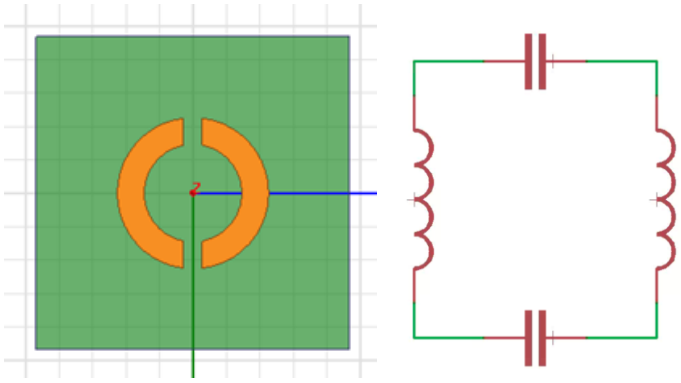

Figure 3.11: Double Split Ring Geometry (left), LC Model (right)

The LC circuit equivalent of the double split right resonator is useful in understanding geometry sizing dependencies as well as on the variable rotation phase control method. In the LC model the gaps within the ring are represented by capacitors and the arc sections are represented by inductors. Considering the resonant frequency of an LC circuit is $\omega_0 = 1/\sqrt{LC}$, this model explains why element resonant frequency decreases from making the gap smaller, which increases the capacitance, and when making the overall diameter larger while keeping the gaps the same, which increases the inductance. In this model, the variable rotation phase control method can be understood by considering an incident CP wave arriving as linearly polarized at a given time, and depending upon if this electric field vector is more aligned with the inductor or capacitor it will

then incur a leading and lagging induced current. HFSS simulation was used to confirm rotating the element does provide the expected phase change, see Fig. 3.12.

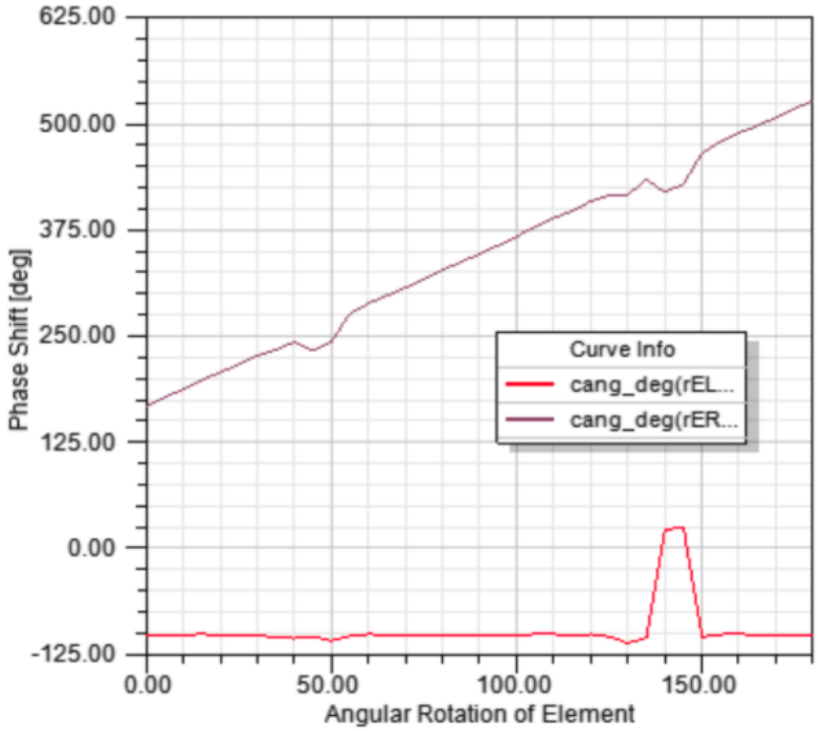

Figure 3.12: Double Split Ring Variable Rotation Phase Shift

Another important consideration of the element design and optimization for certain situations involving low elevation incident angles or low elevation primary beam is the individual element radiation pattern. For the double split ring, most of the energy is directed in the nadir direction which makes this element most optimal for nadir incident and nadir main beam directions. For low elevation angle applications, consideration and optimization is important for wider beam widths for individual elements. See Fig. 3.13 for the double split ring beam width.

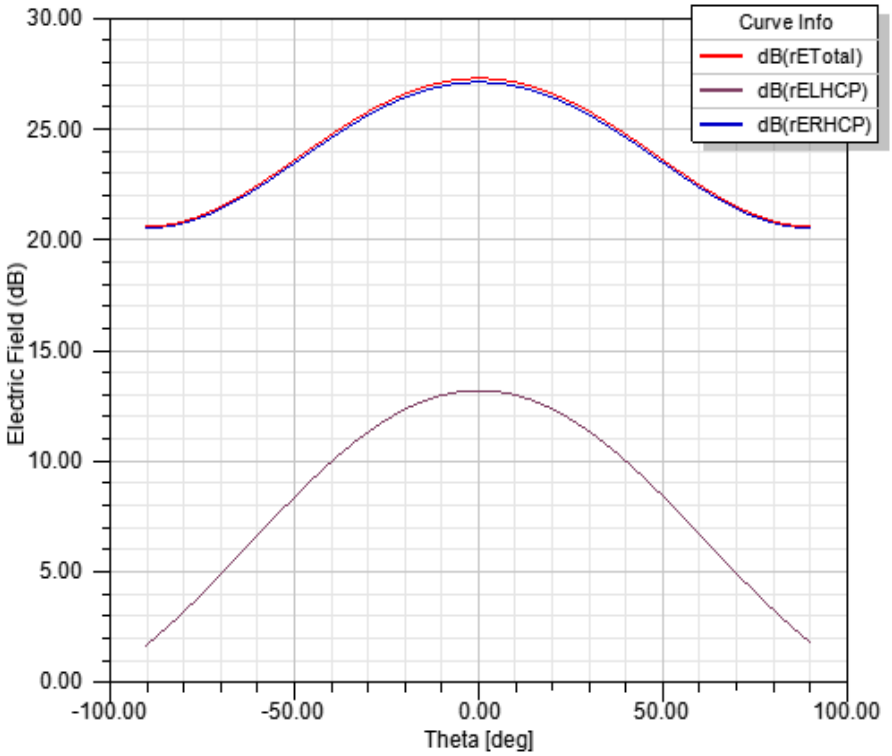

Figure 3.13: Double Split Ring Beam Width

3.1.5 Feed Antenna

Feed antenna design has a significant impact on overall reflectarray performance. The primary considerations for the reflectarray feed are similar to other reflector-type antennas, which are primarily: beam width, co- and cross- polarization, efficiency, and overall size. Although horn antennas are typically preferred for their high efficiency, high power handling, and excellent polarization performance, their volume is not ideal for CubeSat applications. For CubeSats patch antennas are preferred for their low volume, low mass, and highly tailorable beam width. In contrast to ISARA feed antenna, the goal of this feed antenna was low complexity for development and manufacturing, and easy scalability to different frequencies and beam widths for wide applicability to future CubeSat reflectarray applications. The design chosen is two layers where the top layer has the radiating elements as well as the feed network, while the bottom layer serves

as a ground plane. Keeping the feed antenna to two layers significantly reduces fabrication cost and simplifies simulation requirements. With the reflectarray being circularly polarized, and to still provide easy feed antenna element scaling, the simplest feed antenna element is a single fed circularly polarized element. Circular polarization is created using the truncated patch method. These two choices, single fed and truncated corner patch, are limited in providing narrow bandwidth and poor off-axis axial ratio. However, for the intended mission application bandwidth is not a concern since the deep-space Ka-band downlink is 31.8GHz to 32.3GHz which is only a 1.56% relative bandwidth [96]. Off-axis axial was addressed by utilizing the sequential rotation method which improves bandwidth, axial ratio, and overall symmetry [143].

The first stage of the design was to develop an individual feed element, shown in Fig. 3.14. In HFSS, this began with a square patch fed with a waveport port right in the middle of one of the edges. The goal here was to tune the patch side length to the desired 24GHz center frequency and leave the waveport impedance floating. With this completed the truncated corners were added, and the patch was reoptimized for center frequency and on-axis axial ratio while varying both the edge length and the truncated corner size. The final patch dimensions were 4.02mm across and a truncated corner edge length of 0.74mm. A quarter wave transformer was added to adapt from the patch edge impedance of 192 ohms to the 50ohm impedance of the Southwest Microwave connector. The quarter wave transformer dimensions were 2.8mm long and 0.24mm wide. The substrate was Rogers 5880 with 0.254mm thickness.

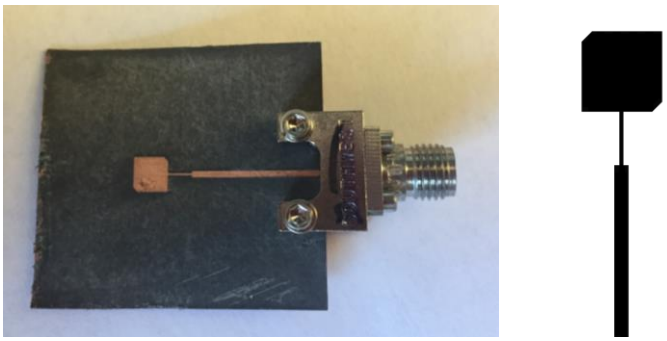

Figure 3.10: Feed Antenna Single Element Prototype

The development process took two cycles to achieve acceptable results. The results from the first cycle were carried into the HFSS by correcting the dielectric constant of the substrate. The performance goals set were an S11 of at least -10dB and an axial ratio of 3dB or better, and the final measured results are shown in Fig. 3.15.

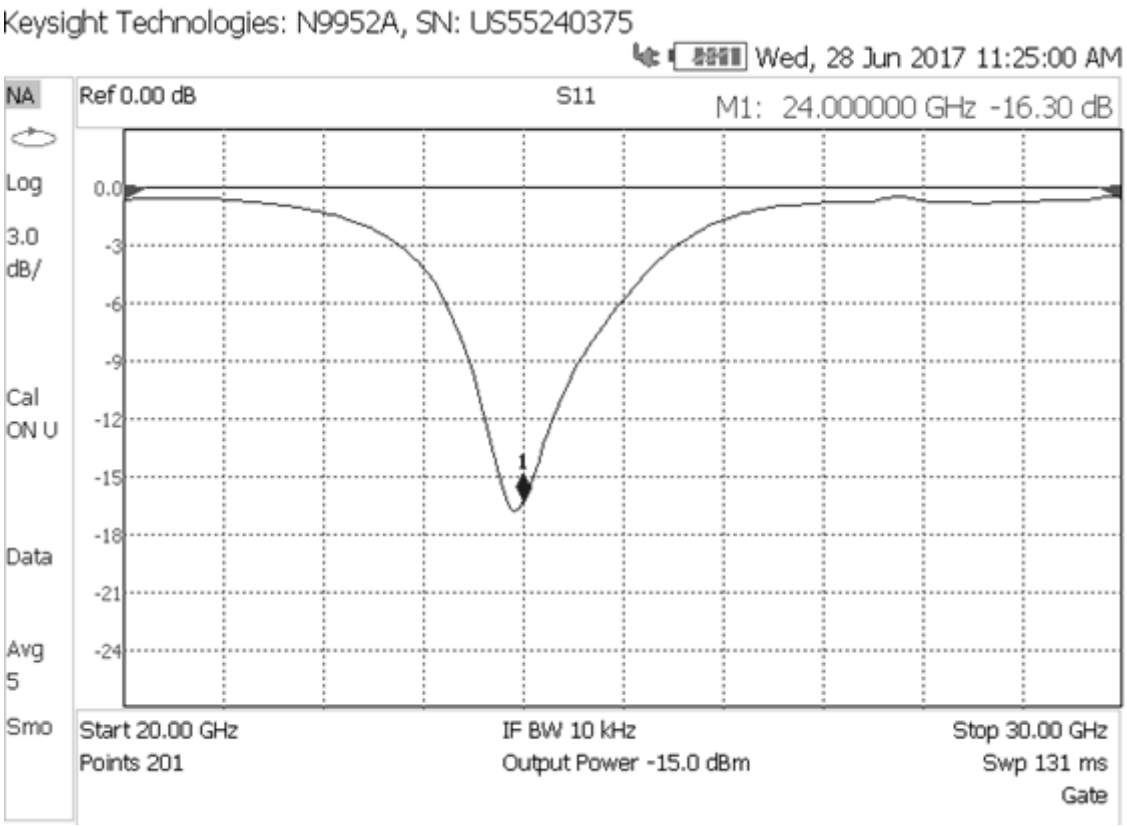

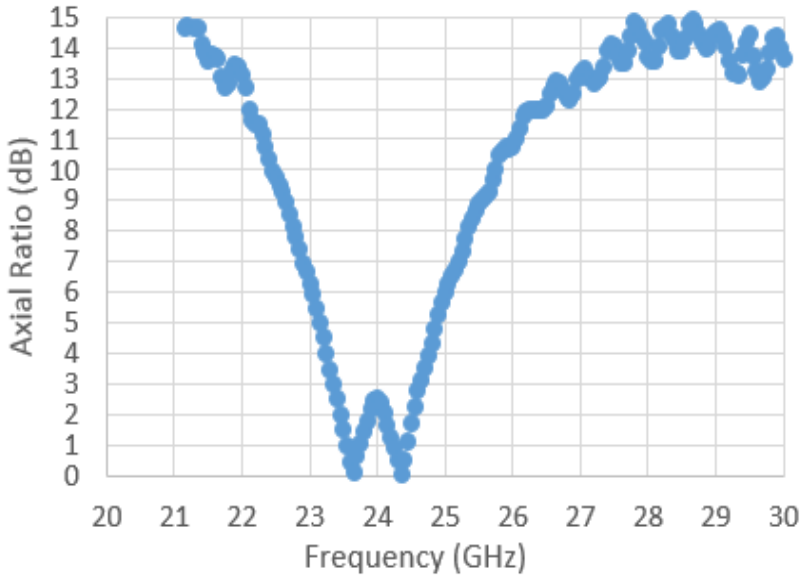

Figure 3.15: Feed Antenna Single Element S11 (top) and Axial Ratio (bottom)

The second stage of the feed design was to design the feed and confirm overall array performance. A 4 element feed antenna was determined to provide an optimal beam pattern for the overall design, see Section 3.1.6 for more detail. Using the sequential rotation method to improve overall array performance, each antenna element is physically rotated 90 degrees relative to each other, and if the array is to create a nadir pointing primary beam, each element must also be fed 90 degrees out of phase relative to each other as well as each antenna receiving an even proportion of power. The implementation used was adapted from literature for this application and uses 7 quarter wave transformers [143]. For this application, from Fig. 3.16, constraints for this application were: ports 1, 2, 3, and 4 each receive 25% of the power, each port is fed 90 degrees lagging the previous port, each port is 50 ohms, and the input impedance, Z0, is also 50 ohms. By making each port 50ohms offered the lowest risk option by using an already verified single element patch previously discussed. Additional constraints on the feed network were: require Z1, Z3, Z5, and Z7 spatially separated by exactly 90 degrees and require them all the same length, and set Z6 to be as narrow as practically possible for fabrication (0.15mm). The first constraints simplifies the geometry of the final 2x2 element array since then each element is the same distance from every other element, and while this makes Z2, Z4, and Z6 not exactly a quarter of a wavelength long the impact is minimal. The problem is fully constrained and all dimensions can be solved analytically.

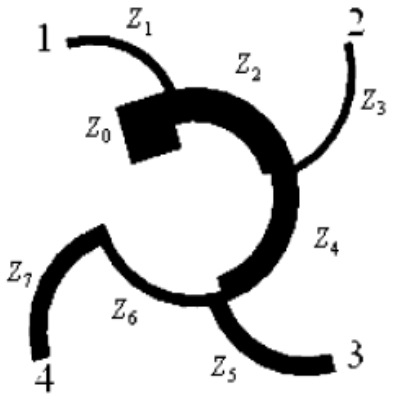

Figure 3.16: Feed Antenna Feed Network Layout [143]

The final feed antenna is shown in Fig. 3.17 and did not require any iterations. The last degree of freedom in this design is the actual element spacing which was selected based on optimal antenna beamwidth. Another verification performed was inadvertent impedance mismatch due to the solder joint. Unlike most antennas, the typical antenna SMA connector was omitted instead relying on a soldered RF cable. Fig. 3.18 shows the small test sample created to investigate this concern; the result showed the impedance mismatch was undetectable on insertion loss. The feed antenna performance is in Figure 3.19.

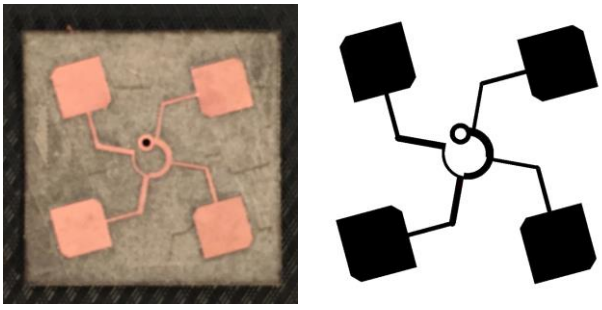

Figure 3.17: Feed Antenna Design and Prototype

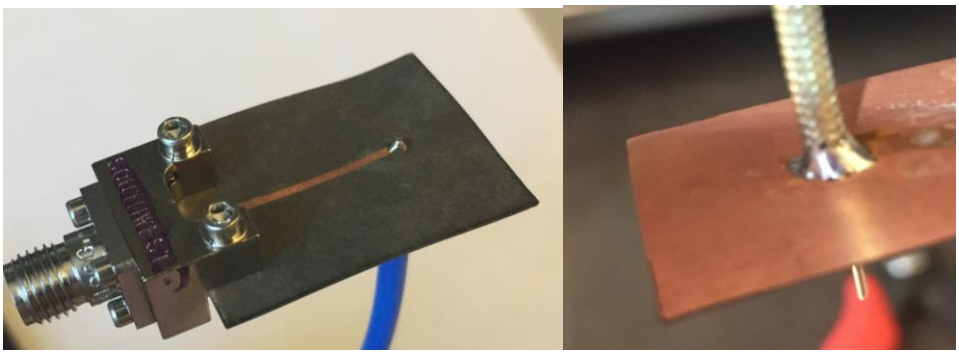

Figure 3.18: Feed Antenna Connection Impedance Verification

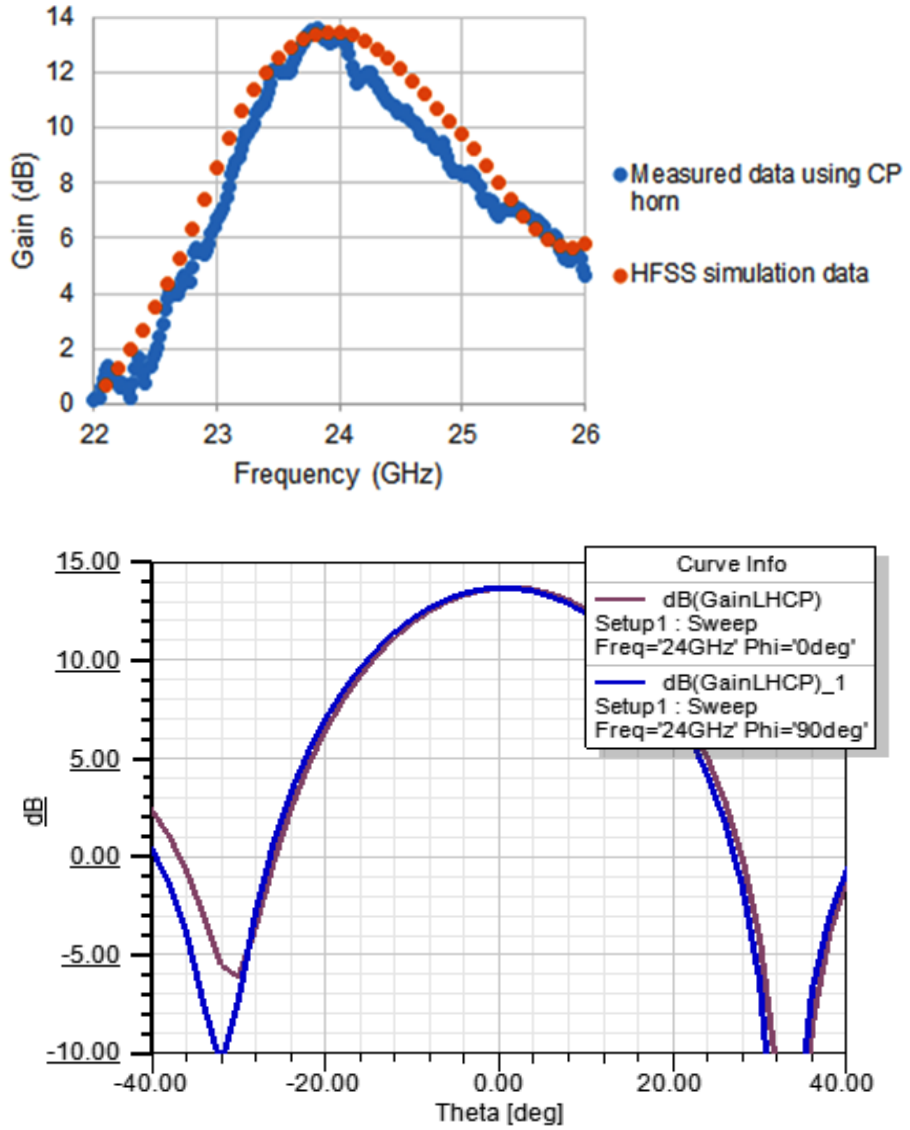

Figure 3.19: Feed Antenna Performance: on-axis gain (top) and lobe shape (bottom)

The 2x2 element feed antenna presented in this chapter can be adapted to other applications as well. It has been previously demonstrated that a similar design can act as a unit cell, whereby the four of the 2x2 arrays can be used to build a 4x4 array [135]. In a similar vein, the 2x2 element array presented can be easily modified to a 2x1 array or to a 4x2 array. In this way, the material presented can be adapted to satisfy a wide variety of CubeSat reflectarray geometries.

3.1.6 Array Design and Implementation

While the theory behind many of reflectarray design considerations are documented, this section seeks to fill a void of practical considerations for low complexity CubeSat applications [144]. CubeSats present unique design challenges for reflectarray applications primarily due to constrained geometry for both stowed and deployed states, as well as thermal stresses causing change of distances between the feed and reflectarray surface leading to phase error. Design objectives for the reflectarray developed were: stowed volume on the CubeSat of 0.5U, or about 5cm x 10cm x 10cm, design decoupling from other spacecraft subsystems, simple and inexpensive design and fabrication techniques, and scalable design attributes to larger arrays. The target band of operation was the Amateur Radio allocation of 24.00GHz to 24.05GHz. The reflectarray PCB substrate was Rogers 5880 with 0.254mm thickness, and the element spacing was lambda/2, or 6.25mm. The array sizes selected were 10x10 for the reflectarray and 2x2 for the feed antenna, see Fig. 3.20.

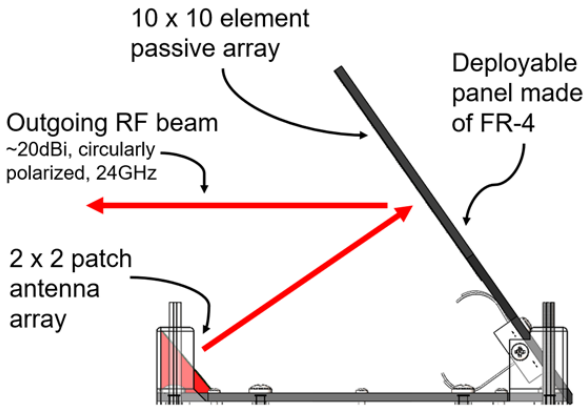

Figure 3.20: Reflectarray Geometry

The next step was to adjust element scaling which was done by building 10x10 arrays with each rotation set to 0 degrees. Two circular polarized horns, model LB-SJ-180400-P03, were to provide incident waves and measure the reflected component. The measurement was identical to Fig 3.10, except with use of a Vector Network Analyzer (VNA) in S21 mode. Port 1 sent out RHCP waves, while port 2 received LHCP waves; this setup is shown in Fig. 3.21.

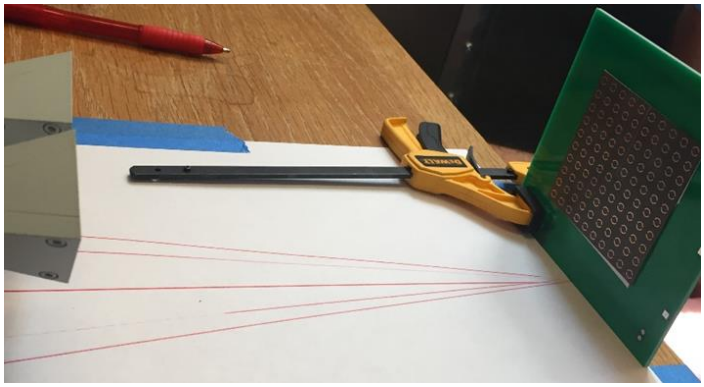

Figure 3.21: Reflectarray Element Resonance Tuning

The spill-over is also optimized for maximum on-axis gain. Spillover relates to how much RF energy is not intercepted by the reflectarray but instead goes past the edges. Minimizing spillover leads to only the center elements on the reflectarray being illuminated and therefore lower

gain. The optimal spill-over is about 10%, or 10dB [134]. In this application the spillover of 10dB was achieved by adjusting the feed antenna element spacing, which affects the feed antenna beamwidth, as well as changing the final angle of the reflectarray angle which changes the distance from it to the feed antenna. See Fig. 3.22 for the incident energy onto the reflectarray. The vertical asymmetry of the incident energy is due the incident angle from the feed antenna being off boresight, see Figure 3.20. Additional asymmetry comes from a slightly non-symmetric feed antenna, see Figure 3.17.

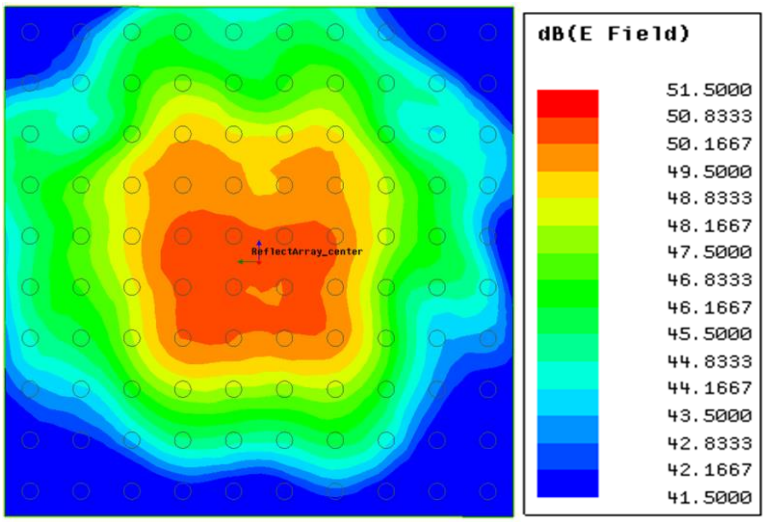

Figure 3.22: Reflectarray Spillover

The next step was to adjust the reflectarray element rotations completed using the ray tracing method described in Section 3.1.2. This was completed by porting over the SolidWorks model into MATLAB. A matrix containing the element rotations could then be imported into HFSS. Incident phase was also determined using HFSS only, whereby the feed antenna illuminated a RF transparent surface in place of the reflectarray outputting a plot similar to Figure 3.22. These methods differ by the latter method taking into account the phase center of the feed antenna. It was found that these two methods generated reflectarray elements phases varying by 0-2 degrees

typically, and the largest difference observed was 7 degrees, but it was within the blue zone of Fig. 3.22 where the impact is low. These two reflectarray designs were both simulated in HFSS yielding the same peak gain in Fig. 3.23. These simulations required 24 hours to run using an AMD-9590 CPU and the full 32GB of RAM.

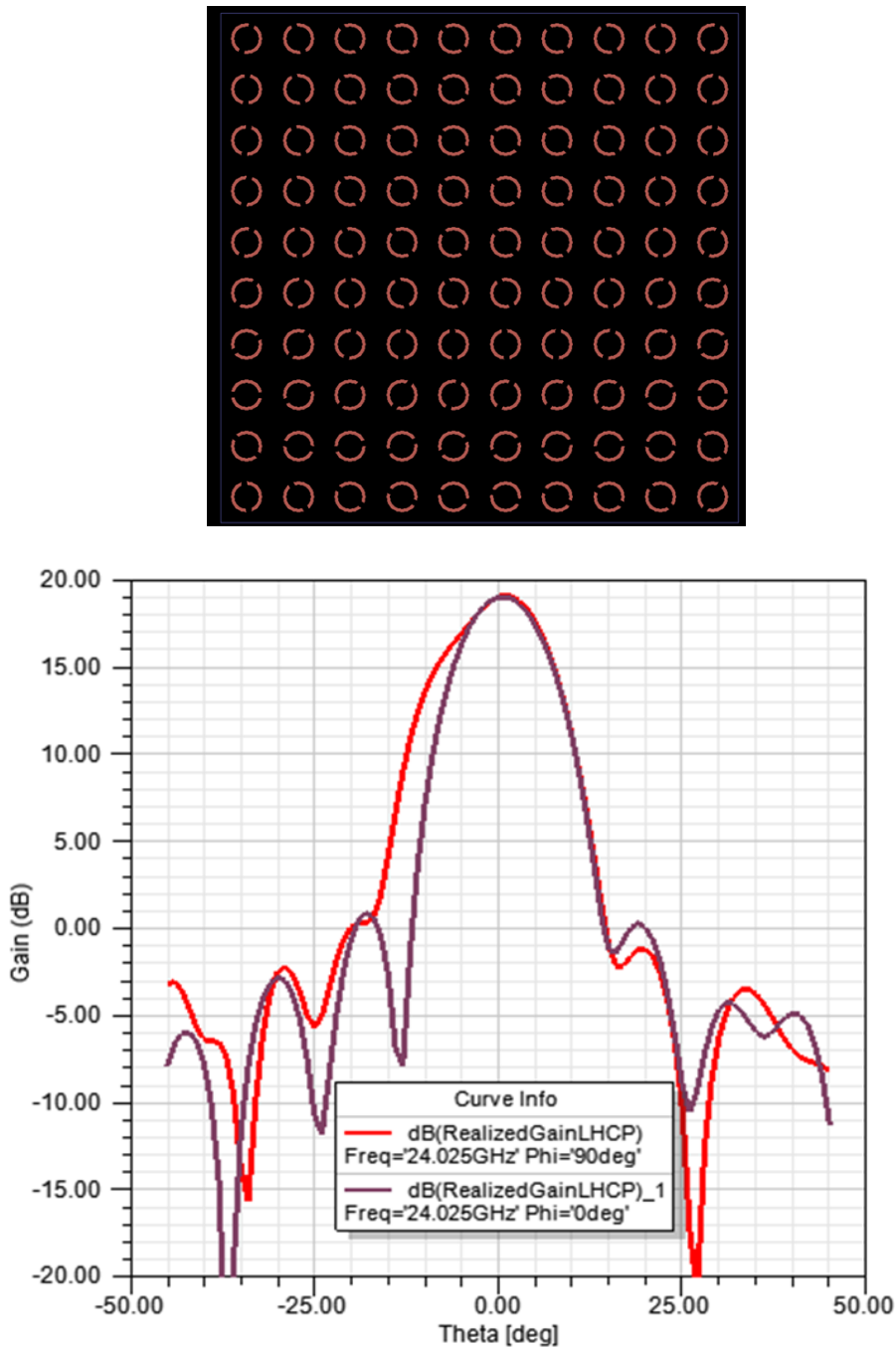

Figure 3.23: Reflectarray Final Design (top) and Performance (bottom)

For fabrication of the reflectarray a Python script was created to generate the Gerber file format commonly used for PCB manufacturing. All fabrication of the reflectarray was completed

using the LPKF laser located within the University of Washington physics department or at the local business Metrix Create:Space. The built prototype used for gain measurements is shown in Fig. 3.24 and achieved 19 dBi of gain matching the simulated prediction. The associated insertion loss between the feed input connector and feed microstrip solder joint is 1 dB.

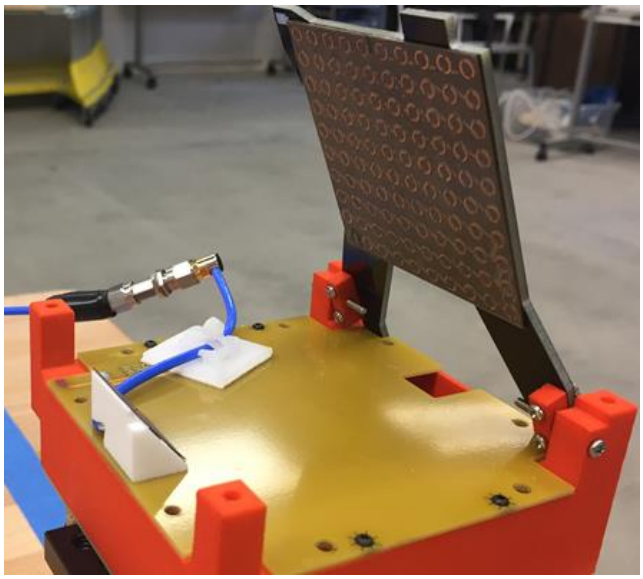

Figure 3.24: Reflectarray Prototype

3.2 RF Front End

From the onset my research in enabling deep-space communications for low-cost CubeSats, the RF Front End was recognized to be a key enabling component which lacked availability. The purpose of the RF Front End is to upconvert and increase the power level of the incoming RF signal. In surveying available communication systems hardware, it was quickly determined that realizing ≤ 6GHz was readily achievable using the commonly used line of Analog Technologies integrated circuits such as the AD9364. However, achieving anything above ~6GHz required additional RF circuitry and has the additional challenges of requiring different PCB substrates, and careful attention to optimizing impedance matching and minimizing RF losses while fitting within the CubeSat geometry and power constraints. Therefore, the development of an RF Front End

extends the current communication technology available providing access to the performance increases necessary for deep space CubeSat missions. The primary goal of the developing the RF Front End was to increase CubeSat access to the K/Ka bands with a low cost and uncomplicated design using robust design techniques with a focus on interoperability with a range of systems. Specific goals of the system were:

- Operate in the 24Ghz or 26Ghz band
- 15-35 watt power consumption
- Solid state architecture: low component count, uses GaN FETs
- Minimal use of custom components
- Use of commercially available COTS in surface mount packages
- Compatibility with existing systems: S-band as input using standardized connector, and will output 24/26GHz using SMA connector.
- At least 1 W of RF output power

3.2.1 Initial Mixing Architecture

Component surveys were completed evaluating all available COTS solutions required in an RF Front End. While many topologies exist for upconverting a modulated RF signal, such as frequency multiplication and multi-stage mixers, a superheterodyne single stage mixing architecture was selected. A single stage mixing setup minimizing component count and board space facilitating compatibility with the CubeSat for factor while at the same time not being hindered by bandwidth increase present in frequency multiplier upconverters. The primary limitation of single stage mixing setups, the undesirable harmonics, was addressed by freedom to shift the baseband (intermediate frequency) as well as using a bandpass filter post mixing.

Additionally, the reflectarray antenna system provides an additional layer of harmonic suppression.

The TGC4510-SM was initially selected, procured, and evaluated to serve as the mixing stage. This option was attractive since it met the power and frequency requirements, and was highly integrated including frequency multiplication and a medium gain amplifier which would minimize additional external RF stages. The initial topology design is shown in Fig. 3.25. While the TGC4510-SM proved to be performant on the bench, problems arose when moving from the bench into the CubeSat form factor and automating its operation. Specifically, the TGC4510-SM requires 10 external DC bias voltages, both negative and positive voltages, needing to be sequenced during turn off and turn on. Two of these bias voltages are also required to be the output of a control loop with the input of the control loop being current consumption of other DC biases. Therefore, while the RF complexity was relatively low, the DC bias and logic complexity was high. A DC bias control board design was initiated, utilizing digital-to-analog converters (DACs) coupled with op-amps to supply these voltages and their sequencing. Calculation of the required board space for DC biasing showed these 10 rails to require a footprint of beyond 8cm x 8 cm which is the size imposed by the CubeSat form factor. This mixing architecture was abandoned is pursuit of a solution requiring less complex biasing.

Beyond the mixing topology, the other two key components are the stable reference frequency, or local oscillator (LO), and the signal amplification. The local oscillator was down selected to the LTC6946 for being high frequency and therefore requiring a minimal number of frequency multiplier stages to reach an end LO of ~22GHz. The signal amplifier stage was selected to be a single power amplifier (PA) IC. This was already required to be within a surface mount

package instead of a die, and a single stage was selected versus combining multiple PAs due to design complexity, limited board space, and limited overall power consumption.

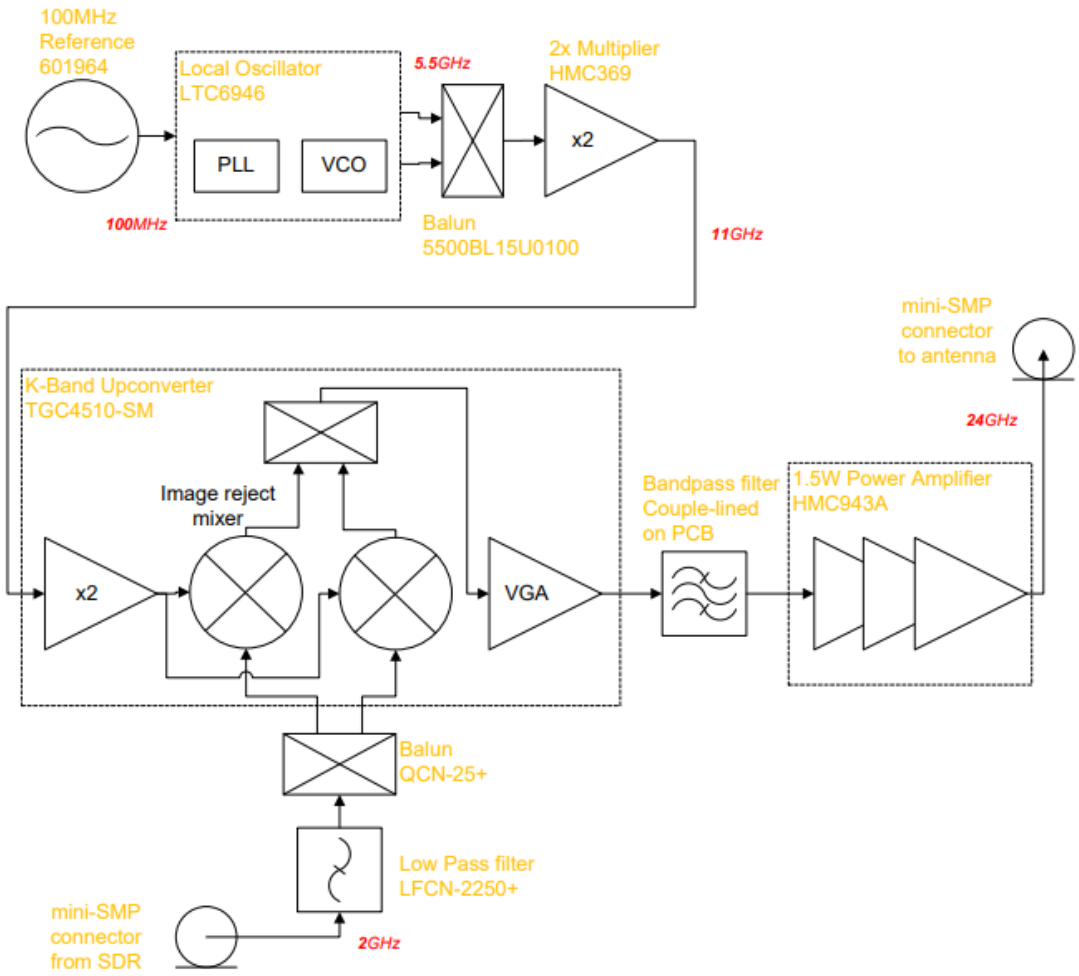

Figure 3.25: Initial Mixing Topology

3.2.2 Final Architecture

The mixing topology shifted to using a passive double balanced mixer. The HMC292 was selected, but other similar components also exist from Analog Devices which would satisfy the same application. The previous architecture was adapted by adding an additional frequency multiplier on the LO as well as adding an external medium gain amplifier before the power amplifier. However, now the mixing stage required no variable DC biasing or any complex power

sequencing which significantly simplifies the supporting electronics required. One key consideration was achieving the required LO drive power. By operating the already chosen combination phase lock loop (PLL) and voltage controlled oscillator (VCO) at full output power, and using the differential output reduced through a balun to single ended, the necessary mixer LO drive power was achieved.

The final RF Front End architecture is shown in Fig. 3.26. One design choice made from the project onset was to design conservatively with respect to hard-to-predict phenomenon. The rationale for this choice was to minimize the number of design cycles required. This is immediately evident on the DC biasing architecture. Each RF stage is driven by an independent low-noise voltage regulator in order to decouple noise between stages. With respect to noise generated from digital switching, a digital isolator was implemented between the microprocessor and the PLL/VCO. During boot up, the PLL/VCO is programmed over SPI, then the digital isolator is unpowered to minimize any digital switching being present during RF operation. The second digital isolator is kept powered on since it is used for high/low telemetry and commands.

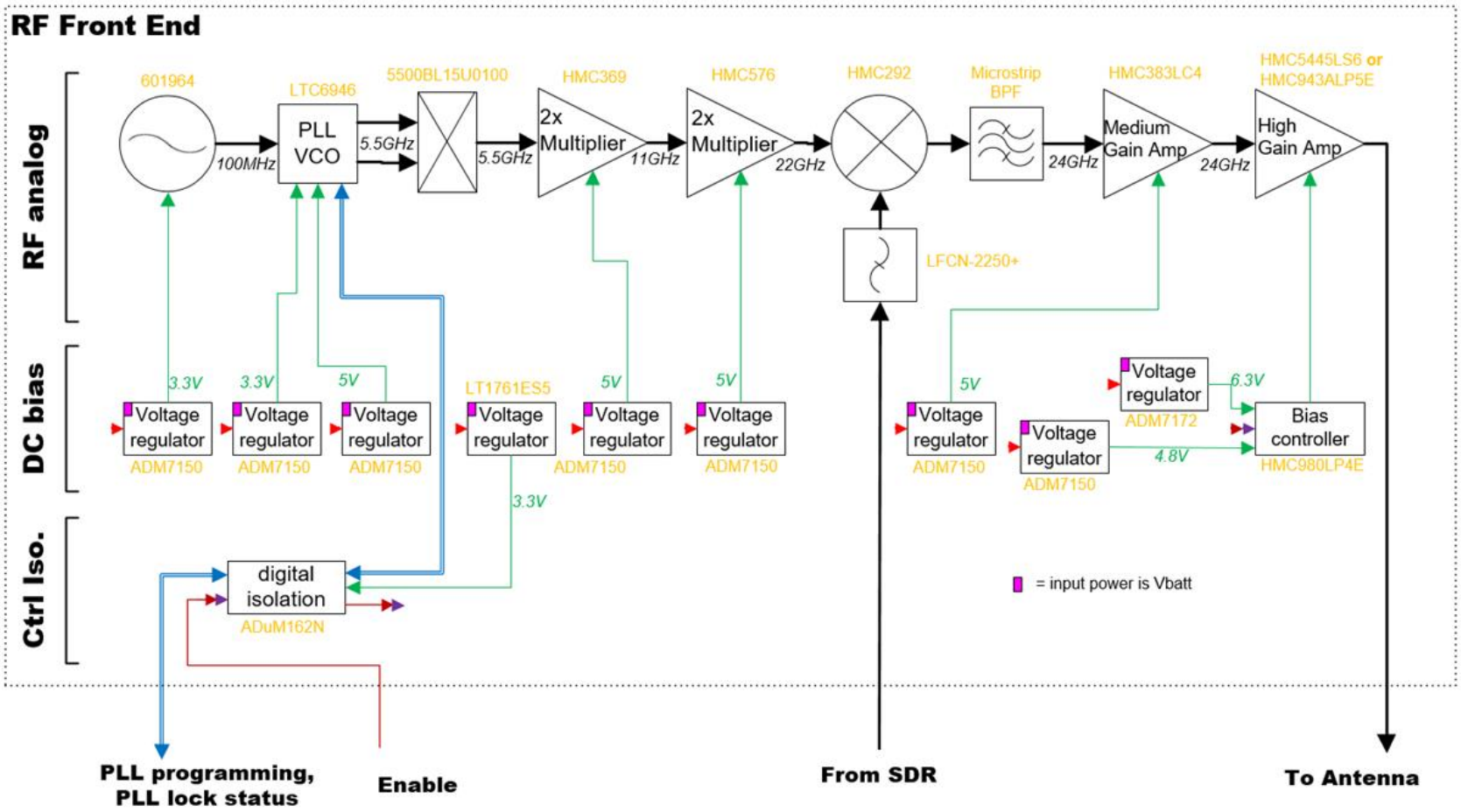

Figure 3.26: RF Front End Topology

The dominant RF performance parameters considered during the design were related to signal fidelity and harmonic suppression. Signal fidelity was addressed by running RF components within their linear region. While not ideal for total downlinking capability due to lower RF output power and poorer system efficiency, the intent with this RF Front End was focused on process development and design demonstration. The second RF performance parameter designed for was harmonic suppression, and was achieved through use of RF filters in addition to optimizing the IF and LO frequencies. The LO harmonics present are all multiples of the PLL/VCO output, corresponding to 5.5GHz, 11GHz, 16.5GHz, 27.5GHz, etc., from Fig. 3.26. The IF frequency, sourced from the USRP B200, harmonics occur at integer multiples of its output frequency. This impact was suppressed by utilizing a surface mount LFCN-2250+ low-pass filter.

Further addressing the resulting harmonics from the LO entering the mixer was done post-mixing. There were no COTS solutions available for the 24GHz band, and with minimizing overall board space a single band-pass filter (BPF) stage was chosen. A microstrip coupled BPF was chosen as it was most readily designable given the available project resources. Agilent Design Software (ADS) was used for the initial design of the BPF, and HFSS was used to validate its performance. Three BPFs were designed and built each with a center frequency of 23GHz, 24GHz, or 25GHz, shown in Fig. 3.27. This being the first BPF design and fabrication, it was unclear if a redesign would be required for frequency adjustment, and doing 3x designs up front was significantly less work compared to if a separate fabrication run was performed. The 24GHz design was successful and is shown in Fig. 3.28. This measurement was calibrated up to the connectors. To calibrate out the microstrip losses the microstrip-only sample was measured from Fig. 3.27 to had 2.3dB of loss. Therefore, the BPF radiated loss is ~2dB.

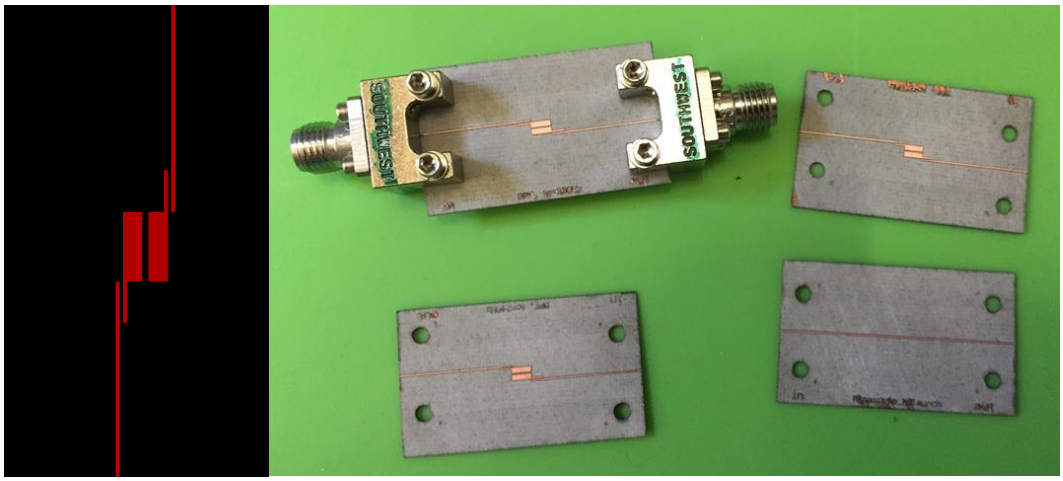

Figure 3.27: Band-pass Filter Design and Prototypes

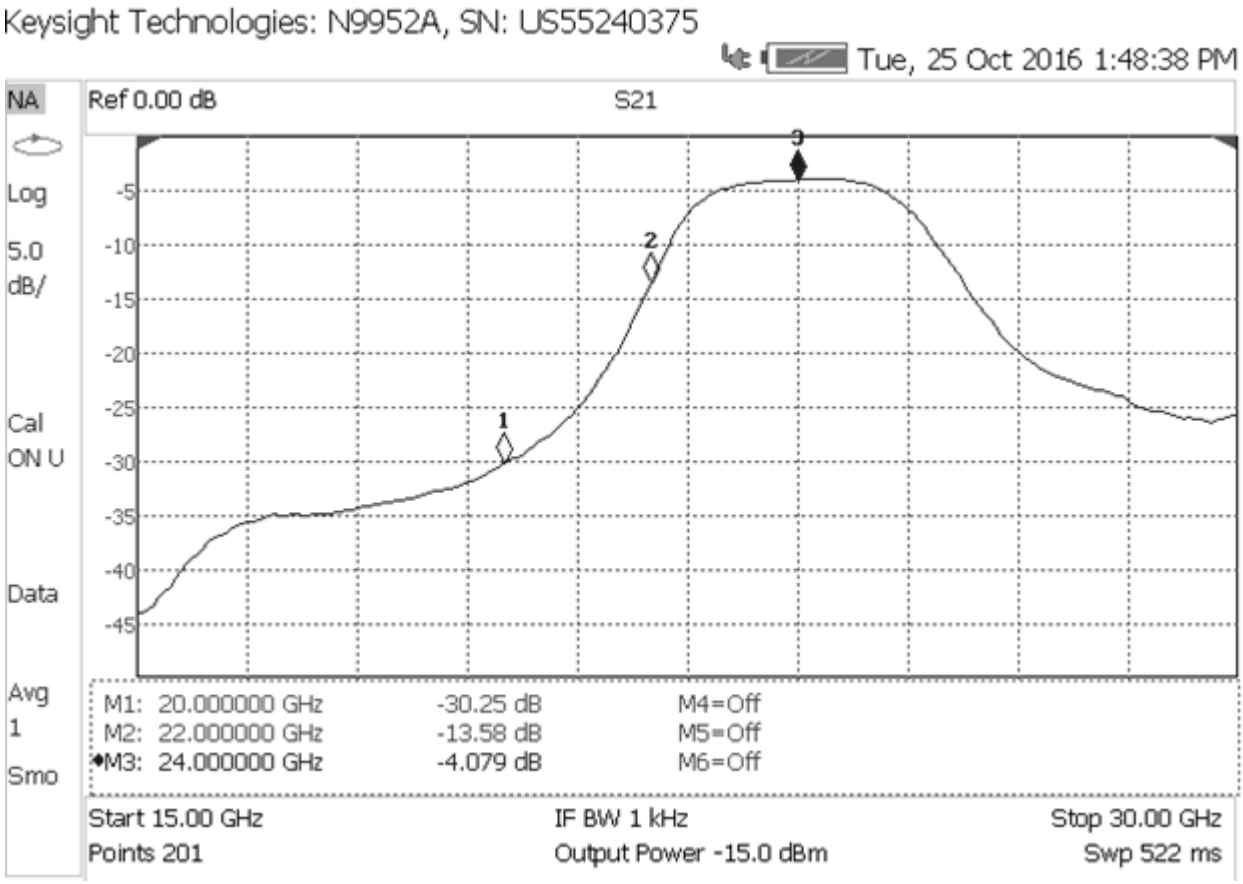

Figure 3.28: Band-pass Filter Passband Measurement

3.2.3 Innovations to Technology Access

Significant challenges in the development of RF PCBAs source from the high design complexity and complex manufacturing processes leading to high costs and long lead times. While the natural evolution of high frequency RF engineering came out of experienced teams with access to significant resources, the graduate student environment is in direct contrast. Simplifying these complexities was therefore recognized as an essential component in enabling the development of COM2. A summary of my efforts in this area lead to the following design methodologies and selections:

1. Adopt an incremental prototyping approach with emphasis on inexpensive and rapid prototyping
2. Use development boards provided by companies as a starting point in all designs
3. Validate proof-of-concept RF operation of all components before integration into the larger RF system
4. Adopt a quasi-multilayer board stackup to significantly lower costs and lead time of PCB manufacturing

Manufacturing of the RF Front End began with converting the LTC6946 PLL/VCO development board layout from a 4 layer design to a 2 layer design. The value of this was allowing for all RF ICs to share a common a 2 layer high speed PCB; this was essential for minimizing the overall size and complexity of the system. The PCB substrate choice was Rogers 4000 series, chosen because it low loss at these frequencies and when performing a survey of commonly available PCB substrates at PCB manufacturers it was a popularly available option. Many development boards also used this same substrate. The RF chain was subsequently prototyped where each individual RF IC and its supporting circuitry was individually validated. All

prototyping utilized the Southwest Microwave end launch connectors as shown in Fig. 3.27. The local oscillator chain prototype and spectral output is shown in Fig. 3.29.

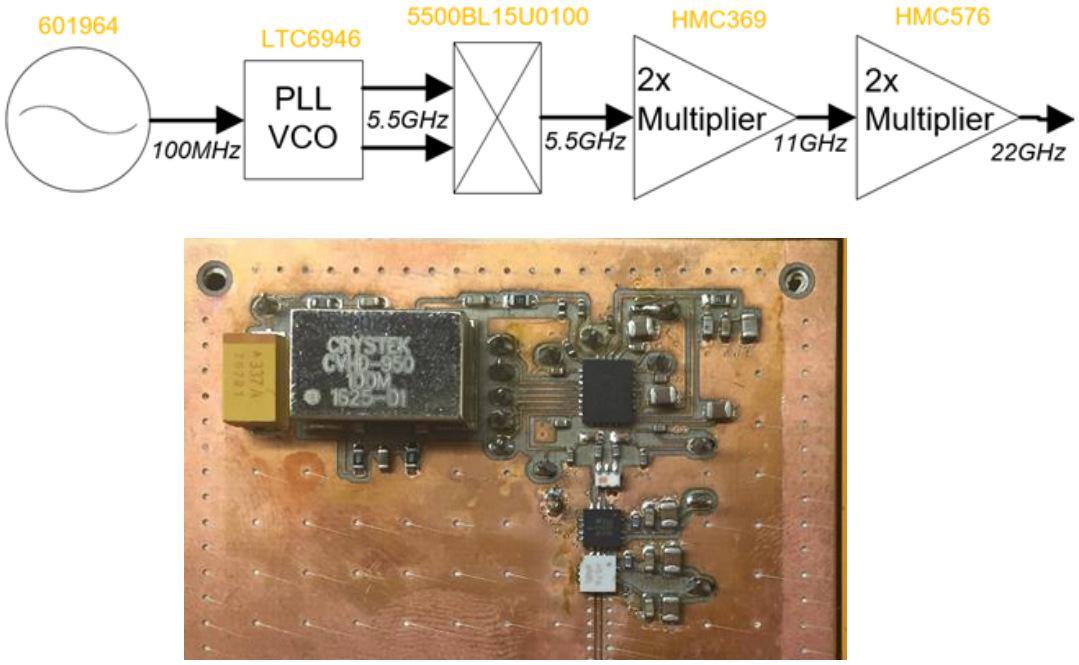

Figure 3.29: Local Oscillator Prototype

The stackup developed consisted of exclusive use of Rogers 4000 2 layer PCB for RF ICs and an FR4 PCB for all DC routing. These two PCBAs were then affixed to each other using a polyimide with pressure sensitive silicone adhesive. Metals pins, removed from 2mm pitch connectors, were then used to make connections between the two PCBs. The result of this stackup is the RF PCB costs around ~$150 to manufacture and the FR4 board is around ~$50. Since the FR4 board is only used for DC routing and rigidity support, this stackup is sufficiently performant. In contrast, the traditional approach is to glue these two different substrates together during PCB manufacturing, resulting in lead time increases from ~3 days to ~3 weeks, and a cost increase of ~10x. The stackup I developed is shown in Fig. 3.30. Thermal dissipation was addressed by

providing cut outs from the FR4 board to allow for aluminum extrusions from the below structure to come directly up to the Rogers board; for an example of this application, see the four hole provisions for fasteners around the power amplifier in Fig. 3.31. Additionally, the flight Rogers's board utilized 2oz copper for increases in plane thermal dissipation.

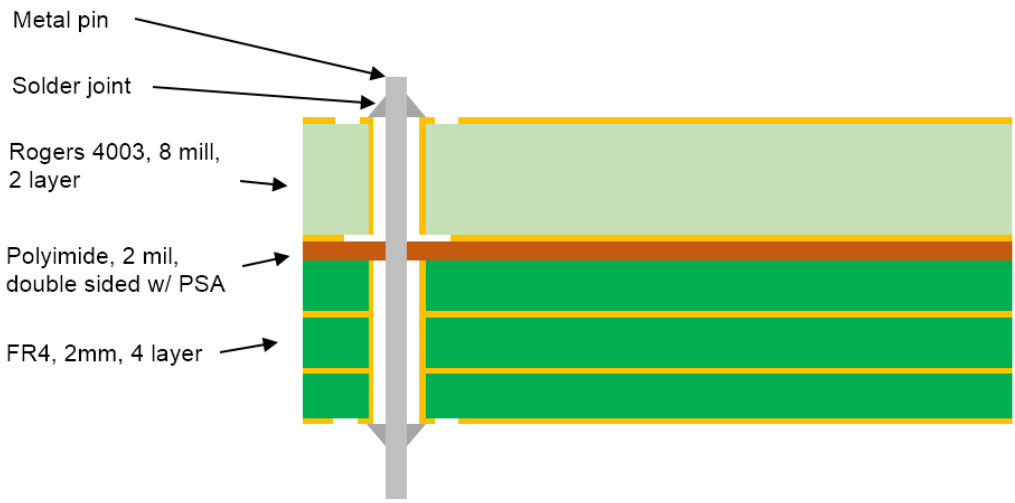

Figure 3.30: RF Front End Board Stackup

The flight RF Front End utilized immersion silver plating no mitigate issues of uncontrolled magnetic permeability of plating's utilizing nickel. Previous to the flight model, all Rogers PCBs were bare copper. Bare copper required special care such as storing in vacuum sealed bags with desiccant and minimizing hand oil contamination during handling. The advantage of bare copper was that an LPKF laser enabled rapid and inexpensive prototyping. The vias were constructed using the paste plus oven technique provided by LPKF. While this method does not provide uniform, consistent, or even well controlled via construction, a test sample was constructed of a ground coplanar waveguide which was found to have expected reflection and insertion loss performance. When switching to the later chemical etched and plated flight model, the BPF was separately manufactured so its performance could be isolated in measurement. Only the BPF

underwent this process since it was the most sensitive component on the RF Front End to changes in PCB dielectric properties.

The layout, shown in Fig. 3.31, was designed to localize functions, and provide continuity from previous prototyping with minimal layout changes of critical functions. In anticipation of the microstrip causing unwanted effects from radiation at RF absorber, Mast Technologies MR11-0041-00, was placed on the surface directly above the filter.

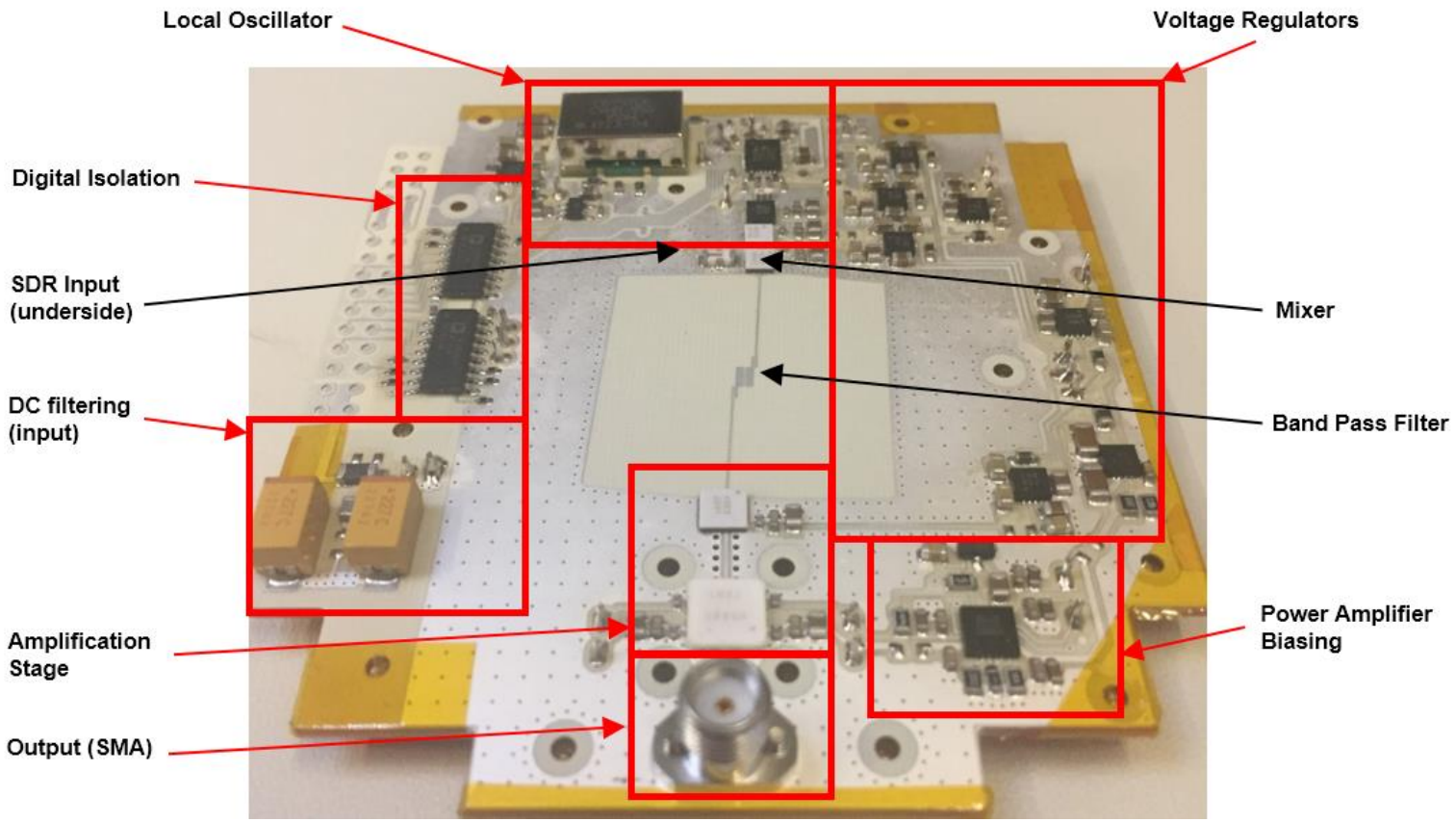

Figure 3.31: RF Front End Layout

3.2 COM2: A Prototype Deep Space Communication System

The final COM2 system was built around pushing the state of the art for high frequency communication technology for the CubeSat applications while still being accessible to University level projects. Enabling this required the development of two innovations described in Section 3.1 and Section 3.2. These parts fit into the context of the overall communication system as shown in Fig. 3.32. A Raspberry Pi 3 Compute Module was used to host the CAN interface, and provide a USB connection to the software defined radio (SDR). A modified, read-only, version of the Raspbian OS was developed and executed GNU Radio to interact with the SDR. The overall system is designed to have as simplistic and minimal as possible interfaces to the CubeSat bus. The interfaces include: (1) data bus interface via CAN to support telemetry and commands to indicate the health of COM2 and change the operating state as well as transmit data, (2) power interface using unregulated battery voltage (~6.6V to ~7.1V), and (3) a mounting via 8x 4-40 fasteners. The spectrum output of the RF Front End provides 28dBc of harmonic suppression and provides a power output of 30dBm, see Fig. 3.33.

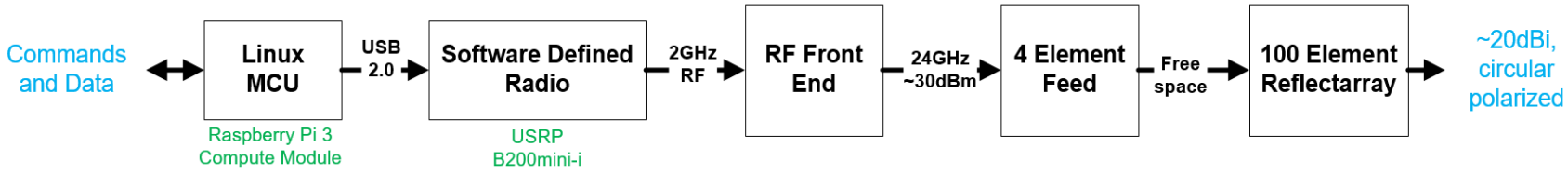

Figure 3.32: COM2 Block Diagram

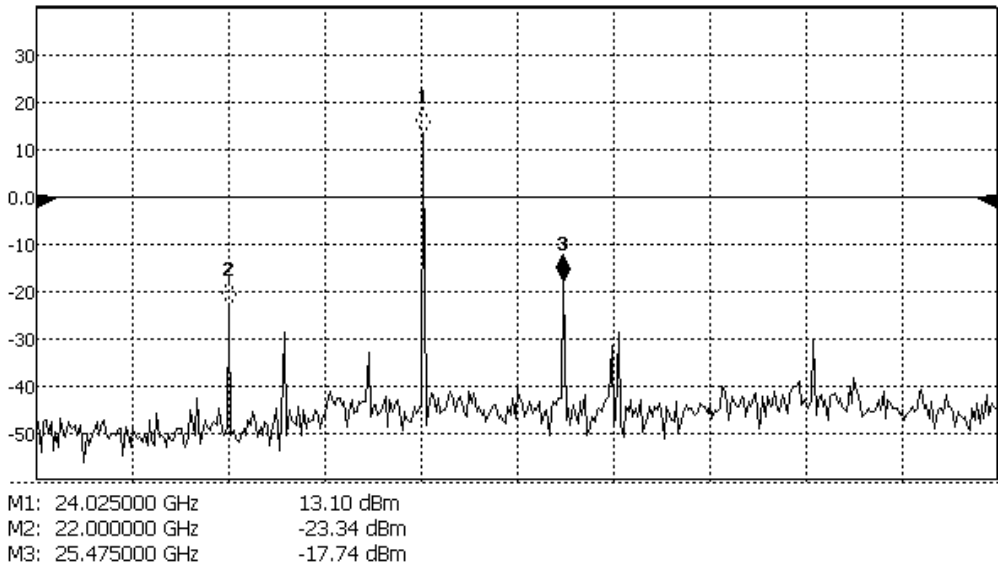

Figure 3.33: Harmonic Spectrum Output

The arrangement of PCBAs within COM2 were functionally separated between baseband and the RF Front End. This distinction was made because the RF Front End is susceptible to digital switching noise. Additionally, the power amplifier on the RF Front End required a low thermal resistance sink. The solution was to split the COM2 electronics into two chambers: the top chamber has just the RF Front End and the bottom chamber contains all other components. Pass-throughs between the sections consist of a standard 0.1" pitch 2x row connector carrying SPI, control and telemetry high/low lines, pins for a deployment mechanism, as well as an RF connection coming from the SDR. See Fig. 3.34 and Fig. 3.35 for more detail.

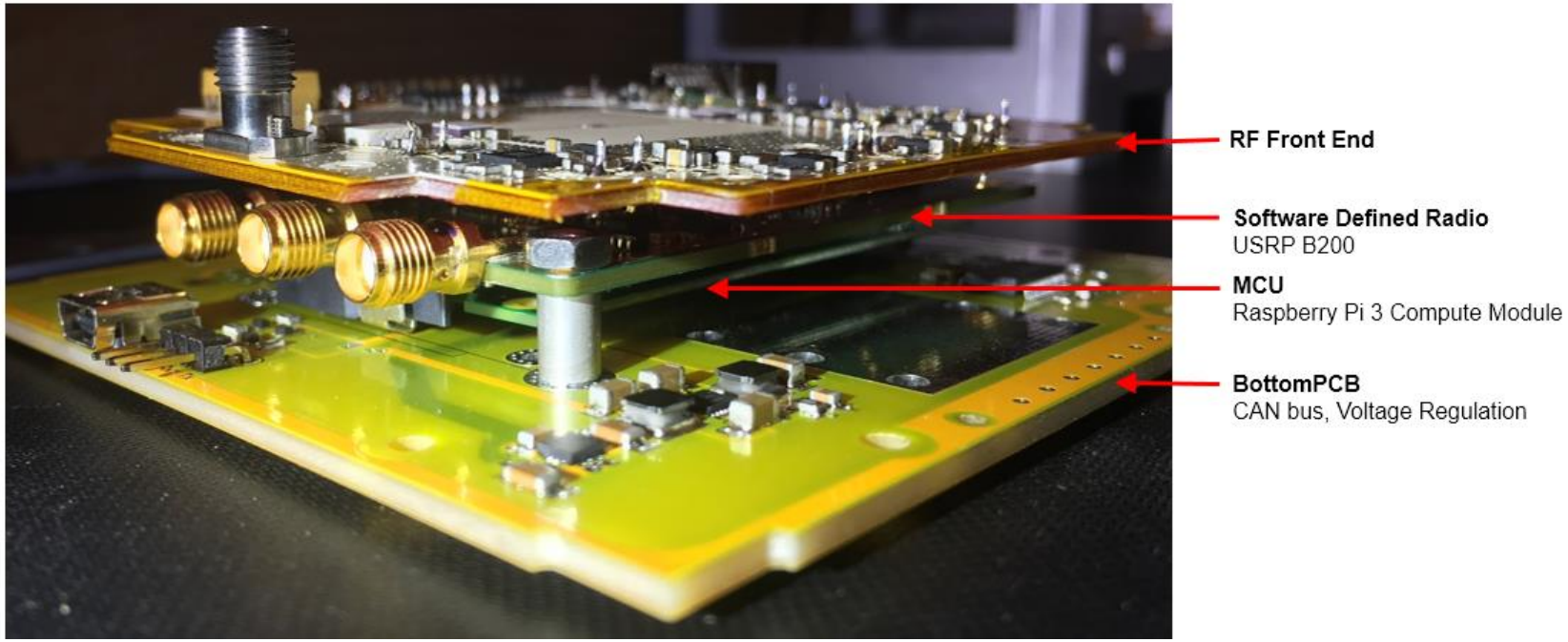

Figure 3.34: COM2 Internal PCB Structure

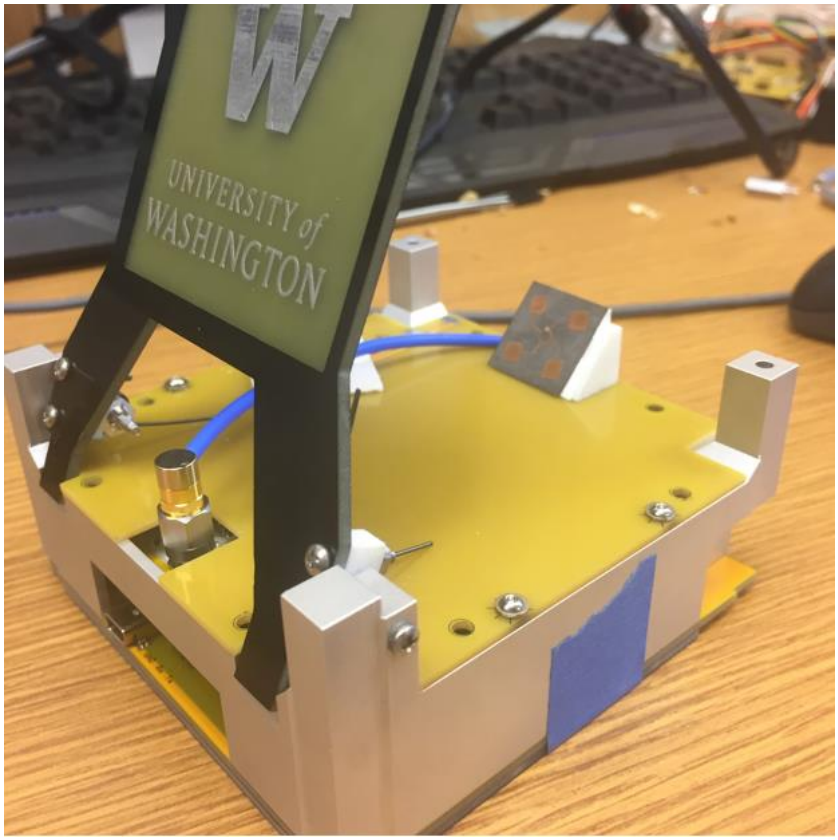

Figure 3.35: COM2 Assembled

Chapter 4. Sun-Earth Trojan Explorer Mission

In this chapter a low-cost CubeSat mission, called SETEM, is defined by analyzing top-level imaging, propulsion, and communication requirements and design. The primary mission objectives of SETEM are to detect new candidate Sun-Earth L4 or L5 Trojan asteroids, and if no new candidates dedicated then improve the current upper bound Earth Trojan asteroid (ETA) limit. Additionally, SETEM is to be a low-cost enabling mission design and executable by universities. The current upper bound ETA count limits are ~73 at L4 and ~97 at L5 for $H \leq 20.5$ brightness, and SETEM is to improve this by a 5x factor by providing an upper bound of 15 ETAs at $H \leq 20.5$ brightness [58][33]. It is shown this can be achieved by utilizing a 10 cm diameter aperture using 20 s exposure times at a maximum ETA detection range is 0.13 AU. To minimize the propulsion requirements and launch vehicle cost for the SETEM, the novel approach of piggybacking on lunar bound mission is evaluated, and it is found shown the minimum ΔV to reach L4/L5 is ~416 m/s. The communication analysis performed derives an equivalent isotropic radiated power requirement of 56 dBWi at the K-band frequency utilizing the Deep Space Network Earth ground station. This communication supports the downlinking of ETA survey images at a 150 kbps data rate at a maximum distance of 1.5 AU. A communication solution for SETEM is proposed, building on top of COM2 presented in Chapter 3, which meets and exceeds the performance needed to successfully carry out SETEM.

4.1: Mission Overview

The Sun-Earth Trojan Explorer Mission (SETEM) is a low-cost CubeSat mission designed to travel directly to the Sun-Earth L4 or L5 regions to identify new candidate Earth Trojan Asteroids (ETAs). The intent of the mission is to be financially and technologically accessible for universities. The scope of this chapter's efforts is the initial study phase for the SETEM mission

defining the key performance parameters, top-level subsystem requirements, and the driving relationships between these parameters and requirements. The idea of sending a CubeSat to the L4/L5 Lagrange points to search for and study ETAs was initially conceived by a small group from NASA [163]. Their two page proposal was to send a 6U CubeSat with a wide-view infrared camera to the L4/L5 to survey the region. My efforts build on top of and add substantial detail to this initial idea but deviate in the following ways: (1) utilize visible spectrum imaging instead of infrared to better leverage COTS components and eliminate any active cooling systems for the imaging sensor, and (2) utilize narrow view instead of wide view optics to provide improved angular resolution of objects in the sky and therefore be able to discern between already identified objects, such as in the main asteroid belt, and new objects.

The primary mission objective of SETEM is to identify candidate Sun-Earth L4 or L5 Trojan asteroids; and a null result shall improve the upper bound limit of ETAs by a factor of 5x. The intent is to send at least one SETEM spacecraft to each of the Lagrange points. If SETEM proves successful, follow-up missions based on the SETEM spacecraft design can be carried out using updated imaging capabilities to target a specific ETA. The current upper bound ETA count limits, which are derived from previous null result searches, are ~73 at L4 and ~97 at L5 for $H \leq 20.5$ corresponding to S-type asteroids of ~210m across or larger [58][33]. The secondary mission objectives of this mission are: (1) provide the university educational system with direct hands-on experience developing and operating a deep-space CubeSat mission, and (2) to provide a low cost and open source deep-space CubeSat design which can be adapted to a variety of other deep-space science missions.

The top-level conceptual operations begins with launching SETEM on an existing cargo mission to the moon, see Fig. 4.1. This novel approach significantly reduces launch costs and

minimizes propulsion requirements to reach either L4 or L5 Trojan region. Once deployed, SETEM undergoes small thrust maneuvers to set up the lunar gravity assist. After passing by the moon, SETEM's primary thrust application begins setting up the survey region trajectory. Once at the Lagrangian survey region, SETEM will survey the region using a narrow field optical camera being scanned in the vertical direction. SETEM will traverse along the Phase IV in Fig. 4.1 over the course of one year. Collected images will be processed onboard and when new candidate objects are detected they will be transmitted back to Earth. Upon an uplinked command SETEM can then revisit regions to provide additional imagery.

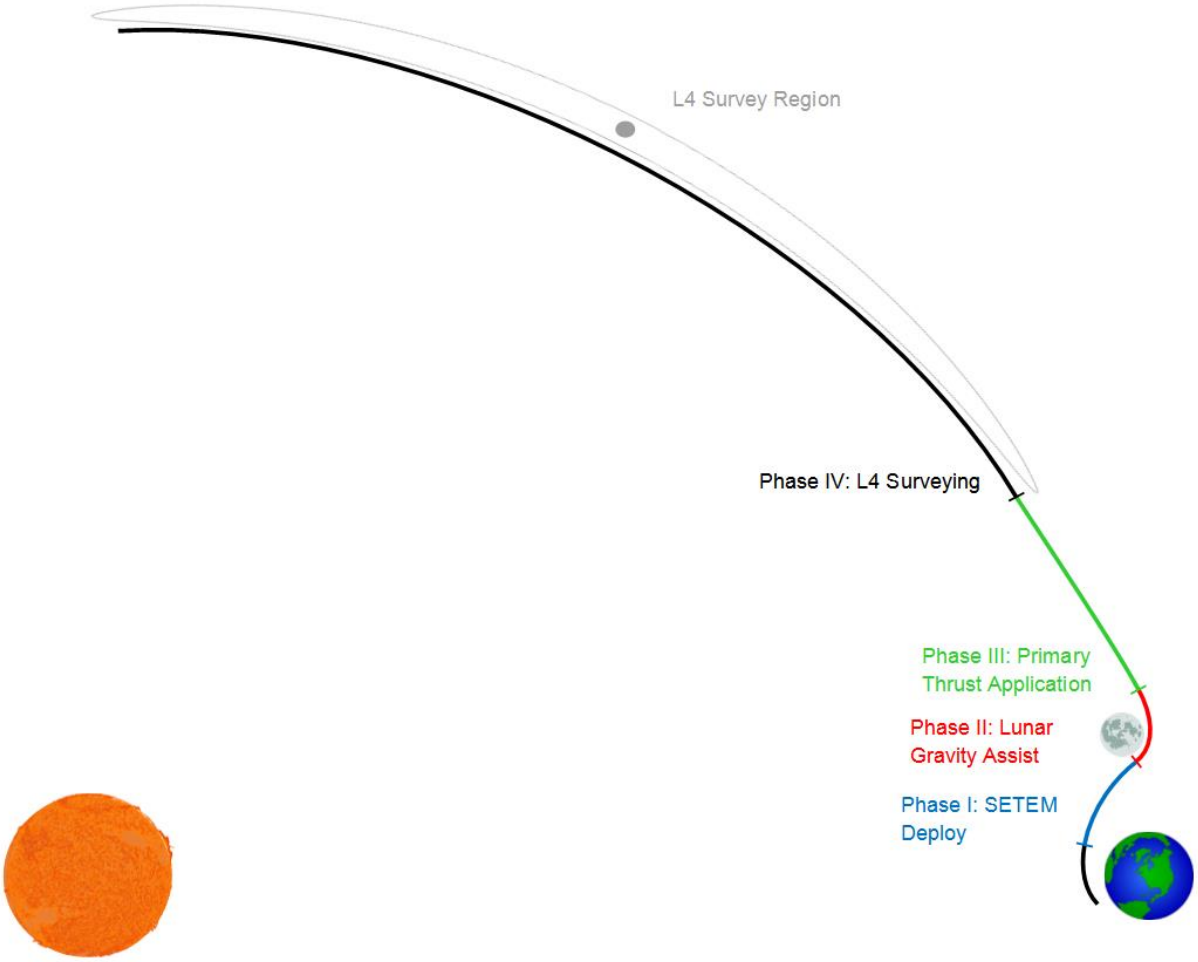

Figure 4.1: SETEM Conceptual Operations: Phase I: SETEM is deployed from lunar bound cargo mission; Phase II: Lunar gravity assist is performed to target L4 or L5 region; Phase III: Primary thrust applications correct trajectory to intercept Lagrangian point; Phase IV: Survey of region is conducted and candidate images are sent back to Earth.

The key performance parameters and top-level requirements are driven most strongly from imaging, propulsion, and communication needs in order to fulfill the mission objectives. In Section 4.2, the imaging and optical requirements are derived assuming the previous null results are to be improved to an upper bound by a 5x factor, or 15 ETAs at $H \leq 20.5$. The absolute magnitude H is a measure of an objects brightness referenced to an observer 1 AU away from the object, the object 1 AU from the Sun, and zero phase angle [164]. In Section 4.3, the propulsion requirements are derived using the novel approach of utilizing a trans-lunar injection orbit to help overcome the

majority of the ΔV requirements. Section 4.4 then focuses on communication requirements are reflectarray design.

The 27U SETEM bus concept is shown in Fig. 4.2. The volume is motivated by a 3U camera body volume, communications also at 3U, propulsion system which at 1000 m/s ΔV is approximately half the spacecraft mass and volume (13U), then left over space for electrical power, attitude determination and control systems and potentially additional science payloads, such as a dosimeter. Fig. 4.2 shows the quad reflectarray communication setup derived in Section 4.4 as well as the 10cm camera lens from Section 4.2. The quad deployable reflectarray keeps the overall setup simple without requiring compound deployments, as well as the feed antenna not requiring deployment. Furthermore, the geometry developed allows for the feed antenna to be operational before reflectarray panel deployment.

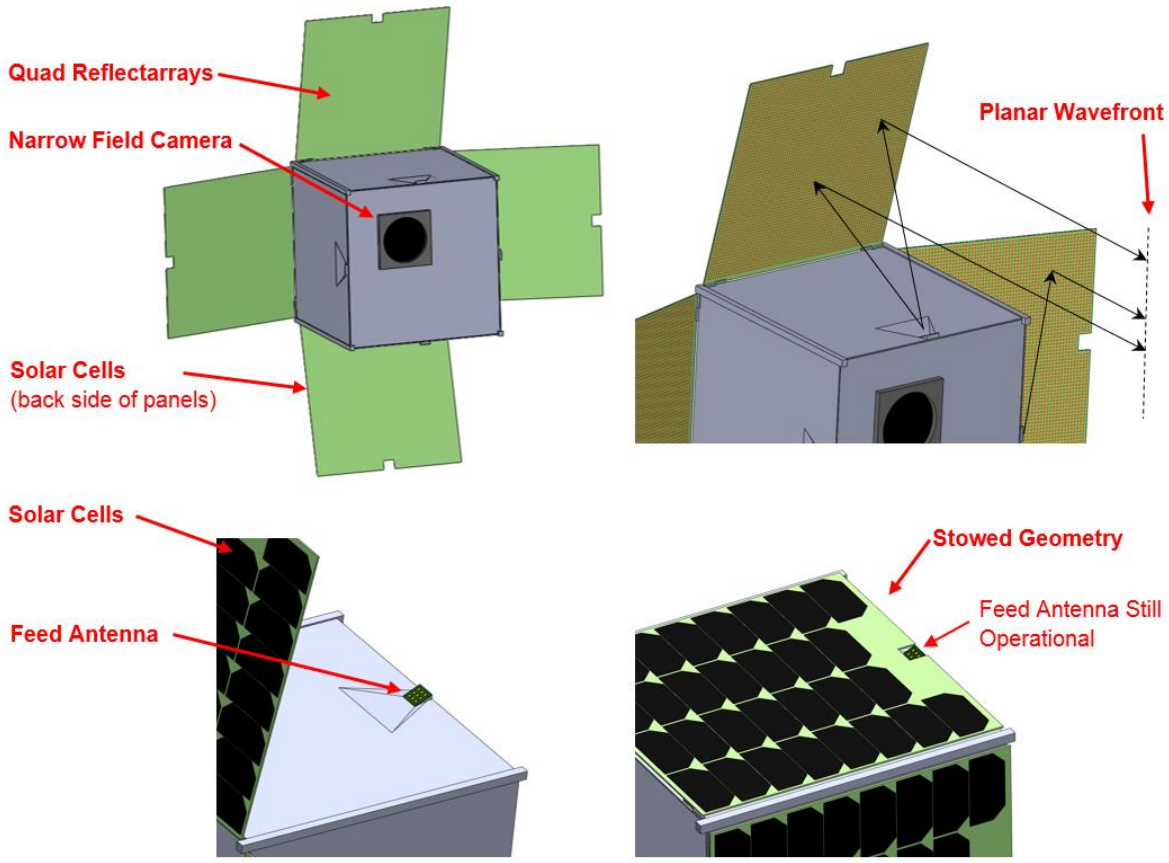

Figure 4.2: SETEM 27U Bus Overview: Quad reflectarray setup (upper left), Reflectarray ray tracing geometry (upper right), Feed antenna inset (lower left), Pre-deployed stowed configuration (lower right)

4.2: Imaging Requirements

CubeSats being a small size, typically in units of 1L, significantly limit camera body sizes. Therefore, it is important to consider the implications and requirements of an imaging system capable of detecting ETAs. It will also be shown that the limiting parameter for this mission is the focal length rather than the optics collection area.

4.2.1 Upper Bound from Null Result

The imaging requirements are driven from the mission requirement of improving the upper bound ETA count to 15 at $H \leq 20.5$ brightness. It is important to understand how an ETA null

result is used to derive an upper bound ETA count. The following description follows from the most recent ETA upper bound published using the DECam instrument [58], and is also the same general approach used in the two other ETA upper bounds published [29][33]. In evaluating the measurement implications to satisfying the null result requirement, the primary question of interest is: what is the largest distribution which could have escaped detection? The first step in answering this question is developing a synthetic set of ETAs which are most likely to exist. This is done by starting with a set of objects with randomized orbital parameters and letting their orbits evolve in an orbit propagation with includes perturbations such as Jupiter. By propagating these objects forward in time a stable set of ETAs is established. The next step is to evaluate the efficacy of the detection instrument which shall include all effects such as background stars and processing algorithms. This is captured by the recovery rate, $R(H)$, which is the ability to correctly identify an object as a function it's brightness. In the case of the OSIREX-Rex null result analysis, $R(H)$ was derived using in-flight data of detected main belt asteroids compared to known main belt asteroids present within the imaging field-of-view (FOV) [33]. For the DECam survey $R(H)$ was derived by injecting the synthetic ETA distribution into the pixel array input of the processing pipeline and looking at identification rate [58]. In designing SETEM, $R(H)$ must be bounded initially and be used to guide the spacecraft design. Once operational $R(H)$ can be refined through measurement data collected. With $R(H)$ known it can then be used to bound the upper limit of ETAs. In the DECam survey analysis, it was found that the detection of 3 ETAs was within 3-sigma for the synthetic population generated, leading to [58]:

$$\mathrm{ETA}_{\max}(H) = \frac{3}{R(H) \cdot C}$$

where C is the coverage of the survey relative to the entire Lagrangian region. This same approach is adopted for SETEM. Therefore, meeting the requirement of an ETA upper limit to 15 at $H \leq 20.5$ is achievable through a very high recovery rate at $H \leq 20.5$ as well as high imaging coverage of the region. For the SETEM missions, the recovery rate for $H \leq 20.5$ is allocated ~90% leaving ~20% to coverage.

4.2.2 Recovery Rate

Recovery rate is primarily a function of: (1) objects brightness; (2) measurement hardware capabilities; (3) and detection algorithm. The recovery algorithm in the DECam consisted of a source extractor, bullseye identification, and verification against previously catalogued objects [58]. For the DECam survey, the recovery rate is shown in Figure 4.3. It shows good performance at higher object brightness, and then quickly tapers down as objects become fainter near $H > 20$.

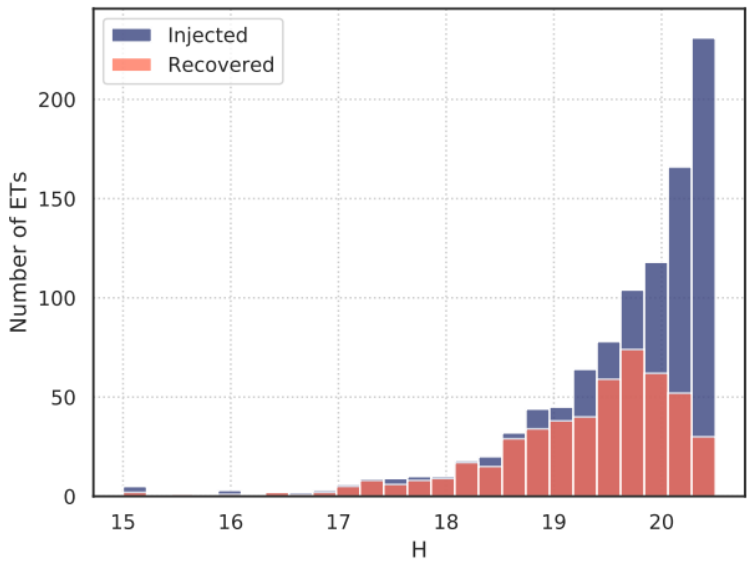

Figure 4.3: DECam Detection Algorithm Performance [58]

It is expected that the SETEM mission will need to perform similar detection algorithm operations using onboard processing due to the large communication distance prohibiting full dataset downlinking, see Section 4.4.1 for more detail. In order to provide a highly usable data input into the detection algorithm, the faintest detection threshold, corresponding to $H = 20.5$ at maximum view distance, is set to $SNR = 30\ dB$ at imaging sensor output. This conservative selection pushes the allocated ~10% error in recovery rate into the detection algorithm implementation.

4.2.3 Coverage

Defining coverage requires specifying the spatial extent of the L4/L5 regions. Figure 1.9 shows the full extent to span inclinations >45° and longitude spans of >100°. Due to inclination changes of the SETEM vehicle being prohibitive due to high ΔV requirements, a primary vertical scanning approach is adopted with the spacecraft staying on the elliptic plane. Furthermore, minimizing the inclination surveyed during the mission is optimal, since this reduces the maximum distance to an ETA. Consistent with the ~20% mission coverage previously defined, and Fig. 1.9, the coverage for SETEM is limited to 5° inclination and 100° longitudinal span.

4.2.4 Comparable Imaging System

The SETEM mission is required to autonomously evaluate images for potential ETAs due to the volume of data generated relative to the downlink capability. One example of this type of ETA detection algorithm was the DECam survey of the L5 region which implemented a centroiding algorithm to identify object centers, and compared these object locations against a known object catalog to identify new potential objects. This type of processing is very similar to another type of component already commonly used on spacecraft, including CubeSats, which is the star tracker. A star tracker is a device which images a star field, and along with on onboard star

catalog and processing algorithms, outputs the spacecraft attitude with respect to the celestial sphere. The primary components of a star tracker consist of a light baffle, lens, imaging sensor, and processing, as shown in Fig. 4.6.

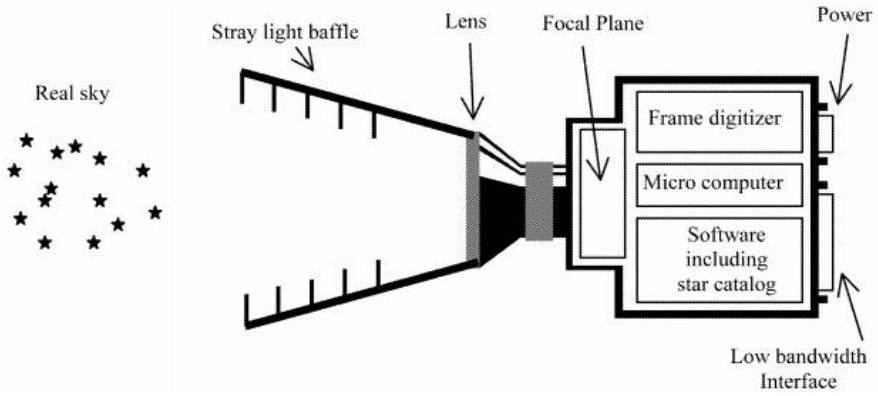

Figure 4.6 Star Tracker Overview [156]

The primary differences between a star tracker and the SETEM imaging payload are: (1) ability to detect fainter objects, (2) larger star/object catalog, and (3) new object identification.

4.2.5 Exposure Time

The first step in determining exposure time is considering the number of photoelectrons reaching the CCD. The spectral contributions from an ETA under consideration are the visible range, 400nm to 800nm. Being reflected from the sun, the spectrum of the ETA is assumed to be a black body of temperature 5800K. Using the Kodak KAF-401 CCD image sensor which has a quantum efficiency of 0.3 – 0.6 across the 400nm to 800nm range, the influx of photons can be converted to a photoelectron count. The result is that for an object of apparent magnitude 0 will result in a count of $R_{object,m=0} = 19100 \text{ photoelectrons}/\text{s}\cdot\text{mm}^2$, where the units of seconds is exposure

time, and the area is aperture size [156]. Shifting from absolute magnitude H to apparent magnitude m is done through [157]:

$$m = H + 5 \cdot \log_{10}\left(d_{OO} d_{BS}\right)$$

where d_{OO} is the distance from the object to observer in AU, and d_{BS} is the distance from the object to the sun. This is evaluated in Section 4.2.7 resulting in $m = 16.1$ at a view distance of $D_{max} = 0.13\ \text{AU}$ as the faintest ETA which shall be detectable. This results in a count of $R_{ETA} = R_{ETA,m=0} \cdot \frac{1}{2.512^{15.4-0}} = 0.007\ \text{photoelectrons}/\text{s}\cdot\text{mm}^2$. The factor of 2.512 comes from the scale definition of two objects having a 5 magnitude difference for a 100 times brightness difference, or $\sqrt[5]{100} \cong 2.512$.

The dominant noise contribution considered is the photon-noise-limited case [162]. This noise source follows from the variance of a Poisson distribution due to the random arrival of photons from the ETA at the image sensor, where this noise power, σ_{ETA}, is:

$$\sigma_{ETA} = \sqrt{R_{ETA} \cdot A_{camera} \cdot t_{exposure}}$$

where R_{ETA} is photoelectrons per second reaching the CCD sensor is, A_{camera} is the aperture area, and $t_{exposure}$ is the exposure time. Two others noise sources present are that of the background sky brightness and the base noise. Base noise is associated with the CCD and associated electronics necessary for sampling, such as analog-to-digital conversion and amplifiers, as well as non-uniformity in the pixel array. By requiring $SNR = 30\ \text{dB}$ the ETA becomes significantly brighter than the base noise and background sky noise, and therefore the photo-noise-limited case becomes valid. The SNR is therefore:

$$SNR \approx \sqrt{R_{ETA} \cdot A_{camera} \cdot t_{exposure}}$$

A is the aperture area. This SNR is evaluated assuming the camera aperture fits with a 3U volume of a CubeSat. 3U is 10cm x 10cm x 34cm, and providing space for the stray light baffle (see Fig.4.6) leaves 10 cm for a lens aperture. The result is that $t = 20\,s$ exposure time is required, assuming: 10 cm aperture, quantum efficiency of 0.3 to 0.6 from the Kodak KAF-401 CCD image sensor, $SNR = 30$ dB, and an ETA of $H = 20.5$ at $D_{max} = 0.13\,AU$.

4.2.6 Field-of-View

The FOV is important since it sets the angular precision of determining an object's center location. It is also important to ensure that the FOV relative to the numbers of pixels allows for sufficient differentiation among detected objects such that an ETA does not go undetected due to being binned with another object. FOV also sets how many individual pictures are taken in order to provide coverage of the Lagrangian region and therefore has direct consequences on communication. A lower bound FOV is derived assuming the camera system is of the simplest type for CubeSat integration, namely the refracting camera where the aperture is made up of a single convex lens and the CCD is placed at the lens focal length. The FOV for a single refracting lens is:

$$FOV_{total} = 2 \cdot \arctan\left(\frac{d_{CCD}}{2 \cdot f}\right)$$

where d_{CCD} is the size of the CCD and f is the focal length. The focal length is restricted by the CubeSat geometry, which limits the overall camera body to fit within 34 cm. As will be shown below, the focal length is the limited parameter in providing sufficient angular resolution in the FOV. Here, angular resolution means the horizontal/vertical field of view divided by the number

of horizontal/vertical pixels on the CCD array. The highest angular resolution occurs using the smallest sized pixels and the longest focal length. As this is a driving performance metric, the maximum focal length compatible with the CubeSat geometry is adopted. Setting $f = 30\ \text{cm}$ provides sufficient margin and volume for the lens, CCD sensor and associated electronics, shielding and thermal management, and CubeSat structure. The CCD chosen for this analysis is highest performance COTS option which is commonly used in astronomy applications, the KAF-3200. It has a useable resolution of 2184 x 1472 pixels, and the pixel size is 6.8 x 6.8 μm [173]. This leads to a horizontal FOV of 2.84° and vertical FOV of 1.91°.

Verifying there is sufficient angular resolution to ensure an ETA does not go undetected requires knowledge of the number of objects within the FOV. The number of objects of given brightness or brighter, N_m, was fitted from data to be $N_m = 6.57e^{1.08 \cdot m}$ [156]. Using $m = 16.1$, leads to a total of 245 million objects and 32160 objects in the FOV. At magnitude $m = 16.1$ there are ~100x fewer objects than there are pixels in the FOV which helps ensure an ETA will not go undetected from insufficient angular resolution.

4.2.7 Spatial Geometry

In SETEM operation imaging takes place during opposition, where the spacecraft imaging apparatus faces directly away from the sun. Additionally, the spacecraft trajectory should be chosen such that the maximum viewing distance is minimized over the entire coverage region. Optimizing for the two drivers leads to a spacecraft trajectory which follows some distance away along the inner edge at of the L4/L5 region within the ecliptic plane, as shown in Fig. 4.1. From the spacecraft vantage point, the maximum view distance, D_{max}, is therefore set by the spatial extent of the Trojan region combined with the distance between SETEM and Trojan region. The

lowest D_{max} is when SETEM follows the inner edge of the Trojan region, which would lead to $D_{max} = \sqrt{\left(\tan\left(5°\right)\cdot 1\text{ AU}\right)^2 + \left(0.006\text{ AU}\right)^2} = 0.088\text{ AU}$ and a vertical scanning angle of $2\cdot\tan^{-1}\left(1\text{ AU}\cdot\tan\left(5°\right)/0.006\text{ AU}\right) = 172°$. Here, the width of the Trojan region is from a previous orbital stability analysis yielding semi-major axis range of 1 ± 0.003 AU [154][155]. It is important to minimize the scanning range since this minimizes the amount of data to be sent to Earth and also minimizes the slew requirements on the spacecraft attitude control system. The maximum view distance is instead set by the result of the previous section and derived from $m = H + 5\cdot\log_{10}\left(d_{oo}\cdot d_{BS}\right)$ which allows shifting from absolute magnitude H to apparent magnitude m is done through [157]. Setting $d_{BS} = 1.003\text{ AU}$ and $m = 16.1$, results in $D_{max} = d_{oo} = 0.13\text{ AU}$. This bounds the scanning range to $2\cdot\tan^{-1}\left(1\text{ AU}\cdot\tan\left(5°\right)/0.096\text{ AU}\right) = 85°$.

4.2.8 Pixel Smearing

While L4 and L5 are defined points, an ETA's region of stability is significantly larger, which can described by the libration amplitude, libration period, and inclination. Libration amplitude describes the longitudinal span of an ETA orbit. Bounding the ETA speed is done by considering the libration amplitude and period generated from numerical analysis of a synthetic ETA population in Fig. 4.4. The upper bound is at high libration amplitudes:

$$V_{max,in\text{-}plane} = 140°\cdot 1\text{ AU}\cdot\frac{2\pi}{220\text{ years}} = 0.038\frac{\text{AU}}{\text{year}} = 180\ \text{m/s}$$

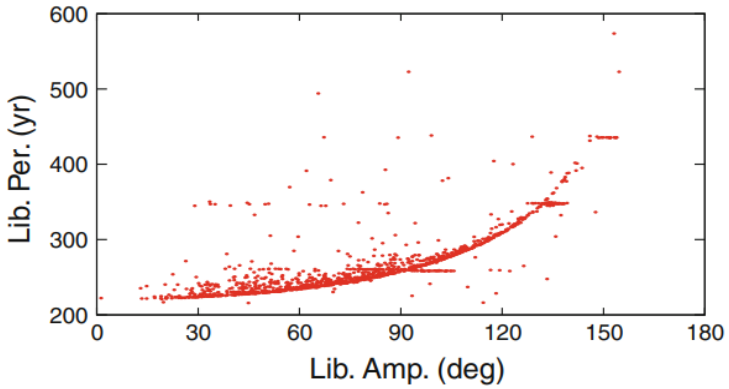

Figure 4.4: ETA Libration Period and Amplitude Dependence [155]

Here, the factor of 2 is for accounting for the full period of motion, and the π is for converting from average speed to maximum. For out-of-plane relative speed, an upper bound is determined from simulation results shown in Fig. 4.5.

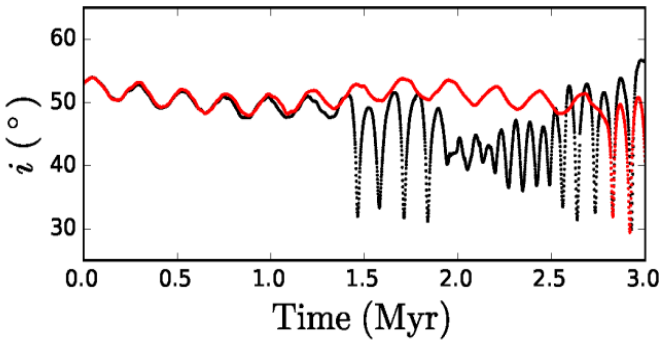

Figure 4.5 Orbital Evolution for Two ETA Models [154]

From Figure 4.5 the last 0.5 Myr is used to set the out-of-plane velocity upper bound:

$$V_{max,out\text{-}plane} = \tan(20°)\cdot 1\ \text{AU}\cdot\frac{2\pi\cdot 6}{0.5\ \text{Myr}} = 2.7e-5\ \frac{\text{AU}}{\text{year}}$$

Since: $V_{max,out\text{-}plane} \ll V_{max,in\text{-}plane}$, then: $V_{max} \approx V_{max,in\text{-}plane} = 180\ \text{m/s}$.

To evaluate the implications of the ETA velocity on exposure time the maximum ETA angular displacement is calculated during a single frame. $V_{max} = 180\ m/s$ over $t_{exposure} = 20\ s$ sets the distance traveled, and at $D_{max} = 0.13\ AU$, the angular displacement is 0.00001°. This angle is then compared to the degrees of sky per pixel on the CCD. In Section 4.2.6 the horizontal FOV is 2.83° and is 2184 pixels wide, leading to a sky pixel coverage of 0.0013 degrees per pixel. The result is that during a single exposure, an ETA at the farthest distance stays well within one pixel which is ideal to prevent pixel smearing.

4.3: Propulsion Requirements

The novel approach proposed for SETEM is to utilize a trans-lunar injection orbit to significantly decrease propulsion demands. A trans-lunar injection (TLI) is a large burn performed by spacecraft to leave Earth orbit to target a lunar orbit. With a renewed interest in space exploration and lunar bound missions, see Section 2.2, upcoming lunar missions will provide low cost opportunities for secondary cargo, such as CubeSats. By minimizing the propulsion requirements for SETEM, the overall cost and satellite complexity are kept to a minimum. The purpose of this subsection is to evaluate the propulsion requirements for SETEM considering launch window sensitivity.

4.3.1: Initial Condition

The reference trajectory used for this analysis is from first launch of the NASA SLS Orion capsule. Along with the development of this new launch vehicle and crew capsule, NASA hosted the CubeQuest Lunar Derby Centennial Challenge. During my contributions for phase I on this challenge, see Section 2.4, NASA provided the Interim Cryogenic Propulsion Stage (ICPS) disposal state as the closest-to-Earth ejection point for contestant CubeSats, which was:

$$R_{x,ICPS} = \text{-}1.502e4 \text{ km}$$
$$R_{y,ICPS} = \text{-}2.357e4 \text{ km}$$
$$R_{z,ICPS} = 2.242e3 \text{ km}$$
$$V_{x,ICPS} = \text{-}4.855e\text{-}1 \text{ km/s}$$
$$V_{y,ICPS} = \text{-}5.049 \text{ km/s}$$
$$V_{z,ICPS} = \text{-}8.780 \text{ km/s}$$

These coordinates are valid at 2.4581031227118e6 Julian time (December 15, 2017) in an Earth inertial reference frame. The ICPS disposal state is visualized using Science Tool Kit (STK) in Fig. 4.7. The design of the ICPS disposal state is to put the ICPS onto a trajectory which leaves Earth's region in order to not become hazardous orbital debris. This disposal state is achieved through a lunar gravity assist, which can be seen as the apparent change of direction in the trajectory. This figure also exemplifies how depending on the lunar calendar day, different outgoing directions are achieved which can be leveraged to target either the L4 or L5 regions. In Fig. 4.7 shown in red is when the ICPS is within the moon's sphere of influence r_{SOI}, defined by [165]:

$$r_{SOI} = a \cdot \left(\frac{m}{M} \right)^{2/5}$$

The sphere of influence applies to a three-body problem when one of the bodies is significantly smaller than either of the other two, and is used to identify what object has primary gravitational influence on the smaller third body. M and m are the masses of the larger and smaller bodies, a is the semi-major axis of the smaller body with respect to the larger body. Using $M_{moon} = 7.342e22 \text{ kg}$, $M_{Earth} = 5.972e24 \text{ kg}$, $M_{Sun} = 1.989e30 \text{ kg}$, $a_{moon} = 3.844e5 \text{ km}$, $a_{Earth} = 1.496e8 \text{ km}$ leads to $r_{SOI,moon} = 6.617e4 \text{ km}$ and $r_{SOI,Earth} = 9.245e5 \text{ km}$.

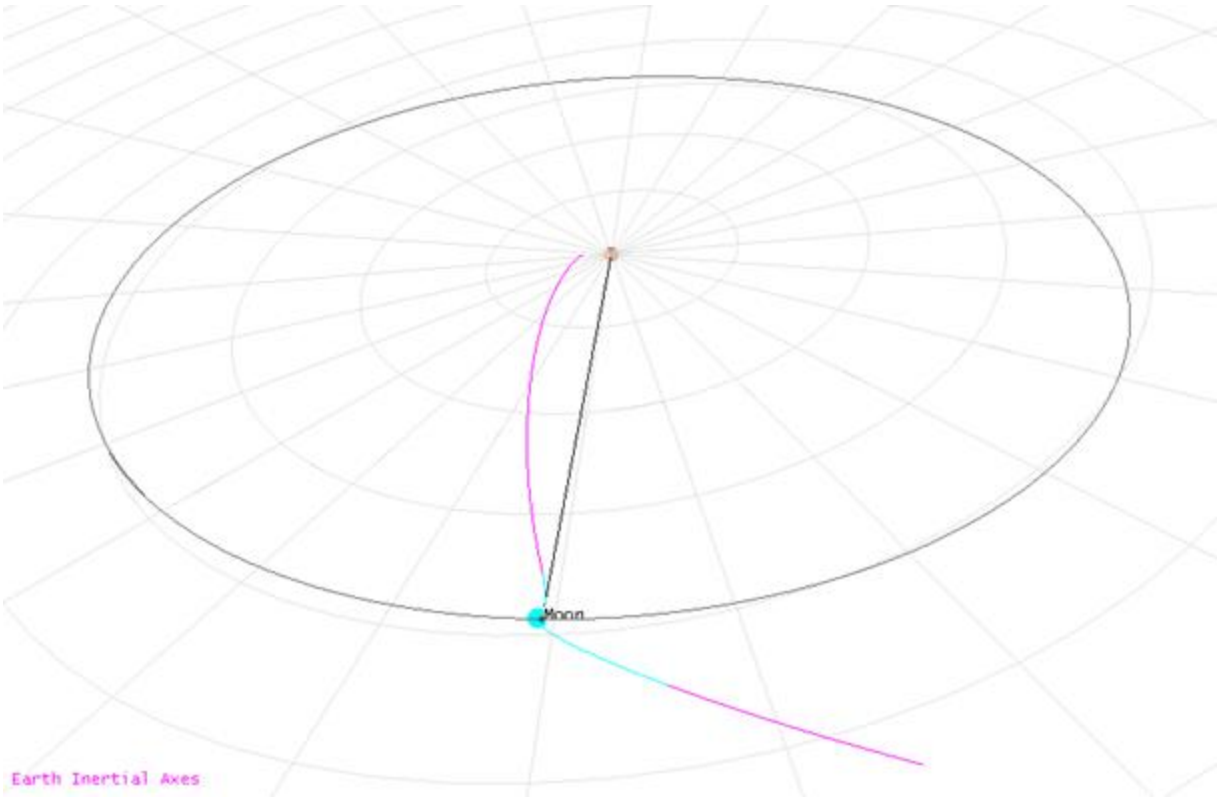

Figure 4.7: ICPS Disposal State Lunar Gravity Assist

To analyze using the ICPS disposal state for the SETEM mission it is important to accurately account for the impact of the lunar gravity assist. STK was used to propagate the ICPS state in various section shown in Table 4.1.

Table 4.1: STK Propagator Sequential Usage

From Section	**To Section**	**Propagator**
ICPS disposal state	distance to moon $r_{SOI,moon}$ (decreasing)	Earth HPOP
distance to moon $r_{SOI,moon}$ (decreasing)	distance to moon $r_{SOI,moon}$ (increasing)	Moon HPOP
distance to moon $r_{SOI,moon}$ (increasing)	distance to Earth $r_{SOI,Earth}$ (decreasing)	Earth HPOP

The usage of different propagators depends on criteria set by the sphere of influence. The Earth HPOP propagator utilizes a 21 order Earth gravity model as the central body and the Sun

and moon as third bodies, and the Moon HPOP propagator is utilized using 48th order moon gravity model and the Earth and Sun as third bodies. The end state which serves is selected at the boundary for when the primary gravitational influence transitions from the Earth to the Sun; this will become especially important in Section 4.3.2 when the Hohmann transfer analysis is considered. The final end state from Table 4.1, hereafter referred to the B_{t0} state, referenced in an Earth inertial frame, is:

$$
\begin{aligned}
R_{x,t0} &= 7.876e5 \text{ km} \\
R_{y,t0} &= -4.673e5 \text{ km} \\
R_{z,t0} &= -1.268e5 \text{ km} \\
V_{x,t0} &= 9.844e-1 \text{ km/s} \\
V_{y,t0} &= 1.940e-4 \text{ km/s} \\
V_{z,t0} &= 6.978e-2 \text{ km/s}
\end{aligned}
$$

Whereas typical space mission trajectories are designed for optimal ΔV considerations, SETEM is intended to be secondary cargo on a lunar bound mission, and therefore not have optimal drop off parameters. It is therefore necessary to consider all launch possibilities, which in the current context is over a lunar month. The initial velocity and position vectors within the B_{t0} state are rotated in the Earth frame by angle ϕ. Shown in Fig 4.8 are the states: $B_{t0} = B_{t0,\phi=0^\circ}$, $B_{t0,\phi=90^\circ}$, $B_{t0,\phi=180^\circ}$, an $B_{t0,\phi=270^\circ}$. Also shown are the direction of Earth's velocity as well as the direction to the Sun.

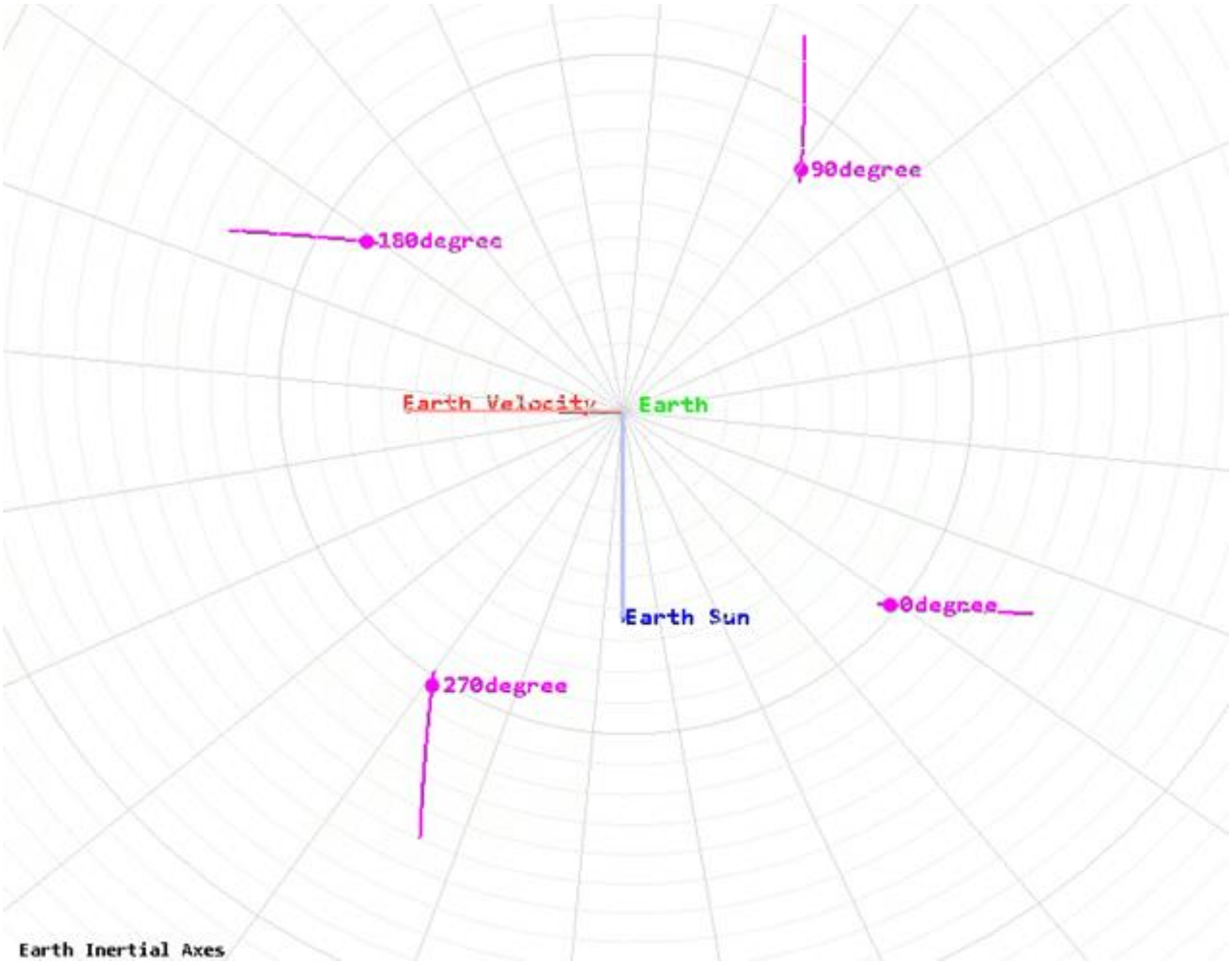

Figure 4.8: SETEM Earth Outbound Direction

4.3.2: ΔV from Specific Energy

The lower bound propulsion requirement is derived from the ΔV required to balance the outgoing kinetic energy term at the B_{t0} state location. In the Sun inertial frame the specific energy, E, from kinetic and gravitational potential energies:

$$\varepsilon_{initial} = \frac{V_{initial,\pm}^{2}}{2} - G \cdot \left[\frac{M_{Earth}}{r_{SOI,Earth}} + \frac{M_{moon}}{r_{SETEM \rightarrow moon}} + \frac{M_{Sun}}{r_{Earth \rightarrow Sun}} \right]$$

$$V_{initial,+} = \left| V_{Earth} \right| + \left| V_{t0} \right| + \Delta V_{E,+}$$

$$V_{initial,-} = \left| V_{Earth} \right| - \left| V_{t0} \right| + \Delta V_{E,-}$$

The distance from the B_{t0} state to the moon, $r_{SETEM \to moon}$, is 6779e5 km extracted from STK. The distance from the B_{t0} state to the Sun is set to the distance from the earth to the Sun, $r_{Earth \to Sun}$, since this generalizes by averaging the B_{t0} state over one year. $V_{initial}$ has two limits, one where the Earth's velocity, V_{Earth}, is parallel with V_{t0} and one that is antiparallel. The freedom between choosing the angle between these two aforementioned vectors is equivalent to considering different launch day opportunities, see Fig. 4.8. ΔV_E is the impulsive change in velocity associated with this specific energy analysis. For the final state at L4/L5 SETEM has the some rotation period as Earth, and is equidistant between the Earth and Sun.

$$\varepsilon_{final} = \frac{V_{Earth}{}^2}{2} - G \cdot \left[\frac{M_{Earth} + M_{moon} + M_{Sun}}{r_{Earth \to Sun}} \right]$$

V_{Earth} is taken as 29.78 km/s and $r_{Earth \to Sun}$ is 1 AU or 1.496e8 resulting in:

$$\Delta V_{E,+} = -972 \text{ m/s}$$
$$\Delta V_{E,-} = +1001 \text{ m/s}$$

The importance behind the spread of the two ΔV_E limiting cases is that it predicts useful bounds for maximum propulsion requirements of ~1 km/s when considering conservation of energy only. It also suggests the minimum propulsion requirement occurs midway between the two limiting cases where the outgoing velocity direction, $\hat{V}_{t0}$, is perpendicular to Earth's velocity, $\hat{V}_{Earth}$, corresponding approximately to the $B_{t0,\phi=90°}$ or $B_{t0,\phi=270°}$ states. In the next section the impact of angular momentum is considered and will provide more insight into the dependence on ϕ.

4.3.3: ΔV from Hohmann Transfer

To understand the impact of the launch day on ΔV requirements Hohmann transfer techniques are applied. The Hohmann transfer is the most energy efficient two-impulse orbit maneuver between two coplanar orbits which share a common focus [167]. In order to use this technique a number of simplifications and assumptions are made. The first is use of the patched-conic approximation where N-body problems are reduced to three-body by separating out different spatial regions of the problem space based on the various sphere of influences each defined by r_{SOI} [165].For the SETEM, there are three regions traversed through: the Earth's SOI, the moon's SOI, and the Sun's SOI. The B_{t0} was passively propagated until the boundary between passing out of the Earth's SOI and into the Sun's SOI which allows all subsequent analysis to occur with only the Sun as the central body.

The Lagrangian point L4/L5 is inherently a three-body problem, so it is important to consider the impact of approximating this problem as a two-body problem. As a two-body there is no Earth included and the only two bodies are the spacecraft and the sun. This can be quantified by considering the summed potential and kinetic energies. Following a similar form from the previous section, below are the specific energies of SETEM including the Earth and not including the Earth while stationary at L4/L5.

$$\varepsilon_{No\ Earth} = \frac{\left(V_{Earth} + \Delta V_{correction}\right)^2}{2} - G \cdot \left[\frac{M_{Sun}}{r_{L4/L5 \to Sun}}\right]$$

$$\varepsilon_{With\ Earth} = \frac{\left(V_{Earth}\right)^2}{2} - G \cdot \left[\frac{M_{Earth}}{r_{L4/L5 \to Earth}} + \frac{M_{Sun}}{r_{L4/L5 \to Sun}}\right]$$

Setting $\varepsilon_{No\ Earth} = \varepsilon_{With\ Earth}$ and $r_{L4/L5 \to Earth} = 1\ AU$ leads to $|\Delta V_{correction}| = 89\ m/s$. This ΔV will be shown to be significantly below the minimum ΔV required from the primary orbit maneuver required.

The next approximation used for this analysis is that $\hat{V}_{t0}$ is in the Earth's orbital plane. This is not guaranteed, since the moon has a 5.15° inclination [166]. The intention is this condition would be met for the SETEM by performing small propulsive corrections before the lunar gravity assist combined with bounding allowable initial conditions on SETEM's drop off point B_i and time. For the scope of this chapter, only a single disposal state is considered for the ICPS, as defined in Section 4.3.1, but further work would be to perform Monte Carlo analysis for a variety of launch vehicle and mission combinations. Another assumption is the use of impulse propulsion maneuvers when SETEM will be outfitted with a low-thrust electric propulsion system; this is expected to lead to an underestimate of ΔV required. The last assumption taken with the approach presented is not quantifying ΔV associated with phasing and survey coverage maneuvers; this section specifically addresses the ΔV for reaching the semi-major axis and eccentricity of the L4/L5 points, and these additional operating ΔVs are accounted for in the mission design in the propulsion margin requirement of +50%.

In considering the two impulses associated with the Hohmann transfer it is useful to parametrize the orbit in terms of its periapsis and apoapsis. The first impulse is to go from the initial orbit's periapsis to the periapsis of the transfer orbit, and the second impulse is to go from the apoapsis of the transfer orbit to the apoapsis of the final orbit [167]. This assumes the apoapsis of the final orbit is larger than the periapsis of the initial orbit. For this application where the Sun is the focus, the angular momentum, h, is [167]:

$$h = \sqrt{2 \cdot G \cdot M_{Sun}} \cdot \sqrt{\frac{r_a \cdot r_p}{r_a + r_p}}$$

Here r_a is the apoapsis and r_p is the periapsis. In addition to angular momentums, the speeds at the apoapsis and periapsis are:

$$V_{a,p} = \frac{h}{r_{a,p}}$$

For the SETEM using B_{t0} as the initial state we have $r_{a,t0} = 0.981\,AU$ and $r_{p,t0} = 0.882\ AU$. The STK software was used to perform coordinate transformation from the Earth centered to Sun center system. The transfer orbit then has $r_{p,transfer} = 0.882\ AU$ and $r_{a,transfer} = 1\,AU$, and the final orbit is circular with $r_{final} = 1\,AU$. This leads to a ΔV of 150 m/s for the first impulse and 948 m/s for the second impulse, or a total ΔV of 1098 m/s. This process is then repeated for various ϕ rotations to show the ΔV dependence for different $B_{t0,\phi}$ states. This was initially performed in 30° steps, and 15° steps were performed near the minimums. The results of these efforts are shown in Fig. 4.9.

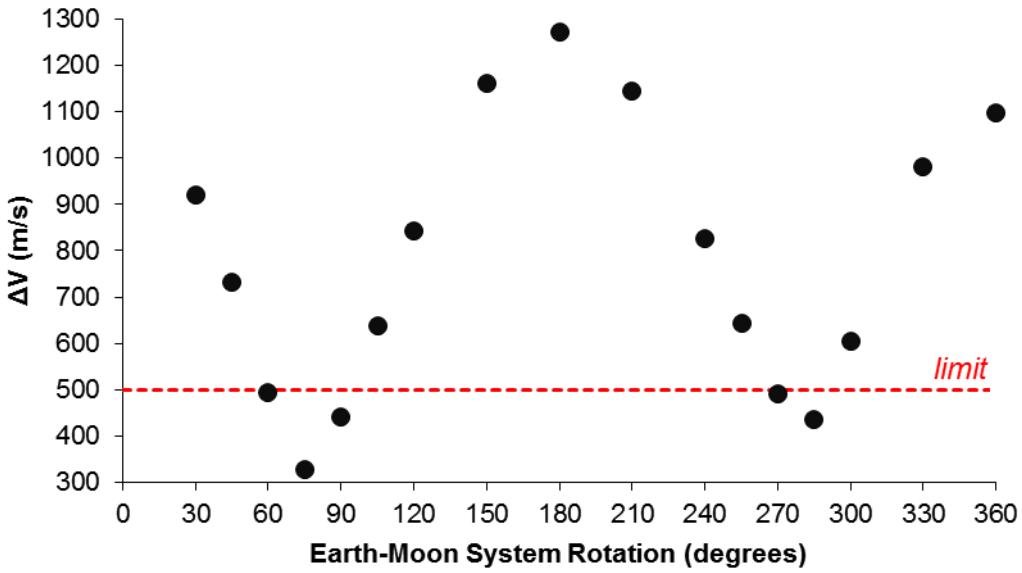

Figure 4.9: SETEM Launch Day Sensitivity

The two minimums, occurring at ~75° and ~285°, correspond to the $B_{t0,\phi=75^\circ}$ and $B_{t0,\phi=285^\circ}$ states. These results show good agreement from the specific energy consideration from Section 4.3.1; namely, there are two separate minimum ΔV states occurring at the predicted locations. The maximum ΔV predicted by the Hohmann transfer is larger than that derived from energy analysis alone, which is expected since the former accounts for conservation of angular momentum. The minimum ΔV calculated was 327 m/s for $\phi = 75^\circ$. For reference, shown on the figure is also a limit line corresponding to 500m/s ΔV which corresponds to launch access for ~15% of Earth rotations.

4.4: Communication Requirements

The purpose of the communications section is twofold: (1) develop top level communication requirements, and (2) apply design techniques established in Chapter 3 to fulfilling these top level communication requirements. The scope of the SETEM communication system addressed in Section 4.4 deals specifically with the downlinking of science data necessary for fulfilling the primary mission objective of providing sufficient imaging coverage. There are additional communication needs not explicitly addressed such as:

- Telemetry: downlinked SETEM data dealing with spacecraft health and state
- Commands: uplinked data to change the state of SETEM
- Reprogramming: uplinked data used to "re-flash" memory states
- Navigation: Doppler ranging and tracking

It will be shown in this section that the volume of image data to downlink is substantially greater than that typically required for telemetry needs; telemetry needs are not a driving design requirement. The uplink capabilities needed for commanding and reprogramming are assumed to not be a design driver because of the asymmetry within the 2-way communication link: the uplink link is significantly easier to close too significantly more performant power amplifiers. The Deep Space Network (DSN) is currently upgrading their system with 100 kW transmitters in S-band and 80 kW transmitters in X-band [169]. The last communication related need is for navigation and is satisfied by selecting the SETEM communication downlink to be compatible with existing DSN Doppler ranging capabilities. It is expected that SETEM will utilize multiple frequency bands. The thesis focuses on the most limited communication channel associated with downloading science data.

4.4.1: Data Rate

The data rate requirement is driven directly from the imaging requirements derived under the assumption of a SETEM null result improving the upper bound to 15 ETAs at $H \leq 20.5$. The coverage region derived spans 5° inclination and 100° longitude. The angular height of this region from SETEM's vantage is 85° from Section 4.2.7.

The vertical and horizontal camera FOV is 1.91° and 2.84°, respectively, from Section 4.2.6. This leads to 45 vertical frames required. The horizontal numbers of frames is determined from knowing the arclength of the region, $1\ \text{AU} \cdot 100° = 1.74\ \text{AU}$, and the camera FOV width of $0.013\ \text{AU} \cdot 2.84° = 0.00064\ \text{AU}$, leading to 2700 frames wide. The total number of frames for the entire mission is therefore 120,000. For reference, at 20s exposure time, this requires ~28 days of imaging. For the Kodak KAF-3200 CCD image sensor with 2184 x 1472 pixels, using 16 bits per pixel, leads to a mission total of 780GB uncompressed collected image data.

The amount of data generated by SETEM requires substantial on board processing to limit the amount required to be sent back to Earth. Historically, space missions have had limited computational resources available. However, recent advancements in industrial grade general purpose graphics processing units (GPGPUs) have begun seeing incorporation onto CubeSat missions such as the NVIDIA Jetson Tx2i. This new opportunity will be highly advantageous for onboard data processing. For SETEM, the purpose onboard processing serves is to identify image frames that are likely to contain a new object not present in the onboard catalog. While it is beyond the scope of this dissertation to design the processing chain to identify ETA candidates, the pipeline developed for the DECam ETA survey is used for reference [58]. This survey had a coverage of 24% and identified 7676 candidate objects. With SETEM targeting a similar coverage to the

DECam survey, 20% compared to 24% coverage, the assumed candidate object count of 7676. Using the limiting case of all candidate objects are on separate frames and a lossless compression ratio of 3:1, the total volume of data to downlink is 16.5 GB [168].

The total data volume of 16.5GB is to be downlink continuously throughout the mission. Due to DSN scheduling restrictions, 1 hour per day is allocated for downlinking. Using a 1 year duration for imaging leads to a data rate of 100 kbps. An additional 50% data rate overhead is included to account for file framing, timestamping, communication layer framing, spacecraft health telemetry, etc. Therefore, the downlink data rate for SETEM shall be $\geq$ 150 kbps.

4.4.2: Link Budget

The link budget is a method of accounting for all the gains and losses in a communication link. It is a tool developed in the early planning stages of any communication link, and is continuously refined as the design of the system is matured and uncertainties are minimized. The primary variables in the link budget for this analysis are the equivalent isotropic radiated power (EIRP), the free-space signal loss (L_S), the receiver antenna gain (G_R), and noise power. The EIRP is a useful metric as it describes the output power necessary by an isotropic radiator to generate a particular peak power flux density. The main contributors to EIRP are transmitter antenna gain and transmitter output power. This EIRP decomposition will be addressed in the next section. The free-space signal loss is due to the geometric dispersion as the signal travels through space, and is [172]:

$$L_S = \left(\frac{4\pi \cdot D_{range}}{\lambda} \right)$$

Here λ corresponds to the wavelength of the center frequency of operation which in this case is the middle of NASA Ka-band of 31.8 GHz to 32.3 GHz and D_{range} is the communication

link distance. This link budget also assumes the link is noise limited, rather than interferer limited such as from multipath, jammers, or background radio frequency interference. The noise power is $kT_S B_N$, where k is Boltzmann constant, T_S is the equivalent noise temperature of the entire receiver system which includes sky temperature and cosmic background contributions, and B_N is the receiver bandwidth necessary for demodulating and decoding the signal.

The planned ground station use for SETEM are the 34 meter parabolic dish Beam Waveguide (BWG) antennas part of the DSN. The DSN is utilized for all of NASA's deep space missions. The BWG antennas are the latest generation to the DSN [169]. They provide the highest performance for the SETEM mission by providing exceptionally high antenna gains, low receiver noise temperatures, great coverage over the entire mission coverage, Ka-band support, and Doppler ranging capabilities. The specific BWG DSN sites which support Ka-band downlink are DSS-25, DSS-26, DSS-34, DSS-35, DSS-36, DSS-54, and DDS-55. These sites are spread out across Mojave Desert in California, Tidbinbilla in Australia, and Robledo de Chavela in Spain. For initial planning. Each of the sites have slightly different noise temperature performance which range from 26.26 K to 35.60 K. For the purposes of this analysis the average across all sites is used at 32.4 K. The maximum range was found from using the 100° longitudinal span from Section 4.3.2 and 1 AU orbit radius.

Another important top level design driver is the required signal-to-noise ratio, or more commonly used for digital systems energy per bit to noise power spectral density ratio, E_b/N_0. Factors here include modulation type as well as coding and error correction schemes employed. For the purposes of simplifying this analysis, binary phase shift keying (BPSK) modulation is used combined with convolution coding at rate ½ concatenated with Reed-Solomon 233-255 coding

[170]. This has a $E_b/N_0 \geq 1.8$ dB at a frame drop rate of 10^{-6} [170]. This combination of inner and outer coding offers strong resilience to dropped bits and offers significant performance advantages on lowering the required E_b/N_0. However, this solution offers poor spectral efficiency of 0.44 [172]. While more advanced and higher performance coding schemes do exists, such as Turbo or LDPC coding, their advantages are minor compared to the fidelity of the current link budget. The link budget is shown in Table 4.2. Once all other parameters were determined, the EIRP entry was varied in order to achieve a final system margin of ≥ 3 dB. The derived EIRP required for SETEM is ≥ 56 dBWi. It is also noteworthy that no reflectarray, or even non-reflectarray systems, on CubeSats have achieved an EIRP of ≥ 56 dBWi. In the following two sections I explain how principles from the developments of COM2 from Section 3.2 can be scaled in size and power to meet the 56 dBWi requirement.

Table 4.2: SETEM Link Budget

	Variable Name	**Value**	**Units**
Transmitter Properties	Frequency	32.05	GHz
	Data rate	150	kbps
	EIRP	56	dBWi
	Polarization	CP	
Propagation	Range	1.532	AU
	Path Loss, L_S	289.8	dB
	Additional Losses	3	dB
	Isotopically received Power	-206.8	dBm
Receiver Properties	Antenna Gain, G_R	79	dBi
	Power received	-127.8	dBm
	Spectrum utilization	0.44	
	Bandwidth, B_N	340.91	kHz
	Equivalent temperature	32.4	K
	Noise power	-128.2	dBm
	Received SNR (single antenna)	0.4	dB
	Array factor increase	4.77	dB
	Array factor implementation loss	0.25	dB
	Received SNR (antenna, array)	4.92	dB
Link	Frame error rate, (BER)	1e-6	
	Required SNR	1.8	dB
	Margin	3.12	dB

This link budget also assumes DSN arraying where 3x 34m BWG dishes are phase combined in order to improve the ground reception gain [170]. This is necessary for closing the link at the maximum link distance of the SETEM mission of 1.5 AU. As shown in Fig. 4.1, the majority of the SETEM is well below a range of 1.5 AU, relaxing the need for DSN arraying. Additional opportunities exist in improving link performance because at this early stage of planning conservative margins are used: the link budget uses an allocated 3 dB overall margin as well as a 3 dB for additional losses to account for polarization mismatch, atmospheric attenuation,

implementation losses, filter mismatch, etc. As the design matures, and allocations are refined to include measured capabilities of prototyped hardware, these margins can be tightened. It is also recommended to utilize an adaptive data rate system which allows for optimum use of the link which would allow for the highest data rate possible; this minimizes the required ground station operation time which bills based on used time.

4.4.3: Increasing Capability

In developing a communication system for SETEM capable of achieving an EIRP of ≥ 56 dBWi it is important to consider this in context of other systems. EIRP is defined as:

$$\mathrm{EIRP} = G_{Tx} - IL_{Tx} + P_{Tx}$$

Here, G_{Tx} is the transmit antenna gain referenced to an isotropic antenna having units dBi. In the case of a circular polarized system G_{Tx} is referenced to a perfectly circular polarization isotropic antenna, and is typically expressed in units dBiC or dBi. IL_{Tx} is the insertion loss in between the output of the power amplifier and the input of the antenna. P_{Tx} is the output power of the radio or transmitter, where in this case it is referenced to 1 W having units of dBW.

Table 4.3: EIRP Comparison of Current CubeSat Reflectarrays

System Name	**ISARA [141][174]**	**MarCO [13][97][175]**	**COM2**	**Units**
CubeSat Size Required for Reflectarray Incorporation	3U	6U	1U	
Reflectarray Deployable Features Quantity	2	2	1	
Deployable Feed?	Yes	Yes	No	
Panel Geometry	3x @ 33.9 cm x 8.26 cm	3x @ 33.5 cm x 19.9 cm	1x @ 6.25 cm x 6.25 cm	
Mechanical Complexity	High	High	Low	
Total Area, A'_{Tx}	840	2000	39.1	cm^2
Frequency	26	8.425	24.05	GHz
Gain, G_{Tx}	33.5	29.2	19	dBi
Total Efficiency, ε	28	42	25	%
Insertion Loss, IL_{Tx}	0	0.5	1	dB
Power Output, P_{Tx}	-7	5.8	0	dBW
EIRP	26.5	35	18	dBWi

In Table 4.3 IL_{Tx} was unknown for ISARA and MarCO so was set to zero.

In designing SETEM's next generation communication system and defining the required size the following gain relationship is useful [176]:

$$G_{Tx} = 4\pi \frac{A_{Tx} \cdot \eta}{\lambda^2}$$

Where A_{Tx} is the area and η is the aperture efficiency. In this form, η also includes feed efficiency and associated losses integrated system losses. For reflectarray design, a more useful form is to replace the area with $A_{Tx} \rightarrow A'_{Tx} \cdot \varsigma$, where A'_{Tx} is the actual reflectarray panel area, and ς is

factor accounting for projecting A' in the direction of the main beam as well as accounting for any other obstructions, see Fig. 3.20 for example. The gain then becomes:

$$G = 4\pi \frac{A'_{Tx} \cdot \varepsilon}{\lambda^2}$$

where $\varepsilon = \eta \cdot \varsigma$ is the totally efficiency and is the most useful metric to use in reflectarray design application to CubeSats since it accounts for RF design as well as incorporation into the CubeSat form factor. The calculated ε is shown for each of the systems in Table 4.3. ISARA and COM2 have similar efficiency, while MarCO has substantially higher efficiency which is attributed to using X-band versus Ka/K-band due to lower dissipative losses.

4.4.4: Design Solution

Achieving an EIRP of at least 56 dBWi for SETEM requires a significant improvement on the state-of-the-art. With the SETEM intended to be university accessible, achieving this breakthrough in communication capability shall be done while keeping the system complexity low. There are three primary areas important to keeping the reflectarray implementation simple. The first is keeping the RF feed design and reflectarray design simple. In Chapter 3, a proof-of-concept reflectarray system was developed with the use of a low complexity feed antenna and reflectarray. These contributions can be directly applied using appropriate scaling for a higher frequency and large reflectarray size. The second are the RF driving electronics which consists of the following main components: baseband processing, Doppler tracking and ranging DSN interoperability, and power amplification. This area of complexity of SETEM is addressed by using and already available COTS power amplification solution. The RF baseband and processing aspects are not specifically addressed in this chapter, but readers are referenced to state-of-the-art COTS options such as the Iris V2.1 CubeSat Deep Space Transponder [175]. The last area of complexity is

mechanical deployables which are challenging to implement due to the vibration and shock environments present pre-deployment and the thermal environments while on-orbit. Both MarCO and ISARA utilized a 3 hinge system: the feed was deployed via a single hinge, and the reflectarray surface was double hinged, see Fig. 4.9. The feed hinge is useful to minimize the stowed feed volume, and the second hinge set on the reflectarray is useful in expanding the useable area of the reflectarray surface. Beyond the actual mechanical complexity of implementing a double hinged reflectarray surface, thermal induced strains are a limiting factor in reflectarray performance. Consider for example the SETEM wavelength of 9.4 mm. To keep the reflectarray element phase error within 10% the reflectarray panel needs to stay within , or 0.47 mm, positional tolerance over all operational thermal environments. For this reason, it is preferred for SETEM to use a single hinged deployable reflectarray surface.

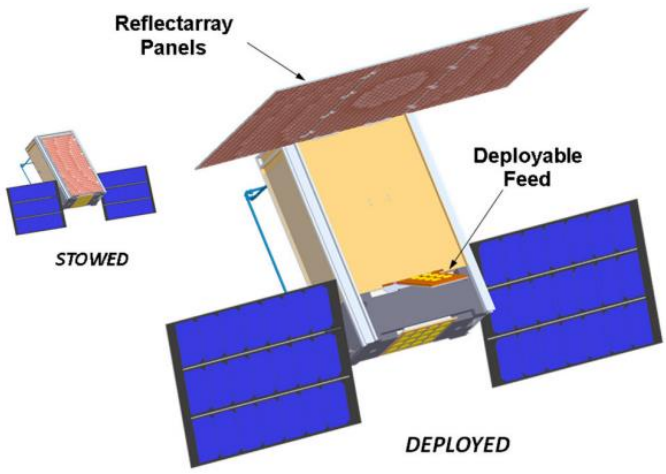

Figure 4.9: MarCO CAD model [140]

For the power amplifier stage, which sets , the SETEM reference design and below analysis utilizes the highest performance low-cost COTS option. The Analog Devices HMC7054 is a fully integrated high power amplifier system designed for single carrier satellite communication systems

[177]. It weighs 1.6 lbm, consumes 0.42 L of volume, and provides 9 W of output power at 32 GHz at 56% overall power efficiency [177]. The insertion loss, , between the output of this power amplifier and the input to the feed antenna is allocated 1 dB. The assumed efficiency for SETEM is a conservative 25%, see Tale 4.3 for comparison to other systems, with opportunity for improvement as the system design matures. See Table 4.4 below for the trade study of various configurations.

Table 4.4: SETEM Reflectarray Trade Study

Configuration Name	**MarCO**	**MarCO Config**	**2x MarCO Config**	**COM2-Scaled**	**4x COM2-Scaled**	**4x COM2-Scaled-XL**	**Units**
CubeSat Size Required for Reflectarray Incorporation	6U	6U or 12U	6U or 12U	6U or 12U	12U	27U	
RA Deployable Features Quantity	2	2	2	1	1	1	
Deployable Feed?	Yes	Yes	Yes	No	No	No	
Panel Geometry	3x @ 33.5 cm x 19.9 cm	3x @ 33.5 cm x 19.9 cm	6x @ 33.5 cm x 19.9 cm	1x @ 33.5 cm x 19.9 cm	4x @ 33.5 cm x 19.9 cm	4x @ 33.5 cm x 33.5 cm	
Mechanical Complexity	High	High	High	Low	Low	Low	
Total Area, A'_{Tx}	2000	2000	4000	667	2667	4489	cm^2
Frequency	8.425	32.05	32.05	32.05	32.05	32.05	GHz
Gain, G_{Tx}	29.2	38.6	41.6	33.8	39.8	42.1	dBi
Total Efficiency, ε	42	25	25	25	25	25	%
Insertion Loss, IL_{Tx}	0	1	1	1	1	1	dB
Power Output, P_{Tx}	5.8	9.5	12.8	9.5	15.8	15.8	dBW
EIRP	35	47.1	53.4	42.3	54.6	56.9	dBWi
Margin Against 56dBWi Requirement	-21	-8.9	-2.6	-13.7	-1.4	0.9	dB

The configurations of Table 4.4 are best understand in descending order:

i. **MarCO**: This information is from Table 4.3. Being the first, and only, CubeSat reflectarray used to support a science mission, MarCO is used as the starting point in deriving the SETEM reflectarray design solution.

ii. **MarCO Config**: This configuration uses the same deployable geometry as MarCO (see Fig. 4.9) but is adapter to SETEM by changing the frequency of operation and total efficiency. It also utilizes the Analog Devices HMC7054 power amplifier. These modifications raise the EIRP by 12.1 dB over the MarCO mission, but it still falls short by 8.9 dB.

iii. **2x MarCO Config**: This configuration uses two identical MarCO Config setups, one on each two opposing sides of the spacecraft bus. Each side has a dedicated power amplifier which doubles the total output power. The power amplifier are fed in-phase, and with identical reflectarray setups on both sides, this creates constructive interference between the two setups resulting in a +3 dB gain increase. This setup is considered the same amount of mechanical complexity because while there are more deployable panels, half of the setup is identical to the other side. The only added piece, phase matching the power amplifiers, is low effort and low risk. This setup still falls short 2.6 dB of the requirement. Improving beyond this setup by simply adding additional panels to further increase gain further is a prohibitive increase in mechanical complexity. Therefore, a different, simpler, approach is sought.

iv. **COM2-scaled**: There are two attractive features from COM2 incorporated: single panel reflectarray deployment and a fixed feed that does not require deployment. COM2-scaled is implementing these simplifications on a single 2U x 3U (33.5 cm x 19.9 cm) panel. This setup is 13.7 dB short of the requirement, yet achieves a 7.3 dB higher EIRP compared to the MarCO mission already flown for a significantly simpler mechanical setup.

v. **4x-COM2-scaled**: Further increasing EIRP is done by duplicating the reflectarray setup on four sides of the spacecraft bus, see Fig. 4.2 for geometry configuration. Each side has

its own power amplifier bringing the total output power to 38 W. While this amount of RF power is substantial, and beyond the typical CubeSat bus, it is important to consider SETEM's use of communication windows. Since DSN scheduling is limited, and the SETEM bus needs to attitude point for image surveying, it is acceptable for the RF power consumption to be beyond the instantaneous solar power generation. At a 12U bus, 4x-COM2-scaled falls short 1.4 dB of the requirement. In this configuration the communication system is allocated 0.5U per power amplifier, and 1U for the communication radio, or 3U total. With the camera allocated 3U, there is only 6U remaining for ADCS, EPS, and propulsion. This motivates the need to increase one size up for 12U.

vi. **4x-COM2-scaled-XL**: This is the 27U configuration as shown in Fig. 4.2. Going slightly larger allows the reflectarray panels to grow in width along with the wider CubeSat. This configuration achieves an EIRP of 56.9 dBWi. The increase in spacecraft volume also provides ample room for all the necessary subsystems.

The feed design for SETEM being non-deployable significantly reducing complexities involved with its deployment. Of primary concern is the RF cable connection between the output of the power amplifier and input of the feed antenna. When using a deployable feed antenna this connection must be flexible and provide a very small bend radius. A small bend radius is typically achieved with a small diameter cable since peak material strain in the cable material is related to the ratio of the outer diameter and maximum bend radius. However, small diameter cables are inherently higher loss relative to larger diameter. The SETEM reflectarray design overcomes this increased insertion loss as well as the associated mechanical complexities related to the

deployment mechanism and utilizes a fixed feed antenna. This builds on the work of COM2, see Section 3.1, except with two additional adaptions: (1) the feed antenna main lobe is off-boresight by ~25 degrees, and (2) the wasted volume of mounting the feed antenna at an angle is eliminated by insetting the feed into the spacecraft structure in addition to providing small cutouts on the reflectarray surface. See Fig. 4.10 for a cross section cut of the proposed reflectarray geometry, and Fig. 4.1 shows the aforementioned cutouts.

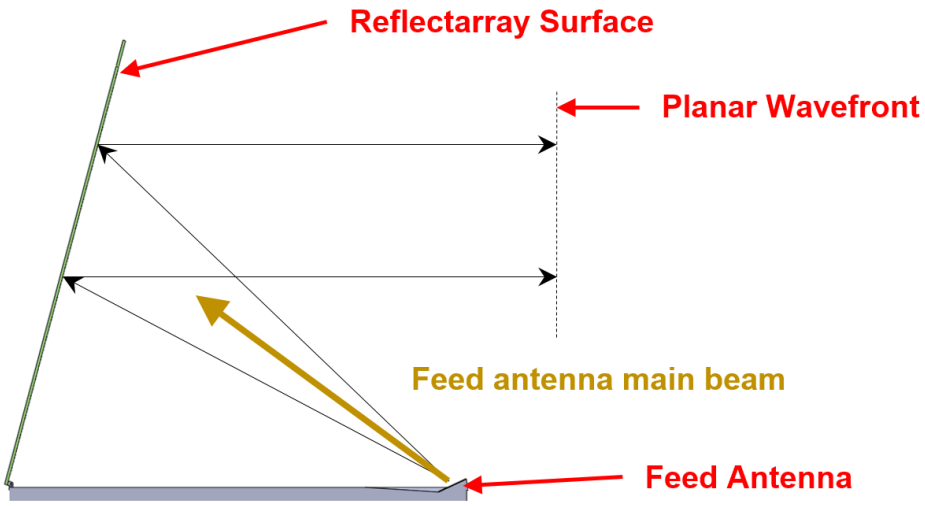

Figure 4.10: Feed Antenna Inset

Chapter 5. HuskySat-1

The HuskySat-1 (HS-1) is a 3.3kg satellite designed, built, tested by an interdisciplinary team at the UW primarily composed of undergraduate and graduate students. Faculty leadership was provided under Professor Robert Winglee and Professor Michael McCarthy. My contributions towards the project was serving as chief engineer and project manager which had the responsibilities of: (1) process development and execution of printed circuit board assembly design, assembly, and testing; (2) programmatic structuring such as constitution development; (3) Emphasis on student participation in the project and learning through curriculum development, hands-on training, and mentoring of undergraduate team members; (4) AMSAT partnership development and primary focal for integration of amateur radio transponder; (5) Developed and enforced all technical developments related to the structural design; (6) HS-1 architecture, including the distributed master-less microprocessor approach; and (7) Ground station hardware and operations planning and implementation. The final design, shown in Fig. 5.1, was deployed on January 31st 2020 at an altitude 465 km with an inclination of 51.6 degrees. This project demonstrates the successful ability of a university, with no prior CubeSat production experience, and with an optimistic mindset, is able to develop a complex endeavor such as the HS-1. Specific innovations of the HS-1 developed under my leadership were:

1. The first university-based CubeSat to fly a pulsed plasma thruster
2. The first university-based CubeSat to implement the CAN data bus
3. The first university-based CubeSat to fly a radio capable of transmitting above 10GHz
4. The first university-based CubeSat to fly a AMSAT linear transponder

These advancements from the HS-1 project are useful to the development of future university based CubeSat projects, and are especially useful to deep space missions such as the Earth Trojan

Asteroid mission outlined in chapter 4. While CubeSat literature is primarily analytical and derivational in nature focusing on basic technology, science research, and feasibility, very little exists detailing the process and implementation workflows required for successful execution of a complex and highly capable full system development and its operation. Therefore, this chapter seeks to fill a void in the current CubeSat literature by providing a descriptory emphasis on procedural development, programmatic, and implementation.

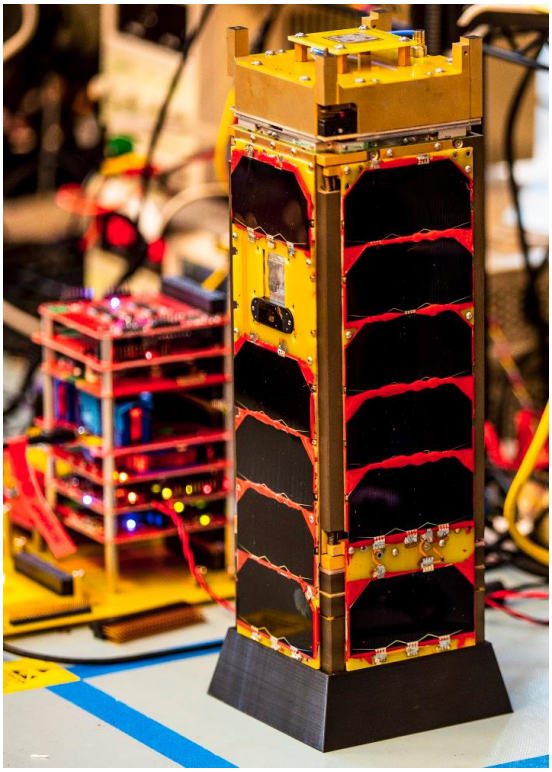

Figure 5.1: HuskySat-1 Flight Model

5.1 Conception and Program Development

Led by Professor Robert Winglee, the initial idea of developing a CubeSat was to provide an on orbit test bed for the Pulsed Plasma Thruster (PPT) under development within the Advanced Propulsion Laboratory (APL). Professor Robert Winglee with his graduate student at the time, Ian Johnson, were experimenting with alternative fuels for the PPT. They discovered that sulfur

provided higher thrust at the cost of lower specific impulse compared to the more commonly used fuel, Polytetrafluoroethylene [102]. During the 2013 academic year they began to further investigate miniaturizing the PPT, specifically the associated electronics, to fit within the CubeSat form factor with the intent of developing a fully operational small satellite. Prior, the PPT had been miniaturized and demonstrated on high altitude balloon projects; the state of the electronics at this time are shown in Fig. 5.2. However, the maturity of the electronics still used a low efficient "black box" DC-DC converter which significantly limited firing rates to 0.25 Hz. Addressing this limitation later on was my first major contribution in the APL.

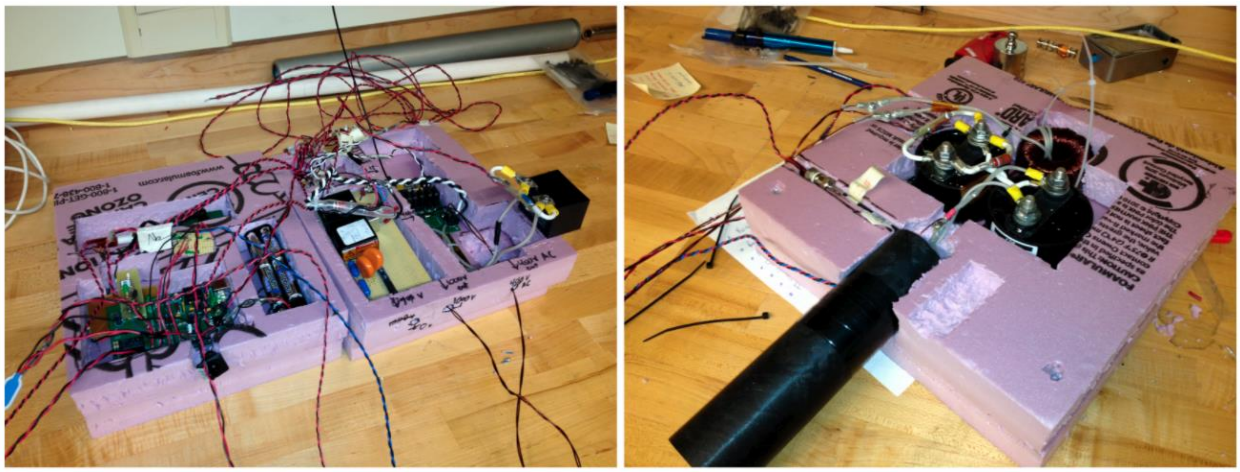

Figure 5.2: PPT Electronics for High Altitude Flight Demonstration [102]

For an overall context of satellite development supported at the UW, the first project was in 1999 with the DawgStar, which was a small satellite with the objectives to study the Earth's ionosphere and demonstrate formation flying [103]. This project did not mature beyond a preliminary design. During the 2014 academic year, graduate student Paige Northway and myself, working in the APL, continued work on adapting the PPT to the CubeSat platform and operate in the space environment. My efforts were towards replacing the sub-optimal high voltage charging in the current design. These efforts led to the development of a highly configurable charging

topology using a 1:10 step-up transformer in a flyback circuit topology based on the LT3750 integrated circuit (IC). The outcome was increasing the previous firing rate of 0.25 Hz to a demonstrated 22 Hz at a charging efficiency of ~80% at an output power of 230 W. These contributions are important for future CubeSat applications since they enable substantial thrust required for orbital maneuvers. And while these electronics were developed for the PPT, they can be adapter to work with any other high voltage electric thruster. My work in development the new charging topology lasted a number of years, providing valuable knowledge of printed circuit board (PCB) design, assembly, and testing strategies used later during the HS-1 development.

In parallel, work began on developing a proposal for the NASA CubeQuest Centennial Challenge which if won, would provide a small amount of funding and an included launch to a lunar trans-injection orbit. The CubeQuest Challenge solicited the development of 6U CubeSats with the primary purpose of increasing communication and propulsion technologies available to small satellites [104]. In support of this proposal, it provided an impetus for me to begin development of the high-frequency reflectarray antenna work, discussed in chapter 3, as well as further mature the PPT electronics charging and firing system. In late 2015, my efforts were put towards another proposal, and was successfully won, for the NASA Undergraduate Student Instrument Project (USIP). USIP provided a small amount of funding as well as included a launch into low Earth orbit. The proposal was titled "HuskySat I – A Precursor for a Lunar Magnetic Field Mapper CubeSat".

In support of carrying out this project, my efforts turned to building and developing the internal resources and skill sets necessary for building the HuskySat-1 project. This began with recruiting undergraduate talent as well as gathering financial support. Encouragement of student participation in this project began with an offering of a one credit course. Additionally, a funding

campaign through USEED was launched with success at raising over $10,000 [105]. The one credit offering was successful in recruitment, but at one credit per student, it fell short of allowing participants to both learn about space systems engineering as well as contribute to the project. Two students involved with this one credit course, Hunter Mellema and Chayse Aubuchon, recognized this weakness and transitioned the overall efforts towards a registered student organization (RSO). As an RSO, the Husky Satellite Lab (HSL), created an environment where student participation was entirely volunteer, and therefore naturally selected students who were dedicated to the mission who more likely would commit the time and dedication required for mission success. Under my leadership the HSL evolved to include an application for joining, applicant interviews, introduction projects facilitating the transition from student guided project within the classroom to open-ended student lead project mindset, a constitution delineating roles and responsibilities, elections, as well as supporting future space systems research. At its peak there were over 50 undergraduate and 5 graduate students involved with the project, see Fig. 5.3 for a team picture.

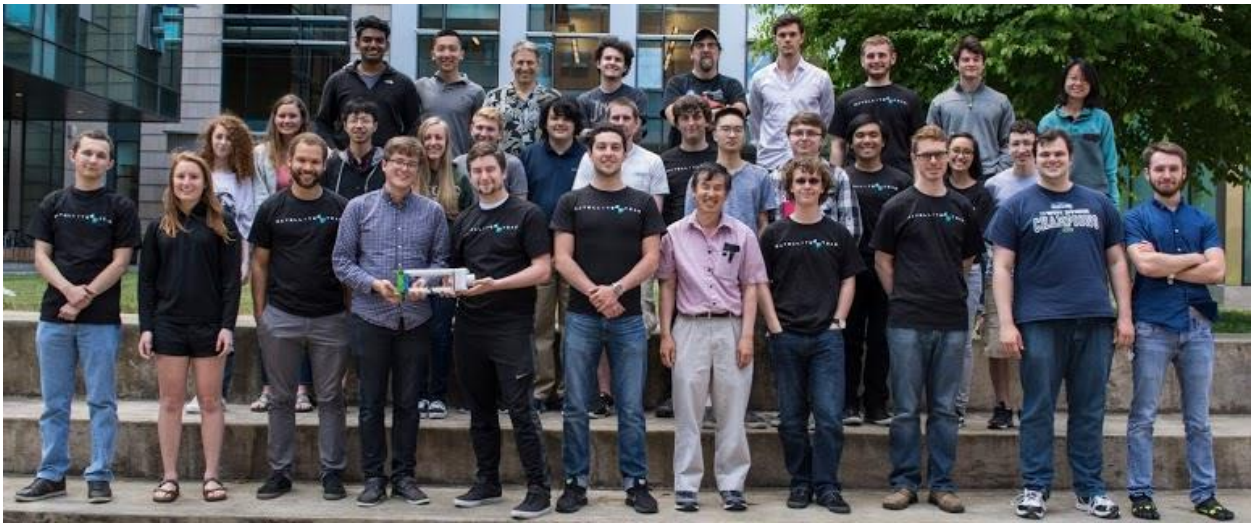

Figure 5.3: Husky Satellite Team

From the Husky Satellite Lab [112]:

Our Mission is to foster interdisciplinary student participation in space systems research, to inspire and train future space scientists and engineers, and to advance spacecraft capabilities at the University of Washington.

Our Team is composed primarily of UW undergraduate and graduate students, as well as mentors from the local aerospace industry. Our lead principal investigator is Professor Robert Winglee.

The HSL continues to live on beyond the HS-1. They have launched two high altitude balloons used as a testbed for further hardware development, are currently working on an electroplating experiment to fly on the Blue Origin New Shepard launch vehicle, and are beginning work on HS-2 [112]. When starting with relatively untrained but highly motivated students, the primary limiting factor to the success of the HSL is financial.

With time the HSL evolved to include an application for joining, structured interviews, introduction projects, and a constitution delineating roles and responsibilities, elections, as well as supporting future space systems research. My contributions were to lead all curriculum development for the introduction projects as well as provide student mentoring through these projects, as well as teaching and mentoring students in PCB design, assembly, and testing. One of the most significant challenges in developing this project was addressing the high turnover of students due to constant graduation as well as the limited time students could volunteer. With any CubeSat program without years of rooted establishment, it is essential to continually evolve to meet these growing demands. In total there have been 100+ students, staff, mentors, and volunteers that have made this project possible. The institutions that provided support were: UW, ME

department, AA department, ESS department, Physics department, NASA, NASA Space Grant Consortium, Molex, Total Phase, Systima, Green Heron, AMSAT, JCATI, Student Technology Fee, and Amazon Catalyst. The latter four supporters were a direct result of my contributions.

5.2 Mission Concept

5.2.1 Objectives

The original mission objectives were split into three categories and defined as:

Primary Mission Objectives

- Delivery of system by August 2017
- 3 months of operation
- Operational PPT with measurable ΔV
- Downlink of 100kb using high frequency K-band antenna

Secondary Mission Objectives

- 3-6 months of operation
- Measure between 100m/s to 250m/s ΔV
- 100Mb downlink from a reflectarray antenna
- Flight of electronics payload from local High School
- Establish ground station with high frequency capabilities

Non-Technical Objectives

- Lay groundwork for future CubeSat missions
- Open hardware and software licensing
- Publishable results

These mission objectives were developed with the intent of developing the HS-1 as the first of a new type of CubeSat bus. In chapter 2, the limitations of the CubeSats were reviewed, such as limited communication and propulsion technologies. Consistent with the original USIP proposal title of "HuskySat I – A Precursor for a Lunar Magnetic Field Mapper CubeSat", the intent was for this mission to push forward the capabilities of CubeSat technology to enable a new regime of deep space science such as the Earth Trojan Asteroid Mapper mission reviewed in Chapter 4. While the original mission objectives were not fully executed, the HS-1 mission nevertheless is a significant achievement.

5.2.2 Initial Concept

The original design was based on fulfilling the requirements set forth in the USIP proposal requirements, such as being a 3U CubeSat, as well as the original mission objectives defined in Section 5.2.1. The next level of flow down consisted of the following drivers:

- Providing 100 m/s to 250 m/s ΔV requires velocity pointing
- Providing enough thrust from the PPT to overcome the drag force uncertainty requires deployable solar panels to generate enough power.
- The reflectarray requires precise pointing capabilities and drives the peak slew requirement.
- The power system needs to support the energy demands of the K-band radio as well as the high peak power demands of the PPT charging system.
- Laying groundwork for future CubeSat missions would be to develop, as much as possible, all satellite systems in-house.

Additionally, the objective of laying groundwork for future CubeSat missions motivated the HS-1 to utilize universal and interchangeable components, as well as develop a system which minimizes the risk of complete mission failure. These motivations were fulfilled by two design decisions: develop a board standard and design the HS-1 to be tolerant to single component failure not impacting fulfillment of other mission objectives. While developing a board standard was not a novel idea, no universal standard existed, and many competing designs were not compatible. I performed a survey of available standards and developed our own standard with the intent that it would be most adaptable to working with other CubeSat COTS solutions. This board standard developed for the HS-1 is shown in Fig. 5.4.

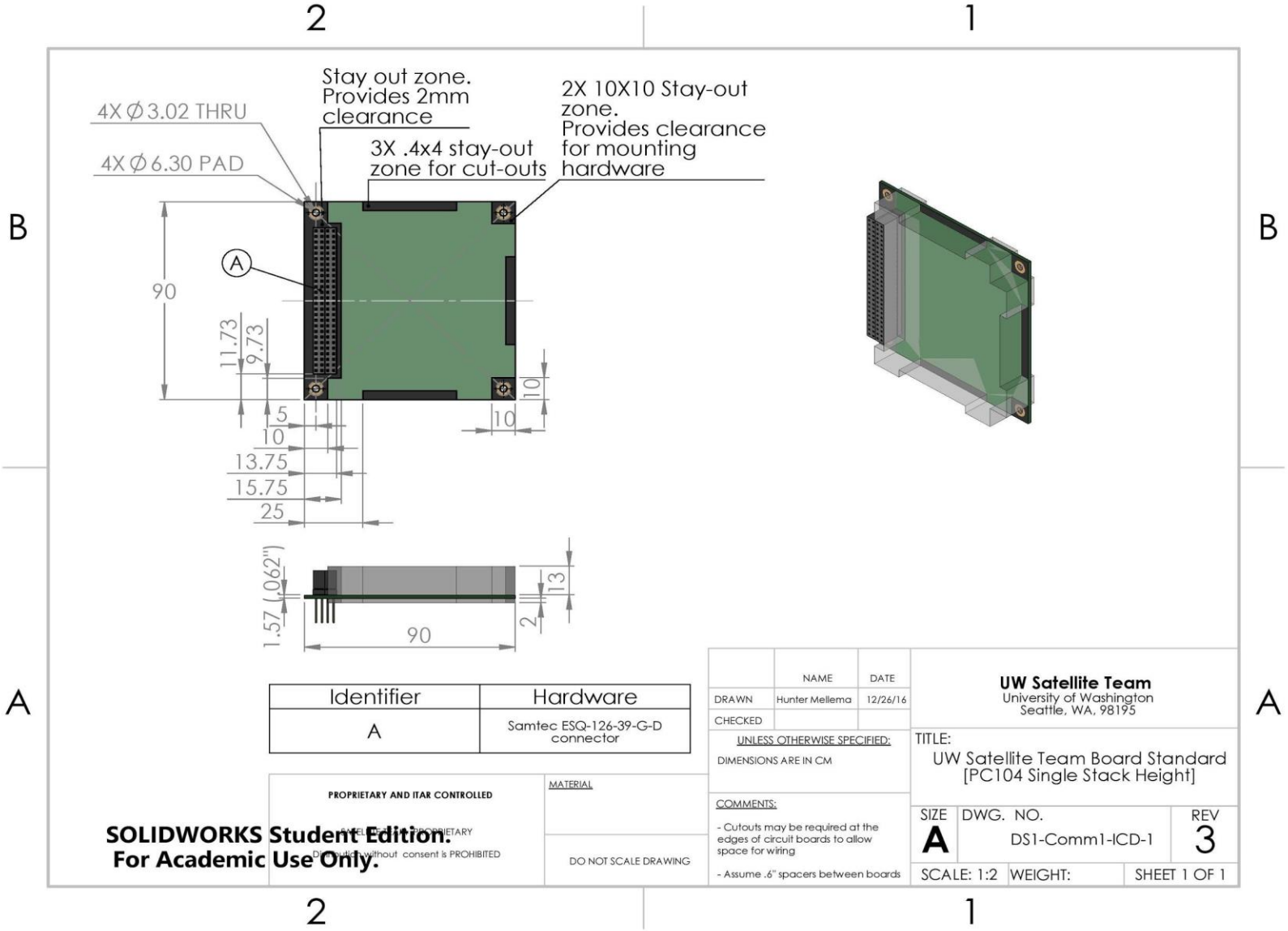

Figure 5.4: Board Standard

Minimizing the risk of a single component failure causing complete mission failure was achieved by adopting a distributed bus architecture combined with prioritizing systems or components which were single point failures for complete mission failure. These single point failures are the telemetry and command communication system as well as providing this system with power. With 31% of CubeSats delivered as dead-on-arrival, the HS-1 design addressed this by using an out-of-house communication radio and antenna system [119]. A partnership with the organization Amateur Radio Satellite Corporation (AMSAT) was created. With AMSAT having a long history of developing satellite radios, and with the HS-1 being under the umbrella of amateur radio, the partnership was mutually beneficial [115][116]. The plan was for AMSAT to provide the radio for the HS-1 and the antenna would be a purchased COTS option with flight heritage, the ISIS deployable VHF/UHF dipole [117]. Another method of addressing single point failures traditional to the aerospace industry is double or triple redundancy. In the HS-1 it was opted to not use these methods as a means to increase reliability due to the increased system complexity: in developing a redundant system a non-redundant system must first be designed. From the onset of the project it was decided no redundancy would be implemented.

The distributed bus architecture, see Fig. 5.5, was realized through various means starting with functional separation of distinct subsystems: power system, attitude determination and control system, propulsion module, telemetry and command communication system, high frequency communication module, and the camera board. More information of these systems if provided in Section 5.3. The design of these subsystems would achieve an overall distributed design by: (1) physical separation of functional components, (2) intra-subsystem data bus traffic to be localized, (3) limit inter-subsystem communication, (4) universalize inter-subsystem traffic using a common CAN bus, and (5) toggleable power domains specific to each subsystem.

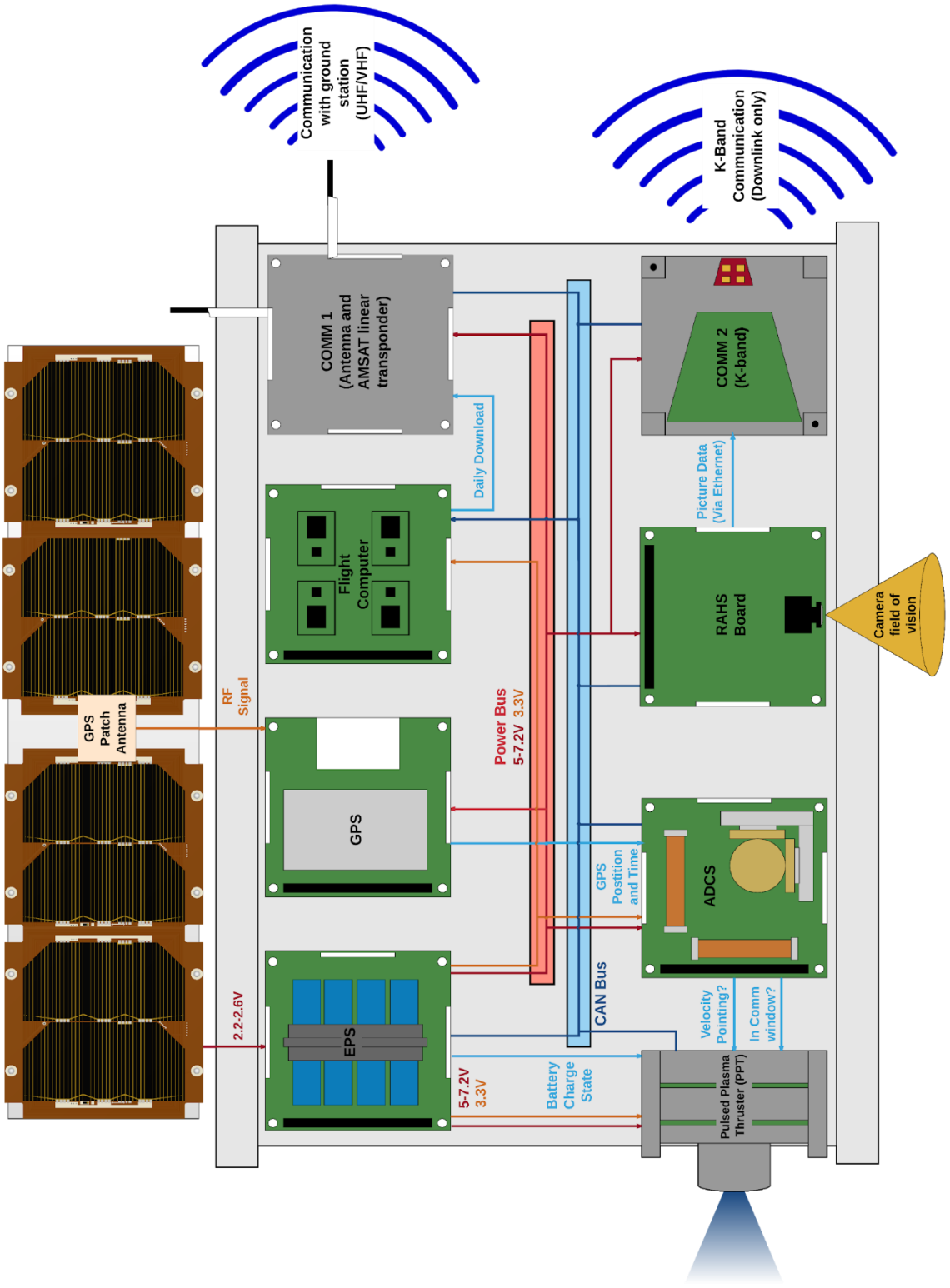

Figure 5.5: Initial Bus Architecture

The physical layout of the subsystems within the HS-1 was broken apart between the two experimental payloads, the PPT and COM2, and the primary stack, as shown in Fig. 5.6. The primary stack consisted of subsystem printed circuit board assemblies (PCBA) following the board standard from Fig. 5.4, while the two experimental payloads were separate due to their unique need of module volume and single point grounding to the spacecraft bus. Both the PPT and COM2 also have their internal electronics fully enclosed by either aluminum structure or PCB ground planes in order to minimize radiated emissions or reduce susceptibility to external radiated emissions.

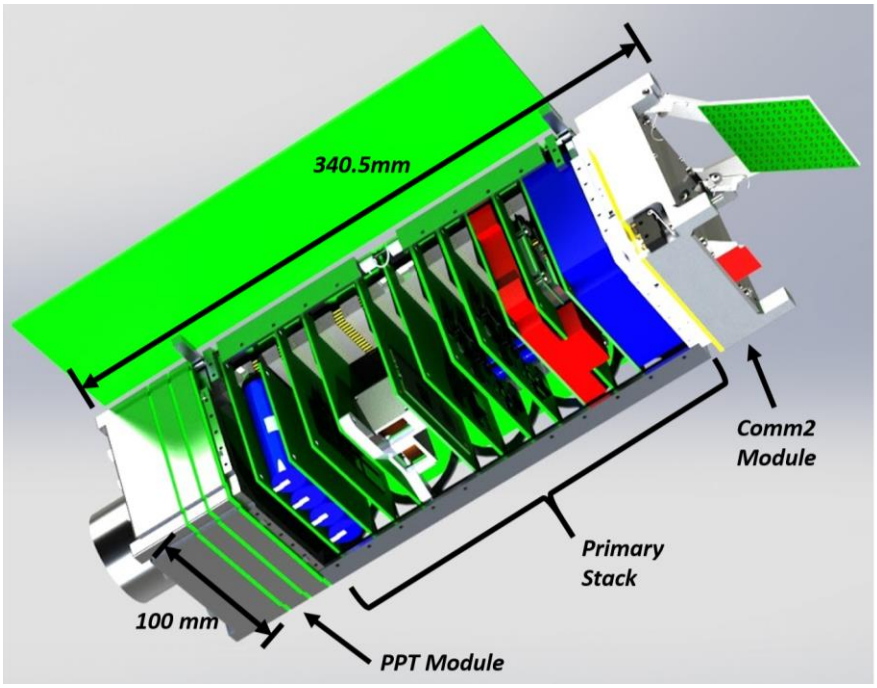

Figure 5.6: Subsystem Organization

Operation of the HS-1 on-orbit was considered for both nominal and off-nominal conditions, see Fig. 5.7. One important tradeoff during the course of this project was the amount of autonomy given to the HS-1 versus required manual control.

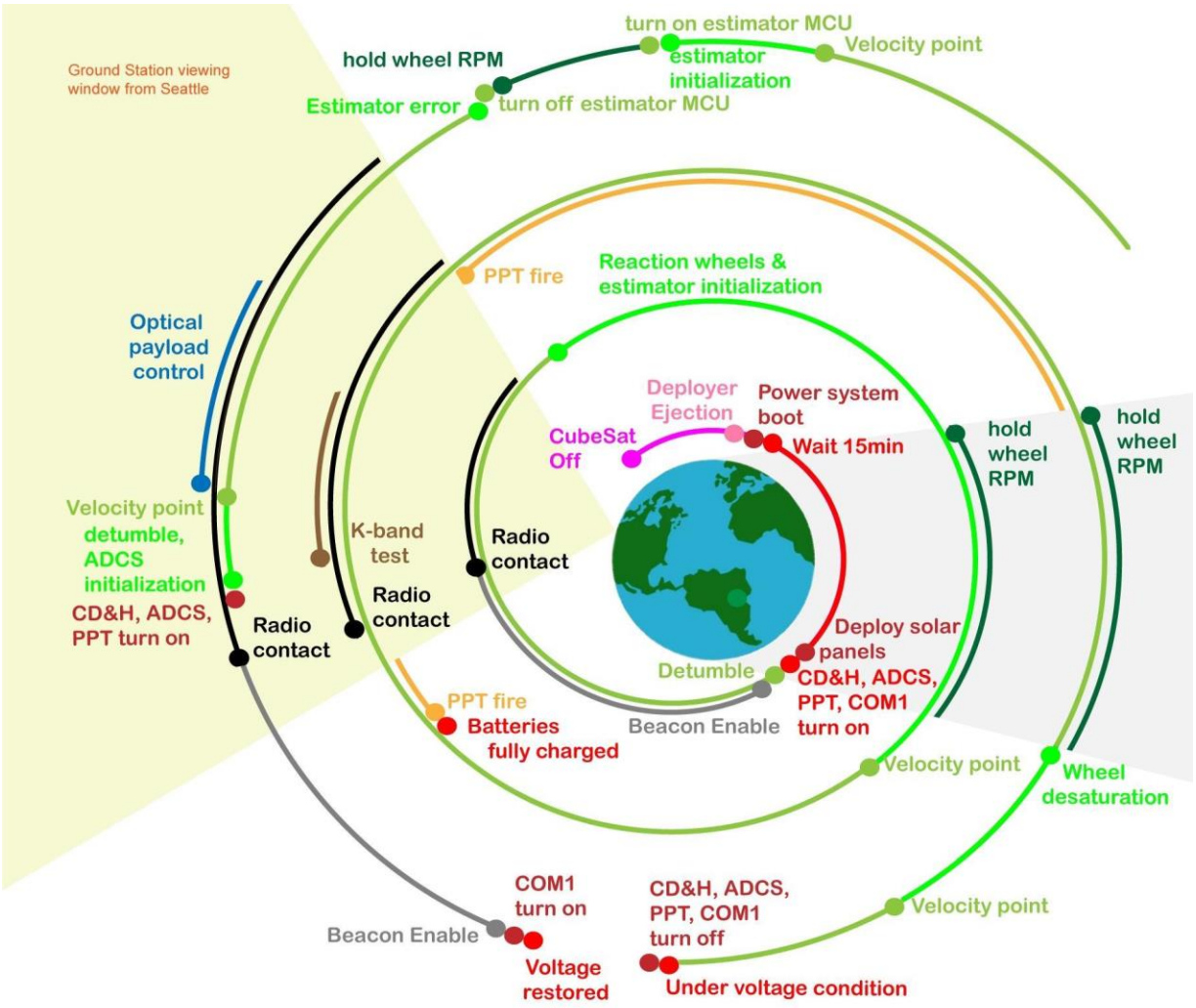

Figure 5.7: Conceptual Operations

5.2.3 Descope

The initial concept of the HS-1 described in Section 5.2.1 and Section 5.2.2 was the baseline design up through the Critical Design Review stage. However, during qualification vibration testing, two failures occurred: (1) the reaction wheels failed post verification testing, and (2) the solar panels did not deploy. The reaction wheel board, as shown in Fig. 5.8, contained three identical strings each utilizing a 1509006B Faulhaber motor which had with it an additional weighted mass and supporting bearing, see Fig. 5.9. The RPM versus power consumption was

measured before and after the vibration testing for each of the wheels indicating two of the wheel's behavior significantly changed. One of the wheels was unable to reach high revolutions per minute (RPM), and another wheel, when commanded to 100% RPM oscillated between lower and higher RPM over a period of a few seconds. Both of these effects were attributed to misalignment of the second bearing within the reaction wheel assemblies.

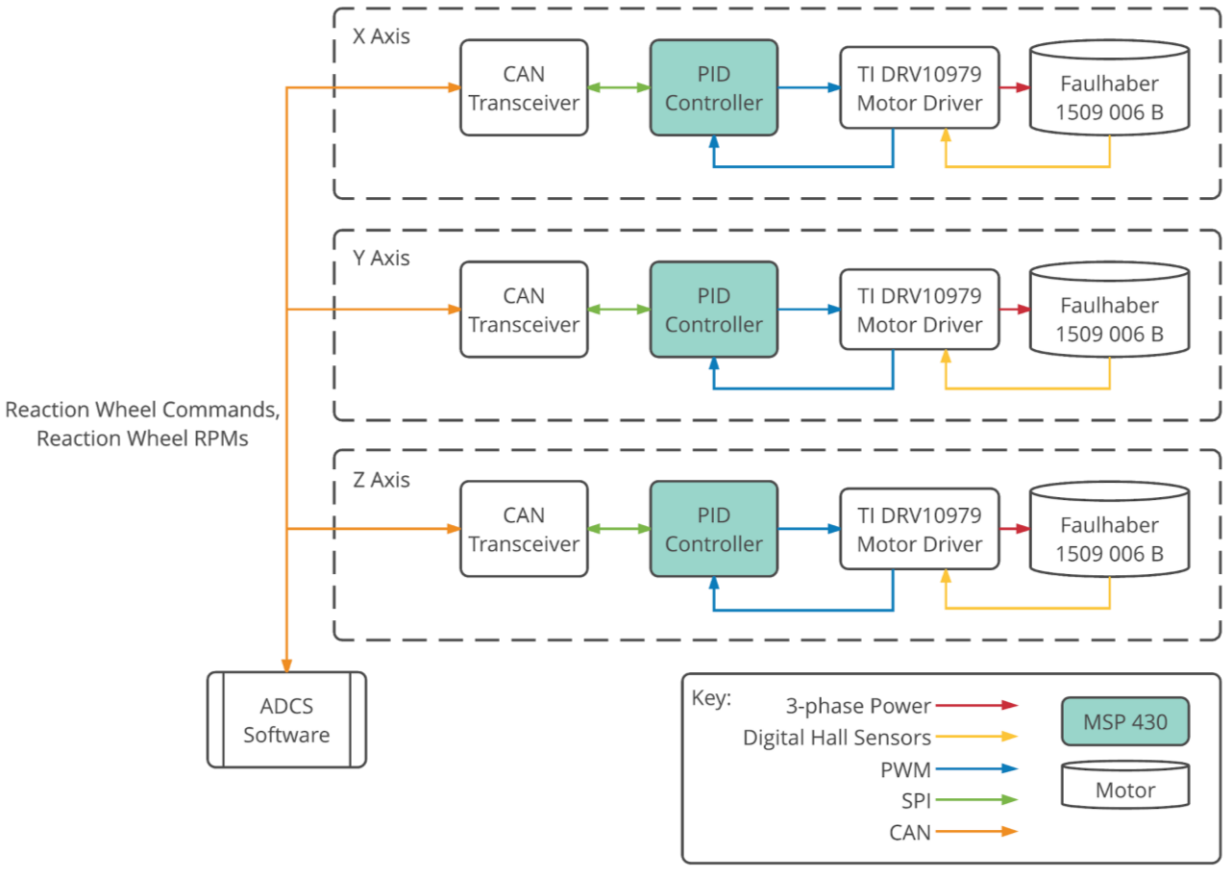

Figure 5.8: Reaction Wheel System Functional Diagram

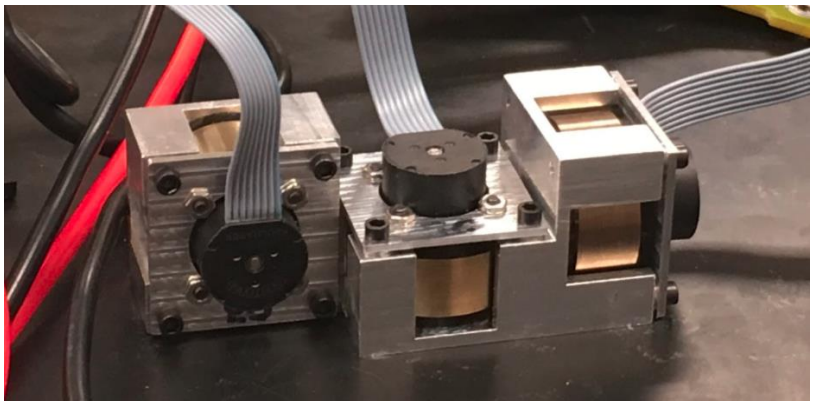

Figure 5.9: 3-axis Reaction Wheel Assembly

The second failure occurred within the hinge of the deployable solar panels. The outer part of the hinge was composed of Aluminum 7075-T6 pivoting via a clearance fit on a stainless steel 18-8 pin, as shown in Fig. 5.10. During post-vibration deployment testing both sets of panels had too much resistance within their hinges to deploy. The panels were carefully removed to identify if the increased resistance was due to misalignment, but even without the panels the issue persisted. The most probable cause of failure was identified to be galling which is a phenomenon whereby friction and adhesion between two surfaces gouges and releases either interfacing materials.

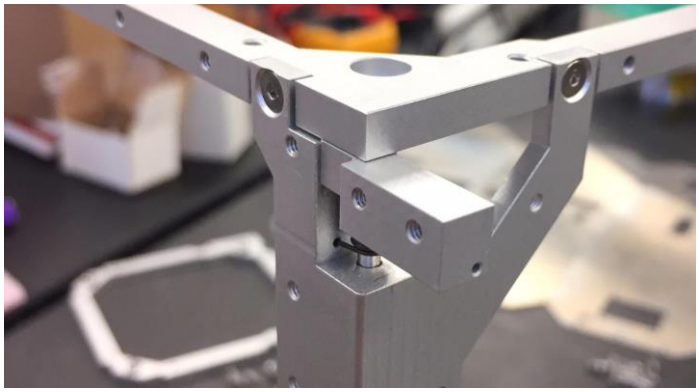

Figure 5.10: Deployable Solar Panel Hinge

In moving the project from a university research activity with a low probability of success to a flight deliverable several additional obstacles were encountered: the Novatel 615 GPS module had intermittent success in achieving expected GPS satellite locks; one of the motor drivers from the reaction wheel board did not work due to an unknown layout issue; graduation of key personnel; and monetary and schedule pressures. I initiated a project descope effort to address these issues, as well as the post-vibe issues, with minimal modification to the mission objectives. Technical changes to the HS-1 were removal of the reaction wheels, deployable panels, and GPS receiver. Additionally, the loss of ability to precisely point motivated the removal of the reflectarray antenna.

5.2.4 Final Design Concept

The HS-1 final design is shown in Fig. 5.11. The HS-1 is a 3U+ CubeSat with primary mission objectives to test an experimental PPT thruster and high frequency communication system, fly a camera payload developed by Raisbeck Aviation Highschool, and operate as an Amateur Radio satellite. Operationally, after deployment from the Cygnus, the power distribution board will turn on as well as the COM1 communication system. After waiting 30min, the ISIS antenna will be deployed, and the telemetry beacon will begin. Beaconing consists of 10s transmissions every 2min at transmit level of 20dBm. Once contact is made with the ground station spacecraft health checkout will begin. After the state is known, and if no anomalies are detected, normal operations will begin. Normal operations consist of the pulsed plasma thruster, COM2 operation, and camera operation. After completing these objectives, the HS-1 re-commissioning by AMSAT was planned with continued operating as an amateur radio transponder satellite until the satellite burns up in the atmosphere.

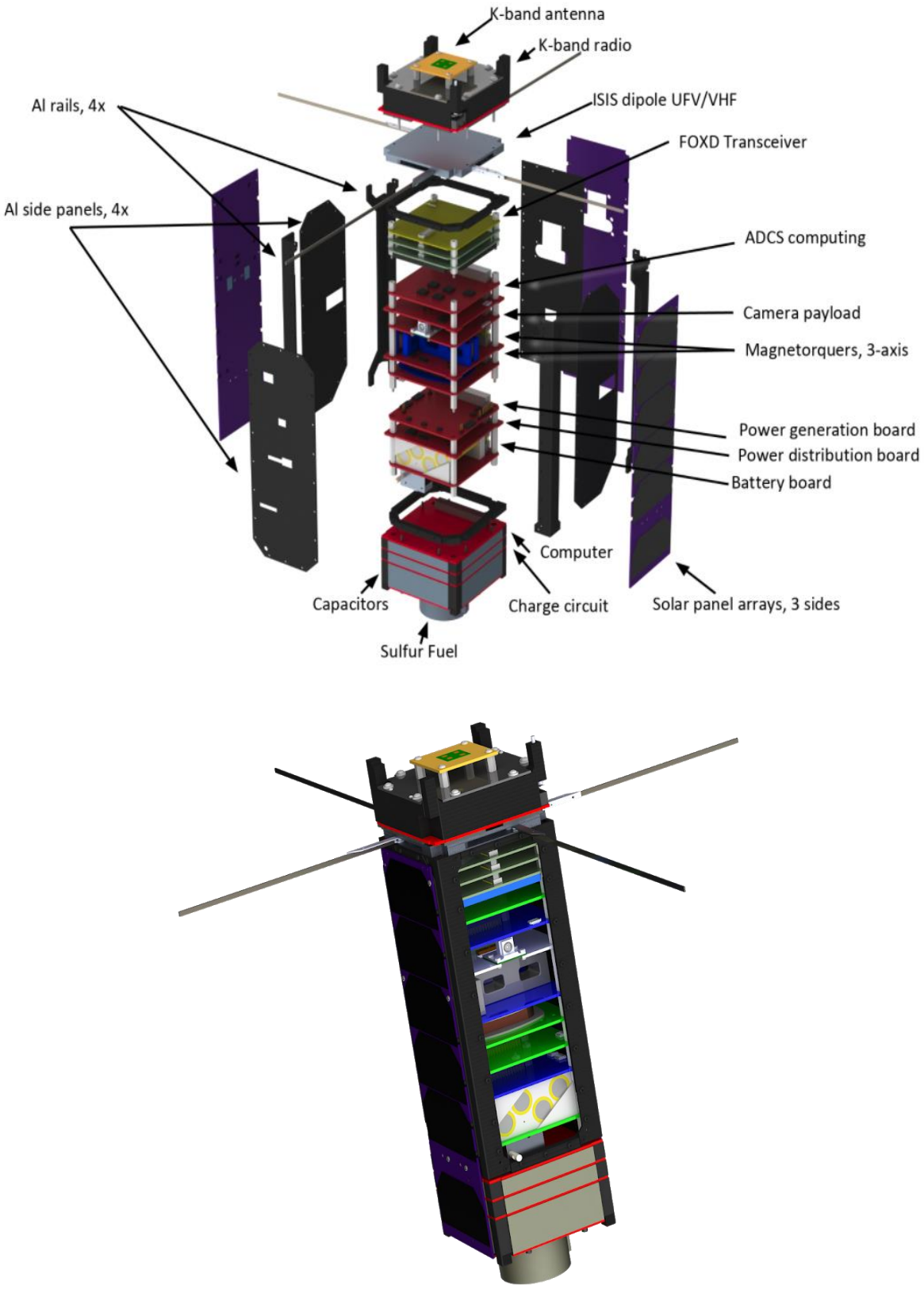

Figure 5.11: HuskySat-1 Final Design Concept Breakout (top) and Assembled (bottom) [101]

5.3 Design Overview

The HS-1 is broken up into a number physically and functionally independent subsystems enabling the easy reuse of the components on future missions, isolation of single point failures, and had the added benefit of more easily allowing students to independently work on various parts.

5.3.1 Structures

The primary purpose of the structure subsystem was securement of the primary stack (see Fig. 5.6) allowing it to successfully operate in the on-orbit thermal environment and survive the launch dynamic environment, as well as shield internal circuits from solar radiation. The primary stack, as shown in Fig. 5.12, consisted of PCBA's separated by McMaster 4-40 threaded, ¼" hex, Aluminum spacers. The structure needed to secure this on both ends for both structural purposes and for heat dissipation.

Figure 5.12: Primary Stack (missing COM1)

The primary stack was connected to the structure using fasteners screwing into the 4-40 hex spacers. Additional strength against the bending moment was provided by modifying the PCB footprint on two of the PCBA's by providing a tight fit of the PCBs to the inside of the structure frame rail. The structure was made up of 6 main components which enveloped the primary stack. Added strength was then added through outer panels made from 2mm thick 6061 aluminum, as shown in Fig. 5.13.

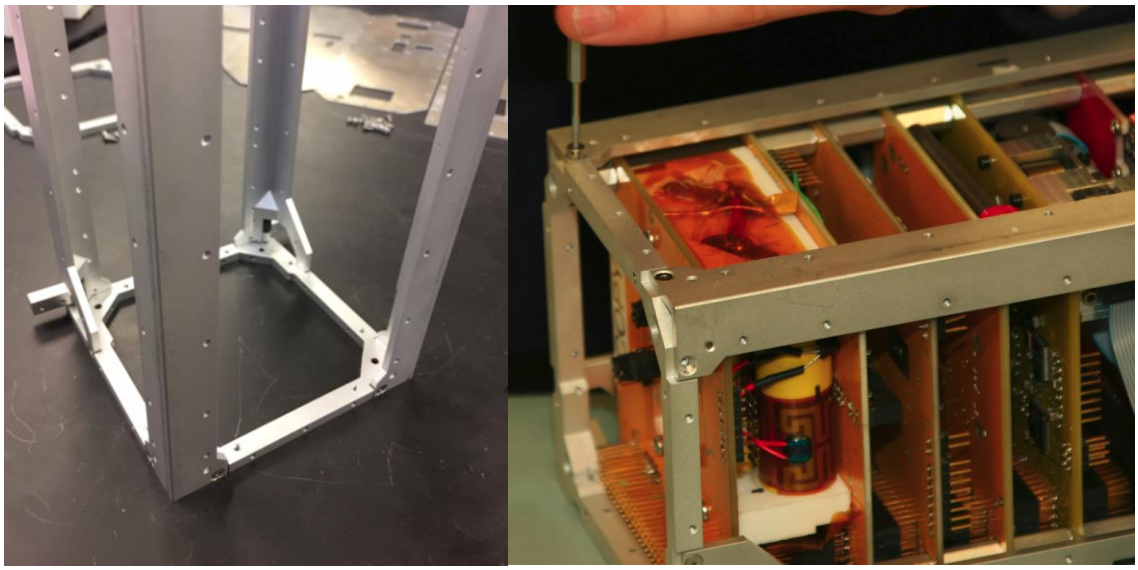

Figure 5.13: Primary Components for Structure Assembly

Machining of structural components was done using ProtoLabs for 3+ axis CNC parts, and for the side panels the UW Mechanical Engineering machine shop water jet was used. All fasteners were procured from McMaster. Prior to installation, all fasteners were cleaned in an ultrasonic bath of isopropyl alcohol at 50C and 20min, and male exposed threads were wiped clean. All fasteners external to the HS-1 had to securement methods: torqueing to specific values and either Loctite or epoxy. Loctite application used 7471 primer with 222 thread locker. Epoxy application used 3M 2216 B/A. Beyond external fasteners, for all other fasteners the following guide was applied: for any fastener securing a component of low modulus of elasticity (plastics, FR-4, etc.) torque if possible and apply epoxy liberally to prevent fastener back-out, see Fig. 5.14 for an example. This guideline was developed from testing performed during the first round of vibration testing which was completed at the NASA specified 14.1 GRMS levels [118]. For this test, half of the #2 pan head fasteners securing the FR-4 solar panel PCBs were torqued while the other half

were torqued with Loctite applied. It was observed that fasteners without Loctite backed out ¼ to 1 rotation.

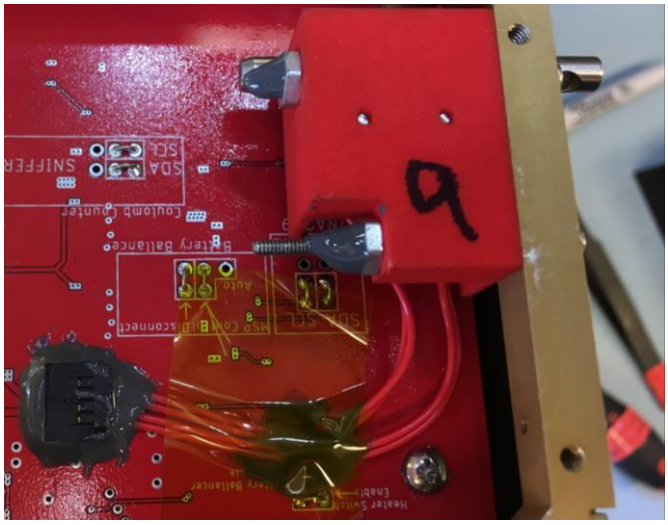

Figure 5.14: Epoxy Application

Surface protection of the aluminum came in two forms, aluminum surfaces touching the deployer were hard anodized per MIL-A-8625, Type III, Class 1, and all other aluminum parts were chemical coated (alodined) per MIL-DTL-5541, Type I, Class 3. The exception to this was the purchased COTS ISIS antenna module which came with no surface treatments. See Fig. 5.15 for a visual example.

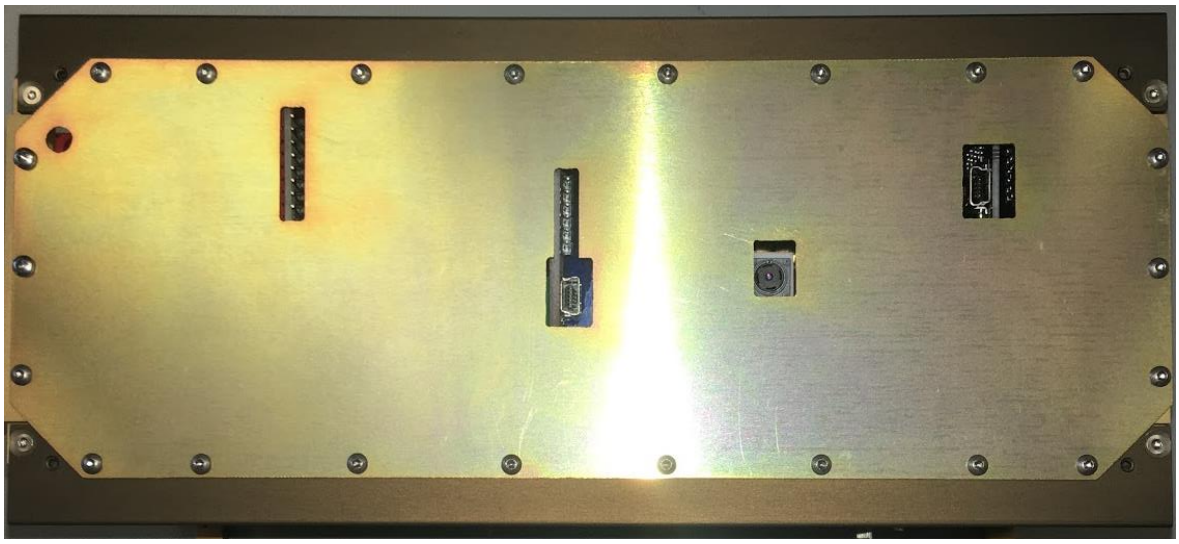

Figure 5.15: Aluminum Surface Treatments; Rails Hard Anodized, Panels Alodined

5.3.2 Power

The power system is responsible for collecting energy from the solar panels, storing it in the battery pack, delivering it to subsystems as needed, identifying and eliminating overcurrent and undervoltage conditions, and reporting telemetry in the form of temperatures, voltages, energy, and currents. Beyond the solar panels on the exterior of the HS-1, the rest of the power system functionality is split between three PCBA's: (1) the power generation board converts solar panel voltage to battery voltage based on the LT3652 integrated circuit providing overvoltage protection while on-orbit by outputting a maximum of 7.05V; (2) the power distribution board provides unregulated battery voltage to the rest of the satellite via high side switching using P-type MOSFETs as well as monitoring the current and voltage of each output at a rate of 10Hz; and (3) the battery board contains the battery pack, monitors pack capacity, balances cells, and provides under-temperature control.

To meet the HS-1 design objective to prevent a single subsystem failure from causing complete bus failure, the power system has 8x power domains whose currents are monitored at

10Hz, see Fig. 5.16. Each of the 8 power outputs has a software adjustable over-current threshold set between 300mA and 8A depending upon subsystem load requirements. The components within the power system are protected by either being a part of a power domain or as in the case of the primary MCU, have a dedicated overcurrent protection. Upon powering on, the HS-1 begins life with as little turned on as possible. Within the power system this consists of the distribution board MCU and the I2C-based current measurers. From there, the MCU has the ability to power on more components, such as the power system power domain which enables the battery board's heater, cell balancer, and coulomb counter, and the generation board's current, voltage, and temperature monitors.

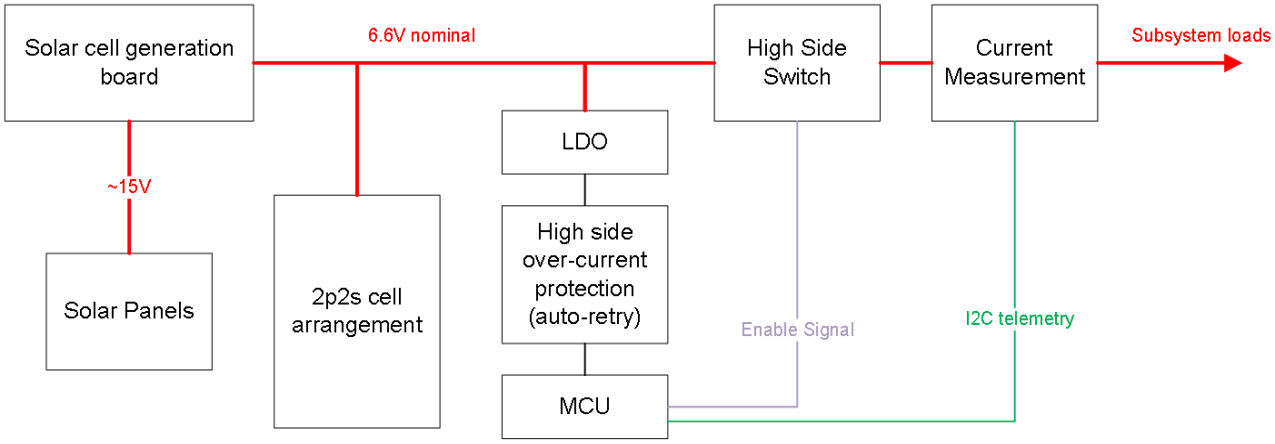

Figure 5.16: Power System Protection Schematic

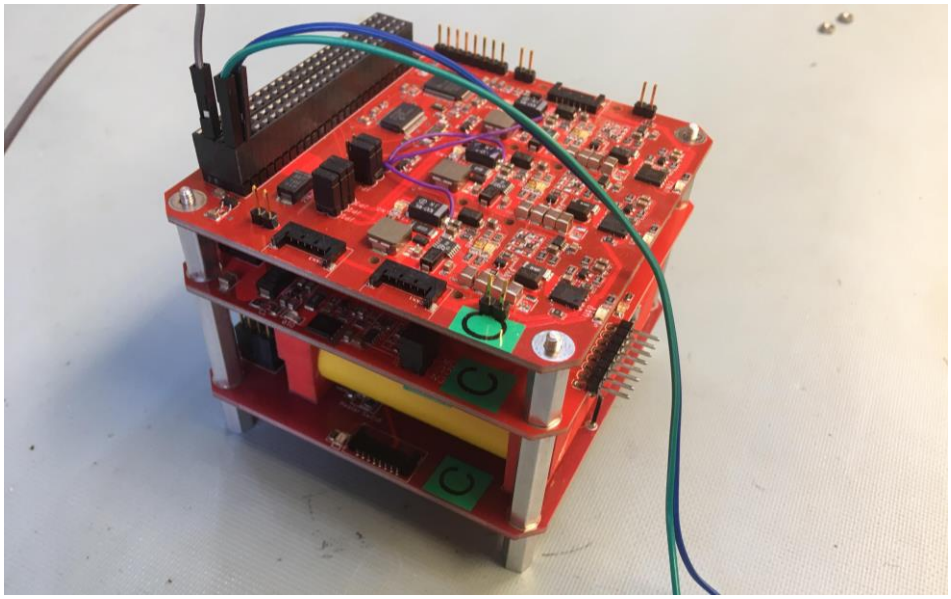

Figure 5.17: Power System 3 Board Stack

5.3.2.1 Solar Panels

The solar panels are built around the Azurspace 3G30A cells triple junction Gallium Arsenide providing 29.3% efficiency [106]. The selection of these cells and the deployable panel layout, utilizing a total of 17 cells, would provide ~16W peak power motivated by the high orbital averaged power required by the PPT of 5W. Beyond assisting with the initial scoping, the solar panel efforts were primarily led by undergraduate student Sean Poulter. Solar cells were mounted using RTV142 silicone, see Fig. 5.18. Assembly of the solar panels was challenging and required use of a jig to aid in alignment, see Fig. 5.19. LM135 temperature sensors were placed on the back of each of the panels. During development one of the cells was cracked and was successfully replaced. Fig. 5.20 shows the final flight panel section. All three panels had their cells wired in series providing up to either a ~16V or a ~13V open circuit voltage.

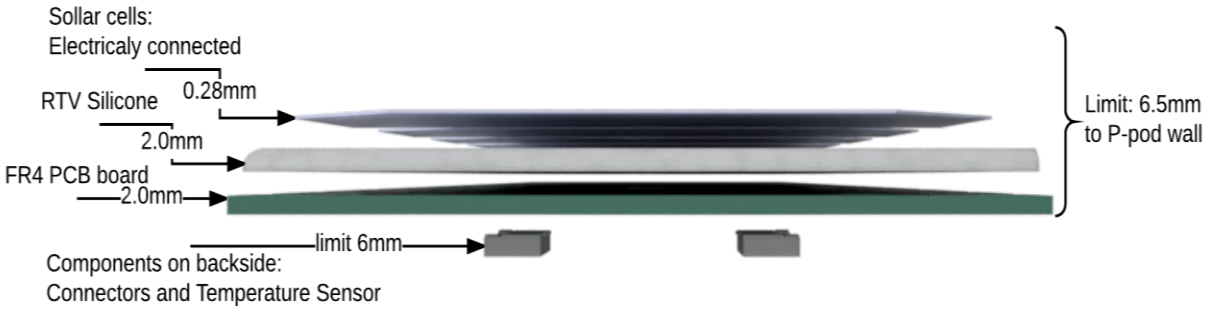

Figure 5.18: Solar Panel Stack Up

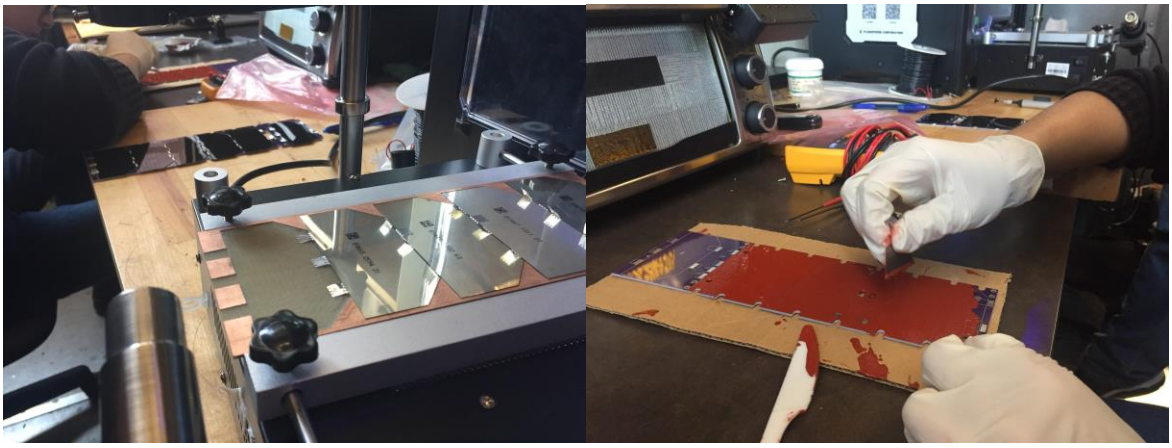

Figure 5.19: Solar Panel Assembly, Left: Alignment Jig, Right: RTV Application

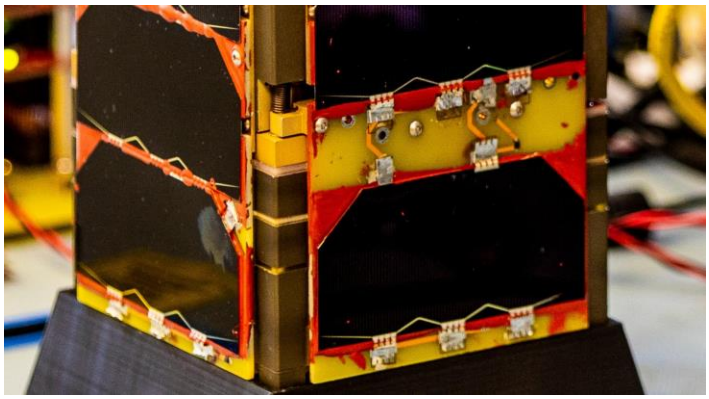

Figure 5.20: Flight Solar Panel Close-up

5.3.2.2 Generation Board

The generation board was based on the LT3652 used to convert from optimal solar panel voltage to bus voltage. There are three nearly identical strings built around the LT3652 with each string connected to one panel. Basic configuration of the LT3652 is a resistor divider network to set the optimal input voltage and a target output voltage. The input voltage was set to correspond to the maximum power point voltage of each panel accounting for any diode drops present. The output was set to the maximum output voltage of 7.05V. The center panel string was set to be slightly higher than 7.05V and the other two were set to be slightly lower than 7.05V to provide a deterministic set of behavior during testing. The LT3652 circuits were default on where their power source is from the panels themselves. Once the power domain is on the microprocessor on the generation board has the ability to disable individually each of LT3652 if desired for limiting the charge current to the batteries. The system is protected against battery drainage due to this feature since the power distribution will respond to an undervoltage event by turning off all power domains. Panel voltage and current is collected using an INA219. Temperatures are also collected by the LM135s placed on each of the panels. The top PCBA in Fig. 5.17 is the generation board. Another important design consideration of this PCBA was the selection of components above the standard +85C limit due to a total assembly heat loss of ~4W.

5.3.2.3 Battery Board

The battery board was designed to provide the high-power demands required by the PPT charging circuitry (8A peak), the energy demands of the COM2 unit (4Whr) and be resilient to the cycle life and on-orbit thermal environment. Previous work developing PPT charging electronics motivated the need for at least 5V input voltage. In addition, the high current and energy demands motivated the need to use a lithium-based battery solution. Lithium chemistries have nominal

voltages of 3.3V to 3.7V [insert citation]. A dual series configuration was chosen (6.6V to 7.2V nominal) as the minimum configuration required to support the PPT charging electronics architecture. A battery trade study resulted in selection of a lithium phosphate (LiFePO4) chemistry 18650 cell A123 APR18650m1-b. Lithium phosphate chemistry has seen prior use in the CubeSat community [108][109][110]. From the trade study this cell was rated for the highest operating temperatures extremes of -30C to 60C [107]. Cell cycle life is rated at over 1500 cycles which is the required number of cycles for a 3 month operation with a 90 minute period [107]. The benefit of selecting a cell which had the required cycle performance meant that additional cell voltage derating was not required, and battery pack lifetime cycle testing could be omitted.

A 2p2s cell configuration was selected as it provided the necessary energy and voltage delivery, as well as being able to accept the originally designed deployable panel peak ~16W charge power. Except for the pre-deployment inhibit switch, covered in Section 5.3.2.5, the battery board is essentially “hot” with no inherent protection systems and a single set of pins providing both input and output current to the 6.6V nominal pack. When the power domain is enabled additional circuitry is enabled:

- Microprocessor: The common microprocessor used throughout the HS-1, the MSP430FR5994, provided battery board GPIO and ADC pins, a local I2C bus, and communication to the spacecraft CAN bus.
- Battery balancer: the BQ29209 ensures the cells stay within 15mV of each other. Monitoring of the cell balancer is done through using an INA219 current and voltage monitor. The need for cell balancing was minimized by selecting flight cells with comparable energy capacity and internal resistance. Cell balancing was set to automatically

be disabled when pack voltage was low per cell balancing guidance provided by Texas Instruments [111].

- Battery heaters: Each cell was wrapped in a Minco HK6908 heating element, see Fig. 5.21. The four heaters were connected in parallel to a Si3865DDV high-side switch. A TO-92 package LM36 temperature sensor was epoxied onto one of the cells. The MCU then provided logic to enable the battery heaters when they reached -10C and to disable them when they reach 0C. The heaters were tested to provide approximately 1C per 3 min of thermal rise. Additionally, a software provision was put in place to completely disable the battery heater logic and permanently disable them as this system was identified as a high risk item to cause premature battery degradation through prolonged inadvertent heater activation.
- Coulomb Counter: The LTC2943 was used to provide a precise voltage and net current into or out of the pack as well as a net accumulated charge. A net accumulated charge was particularly important when developing the spacecraft strategy for autonomously determining if the thruster should fire and at what rate to fire at. The LTC2943 precision voltage measurement, along with the voltage measurement of the INA219, served to provide a means to assess the battery balance state, and provide an external indicator on the efficacy of the BQ29209 circuitry.

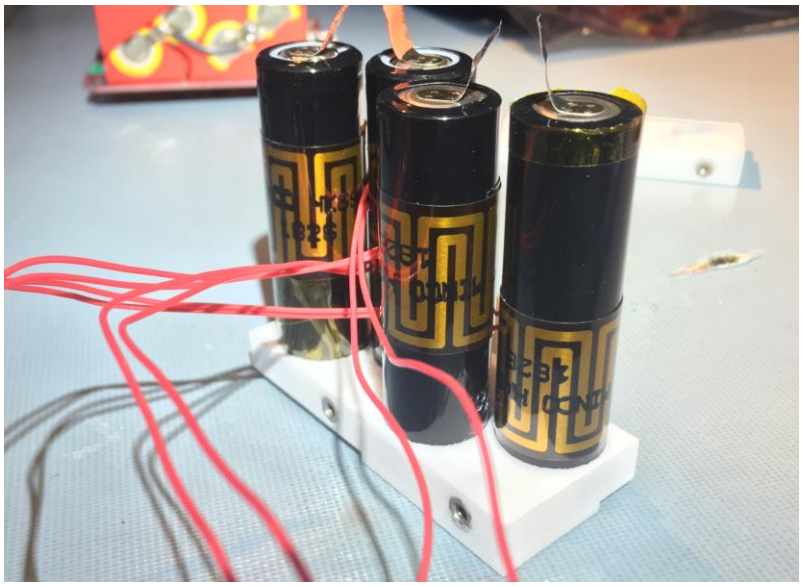

Figure 5.21: Flight Battery Pack during Assembly

The battery holder is made of 3D printed polyimide material manufactured by i.materialise.com, and the hex inserts used are McMaster part number 92398A112. The battery holders are affixed using #4 pan head screws (torqued and epoxied) and then the motion is further constrained by the close-fitting circuit board above. The cells were electrically connected beginning with using commercially available welded tabs from the supplier AA Portable Power Corp which were then soldered to wires. The flight cells, shown in black in Fig. 5.21 had their original yellow protective coverings removed to inspect for any cell damage.

5.3.2.4 Distribution Board

The distribution board is designed around the high-side switch architecture. High side switching was chosen to allow subsystem power toggling while leaving intact a robust and simple ground architecture. A single point, or star ground, scheme was adopted early on in the design phase to assist in mitigating electromagnetic interference and electromagnetic compatibility issues previously experienced in development of the PPT. The distribution board served as the single

point ground for the primary stack where it was electrically connected through one of its standoffs. The PPT and COM2 were then designed to have their structural contact points with the rest of the bus structure to be DC isolated. Like all other PCBAs, the single point ground was provided through the power return connection. Each PCBA, the PPT, and COM2, received a single unregulated voltage sourced from the distribution board. All subsystems were then responsible for providing point-of-load voltage conversion which was conducive to keeping with the single power, single ground return topology. The CAN bus was compatible with this topology since its differential signal based protocol, and by running it at a modest 62.5 kbps, no strict line balancing or PCB impedance control was necessary.

The HS-1 power architecture bus has 8x power domains split across the subsystems. The current demands fell into two regimes: <1 A and >1A. The first solution identified addressed both these current regimes, but after abandoning this fully integrated solution based on the TPS24750 due to difficulties in fully understanding its application features as well as soldering and assembly difficulties due to its 0.5mm lead pitch quad-flat no-leads (QFN) geometry, a discrete multicomponent solution was adopted. Addressing the >1A current demands of the PPT and COM2 was achieved through adopting an already identified and tested solution from the deployment inhibit circuitry, the DMP2002UPS, which was selected for its low on-resistance. More detail on this is in Section 5.3.2.5. In addition to high side switching, each domain utilized an INA219 for current and voltage monitoring, provisions for series shunt filtering, and LEDs to aid in development. With the footprint of a single switch proving too large to fit 8x copies, the two current demand regimes motivated a more compact solution for the <1A power domains. The Si3865DDV was selected as a suitable solution.

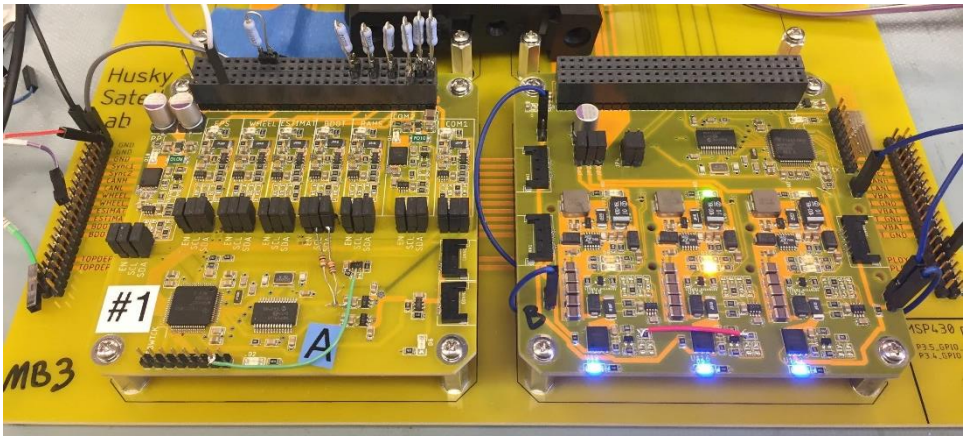

Figure 5.22: Early Prototype of Distribution Board (left) and Generation Board (right)

5.3.2.5 Pre-Deployment Inhibit

The deployment inhibit needed to interrupt the power supply going to all HS-1 components while still providing low on-resistance during normal operation. While the simplest approach used on CubeSats is running the entire bus power through a single toggle switch. This approach was abandoned due to not finding a switch rated to the required current while still being compact. The solution was to use the basic Cherry E62-10H switch sold by the CubeSatShop paired with low on-resistance FETs. The P-type MOSFET DMP2002UPS was selected paired with an N-type MOSFET for gate and slew control. To provide bi-directional current control two identical switches were placed in series with their sources facing each other. The switches are enabled through the "EN" net which connects directly to the battery pack through the Cherry switch. One unforeseen limitation of the switch topology is if the battery is dead, or at 0V, then when the Cherry switch is closed the EN net is 0V which is insufficient for turn on. The minimum voltage for turn-on was measured at ~0.3V.

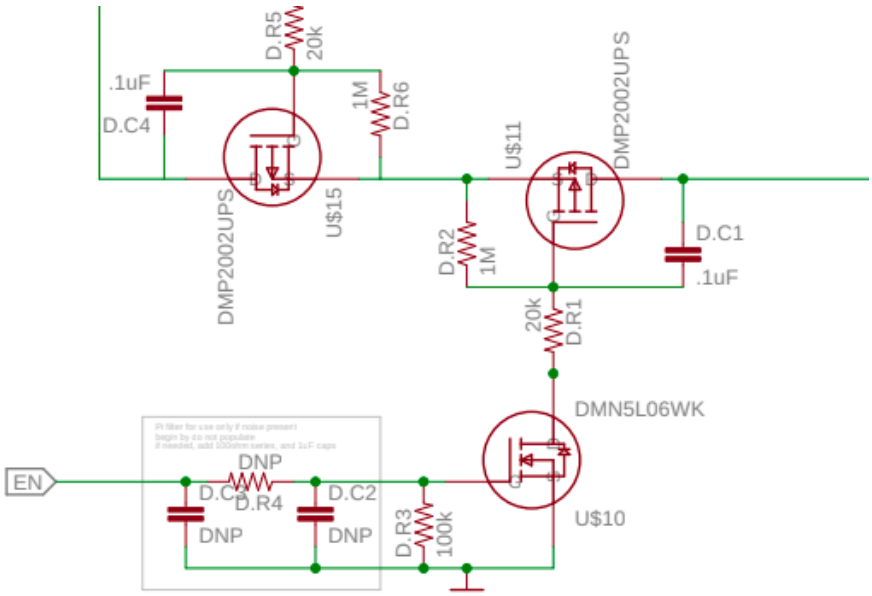

Figure 5.23: Deployment Inhibit Switch

5.3.3 Attitude Determination and Control

The attitude determination and control subsystem (ADCS) underwent the most significant changes during this project's descoping efforts, as discussed in section 5.2.3. The ADCS provides two primary functions: (1) detumbling, and (2) attitude determination and pointing control. Consistent with the aforementioned descoping efforts, limited organizational resources required prioritization of efforts with respect to testing and verification of this system. Efforts focused of the detumbling portion which consisted of hardware-in-the-loop (HIL) testing at the boundary of spoofing inputs to the system using a I2C slave emulator taking the place of the magnetometer, and the output captured by a digital-to-analog converter (DAC) on the magnetorquer coils. Aspects of the attitude determination and pointing control functionality were validated from the perspective of verifying the sensors supplied reasonable values and deployed autocoded MATLAB control software provided valid outputs; however, resources did not allow this latter system to be fully validated using HIL methods.

An overview of the ADCS is shown in Fig. 5.24. The detumbling system is composed of a MSP430 and HMC5983L magnetometer where the logic runs in autocoded MATLAB software. The magnetorquer system has its own MSP430 and 3x 1-axis magnetometers each using A3903 H-bridges connected to hand wound coils. These magnetometer MCU sends coil commands to the magnetorquer MCU. There are various operating modes for system: in normal detumbling operation a duty cycle between the two provides a time for the magnetometer to make a magnetic field measurement when the magnetorquers are off; there is also the ability to read the magnetometers when the magnetorquers are on in order to provide diagnostics; and there is also the ability to utilize the system as a permanent magnet. All MATLAB software running of the HS-1 was developed by the RAIN Lab at the UW with efforts led by graduate student Taylor Reynolds.

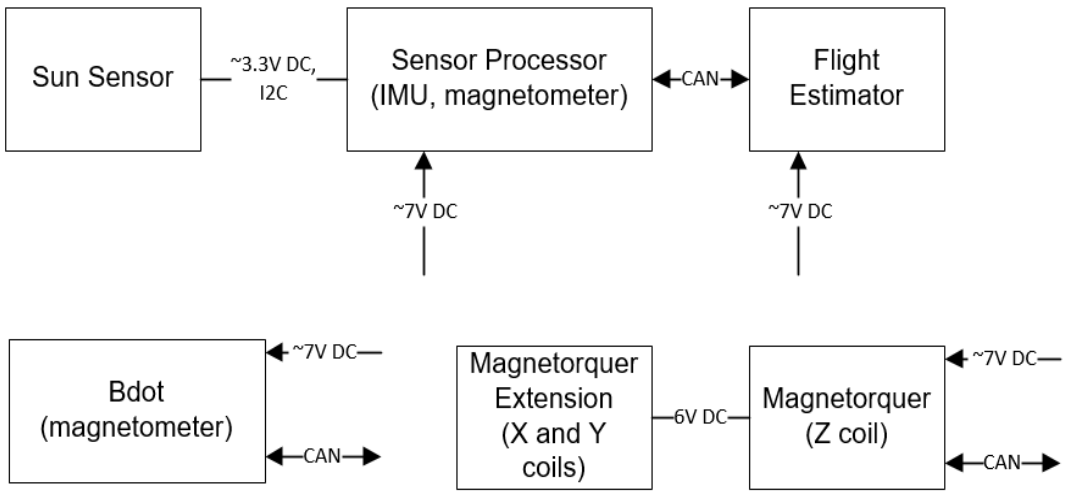

Figure 5.24: ADCS Block Diagram

5.3.4 Raisbeck Aviation High School Camera Payload

The HuskySat-1 mission provided the Raisbeck Aviation High School the opportunity for their CubeSat team to get experience developing a project to fly in space. This partnership was for the development of a camera payload to fly onboard the HS-1, as shown in Fig. 5.25. The design

consists of a Raspberry Pi Zero and Raspberry Pi camera 2 running a modified version of Raspbian. The non-profit Quick2Space provided a tremendous amount of assistance on this project, such as with developing the CAN software stack needed to operate with the MCP25625 CAN transceiver. This software, written in Python, allowed for deployment into the stock Raspbian environment which was used on both this Raspberry Pi as well as the one within COM2.

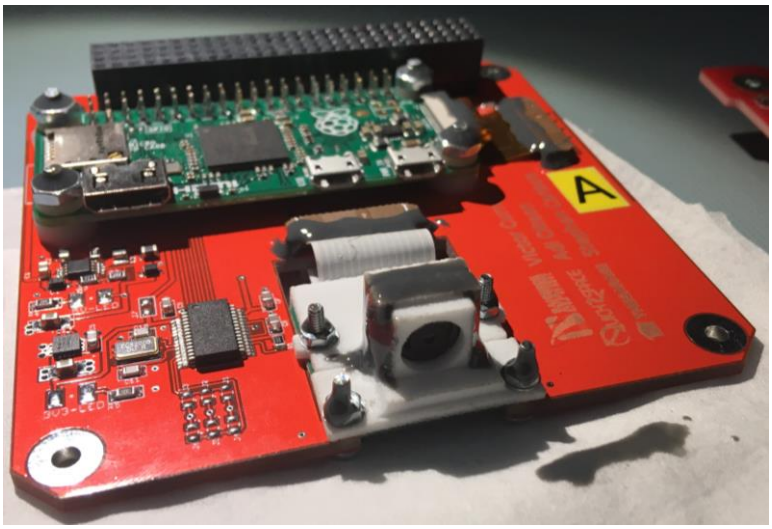

Figure 5.25: Camera Module

5.3.5 Pulsed Plasma Thruster

The PPT development effort was led by graduate student Paige Northway. See reference for additional details for the flight configuration [101].

5.3.6 Amateur Satellite Radio Low Gain Communications

COM1 is composed of an AMSAT Linear Transponder Radio paired with the ISIS deployable UHF/VHF antenna. The intent of using externally procured hardware for this subsystem was for reliability. The radio provided in partnership with AMSAT is based on improvements they made to their heritage Fox-1x family of radios by providing simultaneous multi-channel communications. The AMSAT team was invaluable for making this mission

possible. The radio has an FM uplink in the VHF band, and a 1200 bps BPSK downlink in the UHF band 435.800MHz. COM1 interfaces to the HS-1 via the common CAN bus and a power supply connection, and provides regulated power and an I2C bus to the ISIS antenna. Additionally, various zombie mode signals were white wired to a COM1 ADC to assist in further diagnostic capability. These zombie mode signals were added late in the development to address the risk of the PPT EMI causing fault with the power system MCUs or the CAN bus. These signals include sampling of a monostable vibrator output which converts the distribution board MCU blinking light to a continuous high/low signal as well as each of the outputs of the step down buck converters on the power generation board. The AMSAT Linear Transponder Radio features a 30 kHz wide V/U linear transponder for SSB and CW with an uplink passband of 145.910 – 145.940 MHz LSB/CW and downlink passband of 435.840 – 435.810 MHz USB/CW (inverting). Check with AMSAT news website for the latest status update. Additional detail on operations is in section 5.4.

5.3.7 K-band Transmitter

Development of the 24GHz transmitter system is covered in Chapter 3. The final flight version did not include the reflectarray due to loss of precise pointing of the HS-1, see Section 5.2.3 for further detail. With the removal of reflectarray, the feed antenna previously developed was reoriented as shown in Fig. 5.26.

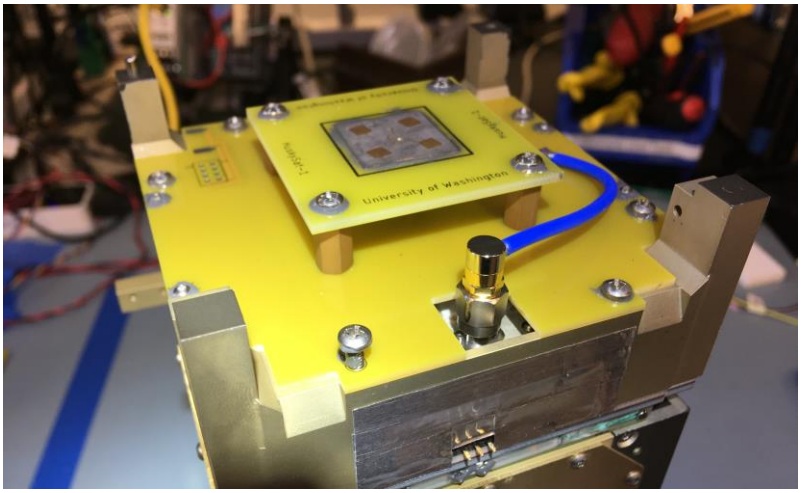

Figure 5.26: Flight Model 24GHz Transmitter

5.4 Printed Circuit Board Assembly Development

Even though from the onset the HS-1 project was significantly financially and technically resource constrained, these challenges turned out to be extremely beneficial in how the project was approached. Financial limitations and PI direction pushed us towards the "build it ourselves" mentality. This quickly materialized into various design standards and procedural practices which are covered in this section.

Developing the HS-1 was initially broken into four main areas: structural, PCBAs, software, and systems engineering. The structure development was addressed using SolidWorks and abundant 3D printing for prototyping. Difficulties arose with any structural moving part (pre-descope) as well as with tolerancing. Standard machine tolerances (0.1mm) stacked up and the net impact was the structure was too narrow. The launch provider accepted this deviation. Another challenge, never fully addressed, was the lack of repeatability in assembly to assembly. Every time the HS-1 was assembled the fit was slightly different. This is likely to be owed to the fact that structural parts were not keyed and could be swapped and even installed backwards. In general, configuration management proved to be overall challenging, but for a project of this scale it was

sufficient to use SolidWorks and a spreadsheet-based bill of materials. The university resources also provided access to FEA through SolidWorks and Ansys. See section 5.3 for specific HS-1 design features.

PCBA development started with the design goal of reusing as many individual components, integrated circuits (IC), as well as schematics and layouts. Commonality was especially important due to the scale: the final HS-1 design had 11x MSP430's. This effort began by selecting an MCU which could be compatible with all intended HS-1 applications. The MSP430 FRAM was selected initially for its naturally radiation tolerant memory [178]. Within this MCU family, the largest and most capable was selected: the MSP430FR5994. Following this, the MCP25625 integrated CAN controller and transceiver was selected. Shown in Fig. 5.27, a layout was developed with dedicated default pin allocations and quickly deployed to the software team for further development. In developing this implementation it was important to consider all use cases for the MSP430 such as the number of GPIO pins, I2C buses, and SPI buses needed for all of the applications. Additionally, a common exposed "programming and debug interface" was developed with 2x GPIO designated as auxiliary. The development choices were extremely valuable since by using a common schematic and layout allowed for highly efficiency PCB development, and the auxiliary GPIO pins were invaluable for debugging on specific case-by-case basis. The one additional improvement to be made would be exposing, directly or indirectly, the programming/debug interfaces to the external of the CubeSat when fully assembled.

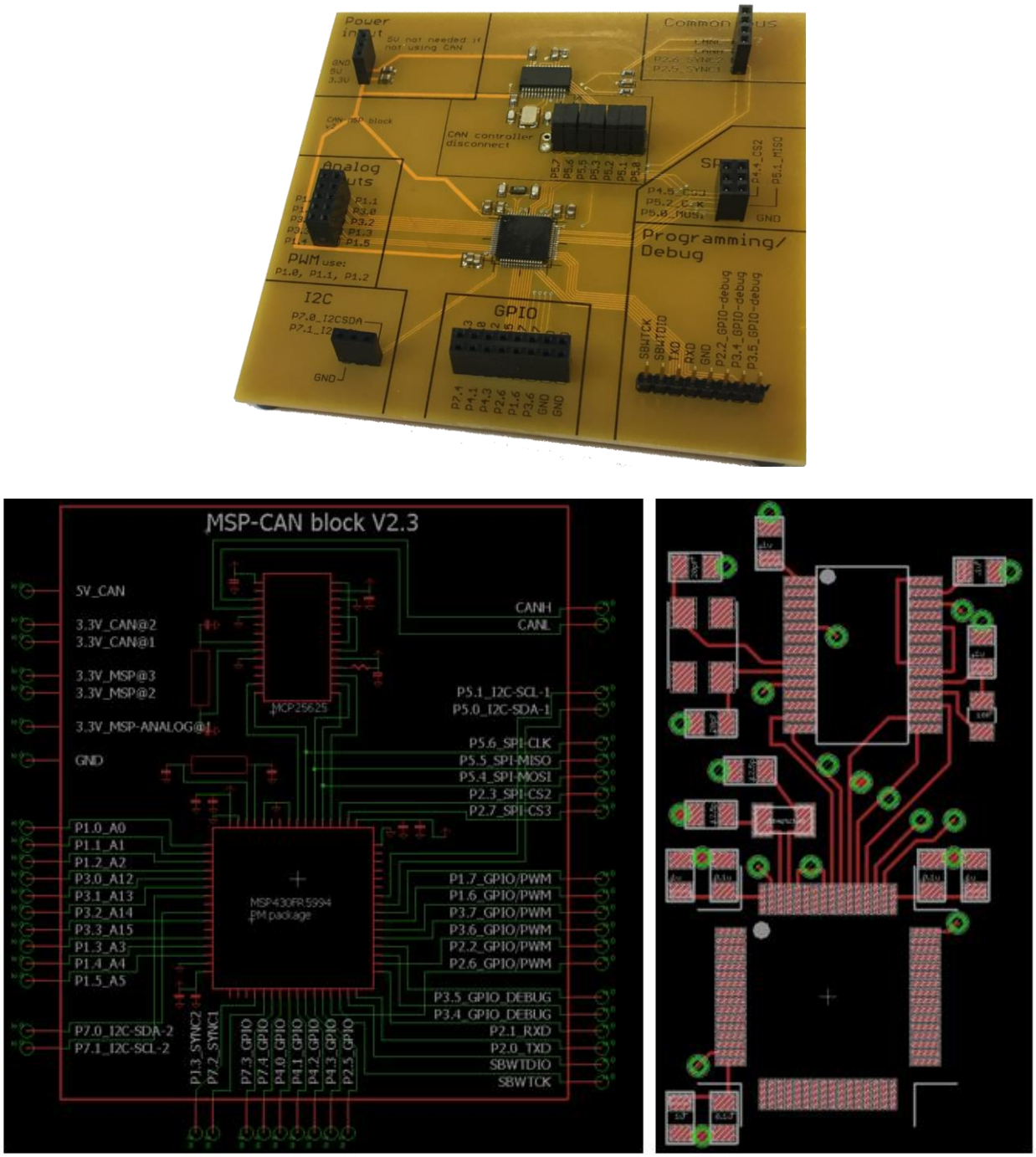

Figure 5.27: MSP-CAN Block: Development Board (top), Schematic (lower left), Layout (lower right)

The PCB design commonality was pervasive: every MSP-CAN block required a 3.3V and 5V regulator, connector types, pre-deployment inhibit switches, etc. To aid in assembly and to relax manufacturing requirements, certain design guidelines were developed: 8mil minimum trace width, 8mil minimum trace spacing, selection of exposed leaded ICs with high aversion to QFN, no BGA, 0805 or larger passives, large and legible silk screens, yellow PCBs for development since they provide best visible to PCB construction, copper weight of 1oz everywhere except high power or high thermal applications receive 2oz, etc. Additional design guides to minimize the chances of requiring revision changes: conservative schematic design such as numerous decoupling capacitors, derating of all components including traces, custom developed footprints for all components, etc. There are many fantastic resources for the design of high speed PCBs. While not directly applicable because the HS-1 was generally low speed, understanding the principles is extremely informative [113].

The use of LEDs was pervasive on the HS-1. The most invaluable was one on each MSP430 which helped debug issues with locking up which was a particularly cumbersome issue because all software, down to the board support package, was developed from scratch. LEDs were also present to provide visual cues of the power system state.

Most IC types used in the HS-1 were previously unfamiliar, and therefore extreme caution was taken during their first implementation. Reading datasheets carefully and testing thoroughly against it cannot be overstated. The implementation approach taken varied slightly with every IC, but as a guide: define requirements, select IC suitable to meeting requirements, order development board, read datasheet, test development in its intended operation and clarify any misunderstandings in the datasheet, implement IC on custom PCB with minimal modification from development board, if tested successfully move to revision change where functionality or behavior is consistent

with intended final application, if tested successfully move to revision adding additional (and many times duplicate) circuitry, keep iterating in these steps until an engineering model is reached, and when ready for flight model change as little as possible from the last engineering model.

The described above IC and PCBA implementation required many iterative cycles. To varying degrees Spice simulations were utilized, but in the end a lot of testing and design modifications were required to achieve the intended functionality. While this approach would be wasteful in many professional PCBA development efforts, learning PCBA development through trial and error worked remarkably well during the HS-1 program. PCB assembly started with use of the foreign PCB manufacturer Elecrow. When shipping via DHL orders placed on Monday would arrive by Thursday. With Digikey or Mouser parts readily available PCBAs could be assembled the day of arrival. Much of the time PCBA revisions were being performed on a weekly cadence. Later in the project, when PCBAs became more numerous and complex, this cadence became 2-4 weeks. Most UW developed PCBAs on the HS-1 underwent 3-7 PCB design iterations.

PCBA assembly began with taking an inventory of needed components. PCBs were inspected for manufacturing defects and an electrical continuity test was completed primarily consisting of verifying if short circuits were present between positive and negative returns. Traces and pours in the regions of through-hole geometries for connector pins were also historically problematic. These types of issues, ideally caught at earlier stages prior to manufacturing, could all be traced back to layout error, Gerber file export error, or manufacturing error. There were many instances where Elecrow was able to identify issues during their initial Gerber review. Once the PCB checkout passed, any leftover residue was cleaned with isopropyl alcohol. At this time, hands were also thoroughly washed to remove excess oil, as the subsequent assembly was typically done without gloves for improved dexterity.

Solder paste application followed. The goal of solder paste application is to apply the correct amount of paste to all pads. Initially this process was with using a toothpick. However, this method does not allow for uniform application and takes too long for higher component boards. The application time is very important, since solder paste has moisture in it and has a limited working time; the goal was for a maximum of ~4 hours to be between the initial solder paste application, component placement, and the reflow oven. Stencils to provide the best paste application, in combination with the type of paste used, were 0.1mm thick laser cut metal from Elecrow. Solder paste application started with securing down the PCB using blue painters tape, and on top of it securing the stencil. MG Chemicals 63/37 leaded solder paste was applied by using another PCB by wiping at a 45 degree angle with firm pressure. The solder paste was normally stored in a refrigerator, and needed to be warmed up to room temperature before the wiping process due to the change in its viscosity. After initial paste application the PCB was inspected under a magnifying glass to verify all pads had the correct amount of paste.

Component placement was performed on an ESD matt using ESD tweezers. A computer was close by for component placement reference, and typically an enlarged screenshot of the layout was previously printed and marked up as part of the initial part inventory check. Working efficiently at this stage was critical to stay with the ~4 hour window. Additionally, multiple copies of the same board were typically assembled in parallel. Assembling is parallel proved to be extremely beneficial since this improved the likelihood that the boards were assembled the same, contrasted to assembling the same PCBA on two days introduced a higher chance of a difference.

After components were placed the entire assembly was placed in the reflow oven. The reflow oven used was an adapted toaster oven based on the Controleo2. This design utilized an additional heating element for increased heating ramp rate, a thermocouple for feedback, solid

state relays on all heating elements, and then a microprocessor which provided the appropriate temperature profile. This reflow oven worked extremely well, but was limited in terms of the thermal mass placed inside of it; this was addressed by performing a test run of baking boards which just had solder paste on them and no components.

Once the boards cooled, they were removed and any through-hole components were installed using a standard solder iron and 63/37 solder. For engineering model development applications the last assembly step was marking/serializing the PCBA. For flight boards, after testing, they were cleaned, staked, and conformal coated. Cleaning was completed by placing them in an ultrasonic bath of MG Chemicals Safety Wash at 50C for 20min. Residue flux also required physical agitation for removal using an ESD brush. Before continuing, a separate party would inspect the PCBAs with a microscope. The next step was staking using 3M 2216 B/A, with examples shown in Fig. 5.25 and Fig. 5.14. The last step was conformal coating with MG Chemicals 422B-340G silicone conformal coating. Conformal coating required meticulous masking of the connector boards and programming pins. PCBAs were also affixed using their #4 mounting holes which served the dual purpose of masking these interfaces. Masking here was important because otherwise the conformal coating would increase the mounting thickness leading to an unplanned longer primary stack.

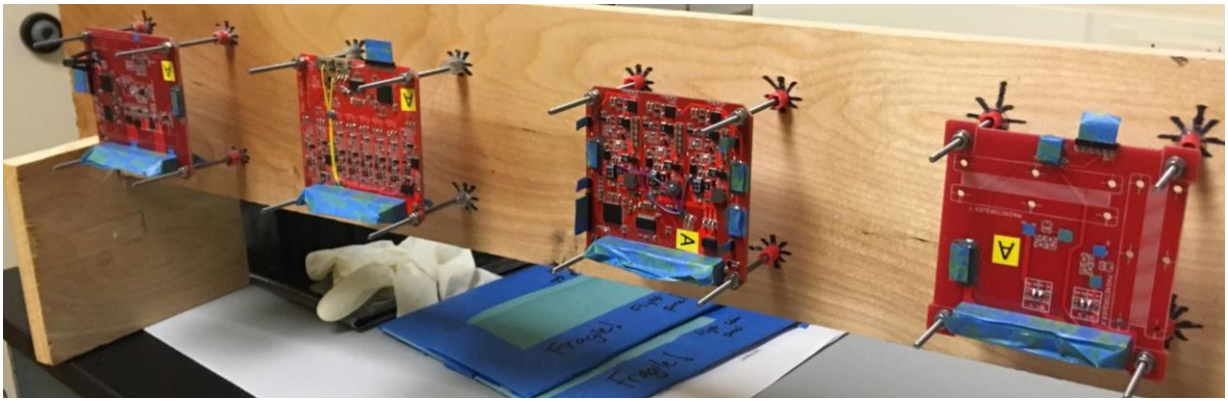

Figure 5.28: Conformal Coating Jig

As shown in Fig. 5.28 four flight boards were coated at a time. Spray application was performed providing a total of 24 coats per PCBA side. The last step was to remove the masking tape and inspect the conformal coating under a UV light; this was enabled by the conformal coating used having a UV tracer.

The PCBA quantity strategy was typically 2x - 5x. 2x was useful beyond 1x during testing as it provided a means to ascertain if it's an issue with the design, or something particular with how it's being tested or unique to that board. During the developing phase, beyond 2x added value by allowing more team members to use the boards. This was especially useful with the MSP-CAN block in Fig. 5.27. For the flight boards the strategy was 3x copies: 1x for initial testing (labelled as C), 1x flight operational (labelled as A), and 1x flight operational spare (labelled as B).

5.5 Testing and Development Operations

5.5.1 Test-As-You-Fly Implementation

The HS-1 bus is composed of multiple subsystems which are interconnected through the common CAN data bus. The CAN architecture was partially chosen due to being a master-less protocol and facilitating a distributed subsystem independent approach. It was also selected so as to provide operational similarity between development operations and on-orbit operational control. This control started with Ball Aerospace COSMOS. COSMOS was utilized during development and operations of the HS-1. Initial interaction between COSMOS are individual MSP430s began through use of a direct UART connection, see Fig. 5.29 example the power system distribution COSMOS interface GUI developed. Each MSP430, in addition to programming pins, had UART pins exposed for this purpose which allowed for 10Hz data reporting from the MCU. Additionally, CAN-to-COSMOS interface was implemented, allowing for COSMOS to interact both directly

with individual MCUs directly, as well as the common CAN bus; see Fig. 5.30 for an example of this state. The CAN-COSMOS interface was developed initially for the CAN-to-Ethernet PEAK adapter, and later implemented for the CAN-to-USB Kvaser Leaf Light v2 adapter. The UART connection was provided using the popular CP2102 USB-to-TTL adapter. With time, UART connections were removed leaving only the CAN connection to COSMOS. In addition to custom interfaces, COSMOS allowed easy plotting of data in real-time. This proved to be very useful in helping process all of the telemetry generated, see Fig. 5.31 for example.

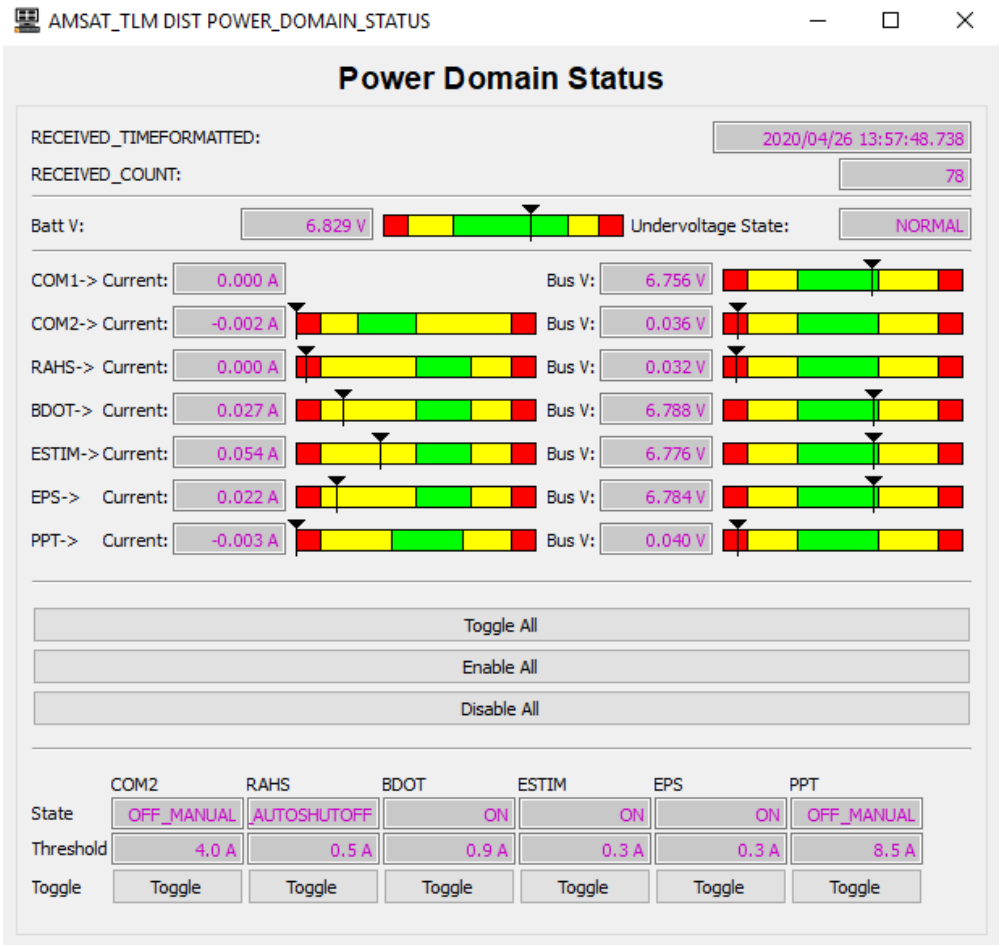

Figure 5.29: COSMOS Interface for Power Distribution

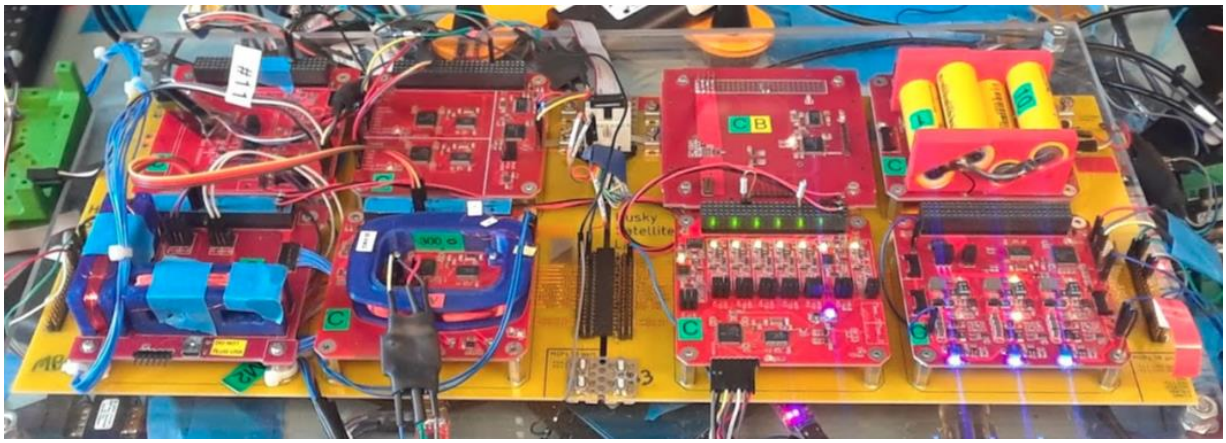

Figure 5.30: FlatSat

Figure 5.31: COSMOS Spacecraft Data Visualization

Moving from COSMOS direct connection to the HS-1 subsystems to on-orbit operations was realized through the addition of the COM1 module detailed in section 5.5.1

5.5.2 Battery Acceptance and Assurance Testing

In addition to the development of the HS-1 Power System, described in section 5.3.2, the battery pack underwent additional flight screening and design verification. This began with

removal of the cell packaging for inspection of any scratches, dents, or otherwise atypical physical characteristics. This proceeded with various tests of charging and discharging the cells. The test setup used for charging and discharging, see Fig. 5.32, consisted of a Rigol DP811A power supply and a Rigol DL3031A electronic load. These two devices interfaces directly to COSMOS. The Ruby-based scripting functionality within COSMOS was implemented for carrying the necessary charging and discharging procedures. COSMOS pulled data from the two instruments at 10Hz and used this information to trigger the transition between constant-current and constant-voltage charging or discharging. Temperature logging was accomplished by using a TMP36 analog temperature sensor sampled by an Arduino serially interfaced to COSMOS. The primary electrical connections made to individual cells or battery packs are shown in the figure below.

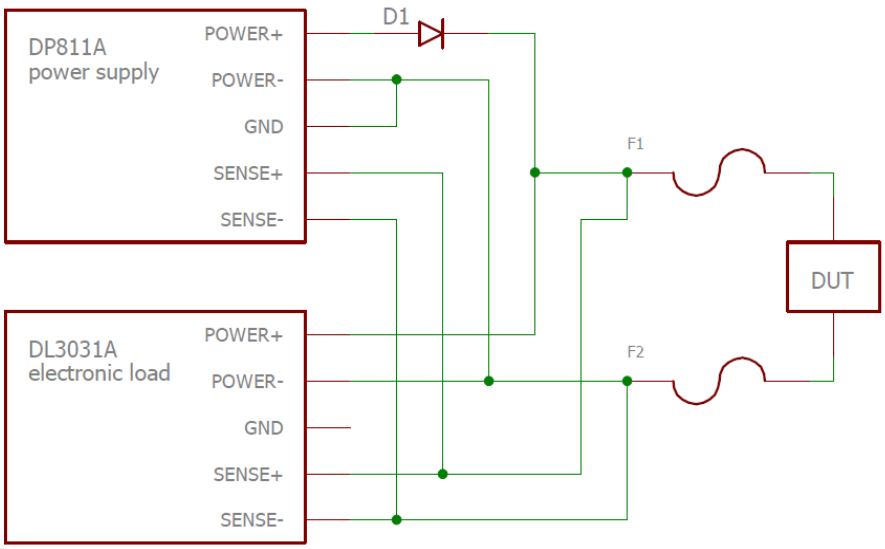

Figure 5.32: Battery Pack/Cell Test Cycling Configuration

A diode was placed in series with the DP811A output to ensure current only flows out of the power supply. Fuses were placed immediately next to the battery cell to provide an extra level of

safety when handling unprotected cells. These two implementations were in response to a battery fire initiated by an external battery being shorted into the unpowered power supply causing damage to the power supply output stage as well as the high current causing heating of insulation of the external cables to the DUT catching on fire. Kelvin sensing was implemented to eliminate voltage error associated with finite cable resistance and the diode drop. When performing testing on individual cells which did not have built-in protection an additional level of precaution was taken by placing them, as well as the two fuses, in a BAT-SAFE box designed to contain battery fires. The testing resulted in all cells being acceptable for flight use. See Fig. 5.33 and Fig. 5.34. Additional testing was performed checking cell capacity before and after vibration and vacuum environment.

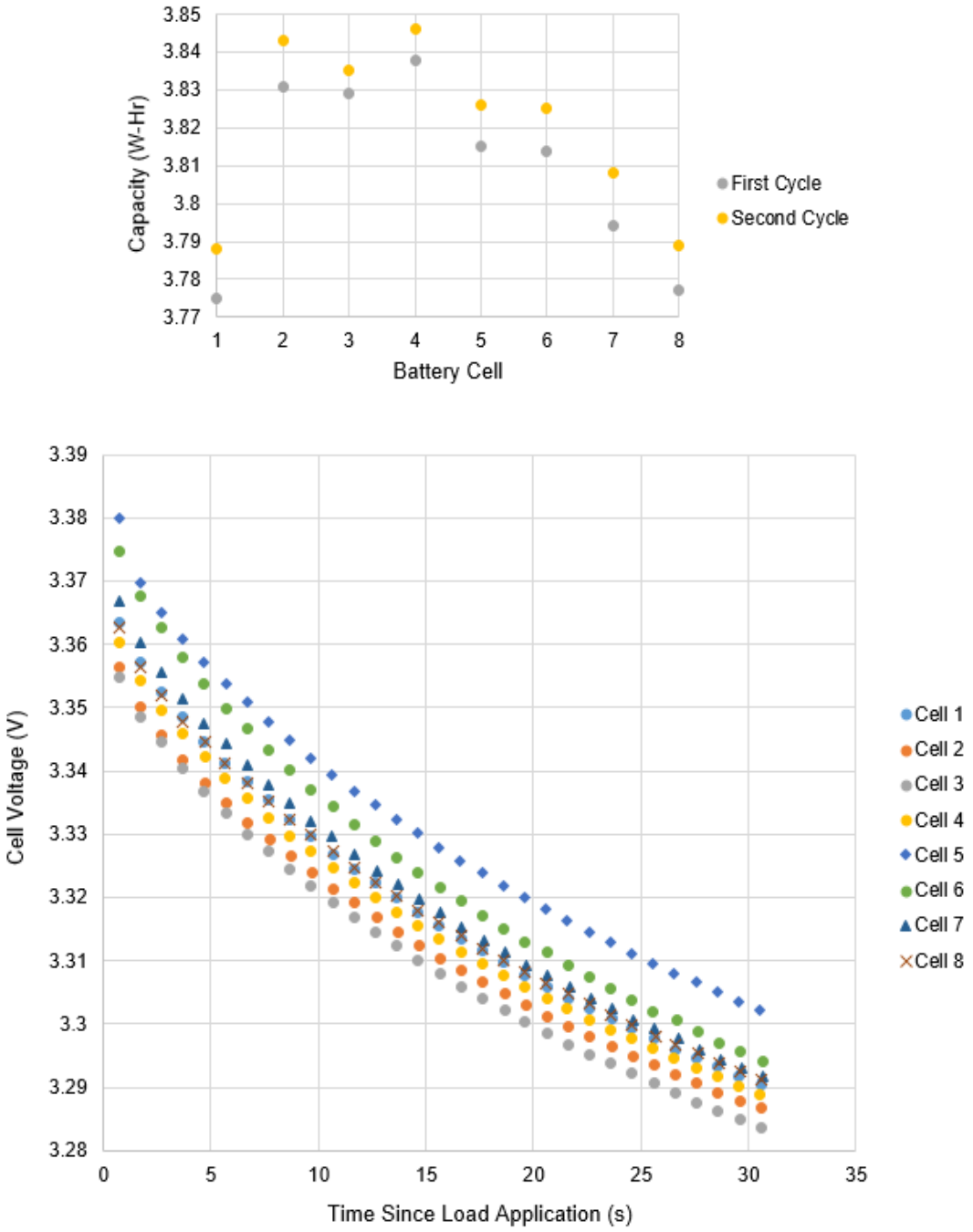

Figure 5.33: Battery Cell Capacity (Top) and Closed Circuit Voltage at C/2 Load (Bottom)

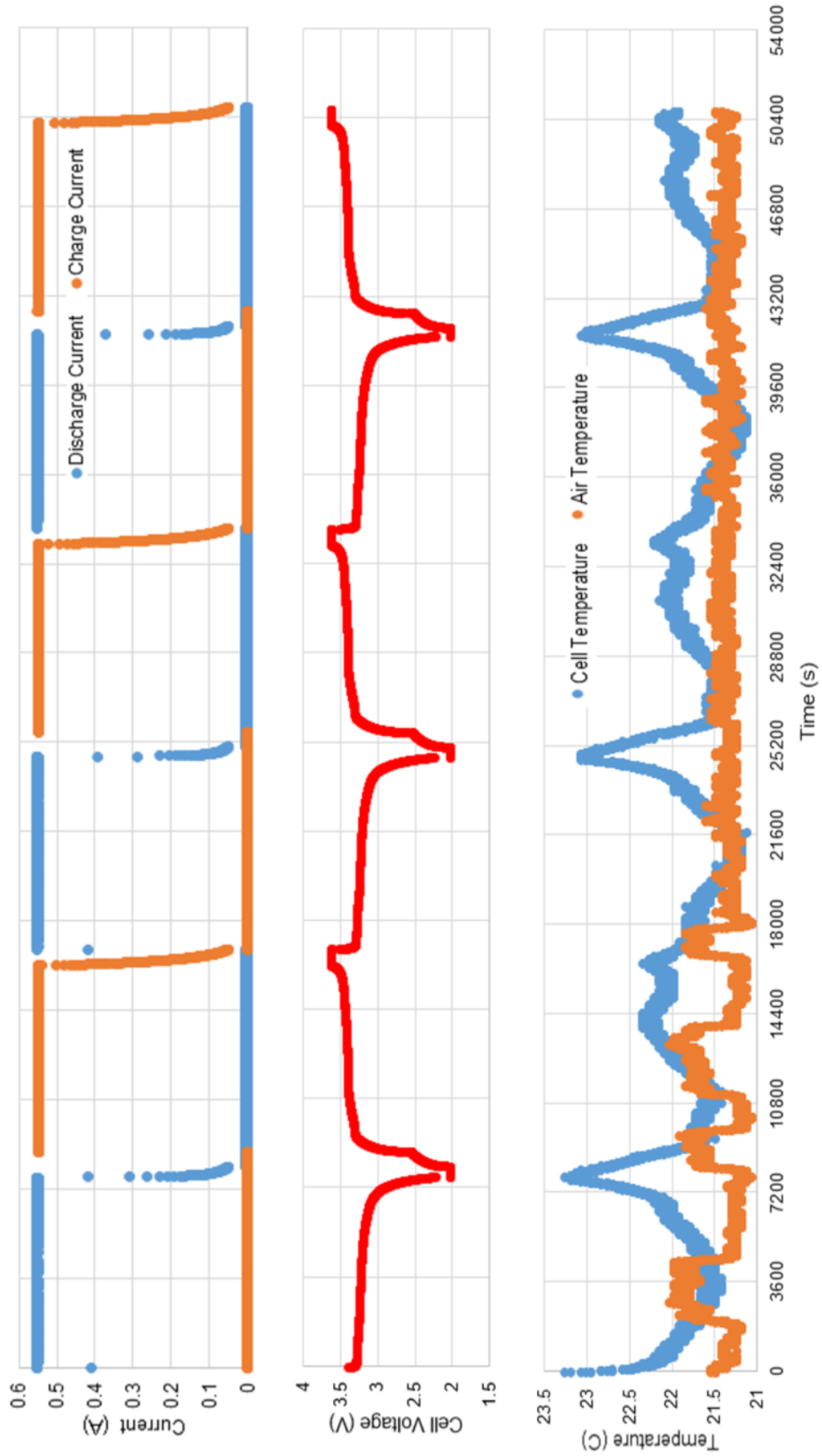

Figure 5.34: Battery Cell Cycling (Cell 1) Data: Charge and Discharge Current (Top), Voltage (Middle), and Temperature (Bottom)

5.5.3 Environmental Testing

The HS-1 and its components underwent vibration, thermal, and vacuum testing. Four rounds of vibration testing were completed, all using different outside facilities. A summary and results of each round chronologically:

1. Confidence testing. Test article was the engineering model structure built up with mass dummies placed inside on the primary stack PCBs. Article passed testing and verified the integrity of the structure.
2. Qualification testing. Test article was an engineering model of the HS-1 except omitting a fully populated PPT module and omitting a COM2 antenna. Post testing revealed the solar panels did not deploy and the reaction wheel performance changed.
3. Acceptance testing. Test articles were fully assembled PPT module and battery cells. All articles passed.
4. Acceptance testing. Test article was flight model HS-1 and passed.

Thermal testing was completed at various stages during development. Resource availability provided easy access to a thermal chamber and vacuum chambers. While a thermal-vacuum chamber is ideal, the combination of the separate thermal and vacuum was entirely adequate since the thermal chamber represented a conservative worst case on the cold side (ambient temperature plus convective cooling), and the vacuum chamber provided a conservative worst case on the hot side (no convective cooling and room temperature surrounding). At engineering model level qualification temperature testing was performed at the low temperature regime looking at cold turn and cold operation as well as the hot regime at 100% system load. An example of one of the tests was placing a CAN-MSP block within the thermal chamber turned off, bringing the chamber to -45C, and verifying the system initialized and could communicate successfully with a CAN node

outside of the thermal chamber. For the hot side, the PCBA receiving the most attention was the power generation board since it had a maximum power dissipation of ~4W. Testing consisted of emulating the thermal resistance this PCBA sees during HS-1 installation and affixing multiple TMP36 analog temperature sensors. Temperature sensor placement was chosen to provide telemetry on the highest thermal rising components as well as along the thermal pathway in order to characterize the thermal resistance, see Fig 5.35.

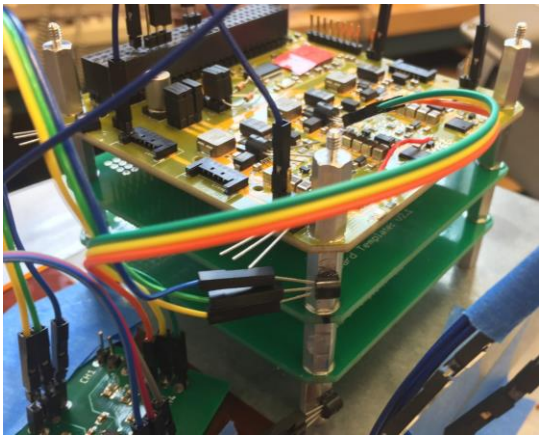

Figure 5.35: Power Generation Board Thermal Test Configuration

5.6 Operations

5.6.1 On-orbit Telecommunication, Telemetry, and Control

Shifting from the lab to long distance communications entailed a significant reduction in received data. In the lab HS-1 generated a high volume of data through both direct UART connections to individual MCUs as well as the full volume of traffic on the CAN bus. Additionally, there was data gathered from the power supplies providing HS-1 life support, the voltage meters, and the numerous LEDs providing visual feedback. The transition was fully completed with COM1 implemented as a hardware layer for the CAN bus; the intent was for COM1 to provide, as

closely as possible, the same user interaction with the HS-1 on-orbit as in the lab. The result of these efforts is depicted in Fig. 5.36.

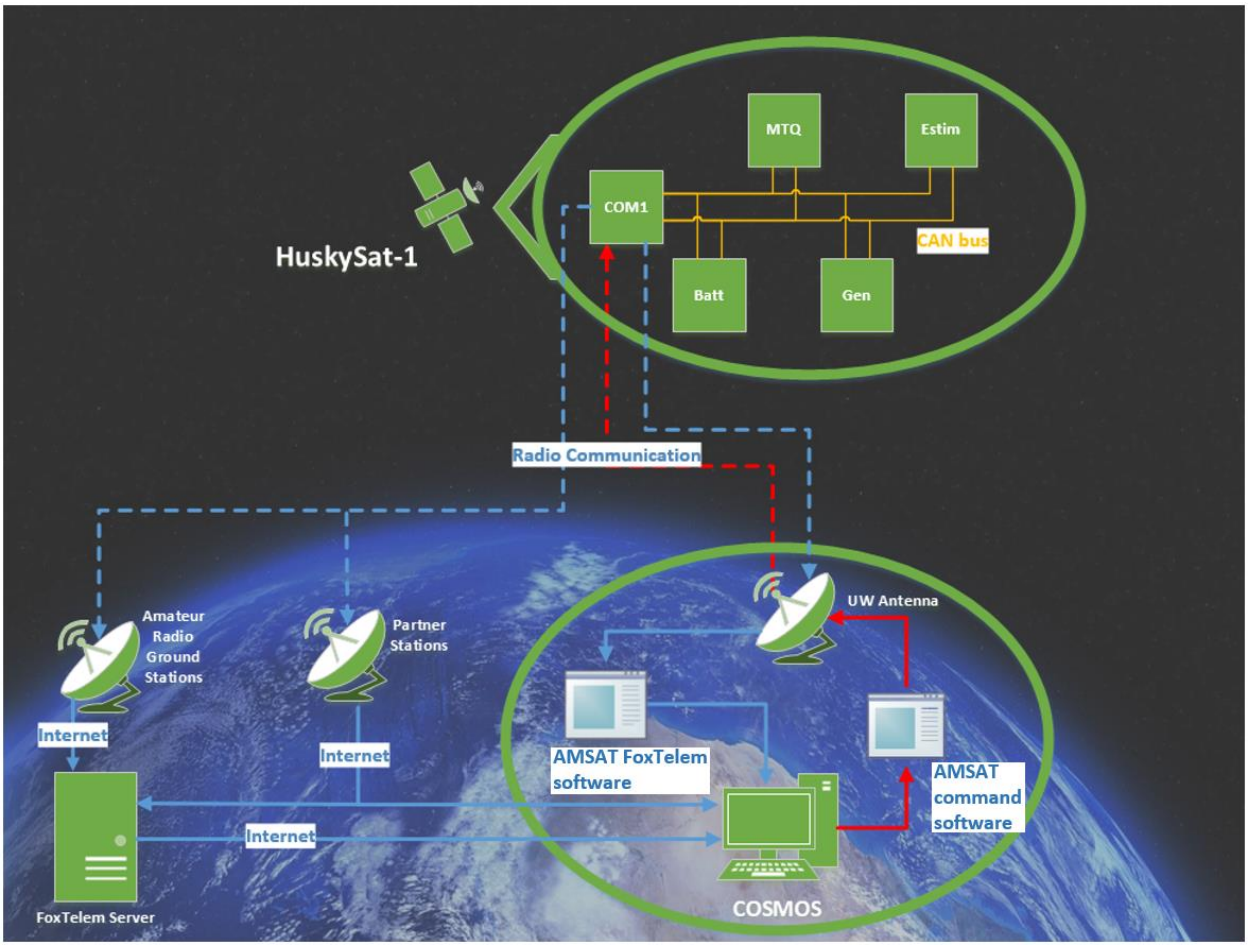

Figure 5.36: On-Orbit Data Flow

There are three primary data flow elements: (1) UW ground station receive and transmit capabilities, (2) a worldwide network of volunteer Amateur Radio ground stations with receive functionality, and (3) dedicated partnered Amateur Radio ground stations with receive functionality. All receiving capabilities utilize the freely available FoxTelem which demodulates, decodes, processes incoming telemetry frames, and forwards the data to the FoxTelem server and/or directly to COSMOS [179]. To provide a smooth transition implementing the COM1

hardware layer, this latter functionality was implemented to mimic the framing of the CAN packets provided by the PEAK-CAN adapter used during development. The uplink of commands begins is COSMOS, passes to an AMSAT provided software package, and is packaged, encoded, and modulated to baseband. The UW ground station utilized an IC9100 radio for the uplink, and a FunCube Dongle Pro Plus software designed radio for the receiver. The antennas were a UHF 13.3 dBic and VHF dBic antennas manufactured by M2 Antenna Systems. The preamp was a SSB-Electronic 1037-NF whose performance was measured in Fig. 5.37. For cabling LMR-600-DB was used between the antenna and preamp followed by LMR400 Ultraflex. The rotator was a Yaesu G-5500 with a controller from Green Heron.

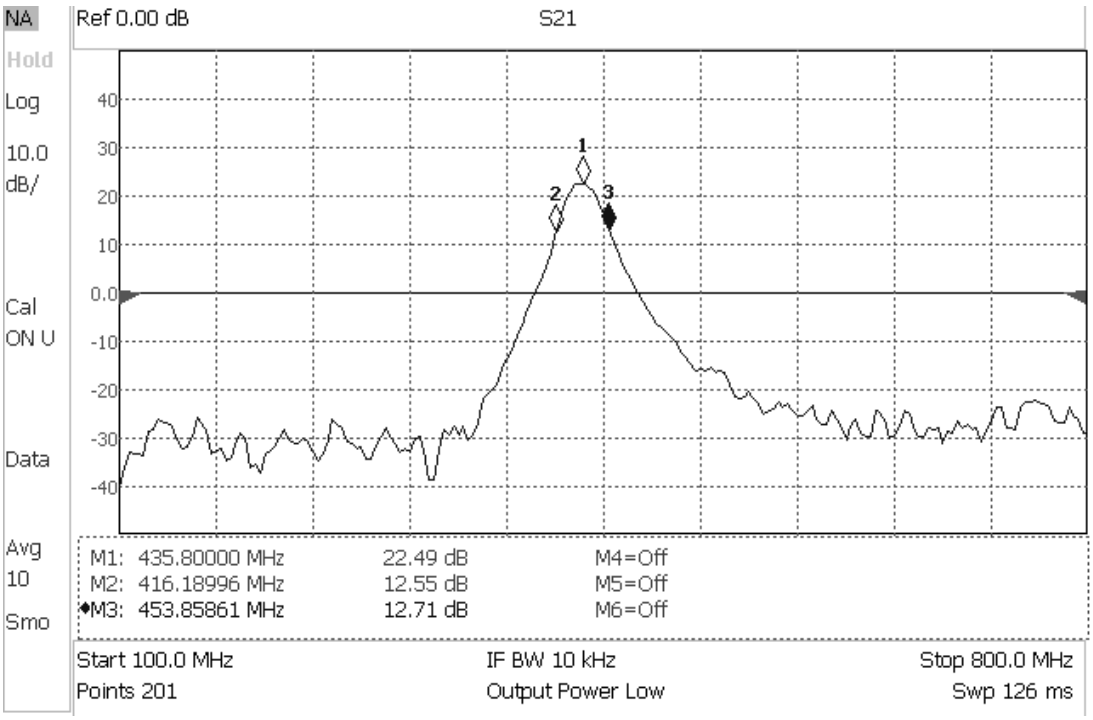

Figure 5.37: SSB-Electronic 1037-NF Pre-amplifier Insertion Loss

5.6.2 On-orbit Performance

On November 2nd, 2019 the HS-1 launched as an external secondary payload as part of the NG-12 Cygnus resupply mission to the International Space Station (ISS). The Cygnus remained docked until January 31st 2020 subsequently raising altitude and deploying multiple CubeSats, including the HS-1, Swamsat-II from the University of Florida, and Orbital Factory 2 from the University of Texas. Post deployment, after waiting ~35min, the HS-1 antennas deployed and it entered SAFE mode beaconing 10s every 2min. First contact was established on February 1st at 4:27 pm (PST).

The UW ground station struggled to achieve sufficiently high reliability. Even though telemetry frames could be decoded for small sections of the sky, it was inadequate for operational checkout of HS-1 systems. This issue was ultimately addressed by partnering with two already existing, highly capable, Amateur Radio ground stations: Kenneth Swaggart's station and the Boeing Employees Amateur Radio Society (BEARS) station at the Museum of Flight. Both of these stations directed their FoxTelem to the UW ground station COSMOS instance. With this augmentation, these two station additions significantly improved the UW HS-1 operations by providing near full hemispherical coverage for reception while transmission was from the original UW ground station antenna system. Beyond these three ground stations, the worldwide network of Amateur Radio operators set up to receive HS-1 data was extremely valuable. It greatly expanded the capability of receiving real-time telemetry from the HS-1. Additionally, a store-and-forward feature within COM1 called whole-orbit-data (WOD) took advantage of the worldwide station coverage by providing HS-1 telemetry to 1min temporal resolution, see Fig 5.38.

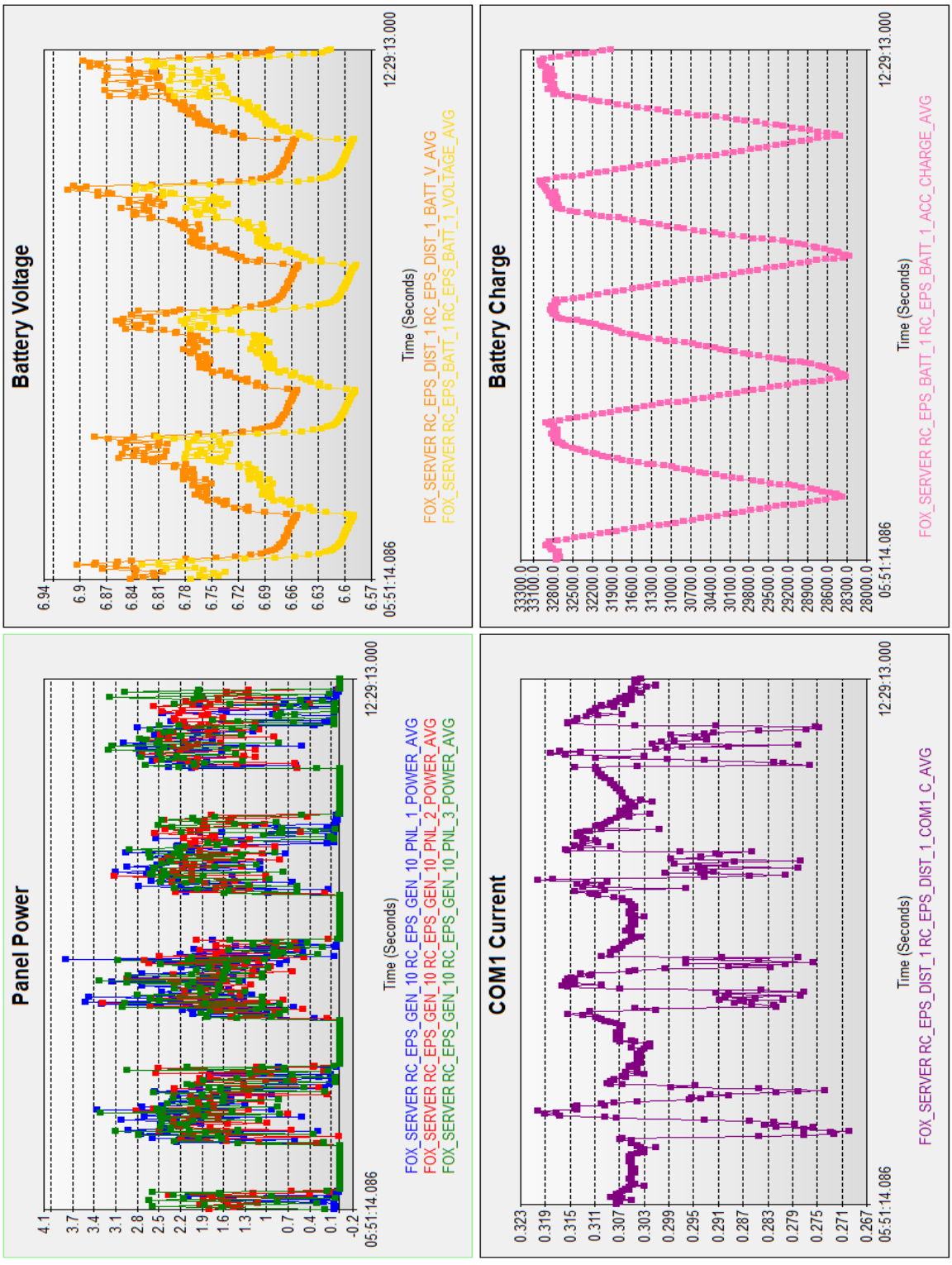

Figure 5.38: HS-1 Gapless Data Collection

The HS-1 temperature over ~3 months of operations oscillates with the orbital period but also changes due to subsystem power consumption states. Tumbling rate was not well correlated to temperature which is consistent with the HS-1 rotating ~10 times per sun exposure. Post deployment the HS-1 tumbled at ~4deg/s and over 2 weeks the tumbling rate decreased to the steady state ~1deg/s. The orbital temperature swing also varied location on the HS-1; a swing of 10-20C was typical for internal components while the backsides of the solar panels experienced swings of~40C, see Fig. 5.39.

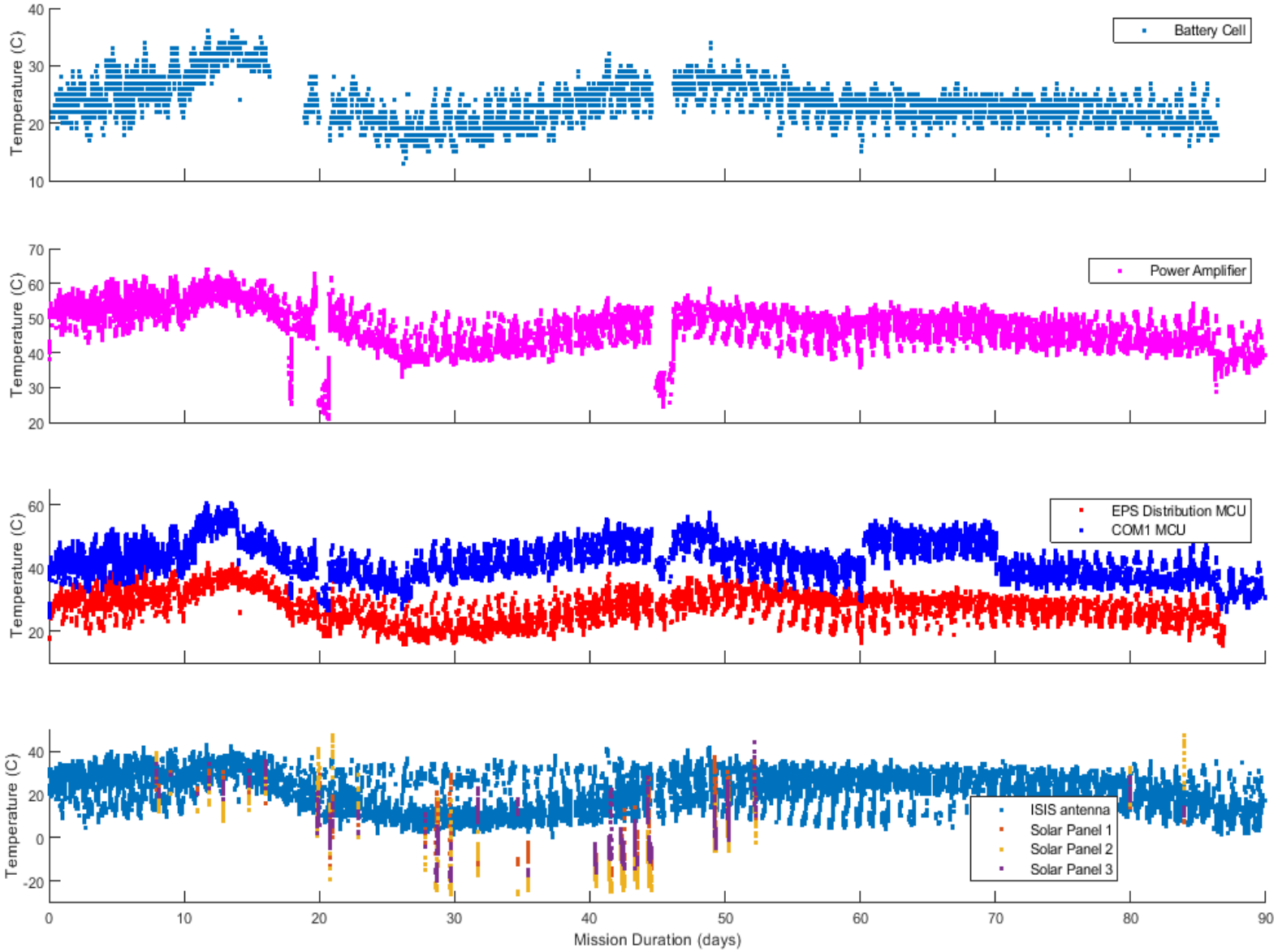

Figure 5.39: HS-1 Temperature over Mission Life

Over the ~3 months of operation the bus voltage remained high constant showing minimal depth of discharge on the battery pack. Orbit period fluctuations are shown in Fig. 5.38 and for the entire orbit in Fig. 5.40. This latter figure shows a drop in bus voltage which coincides with the full power on of the ADCS system.

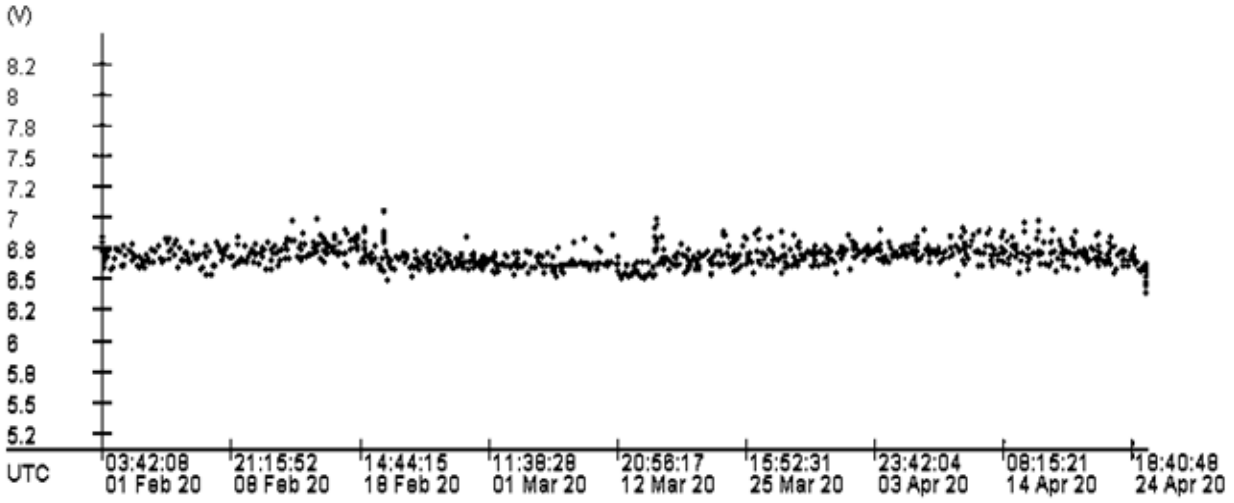

Figure 5.40: HS-1 Battery/Bus Voltage over Mission Life [179]

Initial on-orbit checkout of the HS-1 indicated the power system and COM1 were intact and fully operational. Weeks into the mission anomalous telemetry indicating the COM1 transmitter power had decreased, see Fig. 5.41. Ground stations were able to corroborate this claim, and subsequent investigation determined an additional behavioral alteration associated with the store-and-forward WOD function of COM1. The likely source of this fault was an external radiation event driven memory change. Various fixes were attempted, but none were able to address this issue. The issue did not impact overall operations for the UW team since the weaker telemetry beacon power of 17mW is still receivable by ground stations.

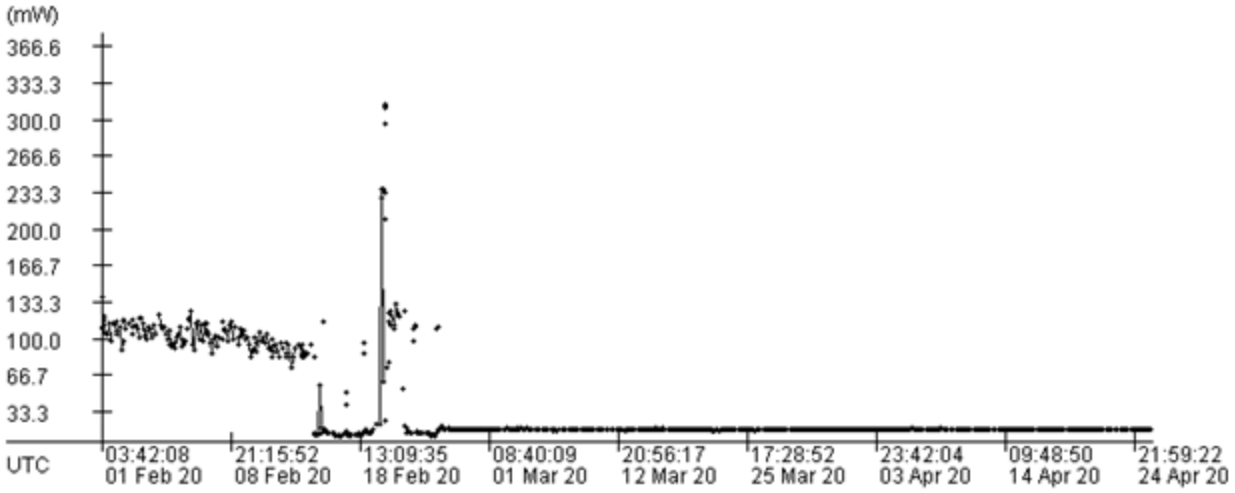

Figure 5.41: HS-1 COM1 RF Transmit Power over Mission Life [179]

Subsystem checkout and performance was met with overall success. The camera payload provided numerous pictures, such as Fig. 5.42. The sensors with the ADCS system, the sun sensor, magnetometers, and inertial measurement unit, all provided reasonable outputs. Further ADCS verification was limited due to the HS-1 tumbling rate threshold already below that of the de-tumbling system to activate. The PPT module checkout indicated that it was able to charge the high voltage capacitors. However, a full system fire operation was not achieved, and further diagnostics suggested the igniter circuit was not providing an ignition spark. COM2 verification was completed using the uplink and downlink provided by COM1. Telemetry showed correct power draw in various states indicating COM2 survived the launch environment. However, fully successful reception of COM2 on the ground was not attempted due to limited project resources.

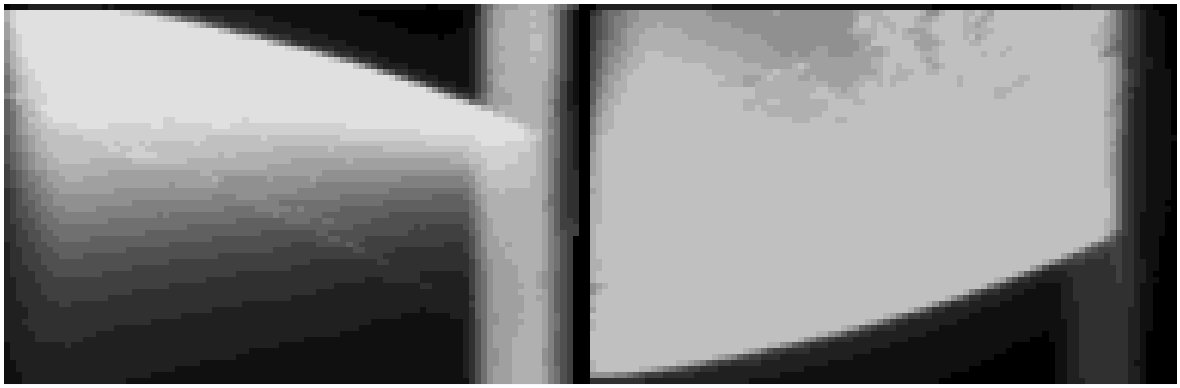

Figure 5.42: HS-1 Pictures of Earth Sent Back

AMSAT members and the amateur radio community continue to support this mission by continually receiving, decoding, sending HS-1 data to the FoxTelem server, and allowing it to be viewable by anyone [114].

5.7 Project Resources

Project resources are found on GitHub:

- PCB designs are available including most engineering model version. The final designs are in folders labelled “flight”. For instance the RF Front End in COM2 is located at: https://github.com/UWCubeSat/DubSat1/tree/master/teams/comm2/flight/RFfrontend_v4
- All HS-1 vehicle software is found in the UWCubeSat/DubSat1 repository
- HS-1 operations software is found in the UWCubeSat repository. Interested readers are recommended to start at: https://github.com/UWCubeSat/DS1Ops/tree/master/COSMOS/flight/outputs/handbooks
- For parsing mission data see run the script `parse_data.py` which should automatically pull down and parse the data from FoxTelem and produce results similar to those in the `_raw` directory: https://github.com/UWCubeSat/DS1Ops/tree/master/mission_data

Chapter 6. Conclusion

This thesis laid out the scientific motivation for the importance of further investigation into the Sun-Earth Lagrange point L4 and L5 regions for additional Trojan asteroids. The existence of Earth Trojans are supported by numerical analysis, yet to date only one Trojan has been identified. As asteroids allow us to peer into the solar system's evolutionary past, discovery of new Earth Trojans are especially valuable because they allow us to infer the conditions of the solar system during the formation of Earth. The Sun-Earth L4 and L5 points are particularly difficult to view from Earth's vantage point due to these regions being in the daytime sky. Here, we have outlined an alternative approach to detect new candidate Earth Trojans: Send a small low-cost CubeSat directly to these regions for in-situ surveying using a narrow field camera. While previous space system development has been primarily military, civil, and commercial, CubeSats present a paradigm shift in spacecraft development enabling research institutions direct access to Earth and space science. CubeSats leverage the ongoing miniaturization of electronics and their related technologies. In the past 10 years CubeSats have proven themselves to be invaluable for carrying out Earth focused science at a fraction of the cost of traditional methods. By contrast CubeSats have seen limited use beyond low Earth orbit as a consequence of immature technology in deep space communication systems and propulsion systems.

Beyond lowering costs of spacecraft development, the other significant cost of access to space on a launch vehicle is beginning to significantly decrease. As evident by the "new space" industry which has begun pushing beyond Earth orbits: Examples include lunar lander missions sponsored by Google, Israel, India, and China. Beyond the Moon, SpaceX continues to push for Mars with development of the Star Ship. The frequency of upcoming launches presents a significant opportunity for universities to ride as secondary cargo to low Earth orbit and far beyond.

The Sun Earth Trojan Explorer Mission was defined with the top-level objective to improve the current upper bound of allowable Trojans by a reduction of 5x. With the current upper bound count at ~73 at L4 for $H \leq 20.5$ brightness, a 5x reduction decreases the upper bound count to 15 for $H \leq 20.5$ brightness. It was shown that this can be achieved using a camera lens size of 10cm at 20s exposure. The survey region size was defined and was used to derive the top-level communication downlink requirement of a 150 kbps data rate. In addition to this data rate, the top-level propulsion requirements were derived with particular emphasis on quantifying the sensitivity of the launch day window.

This thesis addressed two significant developments required for this Earth Trojan mission. The first was the proof-of-concept and prototyping of a compact and low-cost communication system based on the reflectarray antenna. The reflectarray is highly advantageous for CubeSat since it allows for flat surfaces to be deployed which serve as phase-tunable reflectors. Previous use of reflectarrays on CubeSats have seen very limited application with significant opportunities to improve their capabilities. My contributions improved on the previous applications by implementing a simpler and more efficient phase controllable reflectarray element leveraging low-cost fabrication techniques; these contributions result in a reflectarray design which can easily be leveraged to a wide variety of applications enabling the next generation of deep space CubeSat science missions.

The second area addressed in this thesis to support enabling the Trojan Asteroid mission was the in-house development of a CubeSat demonstrator mission, called the HuskySat-1. The HuskySat-1 was developed out of the Earth and Space Science department under the guidance of Professor Robert Winglee. This mission was unique because the majority of the spacecraft software and hardware was developed from scratch and entirely assembled at the UW. The

HuskySat-1 exemplifies how a complex endeavor can be carried out by educational organizations with little to no previous experience in space mission and spacecraft development. As project lead, I stood up and oversaw many of the processes demanded by this project, such as printed circuit board design rules, reflow oven assembly, conformal coating of electrical components, instrument automation, orientation projects and training materials for new students, mentorship for members, etc. At its peak, the HuskySat-1 project involved over 50 undergraduate students and provided a highly interdisciplinary learning experience outside of the classroom stretching students thinking far beyond their experiences with other school curriculum.

When beginning my research on CubeSats I found previous dissertations to be foundational. Dissertations were, and continue to be, an essential part of the strong CubeSat community which has progressed so far with what seems to be so little. I am amazed at what can be accomplished by building off other's ideas and contributions. In this vein, it is my hope that the work outlined in this thesis is carried forward. The decreasing cost of both access to space and CubeSat development, combined with the value CubeSats add to the student learning experience and the fact that they can support valuable science missions, makes this potential irresistible. I anticipate CubeSats, and smallsats in general, will continue to produce significant scientific value and increasingly will see use in applications far beyond Earth such as when searching for Earth Trojans. I dare more students to look up into the stars knowing that it’s no longer beyond their reach: What can we understand about the universe using a deep space CubeSat?

Bibliography

[1] Bland, P. A., & McBride, N. (2004). An introduction to the solar system. Milton Keynes: Open Univ.

[2] Klahr, H., Brandner W. (2010). Planet formation: Theory, observations, and experiments. Cambridge: Cambridge University

[3] Vita-Finzi, C., (2016). A history of the solar system. Berlin: Springer.

[4] Lauretta D. S., Apar D., (2010). Protoplanetary Dust. Cambridge: Cambridge University

[5] Pfalzner, S et al. "The Formation of the Solar System." Physica Scripta 90.6 (2015): 068001. Crossref. Web.

[6] Encrenaz T. (2004). The Solar System. Leipzig: Springer-Verlag

[7] Hilker, Michael. "The High Mass End of Extragalactic Globular Clusters." Reviews in Modern Astronomy (2010): 199–213. Crossref. Web.

[8] Lissauer, J. J., "Planet Formation, Protoplanetary Disks and Debris Disks", in "The Spitzer Space Telescope: New Views of the Cosmos", 2006, vol. 357, p. 31.

[9] Vogel, Manuel. (2015). The Formation of the Solar System: Theories Old and New (2nd Edition), by Michael Woolfson. Contemporary Physics. 57. 1-1. 10.1080/00107514.2015.1081623.

[10] B. Du, F. Gao and J. Xu, "The analysis of topology based on Lagrange points L4/L5 of Sun-Earth system for relaying in Earth and Mars communication," *2017 IEEE 9th International Conference on Communication Software and Networks (ICCSN)*, Guangzhou, 2017, pp. 533-537, doi: 10.1109/ICCSN.2017.8230169.

[11] Lagrange, Joseph-Louis (1867–92). "Tome 6, Chapitre II: Essai sur le problème des trois corps". *Œuvres de Lagrange* (in French). Gauthier-Villars. pp. 229–334.

[12] Doody, D., (2011). Basics of Space Flight: National Aeronautics and Space Administration.

[13] De la Fuente Marcos, C., and R. de la Fuente Marcos. "Asteroid 2013 ND15: Trojan Companion to Venus, PHA to the Earth." Monthly Notices of the Royal Astronomical Society 439.3 (2014): 2970–2977. Crossref. Web.

[14] *Martian Trojans*, The International Astronomical Union Minor Planet Center, 21 Aug. 2020, minorplanetcenter.net//iau/lists/MarsTrojans.html.

[15] *Earth Trojans*, The International Astronomical Union Minor Planet Center, 23 May 2019, minorplanetcenter.net/iau/lists/t_earthtrojans.html

[16] *Jupiter Trojans*, The International Astronomical Union Minor Planet Center, 23 May 2019, minorplanetcenter.net/iau/lists/t_jupitertrojans.html

[17] *Neptune Trojans*, The International Astronomical Union Minor Planet Center, 23 May 2019, minorplanetcenter.net/iau/lists/t_neptunetrojans.html

[18] Alexandersen, M. et al. "A Uranian Trojan and the Frequency of Temporary Giant-Planet Co-Orbitals." Science 341.6149 (2013): 994–997. Crossref. Web.

[19] *MPEC 2016-O10 : 2014 YX49*, The International Astronomical Union Minor Planet Center, 16 July 2016, minorplanetcenter.net//iau/mpec/K16/K16O10.html

[20] Connors, M., Wiegert, P. & Veillet, C. Earth's Trojan asteroid. Nature 475, 481–483 (2011). https://doi.org/10.1038/nature10233

[21] *JPL Small-Body Database Browser: 2010 TK7, Jet Propulsion Laboratory California Institute of Technology, accessed: 2 July 2020, ssd.jpl.nasa.gov/sbdb.cgi?sstr=3548081*

[22] *HORIZONS System, Jet Propulsion Laboratory California Institute of Technology, accessed: 2 July 2020, ssd.jpl.nasa.gov/?horizons*

[23] Zhou, Lei et al. "Orbital Stability of Earth Trojans." Astronomy & Astrophysics 622 (2019): A97.

[24] Wiegert, P. "Earth Trojan Asteroids: A Study in Support of Observational Searches." Icarus 145.1 (2000): 33–43. Crossref. Web.

[25] Connors, M., Wiegert, P. & Veillet, C. Earth's Trojan asteroid. Nature 475, 481–483 (2011). https://doi.org/10.1038/nature10233

[26] Mikkola, S. and Innanen, K., "On the Stability of High Inclination Trojans", Earth Moon and Planets, vol. 71, no. 3. pp. 195–198, 1995. doi: 10.1007/BF00612957.

[27] Todd, M. et al. "An Optimal Earth Trojan Asteroid Search Strategy." Monthly Notices of the Royal Astronomical Society: Letters 420.1 (2011): L28–L32. Crossref. Web.

[28] Todd, M. et al. "Predictions for the Detection of Earth and Mars Trojan Asteroids by the Gaia Satellite." Monthly Notices of the Royal Astronomical Society 437.4 (2013): 4019–4026. Crossref. Web.

[29] Robert J. "A CCD Search for Lagrangian Asteroids of the Earth–Sun System." Icarus, Volume 136, Issue 1 (1998): 154-167. Crossref. Web.

[30] Malhotra, Renu. "The Case for a Deep Search for Earth's Trojan Asteroids." Nature Astronomy 3.3 (2019): 193–194. Crossref. Web.

[31] Todd, M., D.M. Coward, and M.G. Zadnik. "Search Strategies for Trojan Asteroids in the Inner Solar System." Planetary and Space Science 73.1 (2012): 39–43. Crossref. Web.

[32] Todd M. (2013) Trojan Asteroids in the Inner Solar System. In: Badescu V. (eds) Asteroids. Springer, Berlin, Heidelberg

[33] Cambinaoni S. et al. "An Upper Limit on Earth's Trojan Asteroid Population From ISIRIS-REX." 49th Lunar and Planetary Science Conference 2018 (2018): 2083. Crossref Web.

[34] STEREO Hunts for Remains of an Ancient Planet near Earth. National Aeronautics and Space Administration, 9 Apr. 2009, science.nasa.gov/science-news/science-at-nasa/2009/09apr_theia.

[35] "STEREO - What's New?" Stereo Science Center, National Aeronautics and Space Administration, 10 Aug. 2020, stereo-ssc.nascom.nasa.gov/new.shtml.

[36] Dunbar, Brian. NASA Twin Spacecraft May Reveal Secret of Moon's Origin. National Aeronautics and Space Administration, 9 Apr. 2009, www.nasa.gov/centers/goddard/news/gravity_lot_pr.html.

[37] "About the Result of Observation near the L5 Point of the Sun-Earth System." Hayabusa2 Project, Japan Aerospace Exploration Agency, 23 Aug. 2017, www.hayabusa2.jaxa.jp/topics/20170823/.

[38] "Wide-Field Infrared Survey Explorer." Wide-Field Infrared Survey Explorer (WISE), University of California Los Angeles, 23 May 2020, www.astro.ucla.edu/~wright/WISE/.

[39] Prusti T. et al. “The Gaia Mission.” A&A 595 A1 (2016)DOI: 10.1051/0004-6361/201629272

[40] “OSIRIS-Rex Factsheet”, National Aeronautics and Space Administration, ehpd.gsfc.nasa.gov/documents/552572main_OSIRIS_REx_Factsheet.pdf

[41] “JPL Small-Body Database Search Engine.” Solar System Dynamics, Jet Propulsion Laboratory California Institute of Technology, 6 July 2020, ssd.jpl.nasa.gov/sbdb_query.cgi

[42] Bartels, Meghan. “Farewell, Ryugu! Japan's Hayabusa2 Probe Leaves Asteroid for Journey Home.” Space.com, 13 Nov. 2019, www.space.com/hayabusa2-spacecraft-leaves-asteroid-ryugu.html.

[43] M. Yoshikawa et al, "MISSION STATUS OF HAYABUSA2," 49th Lunar and Planetary Science Conference 2018 (LPI Contrib. No. 2083)

[44] “Near-Earth Asteroid Delta-V for Spacecraft Rendezvous” Jet Propulsion Laboratory California Institute of Technology, 26 Jan 2018, echo.jpl.nasa.gov/~lance/delta_v/delta_v.rendezvous.html

[45] “NEO Basics” Jet Propulsion Laboratory California Institute of Technology, cneos.jpl.nasa.gov/about/neo_groups.html

[46] Piazzi, G. et al. “Giuseppe Piazzi and the Discovery of Ceres G. Foderà Serio.” (2002).

[47] "Lucy: The First Mission to the Trojan Asteroids” National Aeronautics and Space Administration, 23 March 2020, https://www.nasa.gov/content/goddard/lucy-overview

[48] Koon, W. S.; Lo, M. W.; Marsden, J. E.; Ross, S. D. (2006). Dynamical Systems, the Three-Body Problem, and Space Mission Design. p. 9. Archived from the original on 2008-05-27. Retrieved 2008-06-09.

[49] Cornish J., “The Lagrange Points”, National Aeronautics and Space Administration, 1998, wmap.gsfc.nasa.gov/media/ContentMedia/lagrange.pdf

[50] Sheppard SS, Trujillo CA. A thick cloud of Neptune Trojans and their colors. Science. 2006;313(5786):511-514. doi:10.1126/science.1127173

[51] Warell, J., Karlsson, O., and Skoglöv, E., “Evolution of Mercury-like orbits: A numerical study”, Astronomy and Astrophysics, vol. 411. pp. 291–307, 2003. doi: 10.1051/0004-6361:20030902.

[52] Roach, John (2002). "Fighter Jet Hunts for "Vulcanoid" Asteroids". National Geographic News. Retrieved 2008-12-24.

[53] Woolfson, M.M. (1993). "Solar System – its origin and evolution". Q. J. R. Astron. Soc. 34: 1–20. Bibcode:1993QJRAS..34....1W

[54] “Ida and Dactyl in Enhanced Color.” Solar System Exploration, National Aeronautics and Space Administration, 28 Aug. 2018, solarsystem.nasa.gov/resources/1031/ida-and-dactyl-in-enhanced-color/?category=planets_jupiter.

[55] Britt, D. T.; Yeomans, D. K.; Housen, K.; Consolmagno, G. (2002). "Asteroid Density, Porosity, and Structure"

[56] P. Goldreich; W. R. Ward (1973). "The Formation of Planetesimals". *Astrophysical Journal*. 183: 1051.

[57] Vision and voyages decadal survey 2013-2022

[58] Markwardt, Larissa et al. “Search for L5 Earth Trojans with DECam.” Monthly Notices of the Royal Astronomical Society 492.4 (2020): 6105–6119. Crossref. Web.

[59] R. Sarma et al. “IAU Planet Definition: Some Confusion and Their Modifications.” (2008). Crossref. Web.

[60] Dunar, Andrew (1999). “The Power to Explore, A history of Marshal Space Flight Center 1960-1990". National Aeronautics and Space Administration.

[61] Howell, Elizabeth. “Navstar: GPS Satellite Network.” SPACE, 27 Apr. 2018, https://www.space.com/19794-navstar.html

[62] McDuffie, Juquai. “Why the Military Released GPS to the Public.” Popular Mechanics, 19 Jun. 2017, https://www.popularmechanics.com/technology/gadgets/a26980/why-the-military-released-gps-to-the-public/

[63] “History of the CubeSat.” Space Daily, 23 Aug. 2016, https://www.spacedaily.com/reports/History_of_the_CubeSat_999.html

[64] Mehrparvar, Arash. "CubeSat Design Specification." CubeSat. CalPoly, 20 Feb. 2014. Web. 31 May 2017. <http://www.cubesat.org/resources/>.

[65] Jackson, Shanessa. "About CubeSat Launch Initiative." NASA. N.p., 17 Feb. 2017. Web. 31 May 2017. <https://www.nasa.gov/content/about-cubesat-launch-initiative>.

[66] "Achieving science with CubeSats: Thinking inside the box (Conference Presentation) ", Proc. SPIE 9978, CubeSats and NanoSats for Remote Sensing, 997802 (September 19, 2016); doi:10.1117/12.2238764;

[67] Swartwout, Michael. "CubeSat Database." Saint Louis University, n.d. Web. 31 May 2017. <https://sites.google.com/a/slu.edu/swartwout/home/cubesat-database>.

[68] Stirone, Shannon. "The Real Cost Of NASA Missions." Popular Science. N.p., 4 Nov. 2015. Web. 31 May 2017. <http://www.popsci.com/real-cost-nasa-missions#page-3>.

[69] Spacex. "Capabilities & Services." SpaceX. N.p., 27 Nov. 2012. Web. 31 May 2017. <http://www.spacex.com/about/capabilities>.

[70] Jackson, Shanessa. "About CubeSat Launch Initiative." NASA. N.p., 17 Feb. 2017. Web. 31 May 2017. <https://www.nasa.gov/content/about-cubesat-launch-initiative>.

[71] Antczak, John (November 9, 2009). "After letdown, solar-sail project rises again". MSNBC. Associated Press.

[72] Saptarshi Bandyopadhyay, Giri P. Subramanian, Rebecca Foust, Daniel Morgan, Soon-Jo Chung, and Fred Hadaegh. "A Review of Impending Small Satellite Formation Flying Missions", 53rd AIAA Aerospace Sciences Meeting, AIAA SciTech Forum, (AIAA 2015-1623)

[73] David, Leonard. On Far Side of the Moon, Chinese Lander and Rover Hit One-Year Mark. Space, 3 Jan. 2020, www.space.com/china-moon-far-side-lander-rover-chang-e-4-milestone.html.

[74] Wall, Mike. *This Is the Last Photo Israel's Beresheet Moon Lander Ever Took*. Space, 18 Apr. 2019, www.space.com/israel-moon-lander-beresheet-last-photo.html.

[75] Dwyer, Colin. 2 Months After Failed Moon Landing, India Acknowledges Its Craft Crashed. NPR, 26 Nov. 2019, www.npr.org/2019/11/26/782890646/2-months-after-failed-moon-landing-india-admits-its-craft-crashed.

[76] “Artemis: Humanity’s Return To The Moon.” National Aeronautics and Space Administration, Retrieved 4 Aug. 2020, https://www.nasa.gov/specials/artemis/

[77] “NASA Selects Blue Origin, Dynetics, SpaceX for Artemis Human Landers.” National Aeronautics and Space Administration, 30 Apr. 2020, https://www.nasa.gov/feature/nasa-selects-blue-origin-dynetics-spacex-for-artemis-human-landers

[78] Kluger, Jeffrey. Bezos Targets the Moon by 2024. Time, 10 May 2019, time.com/5587227/jeff-bezos-amazon-moon-blue-origin/.

[79] “The New Space Race”. Google Lunar XPRIZE, Retrieved 19 Jun. 2020, https://lunar.xprize.org/prizes/google-lunar

[80] Bartels, Meghan. Yusaku Maezawa's #DearMoon Project Aims for Lunar Art. Here's What Some Artists Think. Space, 20 Sept. 2018, www.space.com/41881-dearmoon-art-project-spacex-moon-artists-respond.html.

[81] “New Glenn: Our (really) big step – an orbital reusable launch that will build the road to space.” Blue Origin, Retrieved 18 Jun. 2020, https://www.blueorigin.com/new-glenn/

[83] Knapp, Alex. Apollo 11's 50th Anniversary: The Facts And Figures Behind The $152 Billion Moon Landing. Forbes, 5 Sept. 2020, www.forbes.com/sites/alexknapp/2019/07/20/apollo-11-facts-figures-business/.

[84] Berger, Eric. “The White House Puts a Price on the SLS Rocket-and It's a Lot.” Ars Technica, 6 Nov. 2019, arstechnica.com/science/2019/11/the-white-house-puts-a-price-on-the-sls-rocket-and-its-a-lot/

[85] “Mars 2020 Mission Perseverance Rover”. National Aeronautics and Space Administration, Retrieved 6 Jun. 2020, https://mars.nasa.gov/mars2020/mission/overview//

[86] "China to launch Mars probe in July". China Daily, 23 January 2020, https://www.chinadaily.com.cn/a/202001/23/WS5e2963eea310128217273086.html

[87] Clark, Stephen (8 May 2015). "UAE details ambitious plan for Martian weather satellite". Spaceflight Now. 10 May 2015. <http://spaceflightnow.com/2015/05/08/uae-details-ambitious-plan-for-martian-weather-satellite/>.\

[88] Jones, Andrew (12 March 2020). "ExoMars rover mission delayed to late 2022". Spaceflight Now. Retrieved 12 March 2020. <https://spacenews.com/exomars-rover-mission-delayed-to-late-2022/>

[89] Kasai, Yasuko (13 June 2018). "Tera-hertz Explorer, TEREX, Mission" (PDF). *University of Tsukuba*. NICT.

[90] Jatiya, Satyanarayan (18 July 2019). "Rajya Sabha Unstarred Question No. 2955". Archived from the original (PDF) on 30 August 2019. Retrieved 18 July 2019. <https://164.100.158.235/question/annex/249/Au2955.pdf>

[91] Back to the Red Planet. Johns Hopkins APL. 17 November 2017. <https://www.jhuapl.edu/PressRelease/171117>

[92] Elon Musk: we can launch a manned mission to Mars by 2024 – video. The Guardian. 29 September 2017. <https://www.theguardian.com/science/video/2017/sep/29/elon-musk-manned-mars-mission-spacex-video>

[93] “Starship Users Guide version 1”. SpaceX, Retrieved 5 Jun. 2020, https://www.spacex.com/sites/spacex/files/starship_users_guide_v1.pdf

[94] Wall, Mike. SpaceX's Starship May Fly for Just $2 Million Per Mission, Elon Musk Says. Space, 6 Nov. 2019, www.space.com/spacex-starship-flight-passenger-cost-elon-musk.html.

[95] Singh, Surendra (20 February 2018). "Chandrayaan-2 mission cheaper than Hollywood film Interstellar". *The Times of India*. Times News Network. Retrieved 3 March 2018. <https://timesofindia.indiatimes.com/home/science/chandrayaan-2-mission-cheaper-than-hollywood-film-interstellar/articleshow/62990361.cms>

[96] Shin, Dong (29 October 2014). "201 Frequency and Channel Assignments". Deep Space Network. https://deepspace.jpl.nasa.gov/dsndocs/810-005/201/201C.pdf

[97] Martin-Mur, T. "Navigating MarCO, the First Interplanetary CubeSats." Jet Propulsion Laboratory California Institute of Technology, 18th Australian International Aerospace Congress, 24-28 February (2019). Crossref. Web.

[101] Northway, Paige, and Winglee, Robert M. Innovations in Pulsed Plasma Thrusters to Enable CubeSat Science Missions. University of Washington, 2020.

[102] Johnson, Ian Kronheim, and Winglee, Robert M. Expanding the Capabilities of the Pulsed Plasma Thruster for in-Space and Atmospheric Operation. University of Washington, 2015.

[103] Harrill, Rob. UW Undergraduates Reveal Their Design for 'Dawgstar' Nanosatellite. University of Washington, 9 June 1999, www.washington.edu/news/1999/06/09/uw-undergraduates-reveal-their-design-for-dawgstar-nanosatellite/.

[104] "Operations and Rules". *CubeQuest Challenge Ground Tournaments, Deep Space Derby, and Lunar Derby.* National Aeronautics and Space Administration, 30 Dec. 2015, https://www.nasa.gov/sites/default/files/atoms/files/ccp_cq_opsrul_001c2.pdf

[105] McAllister-Day, Trevor. UW CubeSat program shoots for the moon. University of Washington, 3 June 2015, http://www.dailyuw.com/news/article_8bb8e772-0a75-11e5-b33c-1393e41e510d.html

[106] "30% Triple Junction GaAs Solar Cell Assembly". AZURSPACE, 18 Aug. 2016, https://sourceforge.isae.fr/svn/dcas-soft-espace/support/externalRessources/0003401-01-01_DB_3G30A.pdf

[107] "High Power Lithium Ion APR18650M1A". A123Systems, 2009, https://www.batteryspace.com/prod-specs/6612.pdf

[108] "Electronic Power System CubeSTAR". CubeStar, A Space Weather Satellite Built By Students. Retrieved 9 June 2020, http://cubestar.no/index.php?p=1_19_Electronic-Power-System

[109] Wikipedia contributors. "EQUiSat." Wikipedia, The Free Encyclopedia. Wikipedia, The Free Encyclopedia, 2 Dec. 2019. Web. 20 Sep. 2020.

[110] Katz, S. et al, CSUNSat1: Low Mass, Extreme Low-Temperature Energy Storage. California State University Northridge and Jet Propulsion Laboratory, http://www.csun.edu/cubesat/img/CSUNSat1_Fact_Sheet-07July15.pdf

[111] Barsukov, Yevge. Battery Cell Balancing: What to Balance and How. Texas Instruments. Retrieved 10 Aug. 2020, https://www.ti.com/download/trng/docs/seminar/Topic%202%20-%20Battery%20Cell%20Balancing%20-%20What%20to%20Balance%20and%20How.pdf

[112] Husky Satellite Lab, Retrieved 10 Aug 2020, huskysatellitelab.com/

[113] Archambeault, Bruce R., and Drewniak, James. PCB Design for Real-World EMI Control. United States, Springer US, 2013.

[114] UW HuskySat. www.amsat.org/tlm/health.php?id=6.

[115] Baker, Keith. "A Brief History of AMSAT." AMSAT, Retrieved 11 Aug. 2020, www.amsat.org/amsat-history/.

[116] "Title 47 → Chapter I → Subchapter D → Part 97." Electronic Code of Federal Regulations (ECFR), Federal Communications Commission.

[117] "Antenna Systems". ISIS, Retrieved 13 Aug. 2020, https://www.isispace.nl/wp-content/uploads/2019/08/ISIS-Antenna-Systems-Brochure-V2R-web.pdf

[118] "GENERAL ENVIRONMENTAL VERIFICATION STANDARD (GEVS) For GSFC Flight Programs and Projects". National Aeronautics and Space Administration, 22 April 2019, https://standards.nasa.gov/file/2746/download?token=QzdrIRW2

[119] Swartwout, Michael. CubeSat Data. Saint Louis University, Retrieved 10 Aug. 2020, https://sites.google.com/a/slu.edu/swartwout/home/cubesat-database#plots

[121] Wells, Sarah. Tiny Cubesats Could Do Big Science at the Moon and Venus. Space, 29 Mar. 2019, www.space.com/nasa-cubesats-proposed-moon-and-venus.html.

[122] "NASA Awards Contract to Launch CubeSat to Moon from Virginia". National Aeronautics and Space Administration, 14 Feb. 2020, https://www.nasa.gov/press-release/nasa-awards-contract-to-launch-cubesat-to-moon-from-virginia

[123] Schoolcraft, Josh & Klesh, Andrew & Werne, Thomas. (2017). MarCO: Interplanetary Mission Development on a CubeSat Scale. Jet Propulsion Laboratory. 10.1007/978-3-319-51941-8_10.

[124] Dunn, Marcia. Big Test Coming up for Tiny Satellites Trailing Mars Lander. Phys.org, 22 Nov. 2018, phys.org/news/2018-11-big-tiny-satellites-trailing-mars.html.

[125] Wall, Mike. Rocket Lab Will Launch a Cubesat to the Moon for NASA next Year. Space, 18 Feb. 2020, www.space.com/rocket-lab-launching-nasa-moon-cubesat-2021.html.

[126] Walker, R. et al. "Deep-space CubeSats: thinking inside the box". A&G Vol. 59. October 2018. Crossweb. Ref.

[127] Kovo, Yael. State of the Art of Small Spacecraft Technology. National Aeronautics and Space Administration, 6 Mar. 2020, www.nasa.gov/smallsat-institute/sst-soa.

[128] Howard, David. Centennial Challenges Program Update: From Humanoids to 3D-Printing Houses on Mars, How the Public Can Advance Technologies for NASA and the Nation, 2018 AIAA SPACE and Astronautics Forum and Exposition, Sep. 2018, DOI: 10.2514/6.2018-5221

[129] Bouwmeester, Jasper, and J. Guo. "Survey of worldwide pico-and nanosatellite missions, distributions and subsystem technology." Acta Astronautica 67.7 (2010): 854-862.

[130] "Antennas". ISIS, Retrieved 5 May 2020, https://www.isispace.nl/product/antennas/

[131] Deep Space Network: Canberra Deep Space Communication Complex. "Antennas." NASA, 31 May 2017. <https://www.cdscc.nasa.gov/Pages/antennas.html>.

[132] Talbert, Tricia. Small Spacecraft Technology Program Selects New Projects. National Aeronautics and Space Administration, 3 May 2013, www.nasa.gov/directorates/spacetech/small_spacecraft/baa.html.

[133] D. G. Berry , R. G. Malech , and W. A. Kennedy , “ The reflectarray antenna , ” IEEE Trans. Antennas Propagate ., Vol. AP - 11 , Nov. 1963 , pp. 645 – 651 .

[134] Huang, J., & Encinar, José A. (2007). Reflectarray antennas. IEEE.

[135] A. Chen, Y. Zhang, Z. Chen and C. Yang, "Development of a Ka-Band Wideband Circularly Polarized 64-Element Microstrip Antenna Array With Double Application of the Sequential Rotation Feeding Technique," in *IEEE Antennas and Wireless Propagation Letters*, vol. 10, pp. 1270-1273, 2011, doi: 10.1109/LAWP.2011.2175433.

[136] N. Chahat, J. Sauder, M. Mitchell, N. Beidleman and G. Freebury, "One-Meter Deployable Mesh Reflector for Deep Space Network Telecommunication at X- and Ka-band," *2019 13th European Conference on Antennas and Propagation (EuCAP)*, Krakow, Poland, 2019, pp. 1-4.

[137] A. Babuscia, M. Van de Loo, Q. J. Wei, S. Pan, S. Mohan and S. Seager, "Inflatable antenna for cubesat: fabrication, deployment and results of experimental tests," 2014 IEEE Aerospace Conference, Big Sky, MT, 2014, pp. 1-12, doi: 10.1109/AERO.2014.7024296.

[138] A. Babuscia, T. Choi, J. Sauder, A. Chandra and J. Thangavelautham, "Inflatable antenna for CubeSats: Development of the X-band prototype," *2016 IEEE Aerospace Conference*, Big Sky, MT, 2016, pp. 1-11, doi: 10.1109/AERO.2016.7500679.

[139] Dahri, Muhammad & Kamarudin, M.R. & Jamaluddin, Mohd haizal & Selvaraju, Raghuraman & Inam, Muhammad. (2017). Broadband Resonant Elements for 5G Reflectarray Antenna Design. TELKOMNIKA. 15. 10.12928/TELKOMNIKA.v15i2.6122.

[140] MarCO reflectarray: R. E. Hodges, N. E. Chahat, D. J. Hoppe and J. D. Vacchione, "The Mars Cube One deployable high gain antenna," 2016 IEEE International Symposium on Antennas and Propagation (APSURSI), Fajardo, 2016, pp. 1533-1534, doi: 10.1109/APS.2016.7696473.

[141] R. E. Hodges, M. J. Radway, A. Toorian, D. J. Hoppe, B. Shah and A. E. Kalman, "ISARA - Integrated Solar Array and Reflectarray CubeSat deployable Ka-band antenna," *2015 IEEE International Symposium on Antennas and Propagation & USNC/URSI National Radio Science Meeting*, Vancouver, BC, 2015, pp. 2141-2142, doi: 10.1109/APS.2015.7305460.

[142] Yang, F., & Rahmat-Samii, Yahya. (2019). *Surface Electromagnetics: With Applications in Antenna, Microwave, and Optical Engineering*. Cambridge, United Kingdom; New York, NY: Cambridge University Press.

[143] A. Chen, Y. Zhang, Z. Chen and S. Cao, "A Ka-Band High-Gain Circularly Polarized Microstrip Antenna Array," in *IEEE Antennas and Wireless Propagation Letters*, vol. 9, pp. 1115-1118, 2010, doi: 10.1109/LAWP.2010.2093866.

[144] Shaker, J., Chaharmir, M. R., & Ethier, J. (2014). Reflectarray antennas: Analysis, design, fabrication, and measurement.

[145] Nayeri, Payam, "Advanced Design Methodologies and Novel Applications of Reflectarray Antennas" (2012). Electronic Theses and Dissertations. 207.

[146] Skelly, Clare. NASA Demos CubeSat Laser Communications Capability. National Aeronautics and Space Administration, 9 Apr. 2019, www.jpl.nasa.gov/news/news.php?feature=7371.

[147] "Search results for 'Martian meteorites'". Meteoritical Bulletin. Meteoritical Society. Retrieved 27 April 2020.

[148] "25143 Itokawa." Solar System Exploration, National Aeronautics and Space Administration, 19 Dec. 2019, solarsystem.nasa.gov/asteroids-comets-and-meteors/asteroids/25143-itokawa/in-depth/.

[149] "Stardust Sample Return", Press Kit. National Aeronautics and Space Administration, Jan. 2006, jpl.nasa.gov/news/press_kits/stardust-return.pdf

[150] "Current Status of the asteroid explorer, Hayabusa2, leading up to arrival at asteroid Ryugu in 2018", JAXA Hayabusa2 Project. Japan Aerospace Exploration Agency, 14 June 2018, global.jaxa.jp/projects/sat/hayabusa2/pdf/Hayabusa2_Press20180614e.pdf

[151] "NASA's OSIRIS-REx Asteroid Sample Return Mission". National Aeronautics and Space Administration, FS-206-4-411-GSFC, https://www.nasa.gov/sites/default/files/atoms/files/osiris_rex_factsheet5-25.pdf

[152] Chaikin, Andrew (2007). *A Man On the Moon: The Voyages of the Apollo Astronauts* (Third ed.). New York: Penguin Books.

[153] Weissman, P. R. and Wetherill, G. W., "Periodic Trojan-type orbits in the Earth-Sun system", The Astronomical Journal, vol. 79. p. 404, 1974. doi: 10.1086/111559.

[154] Zhou, Lei et al. "Orbital stability of Earth Trojans". *Astronomy & Astrophysics* 622. (2019): A97.

[155] Marzari, F., Scholl, H. Long term stability of Earth Trojans. Celest Mech Dyn Astr 117, 91–100 (2013). https://doi.org/10.1007/s10569-013-9478-7

[156] C. C. Liebe, "Accuracy performance of star trackers - a tutorial," in *IEEE Transactions on Aerospace and Electronic Systems*, vol. 38, no. 2, pp. 587-599, April 2002, doi: 10.1109/TAES.2002.1008988.

[157] Karttunen, Hannu & Kröger, Pekka & Oja, Heikki & Poutanen, Markku & Donner, Karl. (2007). Fundamental Astronomy. 10.1119/1.2342728

[158] CBolte. "Signal-to-Noise in Optical Astronomy." *AY 257 – Modern Observational Techniques*, www.ucolick.org/~bolte/AY257/s_n.pdf.

[159] Elias, Jay. "Estimating Lunar Phase Requirements." *Cerro Tololo Inter-American Observatory*, vol. 37, 1 Mar. 1994.

[160] "CCD Image Sensor Noise Sources." *Image Sensor Solutions Eastman Kodak Company*, 8 Aug. 2001, www.uni-muenster.de/imperia/md/content/ziv/multimedia/downloads/kodak___noise_sources.pdf.

[161] "KAF- 0401E Performance Specification." *Eastman Kodak Company Image Sensor Solutions,* 16 Oct. 2002, www.bndhep.net/Electronics/Data/KAF0401E.pdf.

[162] Newberry, Michael. (1991). Signal-to-noise considerations for sky-subtracted CCD data. Publications of the Astronomical Society of the Pacific. 103. 10.1086/132801.

[163] John, K. K., et al. "46th Lunar and Planetary Science Conference." NASA Johnson Space Center, Investigating Trojan Asteroids at the L4/L5 Sun-Earth Lagrange Points. , 2015.

[164] "H (Absolute Magnitude)." *Center for Near Earth Object Studies*, Jet Propulsion Laboratory California Institute of Technology, cneos.jpl.nasa.gov/glossary/h.html.

[165] Bate, Roger R.; Donald D. Mueller; Jerry E. White (1971). *Fundamentals of Astrodynamics*. New York: Dover Publications.

[166] Meeus, Jean (1997), *Mathematical Astronomy Morsels*, Richmond, VA: Willmann-Bell, pp. 11–12, 22–23, ISBN 0-943396-51-4

[167] Curtis, Howard D. *Orbital Mechanics for Engineering Students*. 3rd ed., Elsevier Butterworth Heinemann, 2014.

[168] Pence, W. D., et al. "Lossless Astronomical Image Compression and the Effects of Noise." *Publications of the Astronomical Society of the Pacific*, vol. 121, no. 878, 2009, pp. 414–427. *JSTOR*, www.jstor.org/stable/10.1086/599023. Accessed 30 Sept. 2020.

[169] Chang, Christine. DSN Telecommunications Link Design Handbook. Rev. E ed., vol. 810-005, Jet Propulsion Laboratory, 2000.

[170] Pham, Timothy. *Deep Space Network Services Catalog*. Rev. F ed., vol. 820-100, Jet Propulsion Laboratory, 2015.

[171] "Table 13-11." *Space Mission Analysis and Design*, by James Richard. Wertz, 3rd ed., Microcosm Press and Springer, 1999, p. 562.

[172] Wertz, James Richard, et al. *Space Mission Engineering: the New SMAD*. Microcosm Press, 2011.

[173] "KAF-3200 2184 (H) x 1472 (V) Full Frame CCD Image Sensor." *Semiconductor Components Industries*, Rev. 3, Mar. 2015, www.onsemi.com/pub/Collateral/KAF-3200-D.PDF.

[174] Hodges, R. et al. "The ISARA Mission – Flight Demonstration of a High Gain Ka-Band Antenna for 100Mbps Telecom." (2018).

[175] David Bell. *Iris V2.1 CubeSat Deep Space Transponder*, National Aeronautics and Space Administration, www.jpl.nasa.gov/cubesat/pdf/Brochure_IrisV2.1_201611-URS_Approved_CL16-5469.pdf.

[176] Anderson, Harry R. (2003). *Fixed broadband wireless system design*. US: John Wiley & Sons. pp. 206–207. ISBN 978-0-470-84438-0.

[177] "HMC7054 KA-BAND HPA." *Analog Devices*, v03.0216, https://www.analog.com/media/en/technical-documentation/data-sheets/HMC7054.pdf

[178] I. I. Shvetsov-Shilovskiy, A. B. Boruzdina, A. V. Ulanova, O. M. Orlov, Y. A. Matveev and D. V. Negrov, "FRAM test memory cells radiation hardness research," 2017 IEEE 30th International Conference on Microelectronics (MIEL), Nis, 2017, pp. 255-257, doi: 10.1109/MIEL.2017.8190115.

[179] Thompson, Chris. FoxTelem. 1.08i, AMSAT, 10 May 2020